Phase Characterisation of Nickel-Based Superalloys Using Ultrasound

Jennifer Hanako Jobling

A thesis submitted to Imperial College London for the degree of

Doctor of Engineering

Department of Mechanical Engineering

Imperial College London

SW7 2AZ

November 2024

Declaration of Originality

The content of this thesis my own research work, which was completed under the supervision of Dr Bo Lan, Professor Michael Lowe, and Dr Tim Barden. Where the work of others has been used, the appropriate references have been provided.

Jennifer Hanako Jobling

13/11/24

Copyright Declaration

The copyright of this thesis rests with the author. Unless otherwise indicated, its contents are licensed under a Creative Commons Attribution-Non Commercial 4.0 International Licence (CC BY-NC).

Under this licence, you may copy and redistribute the material in any medium or format. You may also create and distribute modified versions of the work. This is on the condition that: you credit the author and do not use it, or any derivative works, for a commercial purpose.

When reusing or sharing this work, ensure you make the licence terms clear to others by naming the licence and linking to the licence text. Where a work has been adapted, you should indicate that the work has been changed and describe those changes.

Please seek permission from the copyright holder for uses of this work that are not included in this licence or permitted under UK Copyright Law.

Abstract

The nickel-based superalloys are a class of materials with excellent mechanical properties and resistance to degradation, oxidation and corrosion at extremely high temperatures. This ability to withstand harsh operating environments makes them invaluable across many engineering applications, and their superior properties means that these superalloys are often used for highly critical components, where failure is catastrophic and unacceptable. It is therefore essential to ensure that no microstructural alterations or defects are present which could cause a loss in integrity of a part, as the microstructure of the material itself strongly influences properties including fatigue life, toughness and tensile strength. One key microstructural characteristic is the material's phase composition, as the amount and morphology of the different phases present can drastically influence overall mechanical behaviour. There are many techniques available for investigating microstructure, but those typically deployed in industry today are time-consuming, costly, and ultimately destructive, including scanning electron microscopy and hardness testing. In addition, only a very localised region can be inspected, and thus measurements are unlikely to be representative of the whole part.

This thesis presents the research undertaken towards developing a robust, rapid and reliable non-destructive technique, using ultrasonic wave speed measurements, enabling one bulk measurement to quantify the phase composition within a given nickel-based superalloy. Building on a method successfully utilised in quantifying texture, it has been found that the ultrasonic wave speed measurements in conjunction with a spherical harmonic framework is able to detect phase changes within a range of nickel-based superalloys with varying microstructures and manufacturing methods, including Inconel 718, Udimet 720Li and RR1000. This thesis details the investigations and analyses carried out on each of these materials, including the ultrasonic experiments and concurrent metallurgical tests, towards building a robust materials characterisation framework which could be deployed across the engineering industry in the future.

Acknowledgements

This EngD project would not have been possible without so many individuals, whose encouragement and support I greatly appreciate and will forever be grateful for. I couldn't have wished for kinder, more encouraging academic supervisors – thank you Dr Bo Lan and Professor Mike Lowe, for your patience and allowing me to return after my recovery, and also to Dr Keith Newton for your continued support from start to finish. I was very generously supported by many at Rolls-Royce; many thanks to Dr Tim Barden, for providing useful insights and research guidance along the way, and also to Eddy Saunders – I am so grateful for all the hours you dedicated to the preparation of samples for SEM and microscopy, and have really enjoyed getting excited about the whacky discoveries we made when looking at the microstructures. I will miss the detective work we have carried out over the past couple of years! Many thanks also to Nick Calcutt for helping me settle at Elton Road and introducing me to some key specialists – Dr Mark Hardy, thank you for your generosity with time and provision of superalloy discs, and Dr Ross Buckingham for assisting with copious amounts of furnace work. I'd also like to thank Rolls-Royce and EPSRC for the funding enabling this EngD, and also Dr Peter Thayer and NDEvR, for enabling me to travel to conferences in amazing locations, including the US, France, and the beautiful Loch Lomond. (I will swim there one day!)

I have had the opportunity to do some exciting experimental work elsewhere using amazing new techniques, including high speed AFM – thank you so much to Eddy for organising this, and to Dr Stacy Moore and Dr Tomas Martin for their time while I visited to use the amazing microscopes at the University of Bristol. Thank you also to the lovely NDE group at Imperial, for making the office such a jolly place to be when not travelling elsewhere; Melody, thank you for the companionship in the lab as we worked with our temperamental experiments, and lots of travel inspiration; André, Ming and Wei Yi, thank you for putting up with my endless questions about theoretical fundamentals; Panpan, thank you for being such a positive and calm desk neighbour whatever the day or hour, and I will treasure the PhD mug forever!

I have enjoyed the EngD hugely, but – as is the nature of all things experimental – it has not always been plain sailing. Thank you First Officer Garrett, for keeping my enthusiasm of aviation alive and providing exciting (and sometimes terrifying) anecdotes from the world of flying. Thank you to Auntie Trina for your encouragement and (Christmas) cheer, and thank you Jane, for being such an

amazing and long-suffering best friend, putting up with my obsession for aeroplanes and nickel-based superalloys, for always being there for me whatever the predicament, and for being an amazing travelling companion when a writing break was needed. Here's to many more JJ adventures!

Finally, to my parents – Dad, Mum, you have been so kind, so patient, so tolerant and always so supportive, even through some terrifically bad times which you didn't deserve! Thank you for helping me to navigate through recovery, for having me home much longer than you probably anticipated, and for never telling me to curb my enthusiasm – even when I end up doing (many) unexpected u-turns in my aerospace journey. Love always, and arigatougozaimasu!

Table of Contents

Declaration of Originality i
Copyright Declaration ii
Abstract iii
Acknowledgements iv
1. Introduction 1
2. Literature Review 9
2.1 Overview of Metallurgical Concepts 9
2.2 Current Methods for Materials Characterisation 10
2.3 Ultrasound NDE and Materials Characterisation 15
2.3.1 Benefits of Ultrasound Techniques 16
2.3.2 Review of Applications to Date 16
2.3.3 Ultrasound Backscattering and Attenuation 18
2.3.4 Ultrasonic Velocity Measurements 20
2.4 The Spherical Convolution Theoretical Framework 21
2.4.1 Origin of Method and Development 21
2.4.2 Theoretical Framework 23
2.4.3 Application for Phase Characterisation 25
2.5 Experimental Methodology – Ultrasonic Wave Speed Measurements 29
2.5.1 Double-through transmission technique 29
2.5.2 Ultrasonic Wave Speed Measurement Experimental Setup 31
2.5.3 Results Processing 35
2.5.4 Novel development: Application to Nickel-based Superalloys 40
2.6 The Nickel-Based Superalloys: An Overview 41
2.6.1 Nickel-based Superalloy Processing Methods 42
2.6.2 Nickel-based Superalloy Metallurgy 47
2.6.3 Phases in Nickel-Based Superalloys 49
2.6.4 Factors Affecting Nickel-based Superalloy Properties 51
2.6.5 Heat Treatment Processing: Precipitation Hardening 53
3. Feasibility Study: Inconel 718 56
3.1 Introduction 56
3.2 Microstructure, Manufacture and Properties of Inconel 718 56

3.2.1 Gamma, Gamma Prime and Gamma Double Prime 61
3.2.2 Delta Phase 63
3.2.3 The Carbide Phases 64
3.2.4 The Laves Phase 65
3.2.5 Thermo-mechanical processing (TMP) of Inconel 718 66
3.2.6 Summary 66
3.3 Feasibility Study Materials and Methods 67
3.4 Microscopy Examinations 69
3.4.1 Optical Micrographs 69
3.4.2 SEM Micrographs 71
3.5 UWS Testing Results 77
3.5.1 Velocity Surfaces 78
3.5.2 Pole Figures 79
3.5.3 Error Analysis of Wave Speed Measurement Platform 81
4. Phase Estimation of Inconel 718 86
4.1 Introduction 86
4.2 Inconel 718 'RR Furnace' Samples – Material Processing Methods 86
4.3 Microscopy Results 88
4.3.1 Kernel Average Misorientation (KAM) and Pattern Quality 96
4.4 RR Furnace Samples – UWS Results 100
4.4.1 Discussion 102
4.5 Hardness Testing 105
4.5.1 Results 107
4.6 Fully Aged Inconel 718 Samples 112
4.6.1 Microscopy 112
4.6.2 UWS Results 114
4.6.3 Discussion 116
4.7 High Speed Atomic Force Microscopy (HS-AFM) 118
4.7.1 Background 118
4.7.2 Experimental Methodology 119
4.7.3 Results 121
4.7.4 Discussion 126
4.8 Phase Estimation Trials of Inconel 718 127

4.8.1 SCECs of nickel for γ, and ImageJ estimates of δ 127
4.8.2 SCECs of Inconel 718 for γ, ImageJ estimates of δ 132
4.8.3 Experimental V00 of HD and aged samples 132
4.8.4 Simultaneous equations using experimental data and theoretical δ volume fraction ... 138
4.8.5 Simultaneous equations using experimental data only 139
4.8.6 Experimental data of WQ1000 and aged samples with theoretical δ volume fraction ... 140
4.8.7 OGHD sample(s) for γ, and WQ1000 with 3% δ phase for δ 141
4.8.8 Discussion and Summary 143
5. Application of UWS Technique to Udimet 720Li and RR1000 147
5.1 Introduction 147
5.2 Udimet 720Li – Microstructure, Processing and Properties 147
5.2.1 Chemistry and Heat Treatments 148
5.2.2 The gamma prime (γ') phase 150
5.2.3 Challenges for inspection 153
5.4 Udimet 720Li – Experimental Materials 156
5.5 Udimet 720Li UWS Results 157
5.6 Udimet 720Li Optical and SEM Micrographs 158
5.6.1 Further Analysis: EBSD and Hardness Tests 163
5.7 ImageJ and Phase Estimation 165
5.8 Attenuation Behaviour 166
5.9 Udimet 720Li: Discussion 168
5.10 RR1000 – Microstructure, Processing and Properties 169
5.10.1 Precipitation Considerations for RR1000 171
5.10.2 Chemistry of RR1000 172
5.10.3 Heat Treatments of RR1000 174
5.10.4 Summary 175
5.11 RR1000: Experimental Materials 176
5.12 RR1000: UWS Results 177
5.13 RR1000 Microstructure Investigations 178
5.13.1 Optical Micrographs 179
5.13.2 SEM Micrographs 182
5.13.3 Attenuation Analysis 185
5.14 RR1000 Experiments: Discussion 186

6. Industrial Relevance of EngD Research 189
7. Conclusions 191
7.1 Future Work 195
8. References 197
9. Appendices 229
9.1 ImageJ Binary Technique 229
9.2 Reduced Order UWS Investigations 233
9.3 Attenuation Measurements 235
9.3.1 Overview 235
9.3.2 Theoretical Framework 237
9.3.3 Experimental Setup 240
9.3.4 Post Processing 241
9.3.5 Attenuation Results 244
9.3.6 Discussion 252
9.3.7 Conclusions 254
9.4 High Speed Atomic Force Microscopy (HS-AFM) 256
9.4.1 Applications of AFM 256
9.4.2 Design Considerations of AFM 257
9.5 Udimet 720Li γ' volume fraction estimates 260
9.6 RR1000 γ' volume fraction estimates 263

1. Introduction

The class of materials known as the heat resisted superalloys (HRSA), or simply 'the superalloys', is a group of materials with the ability to operate for extended periods of time under harsh conditions, including in extremely high temperatures (in excess of 700°C), without significant loss to their mechanical and physical properties; they are often regarded as some of the most highly developed alloys in existence [1]. There are four main groups of superalloy – cobalt, iron, titanium and nickel-based [2]. The family of the nickel-based superalloys in particular is of great importance across the engineering industry, due to their superior mechanical properties – including excellent mechanical strength, toughness and hardness, as well as resistance to degradation, erosion, thermal shock, corrosion and failure at high operating temperatures [3] [4]. Indeed, as well as their outstanding oxidation resistance, they exceed iron- and titanium-based superalloys in their high temperature strength [2] [5]; the strength of Inconel 718 at room temperature (1375N/mm^2) decreases only by 20% at 650°C [6] [7] [8] [9]. Their development is primarily due to the invention of the gas turbine engine in the late 1940s, and the expansion of the aerospace industry – with the associated demand for high temperature resistant materials for use in engine components such as blades, discs, shafts and fasteners [10] [11] – as well as for components downstream of the combustor [12] [13] [14] [15] [16] [17], where operating temperatures exceed 650°C. However, they are widely deployed in many other industries [1]; some key examples include components for hot regions of land-based gas turbines [18], ultra-supercritical pressure thermal power plants (where the combustion temperature is required to increase with time [19]), nuclear reactors, particularly for welds (where Inconel 82 is widely used) [20] [21], and chemical and petrochemical installations and components including bolts, valves and fans [1] [22].

Currently, around 50% of the weight of an aerospace engine is a result of superalloy use, and though this is unlikely to increase (due to the increased use of composites, and developments in titanium-based alloys with increased temperature capability [1]) there is still the need to satisfy global legislative requirements for reduced NOx and noise emissions – such as the ACARE set of targets [23] – which require higher levels of engine fuel economy and efficiency, and thus increased compressor discharge and turbine entry temperatures [1]. This need for increased temperatures can be explained by the Brayton cycle, which outlines the thermodynamic principles for gas turbines [24]; this states that the maximum theoretical thermal efficiency and power output of a

gas turbine increases with both the turbine entry temperature [12], or TET, as well as the pressure ratio at the inlet and outlet of the compressor [25]. Indeed, since their invention, there has been a 700°C improvement in TET (around 10°C per year [2]) which has contributed to the dramatic increase in efficiency of jet engines, and reduction in fuel consumption, over the years [26]. A schematic of the Brayton cycle is shown in Figure 1; the performance curves shown in Figure 2 are also a good method for visualising the impact of both temperature and pressure ratios on the overall performance of the engine.

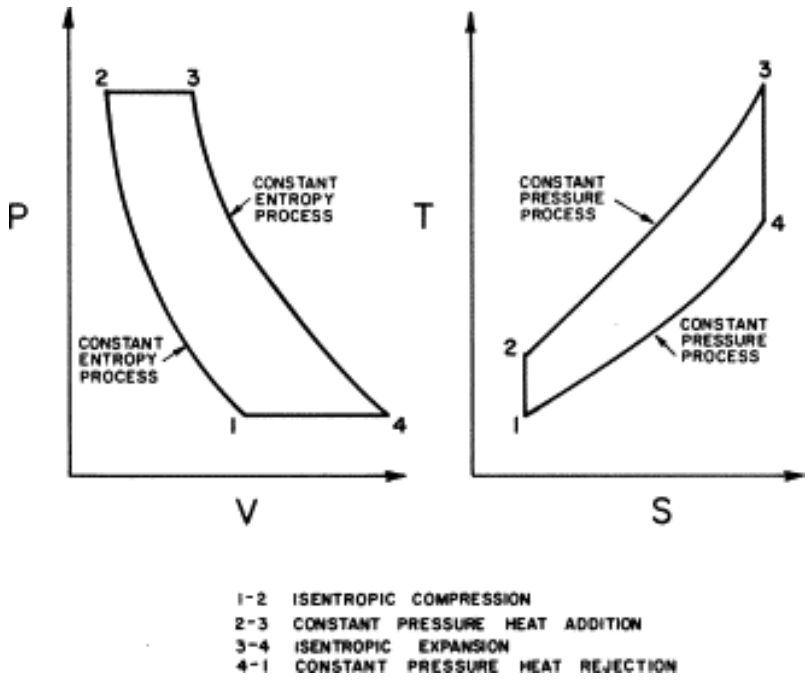


Figure 1: The Brayton cycle, governing the thermodynamic principles of gas turbines [27]. P, V, T and S denote pressure, volume, temperature and entropy respectively.

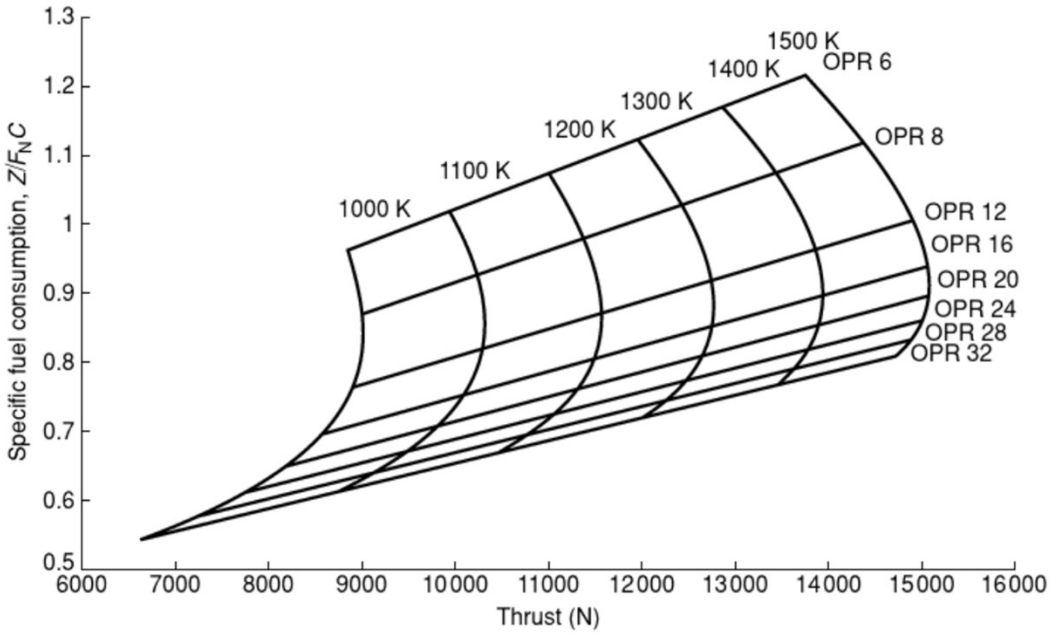


Figure 2: Jet engine performance curves, showing the thrust generated and specific fuel consumption for a given turbine entry temperature (TET) for various overall pressure ratios (OPR). [12]

An additional consideration is the higher climb rate being increasingly required by commercial airlines for aircraft to reach altitude more quickly, in order to reduce fuel burn [28] [29]. The higher engine bypass ratios (as great as 9.6:1 for the Trent XWB, pictured in Figure 3 [30]) have resulted in smaller engine core sizes, which experience increased temperatures and stresses [31]. Consequently, disc rotors in the HP compressor and turbine must be able to accommodate increasingly higher temperatures and stresses, placing significant demands on materials used for these critical components [32]. Such requirements demand the use of more advanced nickel-based superalloys in order to cope with the higher temperatures and stresses than currently experienced [32] [33], and thus it could be argued that they will still be important materials for jet engines and gas turbines for many years to come.

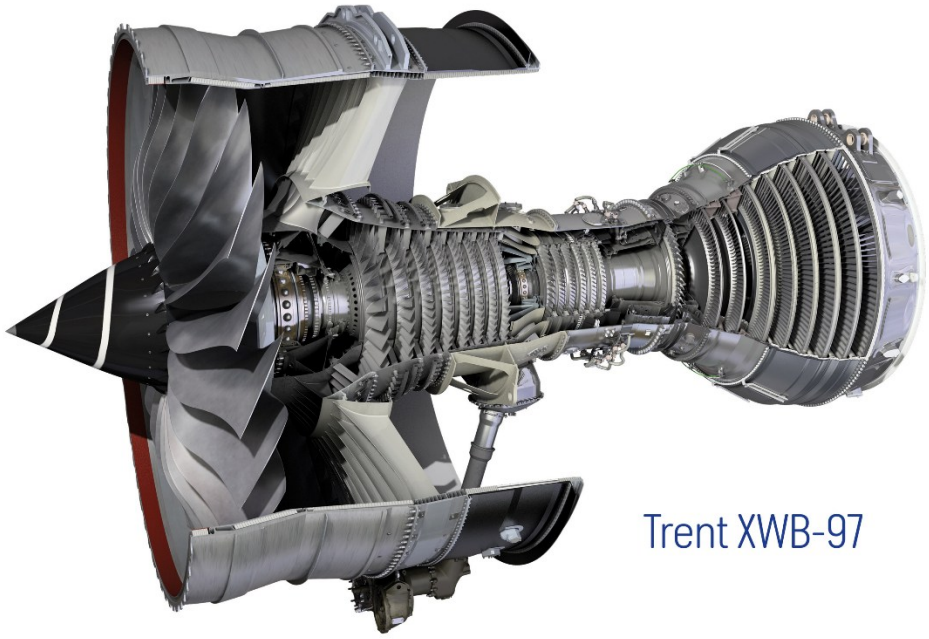


Figure 3: The high bypass ratio Rolls-Royce Trent XWB-97 engine. [34]

The microstructure of these nickel-based superalloys is tailored extremely carefully, as the mechanical properties are intrinsically linked with its characteristics – for example, the grain size, and the size and amount of the strengthening precipitates present (as well as the absence of those which could cause a detrimental effect). Depending on the material, there are different precipitates which are necessary to ensure the correct mechanical properties for a given application, even within a group of superalloys which are all used for high pressure/temperature discs within a jet engine – for example, the chemical compositions (and subsequently the precipitates present) can vary. Examples of these nickel-based superalloys include Inconel 718, Udimet 720Li and RR1000, which have all been investigated during the course of this EngD project; all have slightly different microstructural characteristics, strengthening mechanisms and precipitates. Inconel 718 is strengthened by the 'gamma double prime' (or γ'') precipitate, with other phases present but with either a lesser strengthening effect (the gamma prime, γ') or even a slightly detrimental effect (such as the delta, δ, phase). Udimet 720Li and RR1000 are both conferred their high strength by the γ' precipitate, but in various morphologies; these manifest themselves depending on the solution and ageing treatments that they have undergone. The phases present in these materials depending on thermal processing (namely hold temperatures and times at temperature) are represented using phase diagrams, which will be described in more detail further in this thesis.

These nickel-based superalloys are often used in engine-critical applications, where failure of the part is not permitted under any circumstances; these components are subjected to extremely high operating temperatures (for example, disc rims can reach 720°C for larger engines and exceed this in military applications [35]) while often being subjected to high rotational rates (and the resulting outward forces). They must also be corrosion resistant to fuel mixtures within the turbine [36]. It is therefore essential that the manufacture of these materials is very strictly controlled [12], as well as the accurate and reliable monitoring and characterisation of the microstructure at any point in its lifecycle – whether it be during component fabrication and manufacture, or while in service – as any microstructural variations will have an impact on the material's performance. (These variations could arise as a result of unpredictable stresses or strains under anomalous loading conditions, or exposure to higher temperatures than usual during service, if there is an 'overtemperature' incident [37].) One particular example where the monitoring and tailoring of microstructure could be beneficial is with regards to a 'blisk' (or blade-integrated disc), used in high pressure compressors for jet engines [38] – an example is pictured in Figure 4. The use of a blisk removes the need to attach blades to the disc, and hence decreasing the number of components required; this decreases the overall drag, and improves the aerodynamic efficiency of the engine [39]. The improved efficiency then enables a reduction of around 15% in the weight of the high-pressure compressor, which contributes significantly to the reduction of fuel consumption and hence the CO_2 emissions of the engine (by around 25% for the Trent XWB, for example, compared to previous generations [38]). However, it is extremely important that the different regions of the blisk have suitable microstructures; for example, the disc hub itself must have excellent fatigue resistance (typically achieved with finer grain sizes) whereas the outer blades must not be susceptible to creep (for which coarser grain sizes are more favourable).

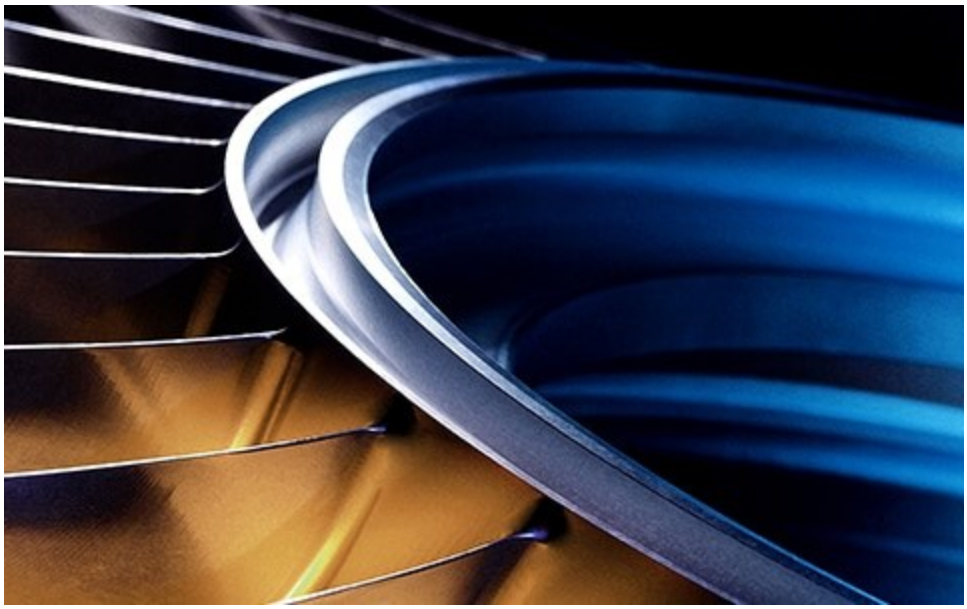


Figure 4: Rolls-Royce Trent XWB blisk. [38]

The aim of this project was to develop a non-destructive technique for the phase characterisation of these high-performance superalloys, using ultrasonic wave speed measurements in combination with an underlying theoretical framework constructed using a spherical harmonic expansion.[1] The need for a rapid, reliable method to characterise the microstructures of nickel-based superalloys (particularly one which was non-destructive) was apparent from a review of the current techniques available, as well as from experience within an industrial lab; the development of such a technique would provide benefits including significant time and cost savings across the industry. This was of particular interest to the sponsoring industrial company, Rolls-Royce; as a leading jet engine manufacturer, there is always the need to support the design of more advanced, high performance components (such as blisks), with efficient and robust materials inspection techniques, to ensure that these jet engines are meeting the required design and safety requirements without compromising quality or time.

Although the EngD research was carried out primarily within the Non-Destructive Evaluation department at Imperial College London, there was an extensive amount of laboratory work carried out at Rolls-Royce Filton, within the Failure Investigation department, under the supervision of a metallurgical expert (with world-class knowledge of jet engine alloy behaviours and phenomena,

[1] The use of a spherical harmonic expansion arose due to the key underlying variables of the theory – the orientation space, orientation distribution function, or ODF, and directional wave speeds – being defined on the surface of a unit sphere. The theoretical framework will be described in detail in Chapter 2.

particularly fatigue striations). There was also furnace work carried out at Rolls-Royce Derby on the Elton Road site under the supervision of a nickel-based superalloy specialist, with samples procured by the Rolls-Royce Engineering Fellow in nickel-based superalloys. Regular meetings with these experts at Rolls-Royce ensured that the research throughout the EngD was relevant, and had the potential to be deployed in an industrial context in the future.

This thesis will begin with a review of some key metallurgical concepts, together with the current state-of-the-art techniques available for materials characterisation, before giving an overview of ultrasonic inspection as a non-destructive technique, and the potential benefits it could offer for materials characterisation. The next chapter moves on to describe the theoretical framework and associated experimental methodology (and equipment design) for the specific ultrasonic wave speed measurement technique which has been investigated and developed for this EngD. The research undertaken for the EngD is then presented chronologically, as illustrated in Figure 5; first, the feasibility study carried out using Inconel 718 to verify that the V00 was indeed sensitive to changes in the microstructure, followed by an investigation into the applicability of V00 measurements to phase characterisation within this material, using a different set of samples with more specific processing histories. (V00 represents the zeroth order spherical harmonic coefficient of velocity, an average of the ultrasonic wave speeds in all 3D propagation directions within the material.) There then follows the work with a second nickel-based superalloy, Udimet 720Li, which was of industrial interest due to its being notoriously difficult to inspect using ultrasonic methods (a result of high levels of noise); it was also a useful alternative nickel-based superalloy to use for experiments due to it being purely dual phase, and thus it was hoped that it would be a more straightforward material to investigate as opposed to Inconel 718 (which had a more complex microstructure, and was more difficult to manipulate via processing than initially thought). The final part of the thesis focusses on the third nickel-based superalloy investigated, RR1000, which was selected due to its significantly different manufacturing technique (powder metallurgy), as well as it being a dual-phase superalloy. This material was chosen to primarily investigate whether the ultrasonic wave speed, or UWS, method was impacted by various phase morphologies, as the proportions of each type of γ’ precipitate depending on its processing is well known. For each of these materials, a brief overview of its inception and development is given, as well as a detailed description of its microstructure, before presenting the results obtained from various experimental techniques, including the ultrasonic wave speed measurements, microscopy and hardness testing. In the case of Inconel 718, there was also the opportunity to carry out high speed atomic force

microscopy (HS-AFM) measurements, which provided additional verification of the various precipitates present in the samples. The appendices include details of further investigations alongside the main UWS technique, regarding the investigation of frequency-dependent attenuation within each sample, as well as the process of determining whether a reduced order integration scheme could be deployed to enable time savings in the calculations for the UWS deconvolution. This thesis concludes with a summary of the findings during this research, as well as its relevance to industry and potential applications, before finishing with some potential further research which could be carried out following the key findings of the EngD.

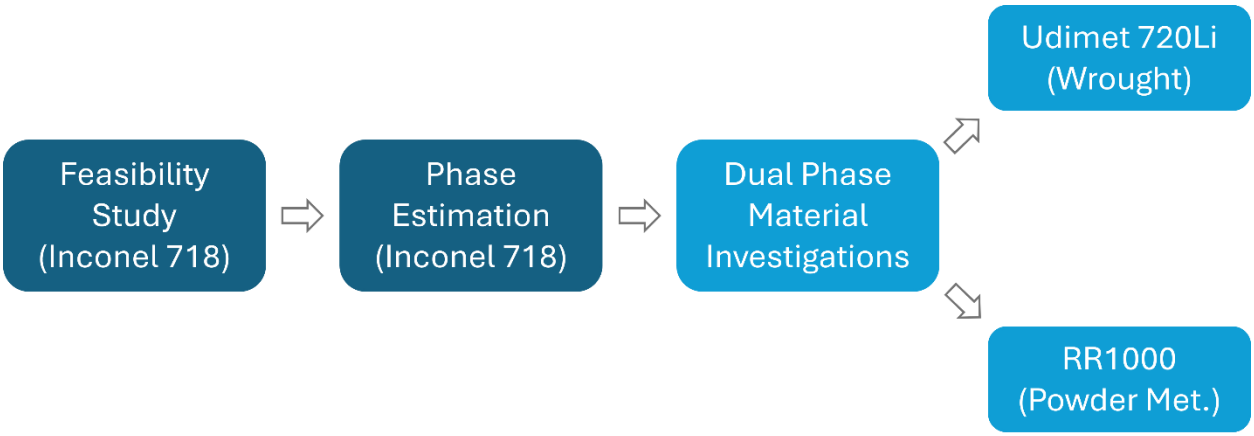


Figure 5: Flowchart of EngD research materials.

2. Literature Review

2.1 Overview of Metallurgical Concepts

A micrograph of Inconel 718 is shown in Figure 6, depicting the main metallurgical features which are typically of interest when investigating material properties and microstructures. These include the main grains, indicated by the green outlines, as well as the precipitates, which can form either on the grain boundaries or within the grains themselves; the notable precipitates in Figure 6 are on the grain boundaries, indicated with blue arrows. The grains and precipitates are also referred to as different 'phases'; the former are the main 'building blocks' of the material, and are distinguishable using electron microscopy imaging due to their each having a different crystallographic orientation to its neighbour, with respect to a given reference plane. The sizes of these grains are not necessarily uniform, as seen in Figure 6; these differences can have an impact on the mechanical properties of the material, though the precipitates are also highly influential in determining these properties. These precipitates which form, both in terms of quantity and morphology, depend on the material composition, crystal structure and processing conditions; nickel-based superalloys commonly have the gamma prime (γ') phase, for example, whereas titanium has the alpha (α) and beta (β) phases. (The phases present in nickel-based superalloys will be discussed in more detail later in this chapter.)

In the case of this EngD, the key aim was to develop a non-destructive technique for determining the amount of these phases, or precipitates, present in a nickel-based superalloy, due to their significant impact on mechanical properties – such as tensile strength and creep resistance; both the amount of these precipitates, and often the morphology, will affect the overall performance of the material. An overview of the current methods available for materials characterisation follows in the next section.

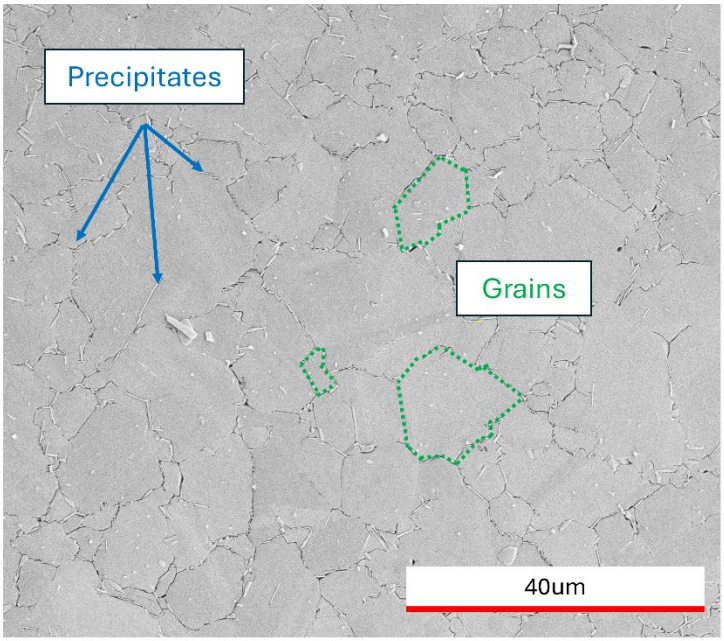


Figure 6: A micrograph of Inconel 718, illustrating the grains (outlined in green) and the precipitates (indicated by blue arrows), which are formed of different phases within the material.

2.2 Current Methods for Materials Characterisation

Despite the existence of numerous techniques for the phase characterisation of materials, there is still the need for a rapid, reliable and non-destructive method for the assessment of the microstructure of nickel-based superalloys; a high reliability is necessary due to the criticality of the components they are often used for, and a quick inspection would enable time and cost savings across the industry. The main state-of-the-art techniques – including a range of microscopy-based methods – tend to be time consuming (often requiring hours for the full preparation and inspection), costly, and destructive. There are a variety of different types available, with three commonly used, including scanning electron microscopy (SEM), electron backscatter detection (EBSD) [40] and transmission electron microscopy (TEM). Of these, SEM is the most straightforward in terms of sample preparation and inspection time; however, one of the limitations (particularly within nickel-based superalloys) is that often some phases can be masked and hence incorrectly identified if the preparation was not adequate [41], and images at multiple magnifications may be required due to the range of morphologies and sizes of a particular precipitate [42], increasing the overall time of inspection. EBSD is a slightly more powerful tool, capable of measuring crystallographic orientations and hence increasing the probability of resolving individual grains which may not be identifiable using SEM; it also has a higher spatial resolution (in the order of tens

of nm) which makes it more suitable for identifying smaller precipitates [43]. An example of an EBSD image is shown in Figure 7, taken of an as-forged sample of RR1000, where the different colours are representing the different grains, distinguishable due to their differing crystallographic orientations. However, there are still many cases within a γ/γ' superalloy system (of which RR1000 is an example) where some phases are still indistinguishable [44] due to similarity in lattice parameters and diffraction patterns. TEM is the most precise of these techniques, and can therefore be used for very fine grained materials, including powder metallurgy nickel-based superalloys [45]; unfortunately, it has the most stringent sample size limitation (of around 100μm thick foils [45]). Regardless of the specific technique, all of these microscopy methods require extensive surface preparation, and often there can be a lengthy trial and error process to find the optimal polishing times and etchants for a particular material.

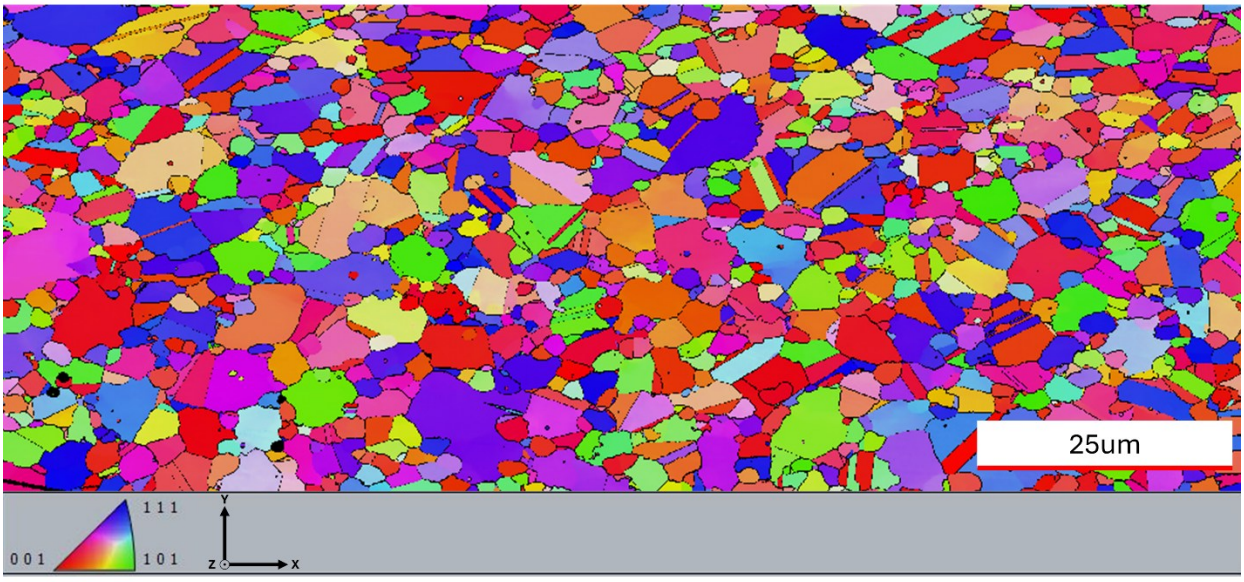


Figure 7: Grain inverse pole figure (IPF) in the normal (Z) direction from EBSD measurements for as-forged RR1000.

Despite the high accuracy of these measurements, and the ability to deduce the presence of different phases (as well as crystallographic orientations in the case of EBSD), there is extensive surface preparation required, and the inspection region is incredibly small. This latter can be a disadvantage where materials show large variations in microstructure within the same billet (such as Udimet 720Li) or the component – in a blisk, for example, where the grain sizes may have been tailored differently for the core in comparison to a blade tip. When using electron microscopy to examine materials through their thickness, the total inspection time can ultimately be very long due to the need for taking multiple images through the layers of the material at different orientations;

each inspection only measures the surface or near-surface region, and every time a repeat of the grinding, polishing and etching process is required. There is also the cost of consumables required for the preparation of the material to consider, which, for etchants, can be chemicals hazardous to health. The fact that these methods are only capable of localised, near-surface measurements of depths around 20μm means that measurements taken are unlikely to be representative of the bulk material being studied [46]. For nickel-based superalloys such as Udimet 720Li and RR1000 in particular, the determination of the γ' size (the main strengthening precipitate) using SEM can result in errors arising from etching artefacts and other stereological effects [47], requiring the need for carbon replication – a further time-consuming activity.

There are more advanced microscopy techniques available, such as high speed atomic force microscopy (HS-AFM), which provides a topographical map of the surface from the traversing over the sample with a small and highly sensitive cantilever; however, there are similar limitations to standard microscopy techniques due to a very localised inspection region, with the additional challenges resulting from a much more involved surface preparation procedure – for this type of microscopy, the samples can also only be microns thick. The different phases which are being imaged must also have sufficiently different properties in order to polish or etch preferentially to create enough of a topographical difference to be imaged.

All of the characterisation methods mentioned above are destructive to an extent; such a large amount of sample preparation is required, in addition to a very small specimen size, that despite being non-destructive in theory there is often some form of destructive machining required. There is also the additional risk that smaller microstructural variations may not be detected by an observer, as image interpretation can often be subjective. However, a very promising non-destructive method which has been recently developed is Spatially Resolved Acoustic Spectroscopy (SRAS), which uses surface acoustic wave velocity measurements to create a velocity map showing the orientation of grains [48] [49]. This is a much more efficient method to acquire texture and microstructure images of nickel-based superalloys, such as in Inconel 617 [50] and powder bed fusion specimens [51]. An example of a SRAS velocity map for Inconel 718 is shown in Figure 8. Although samples required preparation to a mirror finish in early configurations, there have been recent advances in applying SRAS successfully for inspection of rough surfaces using a 'speckle knife edge detector', or SKED, system [52]. However, the grain size which can be resolved is still limited to around 20μm (so it is unable to resolve individual precipitates of smaller scales).

Currently, the equipment required has a large footprint, and the total time of inspection is still relatively long, taking into account sample preparation time combined with the time of the inspection itself (which can range between a few hours to a couple of days, depending on the sample size and resolution required).

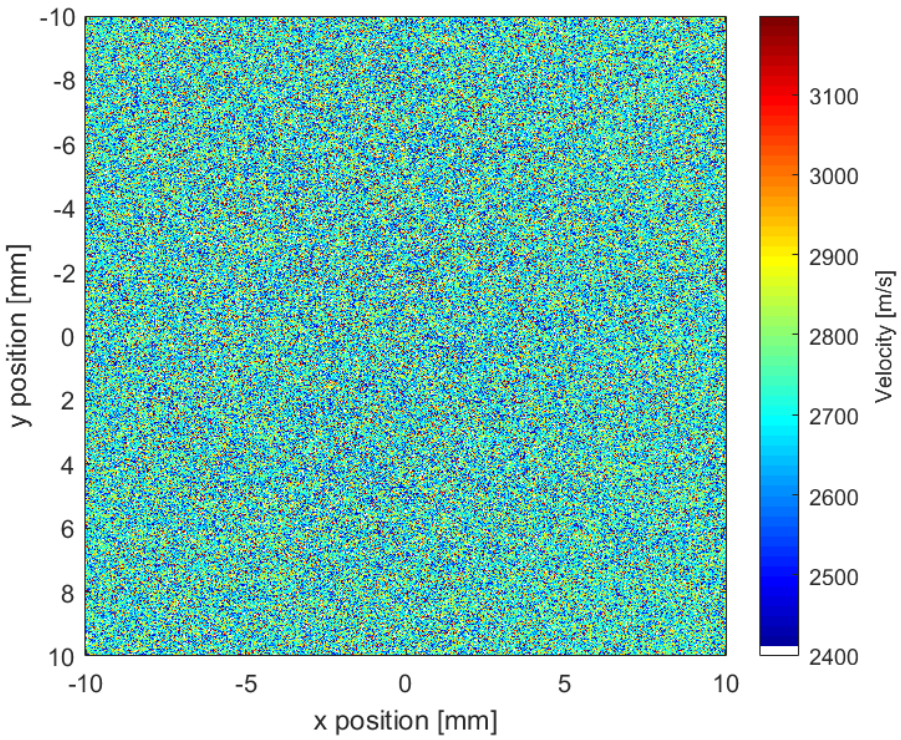


Figure 8: An example of a SRAS velocity map on a sample of Inconel 718.

The fact that micrographs obtained using SEM and other microscopy methods give microstructural information in 2D only can be problematic, especially in the case of materials where the microstructure can vary drastically within one component or sample section (such as with Udimet 720Li). Typically, information in 3D (such as the number of precipitates, and precipitate size distribution) can be inferred from 2D measurements, but require many assumptions to be made [53]. Techniques such as serial sectioning can be used, involving a dual-beam focussed ion beam (FIB) SEM, where the FIB is used to remove slices of the material with the SEM capturing images of the revealed surfaces [54], but this can be time consuming and prone to errors, especially with the slice thicknesses [55]. Even with fully automated data acquisition and the increase in computing power over recent years [56], the full inspection can be lengthy. It can often be more informative and efficient to instead have a bulk average measure of the microstructure of a material, which also negates the need to take multiple measurements of one sample, as is the case for EBSD.

If the access to the required facilities can be obtained, there are more powerful materials characterisation techniques available, such as X-ray (high energy) synchrotron [57] [58] [59] and neutron diffraction measurements [60] [61] . Pole figures generated using neutron diffraction data from Inconel 718 samples are shown in Figure 9, where LPBF denotes 'laser-power bed fusion' and HIP denotes 'hot isostatic pressing' [62]. Both of these techniques have the advantage of being bulk measurement techniques; however, for neutron diffraction measurements, the minimum object size detectable depends on the available hardware, and resolution of systems can vary from between 20 to 750μm [63]. Although X-ray sub-micron tomography has a spatial resolution of around 0.35μm^3, there is the additional drawback of requiring a skilled operator. As with the microscopy methods, the size of a sample which can be inspected is limited, and an extensive polishing and etching process is still required. There is also the additional challenge of acquiring access to these measurement facilities, due to the limited number available; in the UK, there is only one of each (the Diamond synchrotron, and ISIS neutron facility), and competitive proposals must be written in order to bid for beam time.

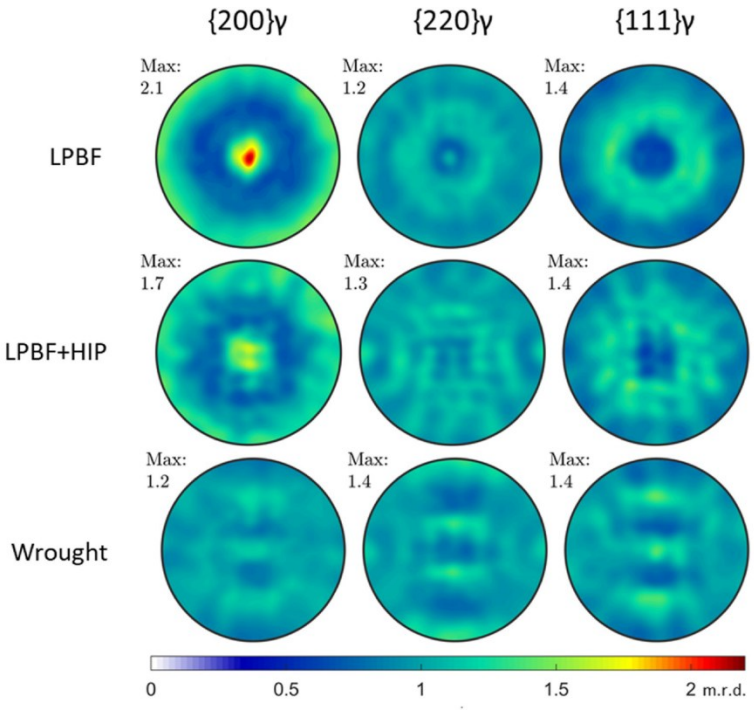


Figure 9: Pole figures of Inconel 718 samples generated using neutron diffraction data. [62]

From this overview of existing materials techniques, it can be seen that there is still the need for a non-destructive, inexpensive and rapid method to be developed for the bulk characterisation of material microstructure within the nickel-based superalloy family, to enable the reliable inspection of critical components across a broad range of engineering applications. One such promising technique is the use of ultrasonic inspection, already widely used throughout industry for the detection and monitoring of defects within materials and components.

2.3 Ultrasound NDE and Materials Characterisation

Non-Destructive Evaluation (NDE) is a broad, interdisciplinary field, with numerous applications across many industries. Its primary use is to ensure structural components and systems perform their function, by testing materials in a reliable, cost-effective manner without causing damage or affecting the material's usage life [64]. Ultrasonic testing is just one of the technologies used in the field of NDE, and involves the use of high-frequency sound waves (of over 20kHz, the upper limit of the audible range for humans, and above), to inspect materials for defects or changes in material properties [64]. An example of a fan blade undergoing ultrasonic inspection is shown in Figure 10.

Traditionally, ultrasound NDE has been used for defect detection in structurally critical components, such as pipes in oil and gas pipeline plants [65], welds in equipment used for nuclear reactor plants [66], and in inspection of aerospace engine components [67]. More recently, however, there has been an increasing amount of development in applications of ultrasound for microstructural characterisation of materials, by exploiting various properties of ultrasonic waves such as velocity, attenuation and the non-linearity of acoustic waves. Techniques have been developed for materials such as aluminium, titanium, and steels, as well as nickel-based superalloys, and there are many examples demonstrating the potential for applying ultrasound to materials characterisation [68] [69].

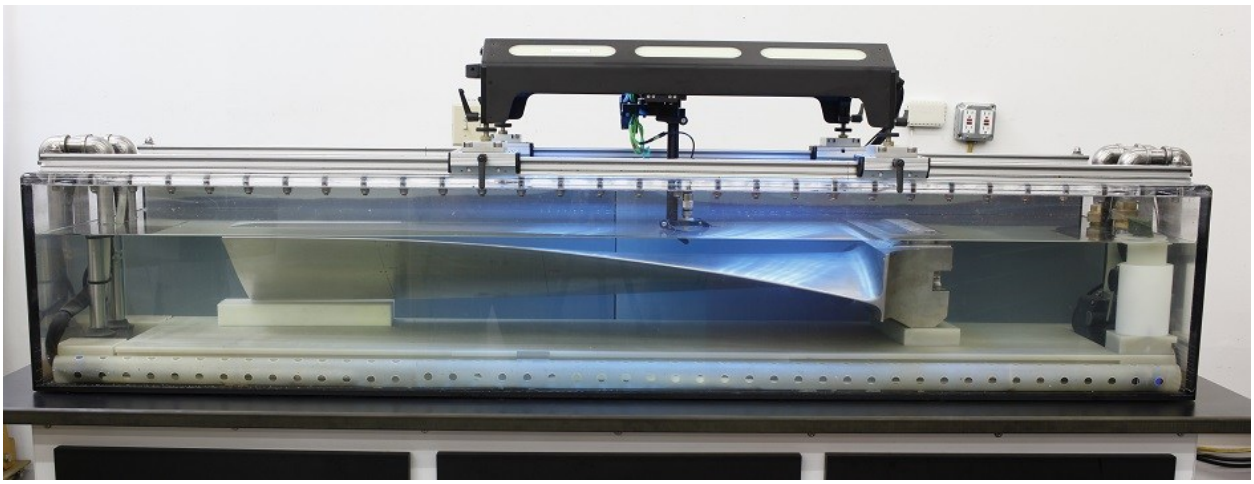


Figure 10: An ultrasonic inspection of a NASA Ames research fan blade. [70]

2.3.1 Benefits of Ultrasound Techniques

Use of ultrasound would have many advantages over the current techniques for quantifying texture and structure of materials, such as the microscopy-based methods discussed in the preceding section. For ultrasonic inspection, there is minimal part preparation required; for example, in the case of the water-tank based procedure used in this project, the only criterion for the specimen is parallel surfaces – and even this is not a limiting factor for the method to be successful, as the water-tank setup is just one of the possible experimental implementations of the method. An ultrasonic NDE technique can be used to assess bulk material properties, as the elastic waves can propagate through the entire thickness of the material (depending on frequency) due to their high penetration power [71], and are therefore not limited to solely the test surface [72]; even powerful methods such as X-ray synchrotron and neutron diffraction are limited in the depths they can measure due to the limited sample sizes that can be used [46]. In addition, the equipment required for ultrasound inspection is relatively cheap and widely available, meaning that implementation in research labs and on production lines could be quick and simple. The non-invasive nature of ultrasound waves minimises risk to the operator with none of the radiation hazards accompanying X-ray, neutron or laser techniques. Finally, the data can be obtained in very little time, resulting in an efficient, low-cost method for quantifying material properties.

2.3.2 Review of Applications to Date

There have been a variety of different ultrasound properties explored which focus specifically on characterisation of nickel-based superalloys, including the quantifying of ultrasonic properties as a

function of grain size, and using these data to find relationships between attenuation and backscattering behaviour of ultrasound waves [73]. There are also a number of studies concerning the use of acoustic nonlinearity, demonstrating that second-order harmonic amplitudes of ultrasound waves can be directly related to microstructural changes, such as dislocations [74]. Although the acoustic nonlinearity parameter varies with each study, in general it is based on the relation between the amplitude of the fundamental and second-order harmonic frequency of the ultrasound wave; the dislocations formed in a material undergoing fatigue and/or creep cause a nonlinear distortion to an ultrasound wave, which results in higher harmonic components of the wave being generated [75]. A further research area involves the determination of the impact of undesirable directional coarsening of the γ' precipitate during creep, using a combination of both the ultrasonic attenuation and nonlinearity. This directional coarsening is also known as 'rafting' (an example of which is shown in Figure 11), and is the process where the γ' phase changes from being finely dispersed throughout the structure into a layered structure, which is perpendicular to the applied stress. This layered texture can then result in a sudden crack growth along the interface between the γ and γ' phases [76]. Nonlinear ultrasonic waves have also been used to characterise fatigue damage in a nickel-based superalloy, via an 'acoustic nonlinearity parameter' [75]. Fatigue damage occurs due to dislocation substructures forming and accumulating at grain boundaries, resulting in localised strain that develops into microcracks. It was found that these substructures have little impact on macroscopic properties (such as elastic modulus and sound speeds), but do cause a nonlinearity effect which can be used to quantify the fatigue damage in the material.

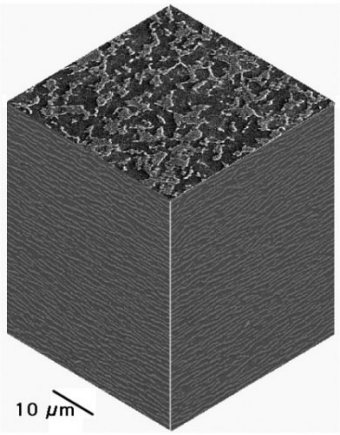


Figure 11: A 3D visualisation of rafting in a single-crystal superalloy. [77]

More broadly, however, the research into use of ultrasound for materials characterisation can be categorised into the study of backscattering and attenuation of ultrasound waves, and the use of ultrasound velocity measurements.

2.3.3 Ultrasound Backscattering and Attenuation

Although attenuation is caused by absorption and scattering, typically only the latter is studied due to the difficulty of measuring absorption, and the fact that scattering effects are more dominant [78]. Also, due to the randomness of the scattering process, attenuation cannot capture information required for texture extraction, and is therefore used for other characterisation purposes such as grain size detection [78]. Examples include the prediction of grain size, strength and toughness in plain carbon steel [79], the evaluation of grain sizes in stainless steels [80] [81], and determining grain sizes in iron alloys [82]. In addition, investigating the relationship between ultrasonic attenuation and sound wave velocity in samples of precipitation-hardened aluminium alloy 2024 found a correlation between these measurements and the hardness of the material; the ultrasonic attenuation was found to decrease consistently as hardness increased [83].

Other applications of ultrasonic scattering include the detection of macrozones in titanium alloys [84] [85], where macrozones (or micro-textured regions, MTRs) are regions of common crystallographic orientation of the alpha-Ti grains which can cause dwell fatigue cracking in titanium alloys [86]. An EBSD map of Ti-6Al-4V is shown in Figure 12 below, where each colour corresponds to a certain orientation with respect to the polished plane of the sample; the MTRs are clearly visible where there are clusters of the same colour [87].

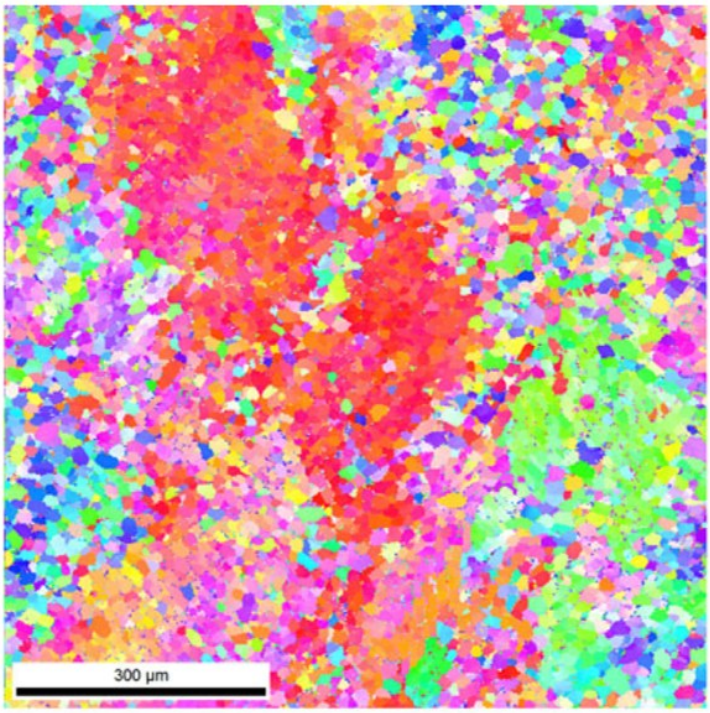


Figure 12: EBSD map of Ti-6Al-4V, where the macrozones are clearly observable as the groups of grains with similar colours. [87]

2.3.4 Ultrasonic Velocity Measurements

In comparison to attenuation, the bulk wave velocity is coupled more closely with polycrystal orientation [78] which is reflected in the research areas using ultrasound velocity information for characterisation. Some examples are given below:

- Determining grain sizes in austenitic stainless steel [88] – where it was found that the grain size estimates using velocity measurements were more accurate than when using attenuation measurements;
- Studying recrystallisation processes in austenitic stainless steel, correlating these with the material's mechanical properties [89];
- Texture measurements in thin copper and aluminium plates [90];
- Analysis of residual stresses, responsible for weld cracking, in ferrous alloys [91];
- Evaluating mechanical properties [92] and elastic constants of stainless steels [93];
- Tracking of processes such as nitride precipitation in nuclear grade 316LN stainless steel [94], and precipitation during age-hardening of aluminium [95];
- Characterising the annealing behaviour of cold worked austenitic stainless steel [96];
- Characterising the microstructural effects of fatigue and creep-fatigue damage in 316L(N) stainless steels [97].

There has also been another field of research concerned with materials characterisation using ultrasonic velocity measurements, which has led to the development of the spherical convolution method; it has been found that there is a physical connection between the polycrystal wave speeds and texture which can be described by a convolution relationship, from which texture and phase information can be inferred from wave speed measurements. This is the materials characterisation method which has formed the basis of this EngD, and will be discussed in more detail in the following section.

2.4 The Spherical Convolution Theoretical Framework

2.4.1 Origin of Method and Development

The theory of the spherical convolution approach – and its enabling the extraction of material characteristics from measurements of ultrasound velocities through the material – is a recent development in the field of non-destructive evaluation. Its advancement over the last decade is summarised in this section.

The first stage in the framework development involved the investigation of the relationship between bulk texture (i.e. the crystallographic orientation) and ultrasonic wave velocity in cubic and Hexagonal Close-Packed (HCP) grains, using experimental ultrasound studies and neutron diffraction measurements – as well as predictions from computational models on random, unidirectionally rolled and cross-rolled textures. There was good quantitative agreement, demonstrating that ultrasonic velocity profiles exist, showing potential for bulk texture determination using ultrasound [98]. This was supported by further research which found good agreement between surface ultrasonic and electron backscatter detection, or EBSD, texture measurements in a titanium sample containing macrozones [99].

Following this research, the spherical convolution method was introduced, where the HCP single crystal wave speed is coupled with the polycrystal c-axis pole distribution function to give the polycrystal wave speed response (where the c-axis is the out-of-plane axis of the crystal). This enabled the solution of the 'forward problem' (determining polycrystal wave speed from single crystal wave speed and the pole distribution) as well as the more challenging 'inverse problem' (finding texture from polycrystal and single crystal wave speed) [78]. The method was so named due to the use of spherical harmonic expansions to express each of the functions.

Further developments involved the extension of the spherical convolution method for HCP materials (such as titanium and zirconium) into a generalised form, to obtain bulk texture measurements in any cubic polycrystalline material through the use of Orientation Distribution Functions (ODFs) [100]; the ODF is a statistical probability function for the three Euler angles describing the specific orientation of a crystal [101]. This ODF enables a concise, graphical representation of texture through the use of pole figures – these depict a subset of the full ODF

information, as they only show the orientation distribution of reciprocal vector directions in a crystal lattice [102].

Some example pole figures are shown in Figure 13 below; on the left hand side is the pole figure for the c-axes of rolled zirconium, where the different symbol sizes represent the weighting of the grain representing the initial texture, and on the right is the data which has been converted into a continuous distribution [102] – this latter is the form more commonly presented in the literature.

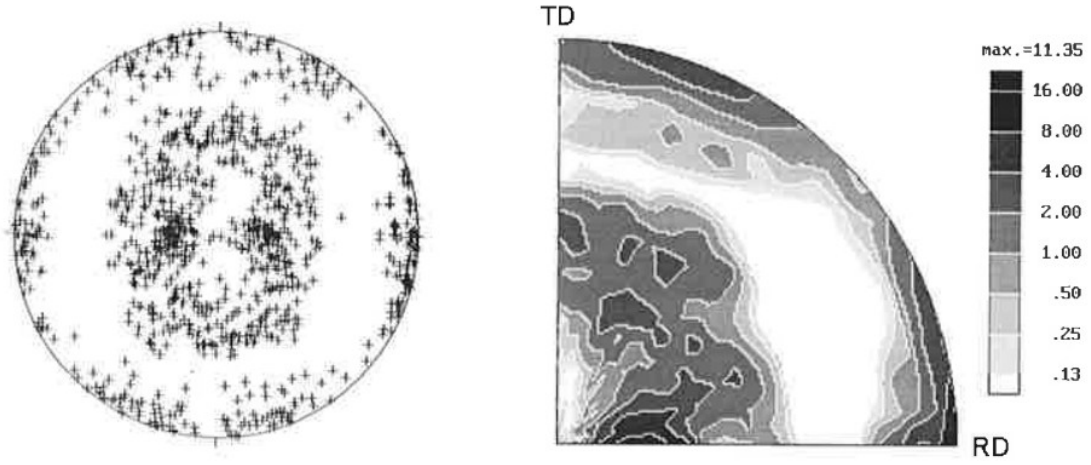


Figure 13: Example pole figures for the c-axes of rolled zirconium. 'TD' represents transverse direction, and 'RD' is the rolled direction. [102]

Having established the background and motivation for the development of the theory, the spherical convolution framework as described by Lan et al [100] will now be summarised, as an overview to the theoretical basis of the model, as well as its extension to phase characterisation in crystalline materials and application to nickel-based superalloys. The fact that the theory is termed a 'convolution' simply refers to there being a physical connection between the polycrystal wave speeds and texture, which can be described by a mathematical relationship. The implementation of this method through post-processing of experimental results will be described in the 'Experimental' section of this thesis.

2.4.2 Theoretical Framework

For a homogeneous polycrystalline material, where an acoustic wave propagates through the same texture regardless of the direction it travels in, the wave speeds along the propagation route can be averaged to find the 'wave phase velocity variation function', v, in 3D space. The speed at any point in the material can be specified by the crystallographic orientation at that point, so v can be expressed as a spherical convolution between the ODF, ω, and the 'single crystal velocity variation function', k. This latter function k can be calculated from the single crystal elastic constants (which can be found in the literature – for example, the elastic constants for Inconel 718 have been found by Haldipur et al [103]). It was found that the spherical harmonic expansion coefficients of these three functions satisfy the following point-wise multiplication relationship [78]:

$$V_{lm} = \sum_{n=-l}^{l} W_{lmn} K_{ln} \tag{1}$$

This can be regarded as the fundamental equation of the spherical convolution theorem, where essentially the wave phase velocity variation function v can be approximated by taking an average of the wave speeds along the propagation route at each point, and the crystallographic orientation determining the speed at each point [104]. This relationship can be thought of as analogous to the Fourier series, but for a spherical field, rather than a 2D series; where the Fourier series expresses a periodic (or circular) function in terms of a sum of trigonometric functions, the spherical harmonics separate a spherical field into different shaped components. It is these components which are defined by specific orthogonal functions. A visualisation of these specific shapes determined by the spherical harmonics is shown in Figure 14 [105].

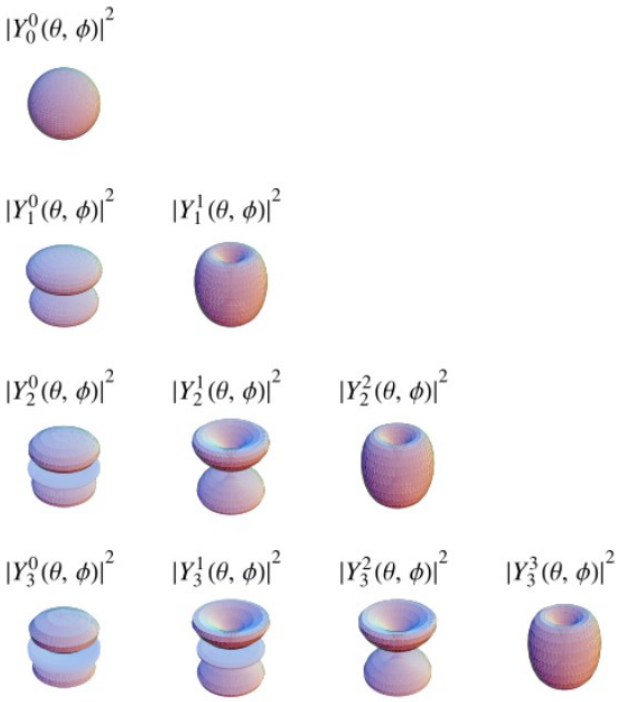


Figure 14: A visualisation of the spherical harmonic functions. [105]

V_{lm} and K_{ln} are the series expansion coefficients of the polycrystal and single crystal wave speeds respectively [71], and are expanded with respect to the spherical harmonic bases $Y_{lm}(\theta, \varphi)$, the polar and azimuthal angles respectively, where

$$Y_{lm}(\theta, \varphi) = P_{lm}(\cos\theta)e^{im\varphi} \tag{2}$$

$P_{lm}(\cos\theta)$ is the normalised Legendre polynomial [78], where l and m are the 'degree' and 'order' respectively, where $(l \geq 0)$ and $(-l \leq m \leq l)$ [100]. As K connects the functions V and W, it is often referred to as the 'kernel' function [100].

W_{lmn} represents the coefficients of the ODF. The ODF is expanded in terms of the Wigner-D function, ${D_{mn}}^{l}(\alpha, \beta, \gamma)$, of the three Euler angles. (The Wigner-D matrix is a $(2l + 1) \times (2l + 1)$ dimensioned matrix, which is used to express a set of l-degree harmonics as a linear combination of another set of rotated l-degree harmonics [100].) Its use here is necessary to link the global and local crystal coordinate systems – a more detailed discussion and derivation is found in Reference [78]. The variables in Equation 1 are linked via pointwise multiplications of expansion coefficients, which can be used in both forward and inverse directions [71]. The ODF can then be recovered as

its spherical harmonic expansions via a deconvolution process, to give information on the material crystallography.

One limitation of this method is that only ODF coefficients up to the 4th order can be reliably calculated from elastic waves, due to the 4th rank elastic tensor having very little physical coupling with higher-order expansions [71]. (The 4th rank tensor is a 4-dimensional array of numbers describing the elasticity of a single crystal [106].) It was found that the spherical harmonic coefficients for the polycrystal velocity, V_{lm}, of the 6th degree and higher, were all small with respect to those of the lower degrees, as the ODF coefficients W_{lmn}were also small; hence after convolving with the kernel function they resulted in velocities less than 10m/s [100]. As this is in the same order as experimental errors associated with ultrasonic experiments, it was deduced that these higher order velocities should be neglected, and that the process of retrieving texture information from wave speeds was a 4th-order truncation relationship [100].

2.4.3 Application for Phase Characterisation

This texture measurement method was then developed further to approximate the volume fraction of phases in dual-phase materials. It was found that phase information can be extracted from the 0th order coefficient of velocity, V_{00}, which is directly related to the material's single crystal elastic constants. Each of the velocity coefficients are calculated using wave speeds in discrete evaluation directions, as determined by the Gaussian-Legendre numerical integration scheme, which can be expressed as follows [37]:

$$V_{lm} = \frac{\pi}{N} \sum_{i=0}^{2N-1} \sum_{j=0}^{N-1} v(\theta_i, \varphi_j) Y_{lm}^*(\theta_i, \varphi_j) \omega_N \tag{3}$$

The order of the integration scheme is denoted by N; there are N number of discrete Gaussian-Legendre polar angles (or nodes), θ_i, and 2N equi-angular azimuthal angles from 0 to 2π, φ_j, in which the wave speed measurements must be taken [37]. ω_N represents the weight function for the ith Gaussian node, and φ_j is a factor which ensures that the azimuthal angle is equally spaced from 0 to 2π, calculated using the following equation:

$$\varphi_j = (j-1) \times \frac{\pi}{N} \tag{4}$$

The complex conjugates of the spherical harmonic (SH) bases for a given orientation, (θ_i, φ_j), are represented as $Y_{lm}^*(\theta_i, \varphi_j)$. This particular integration scheme was selected over others, such as the equiangular scheme, as it can achieve a given degree of accuracy with less data; for a discrete data set of 2N by N, a degree of accuracy of (2N – 1) can be obtained [107] (whereas for the same degree of accuracy using the equiangular scheme would require 16x16 data points). The spherical convolution theorem requires a 4th degree of accuracy, so in theory only 10 x 5 discrete data are required; however, for accuracy and efficiency, the scheme is used here with N = 6 [78]. (There is also an additional consideration in terms of practicality; if N is odd, the directions required are along the surface of the sample, which cannot easily be measured experimentally.)

From previous experiments [104], it was found that this value of 6 for N was sufficient in achieving the required numerical accuracy for the targeted truncation order of 4; this order therefore determines that there are 6 polar and 12 azimuthal directions for which wave speed measurements are required. However, using the antipodal symmetry of waves, this number can be halved (which also has the advantage of reducing the total time required for the experiments). The experimental wave speeds measured in these discrete directions can then be used in the spherical convolution inversion process, in order to extract the spherical harmonic coefficients – specifically the zeroth order velocity coefficient, V_{00}, which contains the phase information of the material [37].

According to the convolution theory, the 0th order polycrystal's spherical harmonic term, V_{00}, and the single crystal term, K_{00}, are linked by the 0th order ODF coefficient, W_{000}, as follows [46]:

$$V_{00} = W_{000}K_{00} \tag{5}$$

Returning to the earlier comparison of the framework with the Fourier series, the first term of the spherical harmonic expansion will, like the first (or zeroth order) coefficient of the Fourier series, be a constant, for a given material. The zeroth order term of the ODF, W_{000}, is always 1 regardless of texture, as it is analogous to taking the sum of all probabilities (of the ODF) over a spherical volume (as dictated by the shape of the zeroth order spherical harmonic, illustrated in Figure 14). This can also be thought of as taking an average over all directions over this volume – which should always sum to 1. As a result, the value of V_{00} is independent of texture; any variations in the texture will not have any effect on the W_{000} term. Hence, in a material which comprises just one phase, the zeroth coefficient of velocity V_{00} will always be equal to the stiffness constant term K_{00}.

V_{00} is thus an intrinsic feature of that particular phase, reflecting its acoustic properties and being directly linked to the single crystal elastic constants, or SCECs. The fact that phase information can be inferred from this particular coefficient is a result of the presence (or absence) of various precipitates altering the overall SCECs of the material; these precipitates also have their own individual stiffnesses, and SCECs, which would contribute to that of the whole material. As an example, if there was a large proportion of a stiffer precipitate present in a sample, the SCECs of this would be different to a different material where there were very little of the same phase. The changes in SCECs caused by the different phase amounts allows for this ultrasonic wave speed method to detect microstructural variations, that are spatially homogeneous on the macro-scale, which have occurred [37].

The relationship in Equation 5 can be written more explicitly in terms of volume fractions in a dual-phase material. Taking the alpha and beta phases in titanium as an example, with h denoting the fraction of the alpha phase present in an alpha and beta dual-phase material such as titanium, the overall polycrystal term can be expressed as follows [46]:

$$V_{00}|_{overall} = h \times V_{00}|_{alpha} + (1 - h) \times V_{00}|_{beta} \quad (6)$$

The overall polycrystal term (or the zeroth velocity coefficient) $V_{00}|_{overall}$ is obtained from the experimental measurements; the zeroth velocity coefficients of the individual phases in a dual phase material, such as the alpha and beta in Ti-6Al-4V as shown in Equation 6, can be found using the specific single crystal elastic constants for each material which can be found in the literature, or measured using experimental techniques such as nano-indentation. These can be used to calculate the coefficient K_{00}, which is then related to the zeroth coefficient of velocity via the following relationship (derived from the spherical convolution expansion):

$$K_{00} = V_{00} \times \sqrt{4\pi} \quad (7)$$

Results from experiments with the dual-phase Ti-6Al-4V alloy gave an estimate that the alpha phase had a percentage of 86.8% based on calculations using this method [46], which was reasonably close to the 90% data value found in literature [108].

It should be noted that the precision of the texture estimation using this method is dependent on the accuracies of the single crystal elastic constants and the experimentally measured V_{00} values

(which are the average speed of the velocities in all directions); for experiments using the titanium alloy Ti-6Al-4V, it was found that there was an uncertainty of ±4-7% in the estimated phase composition [46]. This could be a result of errors in the ultrasonic testing procedure (for example some energy dissipation occurs as transverse waves in the water tank, whereas only the longitudinal wave velocities are being measured), but also the fact that the difference in values of V_{00} in each phase also affects the accuracy of predictions [46]. However, ultimately it is not the absolute precision of the ultrasonic measurement of the phase which is the most crucial, but the sensitivity and reliability in detecting the changes. If it can be proved that these are sufficient, there would be enough confidence in the method for use in industry, such as monitoring the degradation of a material during service.

Having established the underlying theory for the ultrasonic wave speed measurement technique, the experimental rig required to acquire the wave speeds in the specific orientations determined by the theory (Equation 3) for the deconvolution will be described in the following section. For these experiments, the double-through transmission signals are being acquired; these are the waves which have passed through the sample, and reflected off an acoustic mirror below the sample before returning back to the transducer, and can be identified by their distinct pattern of increasing amplitude, as highlighted in red in Figure 15. An overview of this acquisition method is given in the following section, before describing the experimental setup used for the ultrasonic wave speed measurements.

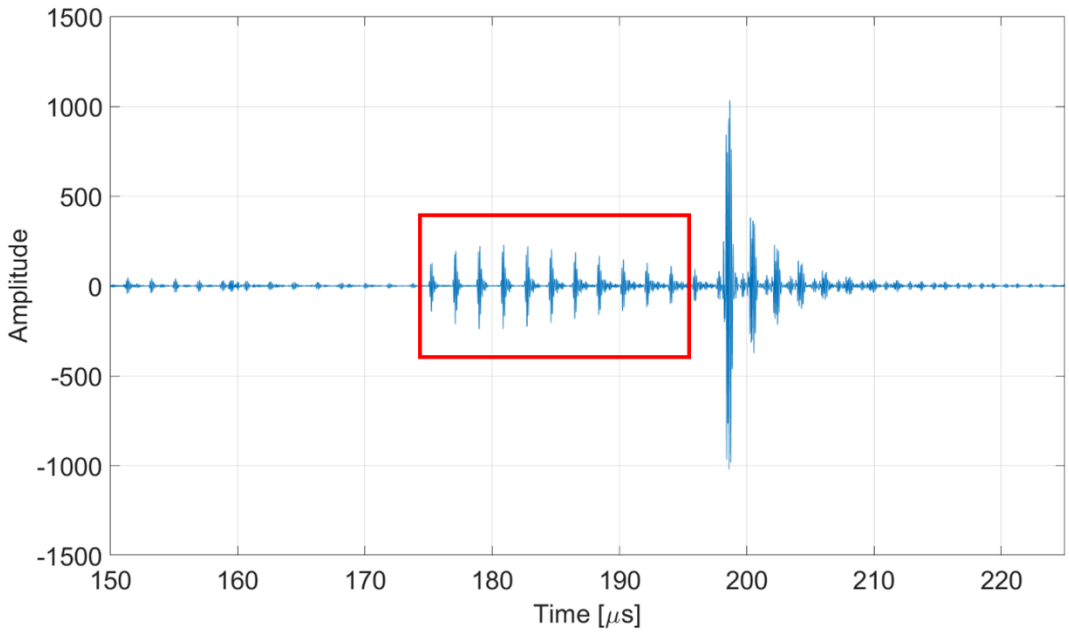


Figure 15: A-scan showing the double through transmission signal, highlighted in the red box. The high amplitude signal appearing around 200μs is a subsequent reflection from the sample surface.

2.5 Experimental Methodology – Ultrasonic Wave Speed Measurements

2.5.1 Double-through transmission technique

The double through-transmission bulk wave method was originally developed in order to determine the elastic moduli of composite materials non-destructively, through measuring ultrasonic velocities (specifically the phase velocities) in different directions in a composite material, and then using an inversion technique to reconstruct the elastic constants [109]. The originally proposed measurement method in the 1970s [110] involved a pitch-catch transducer configuration; however, for this setup, the exact position of the receiving transducer was critical for precise time delay measurements, and had to be adjusted carefully for each new angle that the sample was being tested in. Instead, to improve the measurement precision and reduce complexity, a modification was proposed [109] where just one transducer is used in pulse-echo mode, with a large flat reflector (oriented parallel to the transmitter) underneath the sample. This is such that the back-reflected wave travels along exactly the same path as the incident wave in the opposite direction

[109], and means that when the sample angle is changed, the position of the beam arriving at the receiver is not affected – even when the position of the incident beam on the back reflector is changed. There is also the additional advantage of a greater sensitivity in measurements, since a double acoustic path in the material is used for calculating the phase velocity. A schematic of this configuration is shown in Figure 16.

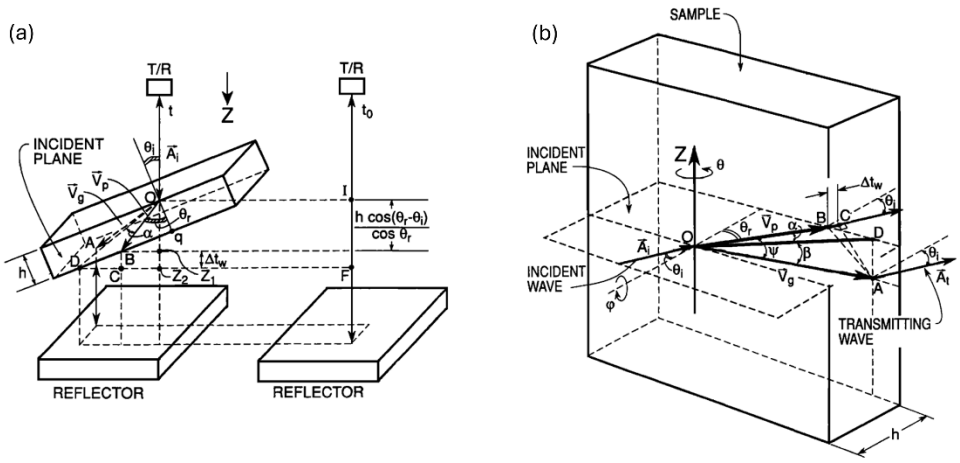


Figure 16: (a) Schematic of the DTT acquisition method, where (b) depicts the wave angles and directions. Adapted from Rokhlin and Wang [109].

There are two possible configurations of this further improved set-up, named the 'fluid reference method' (FRM) [111] [112] and the 'self-reference method' (SRM) [113] [114], with the main difference being the reference acoustic path; the former uses through-water, and the latter through-sample. For the FRM technique, the time difference between the doubly transmitted wave through the acoustic path with and without the sample is used to obtain the phase velocity in arbitrary directions. However, the use of the immersion fluid path as a reference has the potential to introduce systematic error into the measurement, for two reasons [115]; first, even a slight non-parallelism or curvature of the sample surface gives a small change in the refraction path in the immersion fluid, which would lead to a change of the acoustic path in the fluid with respect to the reference path – hence the parallelism of the surface is critical. Additionally, for a sample with high attenuation, the transmitted signal will change shape from the reference signal, which may cause difficulty in measuring the time delay difference of the signal compared to the measurement and result in inaccurate results.

In contrast, the SRM configuration improves the results by taking a reference velocity in the sample at normal incidence, and had several advantages over the FRM setup [115]. These include increased precision (as only relative changes in the TOF are measured, rather than the absolute TOF for a long acoustic path), and the elimination of possible cumulative error, as the phase velocity at normal incidence is measured in a more precise way. In addition, the attenuation-induced difference between measured and reference signals is reduced, and the technique is less sensitive to small changes in curvature of the sample surfaces – the effect of sample geometrical imperfection is minimised during the sample alignment process at normal incidence. It is the SRM setup which has therefore been used for the ultrasonic wave speed measurements for these experiments.

Regardless of the configuration, it is essential that the temperature is monitored and recorded at the time of taking the velocity measurements, as the signal drift caused by small temperature changes is on the same order of magnitude as the measured TOF differences. (For a +/- 2ns accuracy in time-delay measurements, the temperature must be measured to an accuracy of 0.01°C.) In the case of SRM, the TOF differences are usually less than 1μs, whereas a few degrees temperature drop can result in a signal drift of several hundred nanoseconds (caused by the variation of the speed of sound in water – for a 1°C increase in temperature, the speed of sound in water increases by around 2.4m/s [115]). In most cases, the temperature control of the immersion fluid is not straightforward; hence the alternative approach is to measure the temperature at the same time as the velocity measurements are being acquired, to then find the correct time delay for the velocity calculation. The speed of sound in water can either be found using experimental data, or analytically, such as through using a fifth order polynomial as a function of temperature [116]; it is the latter which has been used for these experiments.

2.5.2 Ultrasonic Wave Speed Measurement Experimental Setup

Over the course of this EngD, the required equipment and measurement codes have been drastically improved and streamlined such that the only apparatus required are the water tank, with a non-focussed piezoelectric transducer and mount (connected to a control box), a thermometer submerged in the water (to measure temperature, and ensure the most accurate calculation of the speed of sound through water as possible – as explained previously), an acoustic mirror at the base of the tank and directly underneath the sample, and a sample holder, which can be adjusted in the X direction automatically via the measurement codes (written in Python) and in the Y direction

manually using a micrometre-style adjustment wheel (left to right, and top to bottom respectively, as viewed by the observer at the front of the tank). The full experimental setup schematic is shown in Figure 17 [46] with the equipment itself in Figure 18. The default transducer frequency used is 10MHz, as the wavelengths at this frequency are typically over 10 times the grain size in materials which have been previously tested, such as Ti-6Al-4V; this allows the waves to propagate through the polycrystals with minimal scattering and a good signal-to-noise ratio [46]. It was found that this was also a suitable frequency to use for the first set of nickel-based superalloys samples which were tested. A thermometer is also required for the measurement of water temperature at the time of the velocity measurements; temperature changes must be compensated for (with there being no straightforward way to control the water in the tank) due to the signal drift caused by small temperature fluctuations being comparable to the time-delay differences occurring due to the change of the acoustical path in the sample (and its anisotropy) [115]. The transducer is a transmitter-receiver, both sending the ultrasonic waves through the sample as well as receiving the DTT signals; the use of the DTT ensures that the macro-texture being inspected is an average across the volumetric region of interest, or VROI [46] [37]. This VROI is around 5 times the thickness of the part, as determined by the largest angle of the Gaussian-Legendre nodes, and assumed to be homogeneous – as validated from previous experiments [37] [46].

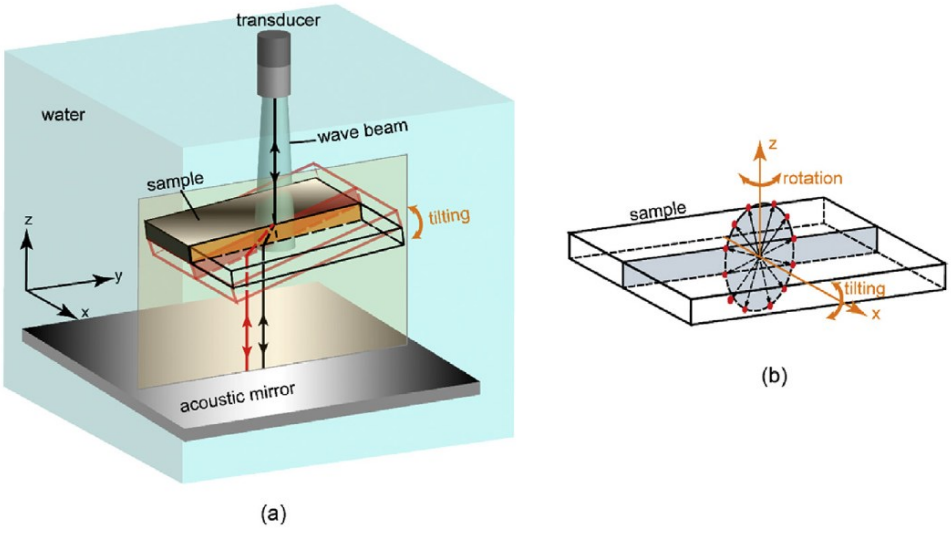


Figure 17: Diagrams of the ultrasonic experimental platform, with (a) showing the overall set-up and (b) depicting the adjusting of wave refraction direction through sample tilting. [2]

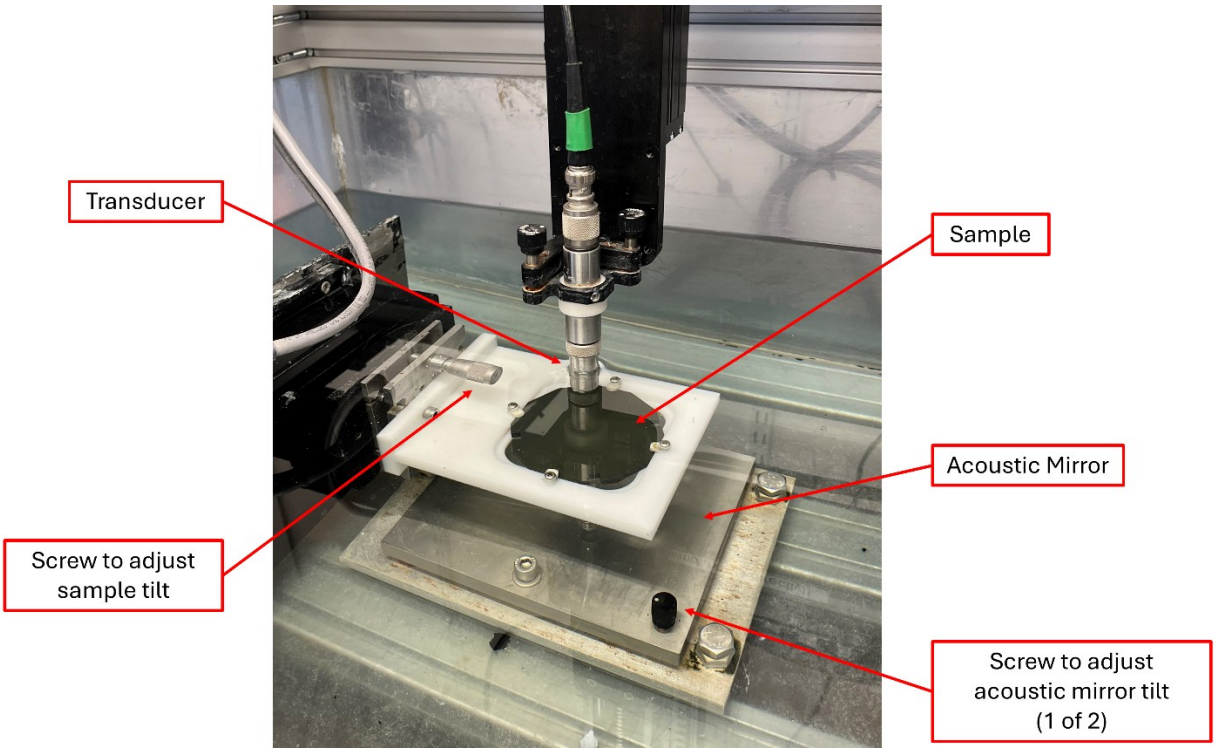


Figure 18: Lab setup for UWS measurements, showing the transducer, sample and acoustic mirror.

Before beginning the experiments, the acoustic mirror must be calibrated to ensure it is parallel to the transducer surface. The transducer is moved from one side to the other in both the X and Y directions, and the time shift between the first reflections at each end is calculated. The tilt of the mirror is then adjusted as required, using the screws in the corners (as pictured in Figure 18), which are linked to ball bearings controlling the height of the platform. The use of the reflections at each end, rather than measuring the time of flight at discrete points along the sample surface and plotting a line of best fit, ensures that the surface roughness does not affect the measured height difference between the ends. This calibration process is repeated until the height difference between the ends is no more than 3 microns, the minimum value possible with the sensitivity of the adjustment screws. Once the tolerances for each axis are met, the transducer is returned to the centre and then adjusted such that the ultrasonic signal being received is of the maximum amplitude possible (ensuring that the transducer beam is directly perpendicular to the mirror).

This concludes the pre-adjustment procedure that the measurement system requires. Once fully calibrated, the ultrasonic wave speeds through the sample can be acquired as follows:

1. It is initially ensured that the sample is parallel to the transducer surface. Similar to the calibration of the acoustic mirror, this is carried out by traversing the transducer across the surface of the sample for as great a distance as possible (which was generally +/- 5mm in each direction, due to the sample size), and adjusting the tilt of the sample accordingly to be within 3μm height difference between the two ends.
2. The acquisition gate is set to capture the first three double-through transmission (DTT) signals through the sample.
3. The acquisition of these three DTT signals at the required tilt angles (in the Z direction) is carried out, with the data being saved for each orientation automatically.
4. Once these signals have been saved, the tilt is then returned to zero degrees, and the sample is rotated by 30 degrees to be the second position of six in which the measurements are required. The calibration of the sample and subsequent data acquisition is then repeated until it is completed in all 6 of the required positions. These positions must be sequential for the application of the spherical convolution framework.

For the current apparatus configuration, the tilting and alignment of the sample to be parallel to the transducer are done automatically; the only manual adjustment required is to rotate the sample by 30 degrees to capture the signals in the 6 different orientations determined by the convolution theory.

The maximum sample tilting angle in the Z plane (for both directions) is determined by the first critical angle of the particular material being measured. This is in order to avoid platform collision, as there is no need to go beyond this first critical angle with only the longitudinal wave being of interest. This angle can either be found using Snell's Law [117], or experimentally; the former would only give a rough estimate, due to the fact that wave speeds are affected by texture. Hence the experimental approach was used, where the sample was tilted to the point where the longitudinal wave was no longer detectable, just at the point where the shear wave began to be seen (giving the first critical angle), and where the shear wave disappeared (which is the second critical angle). For Inconel 718, the first critical angle was found to be 13 degrees, and thus the sample was tilted between +/-13 degrees, with the ultrasonic wave speed data being saved at each orientation. It was assumed that this would be applicable for any further nickel-based superalloys which would be tested using this equipment.

2.5.3 Results Processing

On completion of the experiments, the data consists of wave speeds acquired in all 6 orientations and at tilt angles between the critical angles. The tilting and rotating of the sample in the water tank shifts the arrival time of the reflected signals, which are then cross-correlated with the arrival times of the normal-incident waves. The autocorrelation (or time correlation) process involves the comparison of the peak separation between the first and second echo signals by moving one peak to overlap the other; this enables the calculation of the refraction direction and the wave velocity.

The amount of peak separation is in the time domain, and together with the known thickness of the sample this can be used to calculate the velocity for the normal incident wave through the sample, using the standard velocity formula below [94]:

$$v = \frac{2d}{t} \tag{8}$$

The variable d represents the thickness of the sample and t is the measured time interval.

The cross-correlating of the results with respect to the normal incident wave allows a fitted 4^{th} order polynomial curve to be generated, which contains the required data points to extract the texture information through numerical integration. As discussed previously, this curve is a 4^{th} order polynomial (with velocity to texture being a 4^{th} order relation). The polycrystal wave velocities are then written in a matrix from which the single crystal wave velocities can be calculated to give the texture coefficients, which can subsequently be used to find the ODF. For good experimental practice to ensure reliable results, the data acquisition procedure is repeated 3 times per sample.

The steps required to post-process the signals obtained from the ultrasound experiment are summarised in Figure 19, and described in detail below.

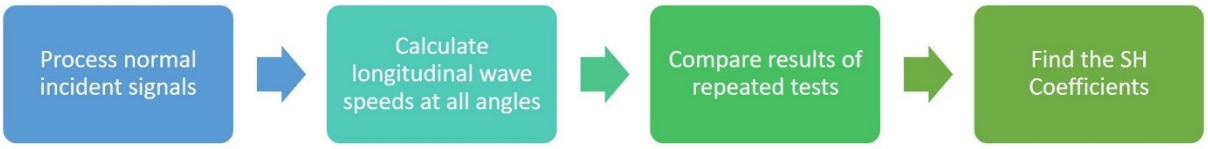


Figure 19: Overview of post-processing procedure to generate spherical harmonic (SH) coefficients.

1. **Process the normal incident signals**. In total there are 12 recorded normal incident signals (as there are 6 orientations, each time being tilted in the positive and negative directions), and each signal contains 2 to 3 reflection peaks. By averaging all 12 signals, the normal incident time of flight values (TOFs) can be calculated. The cut-off time containing the full first-arrival peak is similarly averaged. Both the TOF and the cut-off time are used for the next step (obtaining the oblique-incident wave speeds), as well as the time difference between the front-wall and back-wall echoes, Δt, which is also calculated here. (The cut-off time is automatically shifted as required when using the data for the tilted samples.) Figure 20 is an illustration of the process, with one recorded normal incident signal being shown, followed by its autocorrelation function.

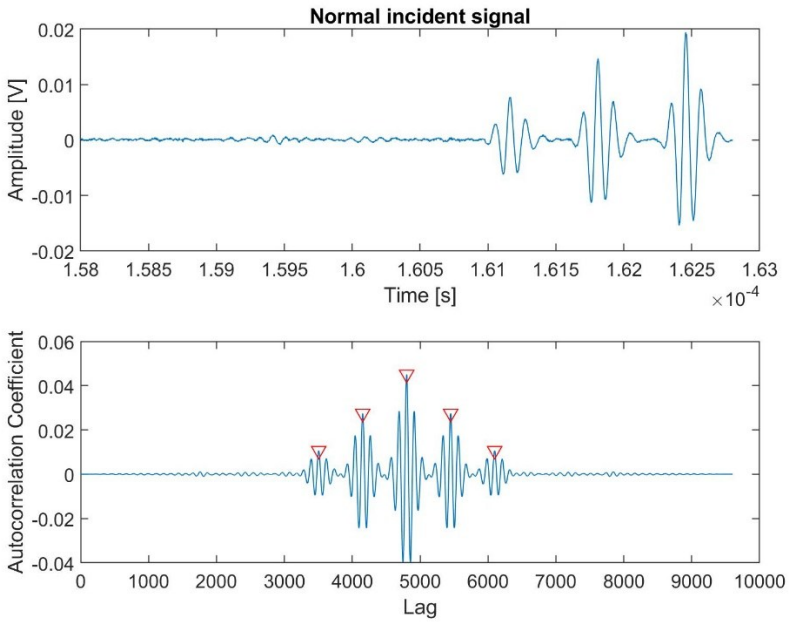


Figure 20: Calculating TOF of normal incident wave, and cut-off time shown for a test sample.

2. **Obtain the longitudinal wave speeds for all angles**. Tilting the sample shifts the TOF of the first-arrival signal; both the tilt angle and the signal are recorded, the signal is filtered to reduce high-frequency noise, and then is cross-correlated with the normal-incident signal to obtain the TOF (shown in Figure 21). Using a method described by Chu and Rokhlin [115], the tilting angle and the TOF are used to extract the refraction angle and refracted wave phase velocity.

In order to reconstruct the polycrystal wave speed surface, and hence calculate the SH coefficients, the wave speeds in particular directions are required – these are found by fitting the densely populated experimental results, and taking values at these exact directions (see Figure 22, where the yellow diamonds represent the points at which the velocities are required). These angles are the Gaussian nodes, and the need for velocities at these 6 specific angles (see Table 1) is a result of the Gaussian Legendre quadrature, used in obtaining SH coefficients up to the 4th order, which requires Gaussian nodes up to the 6th order [78]. These nodes are combined in different ways to generate the required SH coefficients (see step 4).

Table 1: The specific Gaussian angles at which the velocities are extracted (as determined by the spherical convolution expansion).

Gaussian Angles		
	Degrees	Radians
1	21.1769	0.3696
2	48.6078	0.8484
3	76.1949	1.3299
4	103.805	1.8117
5	131.392	2.2932
6	158.823	2.7720

The advantage of using this quadrature scheme as opposed to others, such as the equiangular scheme, is that it can achieve a given degree of accuracy with less data; for a discrete data set of 2N by N, a degree of accuracy of (2N – 1) can be obtained [107]. The spherical convolution theorem requires a 4th degree of accuracy, so in theory only 10 x 5 discrete data are required; however, as previously mentioned, the scheme is used here with N = 6 for increased accuracy and efficiency [78].

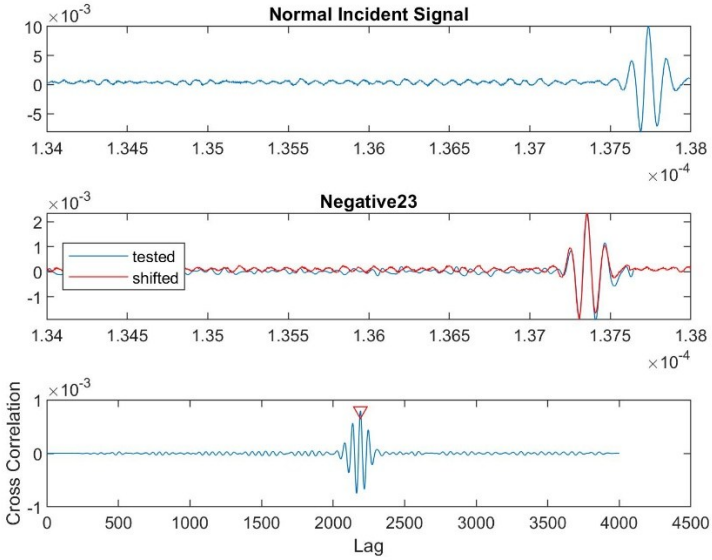


Figure 21: Cross correlation of (filtered) oblique incident signal with normal incident signal, for a sample in orientation 6.

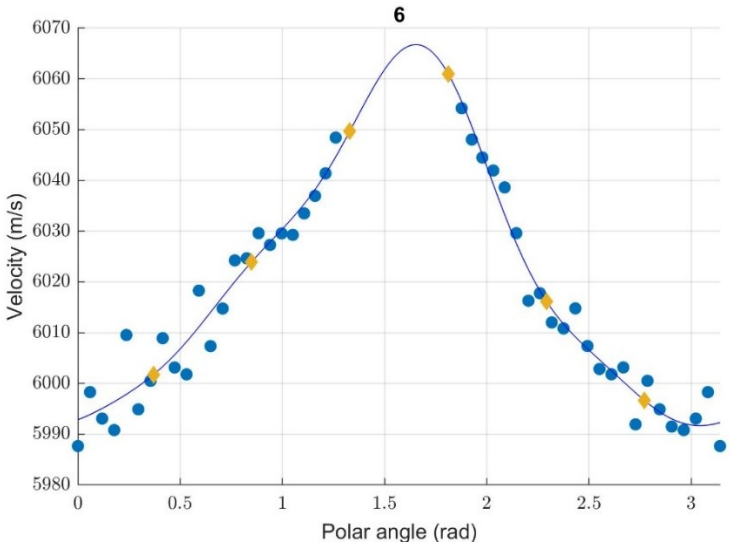


Figure 22: Fitting experimental results and extracting velocities at required angles (yellow diamond points) for a sample in orientation 6.

3. **Check the amount of overlap between repeated tests**. For repeated tests of the same sample, the wave speed results are compared; those within reasonable error bars of ±10m/s are averaged, and then final data set for velocity values is generated. Examples are shown in Figure 23a and b for a sample in its 6th orientation, where part (a) has been taken

from an experiment in early iterations of the test equipment to better illustrate the individual curves; the configuration used for this EngD had significantly better repeatability, to the point where the individual test results were not visibly separable (as shown in part (b), where the individual curves are no longer distinguishable).

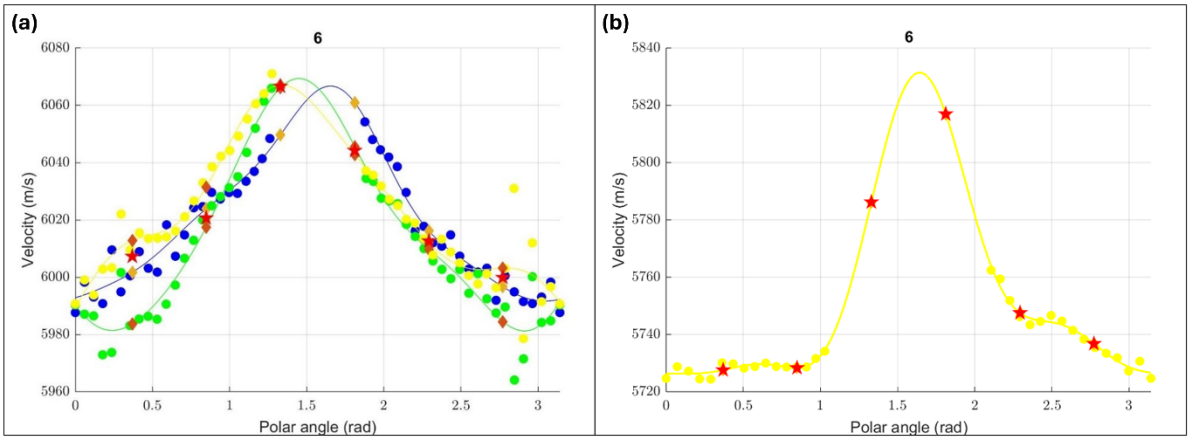


Figure 23: Averaging velocity values for a sample in orientation 6, where (a) show data from early experimental trials to illustrate data from individual runs, and (b) the data from later experiments with significantly improved consistency. The average fit line is in yellow, and averaged velocity values are represented by red star points.

4. **Find the SH coefficients, V_{00}.** The wave speed values at the given Gaussian-Legendre nodes are used to calculate the SH coefficients of the polycrystal surface; the input data is given in such a format that each column gives the velocities at a fixed azimuthal angle. These SH coefficients are then used to calculate the texture coefficients. The zeroth order coefficient is also displayed. A stereographic projection[2] plot of velocities is also generated – it is these velocities which are numerically integrated to find the SH coefficients. The equations required to calculate the spherical harmonic coefficients are as described previously in the theoretical framework section.

[2] A stereographic projection plot is a representation of velocity, showing the variation of wave speeds changing with direction in 3D space. It is generated by taking a unit sphere in a 3D x-y-z coordinate system, and connecting every point on the northern hemisphere of the sphere to the south pole, and mapping this vector onto the equatorial plane.

Having found the zeroth order coefficient of velocity, V00, Equation 6 can then be applied after finding the individual zeroth coefficients of stiffness, K00, for the two phases of interest for the material (or, specifically, the nickel-based superalloy) being inspected.

2.5.4 Novel development: Application to Nickel-based Superalloys

Although the main phases present in nickel-based superalloys differ from those in titanium alloys (used in Equation 6), the theory is such that the same principle of volume fractions can be applied. This is because the various phases which can develop in nickel-based superalloys (including the strengthening γ' and γ'' precipitates) form as finer particles within the larger γ matrix, and thus increases the stiffness of the overall crystal structure. This in turn effectively alters the single crystal elastic constant values, affecting K which therefore results in a change in V; this change can theoretically be detected by the ultrasound measurement, which in turn can be used to determine whether a phase change has occurred. This is the key further development of the spherical convolution theory and its practical application which the EngD research was focussed on; this technique had not yet been deployed on the nickel-based superalloy group of materials, for which the ability to be able to characterise the phase composition would be highly beneficial. It is not solely the amount of the strengthening phases present (such as γ' in Udimet 720Li and RR1000, and γ'' in Inconel 718) which has a significant impact on the mechanical properties of the material; the presence of other, potentially detrimental phases (such as the δ phase in Inconel 718) can similarly cause changes in mechanical properties. It is therefore extremely important to be able to detect whether the microstructure has been altered such as to pose a risk to the integrity of the part, whether it be due to depletion in strengthening phases or an increase in the more detrimental ones. The ability to rapidly determine whether the distribution and amount of these precipitates have impacted a component or material to the extent where it is unfit for service (or still suitable, but as a concession) could enable vast time and cost savings across industry. Indeed, improving the understanding of the phase content of a nickel-based superalloy may also open up possibilities for improving component life, subsequently extending the life of future aerospace engines.

The specific precipitates and their effects on material properties for the different nickel-based superalloys which have been investigated will be discussed in greater detail in following sections; first, an overview of this material family follows.

2.6 The Nickel-Based Superalloys: An Overview

Nickel-based superalloys are widely used in industrial applications where significant resistance to fatigue and creep under harsh working conditions is required. Two key applications include the nuclear and aerospace industries; for the former, nickel-based superalloys are often the material of choice for steam turbine blades and generator tubes in nuclear power plants [72]. In aerospace, nickel-based superalloys are used in gas turbines for jet propulsion, an example being high integrity rotating components, such as high-pressure turbine discs [118]; for a civil turbofan engine such as the Trent 800, turbine discs account for around 20% of the total engine weight, and 10% of the engine value on entry into service [119]. Although jet engine components are made of a wide variety of materials, including different types of metallic alloys including titanium-based materials, composites and ceramics (as shown in Figure 24), the nickel-based superalloys are vital for components within the hotter regions of the engine, primarily due to their superior mechanical properties and ability to resist mechanical degradation, oxidation and corrosion [72] at extremely high operating temperatures (beyond 800°C) [119]. These superalloy properties are a result of a balance between various alloying additions due to the trade-off in properties which these different elements provide, as well as the processing routes taken from ingot through to final forging, and as a result have some of the most complex metallurgy of all metals in existence [36].

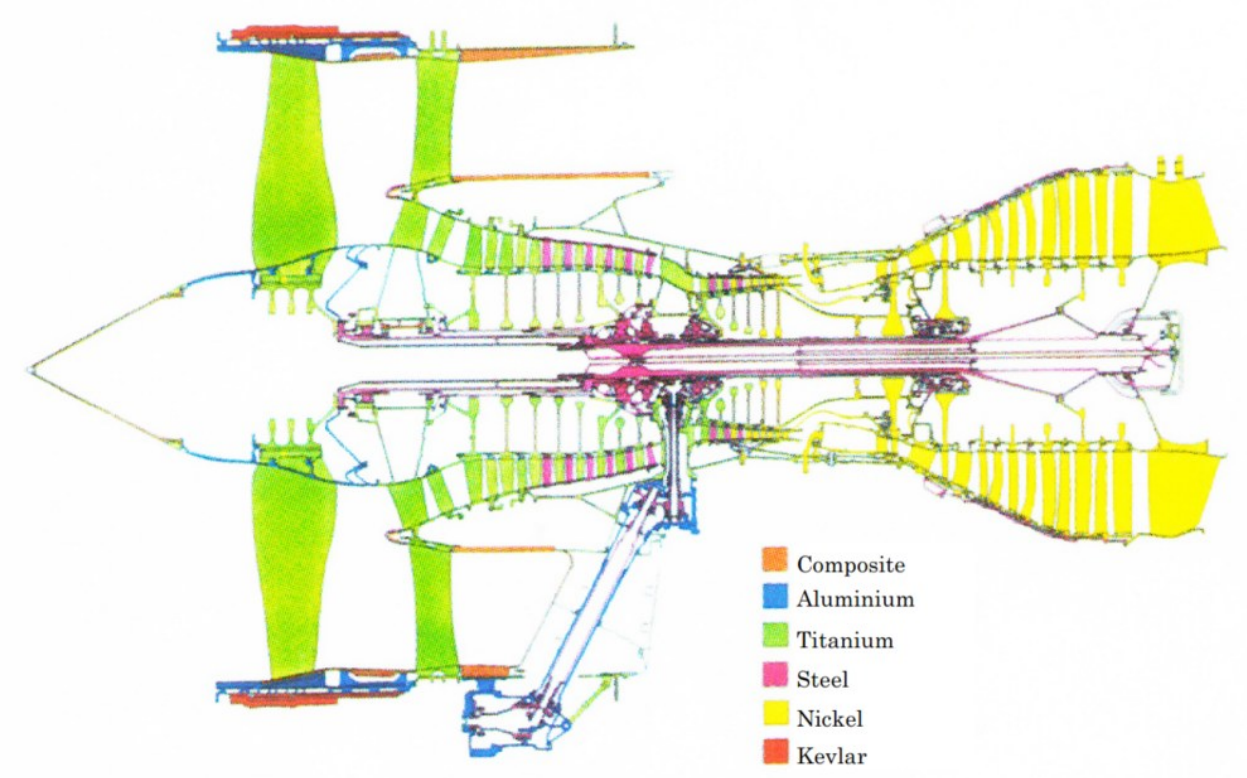


Figure 24: Schematic showing commonly used materials in a typical jet engine (a Trent 800 is shown here). [120]

2.6.1 Nickel-based Superalloy Processing Methods

Nickel-based superalloys are often designed for a specific purpose or industrial application – for example, Udimet 720Li was developed as an aerospace engine disc alloy. The two main processing routes for these turbine disc alloys are the wrought and powder metallurgy methods; to date, the wrought route has been most widely used.

2.6.1.1 Wrought Processing Route

For wrought processing methods, the superalloy ingots are cast in a double or triple melt process; a double melt comprises a vacuum induced melt (VIM), followed by either electro slag remelting (ESR) or vacuum arc remelting (VAR), as depicted in Figure 25; these reduce alloy segregation and eliminates cracks and porosity [36]. In the case of a triple melt process, the VIM is followed by both ESR and VAR [121]. These ingots are then thermo-mechanically processed to convert them into billets, breaking up the as-cast structure. This process is referred to as cogging, which helps to reduce micro-segregation, eliminate cast textures, and reduce grain size [122]. Further refinement

of the grain size is then carried out, to turn the billet into a useful forged shape which can be machined [36]; this is typically a 3-stage forging process, involving ‘upsetting’, ‘blocking’ and ‘finish forging’ [12]. Grain size is an important parameter to control, as it heavily influences the mechanical performance of the superalloy. However, there is a compromise made between fine grain size, which gives higher tensile strength and improved high-cycle fatigue (HCF) performance [123] as required for bore regions of discs (which operate at relatively low temperatures and high stresses), and coarser sizes which favour enhanced creep resistance, such as for the rim regions of discs where there are less severe mechanical loads but at higher temperatures [124].



Figure 25: An alloy undergoing a melt process. [125]

The primary considerations when manipulating and controlling grain size during deformation are strain, strain rate and forging temperature [126] (though other factors need to be taken into consideration, such as initial grain size and the volume fraction of second phase precipitates [127])[3]. The final grain size of the material will be smaller with reduced forging temperature, and increased strain and strain rates [123] [126] [128]; the extent of recrystallisation achieved will also depend on these factors. After forming, the disc forging is finally annealed to fully recrystallise the microstructure, as well as dissolving unwanted precipitates [36]; during age-hardening, these can be re-precipitated in a more ordered and desirable manner [129]. Having been age-hardened, the part can then be machined, which can involve removing a large amount of the original stock (usually between 80-90%) for a wrought process [12].

The recrystallisation process itself has a strong influence on the final microstructure, particularly the grain size distribution of the material. Recrystallisation is defined as the formation of a new grain structure in a deformed material through the formation and migration of high angle grain boundaries, and is driven by stored energy of deformation [130] (where a 'high angle grain boundary' is a boundary with a misorientation greater than 31 degrees [131]). The final grain size is highly dependent on the extent of the deformation performed on (and hence, the recrystallisation undergone by) the material [132].

The main three types of recrystallisation occur at different stages in the deformation process; dynamic happens as a result of continuous deformation, during which there is necklacing of new grains at grain boundaries [36], as illustrated in Figure 26. Meta-dynamic recrystallisation occurs directly after the deformation has stopped; microstructural changes can still occur due to the material still being hot, and therefore the dislocation movement is able to continue [133]. There is finally static recrystallisation, which occurs where there is deformation within a material but it is not undergoing deformation; an example is a cold rolled metal that is heat treated to relieve stress, resulting in new grain structures forming as a consequence of dislocation build up [133].

It should also be noted that, even after all recrystallisation processes have concluded, the microstructure is still not stable; the presence of grain boundaries, and the misorientation between grains, means that there is still a drive for change [36]. In reality the microstructure reaches a

[3] An additional consideration is the die temperature, as die chill will lead to uneven cooling in forgings; the cooler regions will then require greater forces to deform, ultimately resulting in inhomogeneous working of the part [21].

'quasi-stationary' state, where the potential for growth is so small that it can be assumed to have stopped [134]. Indeed, the potential energy stored within grain boundaries is so small that the driving pressure is two orders of magnitude less than required for primary recrystallisation [131].

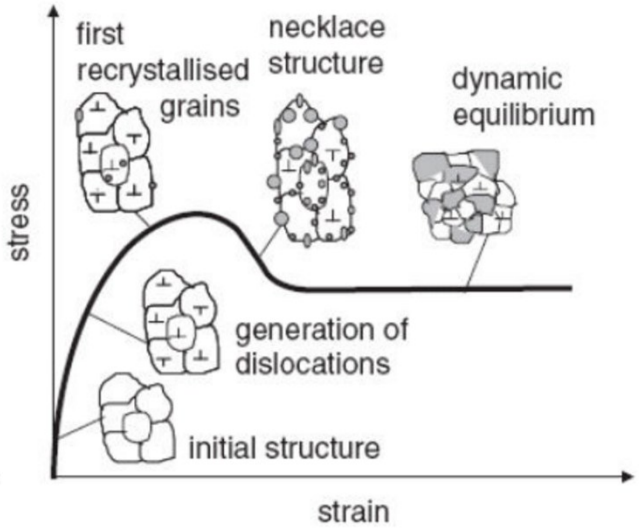


Figure 26: Schematic of dynamic recrystallisation process. [135]

As well as recrystallisation, there is an additional process which can occur that affects the grain sizes within the material; this is recovery, which is defined as the process during which stored energy is released from a material without the migration of a high angle grain boundary [130]. Recovery can be thought of as a competing process to recrystallisation, as the same stored energy is used to fuel the changes, and can often precede it [131]. There are several mechanisms through which stored energy release can occur during recovery, including point defect annihilation, mutual dislocation annihilation, and the organisation of free dislocations into dislocation walls [131]. Much like recrystallisation, there are two ways in which recovery can occur, where 'dynamic' takes place during deformation (where grains become more elongated, and subgrains remain equiaxed), and 'static', which occurs during subsequent heat treatments [36]. Static recovery acts similar to annealing processes, where the ductility of a metal is increased without changes in the grain size [131]. The ability of a material to undergo recovery tends to depend on its stacking fault energy, which is the energy resulting from an interrupted stacking sequence [136]; this is shown in Figure 27 for an FCC material. In general, an increased stacking fault energy makes it easier for the material to recover [131]; however, the large amounts of alloying additions in nickel-based superalloys result in low to medium stacking fault energies [131].

Materials with this low to medium stacking fault energy can, however, be susceptible to the formation of annealing twins, a phenomenon that tends to occur at high temperatures as part of the recrystallisation process [36]. Twinning results in the production of new orientations that were not present in the original microstructure, which can lead to highly immobile and very stable grain boundaries [137]. Coherent twin boundaries are particularly stable, as the atoms fit perfectly across an interface (as opposed to an incoherent twin boundary, which does not have a large amount of coincident atoms) and can prevent high temperature crack propagation at grain boundaries [138].

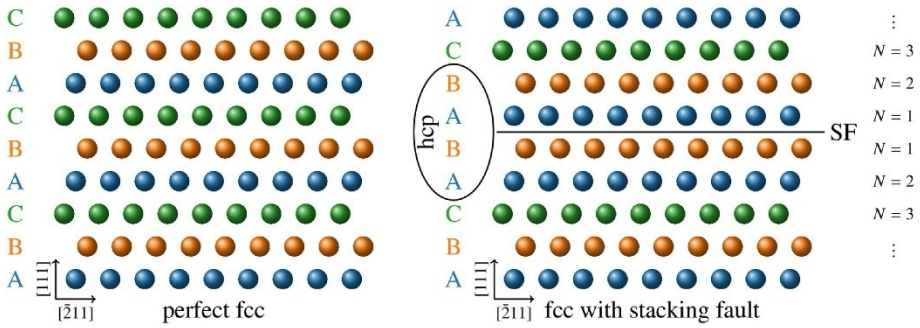


Figure 27: Illustration of stacking faults in FCC materials. [136]

Both recovery and recrystallisation can result in variations between grain sizes within nickel-based superalloys, which can pose problems in terms of ultrasonic inspectability as well as mechanical performance. This is a particular issue in Udimet 720Li, which is notoriously difficult to investigate using ultrasonics due to the non-uniform amounts of recrystallisation through the material. However, there is an alternative manufacturing method for nickel-based superalloys that can be used to minimise the variations caused by phenomena such as recrystallisation and recovery; this is the powder metallurgy technique.

2.6.1.2 Powder Metallurgy Processing Route

The powder metallurgy processing route is an alternative method for the manufacture of nickel-based superalloys which reduces the amount of micro-segregation and non-metallic inclusions in more complex alloys [36] [139]. This technique involves the production of a powder which is first sieved, in order to remove large non-metallic inclusions, before being degassed, sealed and then either hot isostatically pressed or undergoing extrusion into a billet [36]. There are several

techniques in use for the production of powder, including gas atomisation, electrode induction melting gas atomisation, and hydrogen reduction to powder from an aqueous solution [140].

The powder metallurgy process has several advantages over the traditional wrought route, including the improved property uniformity [141] (due to elimination of micro-segregation), the ability to manufacture materials with very fine grain sizes, and hence good fatigue performance [142], and to reduce the thermal cracking tendency of the alloy during hot working [143]. Nickel-based superalloys typically manufactured via the powder metallurgy method include such as RR1000 [144], and RR1073. The main drawback of this technique, however, is the significantly higher cost; as such, powder metallurgy tends to only be used where the cast-wrought route would be unsuitable, such as where there is complex alloy chemistry which has the risk of chemical and microstructural inhomogeneity [12].

Regardless of the processing route taken, the nickel-based superalloys have the same, often complex, metallurgy, which will be discussed in detail in the following section.

2.6.2 Nickel-based Superalloy Metallurgy

Although there are different types of superalloys, including the aforementioned cobalt- and iron-base, the nickel-based superalloys are often preferentially used due to some key advantages, including their face-centred cubic (or FCC) crystal structure, shown in Figure 28; this structure is retained from ambient conditions to its melting point, 1455°C, the absolute limit for the temperature capability of the nickel-based superalloys [119]. This means that they are both tough and ductile [145] – in contrast to titanium alloys, for example, which have a Hexagonal Close-Packed (HCP) structure [108]. (It has also been found that FCC metals have a steady-state creep rate of one or two orders of magnitude lower than for BCC metals, which further supports the choice of nickel as a superalloy base for high temperature applications [146].) The differences between these crystal structures' ductility behaviour can be illustrated with impact energies, which indicate the toughness of a material at a specific temperature; in Figure 29, which shows the impact energy variation with temperature, the region of a dramatic increase in impact energy is defined as the ductile-brittle transition temperature [147]. The lower the temperature, the more susceptible to brittle fracture a material is; it can be seen that HCP metals have a very low transition temperature due to their limited systems; in contrast, the energy barrier for plastic flow is very low in FCC metals, resulting in there being no transition for this lower temperature range.

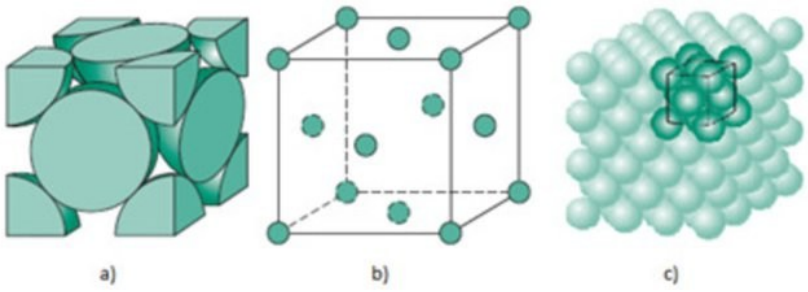


Figure 28: The FCC Crystal structure as (a) a hard-sphere unit cell, (b) a reduced sphere unit cell and (c) an aggregate of many atoms. [148]

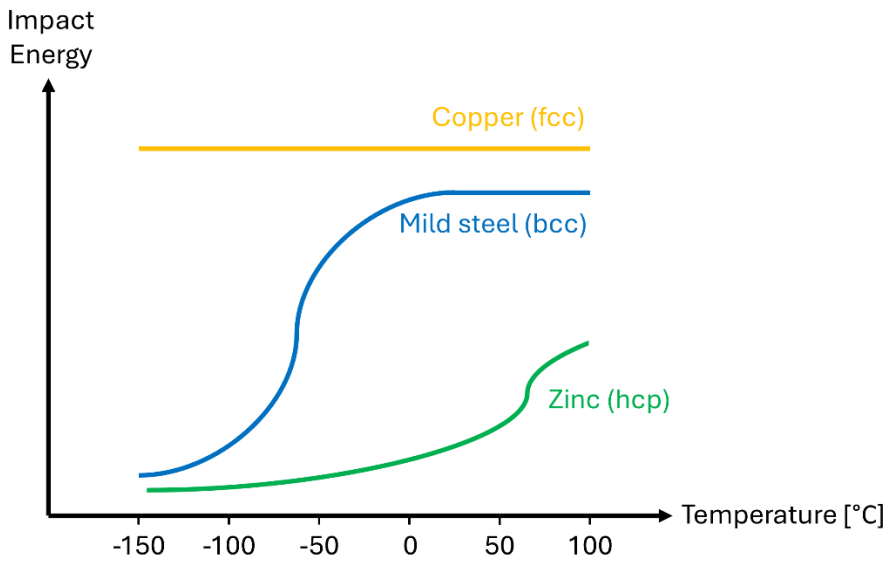


Figure 29: Plot of impact energy (and ductile-brittle transition range) for various crystalline structures in metals. Adapted from [147].

The strength of nickel-based superalloys arises from the combined effect of precipitation hardening, solid solution hardening, and the existence of carbides at grain boundaries [149]. The fact that nickel can be precipitate-hardened means that its high temperature creep resistance can be enhanced, and components do not elongate as rapidly as other metals, such as steel [122]. (Indeed, nickel-based superalloy components tend to be comparatively more compact and lighter than those produced from conventional steel [2].) An additional benefit is the fact that nickel does not undergo any allotropic phase changes (i.e. changes in crystal structure, leading to volumetric changes) from room temperature to its melting point, unlike steel and titanium [12]. However, both titanium alloys and nickel-based superalloys are widely used in jet engines, but with different applications and are thus not direct competitors. Titanium alloys are favoured mainly due to being

lightweight with a lower density (4420kg/m^3 at 25°C, compared to 8190kg/m^3 typical of nickel-based superalloys [2]), and hence have a higher specific strength. However, their peak operating temperature is lower (under 600°C) with reduced strength at higher temperatures [150] [151], and they also have poor oxidation resistance – this restricts them to applications of below 700°C [152], and limits their use to upstream of the combustor. Downstream of the combustor, where temperatures far exceed 600°C, nickel-based superalloys are used instead – including Inconel 718, Udimet 720Li and RR1000.

An additional difference between titanium alloys and nickel-based superalloys is the type of phase present – titanium alloy phases include alpha, beta and alpha-plus-beta [153], and the main phases in nickel-based superalloys are the gamma (γ) matrix, together with the gamma-prime (γ'), and gamma double-prime (γ'') precipitates – although other phases can develop including the carbides and borides phases (which tend to reside on γ grain boundaries [119]) or the topologically-close-packed (TCP) phases, such as the delta (δ) phase, particularly in service-aged superalloys [154]. A brief overview of these phases and their crystalline structures are given in the following section.

2.6.3 Phases in Nickel-Based Superalloys

A time-temperature-transformation diagram for Inconel 718 is shown in Figure 30 to illustrate the typical phases which are present in nickel-based superalloys. The main phase within which all other precipitates are formed, both coherently and incoherently, is the γ phase, which is an austenitic FCC crystal matrix with an atomic arrangement as shown in Figure 31a. (Coherency refers to the type of interface between the solid phases; if coherent, there is a perfect registry of the lattices, where in the case of incoherency there is no matching of the interface [155].) In nickel-based superalloys, this continuous γ matrix contains elements in a solid solution with nickel, including cobalt, iron, molybdenum and chromium [36].

One of the main strengthening precipitates within this γ matrix is the γ' phase, with an ordered $L1_2$ crystalline structure [156], as illustrated in Figure 31b. The γ' phase is formed during heat treatments, and is key in improving the hardness of the materials due to being a barrier against dislocation movement; the location and morphology of this precipitate is also key in ensuring the creep life and high temperature performance of the material [36].

The γ'' phase is an additional strengthening precipitate, which has a body-centred tetragonal (or BCT) $D0_{22}$ crystal lattice structure as shown in Figure 31c, and chemical composition Ni_3Nb [157]. The γ'' phase tends to be the primary hardening phase; however, in recent years, γ''-strengthened superalloys have been pushed further back in the turbine with the advent of newer materials with higher temperature capabilities [158].

Although it has the same chemical composition as the γ'' phase, the δ phase differs in that it is an incoherent, brittle orthorhombic precipitate [36]. Despite it not contributing to the overall strength of a material, it can help to control grain size via the pinning of grain boundaries during thermomechanical processing [159] [123]; as previously discussed, grain size itself is an important characteristic which can affect the mechanical performance of the material.

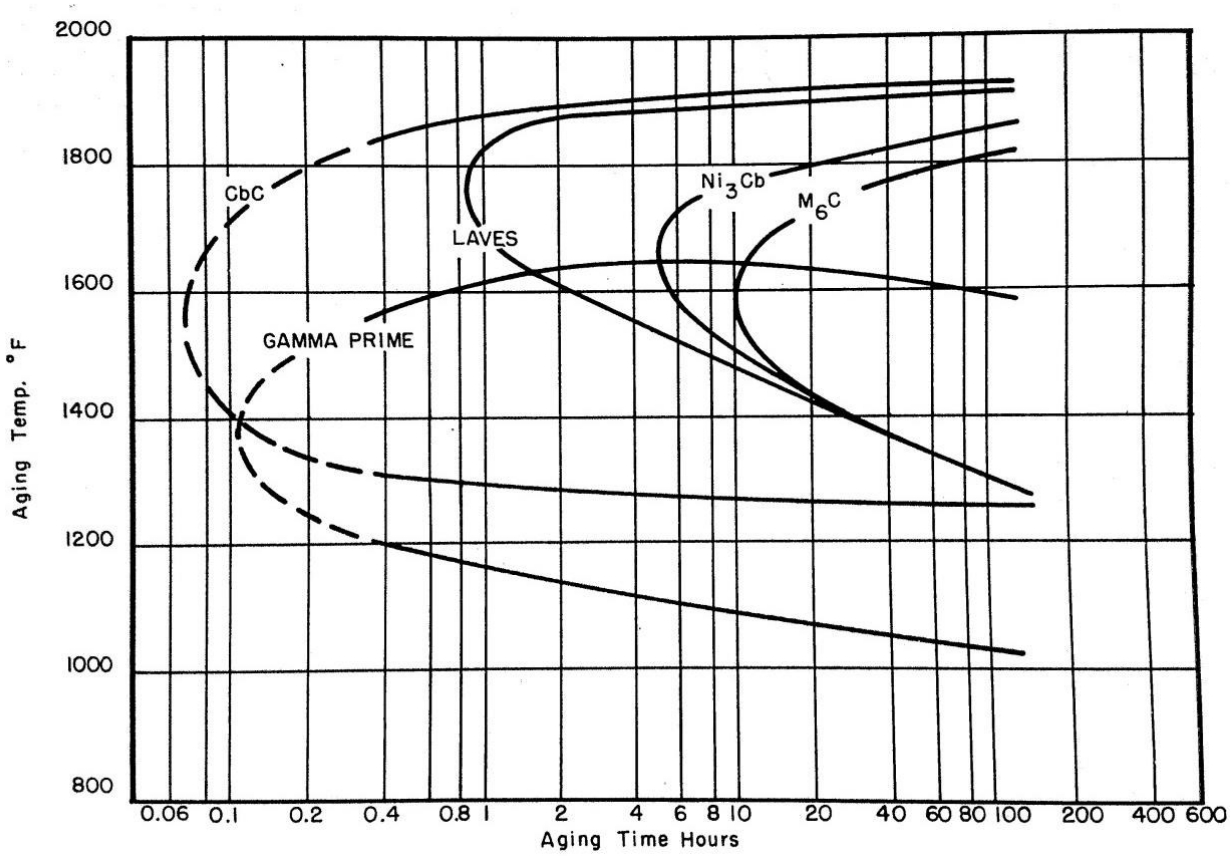


Figure 30: The original TTT diagram for Inconel 718 as proposed by Eiselstein. [160]

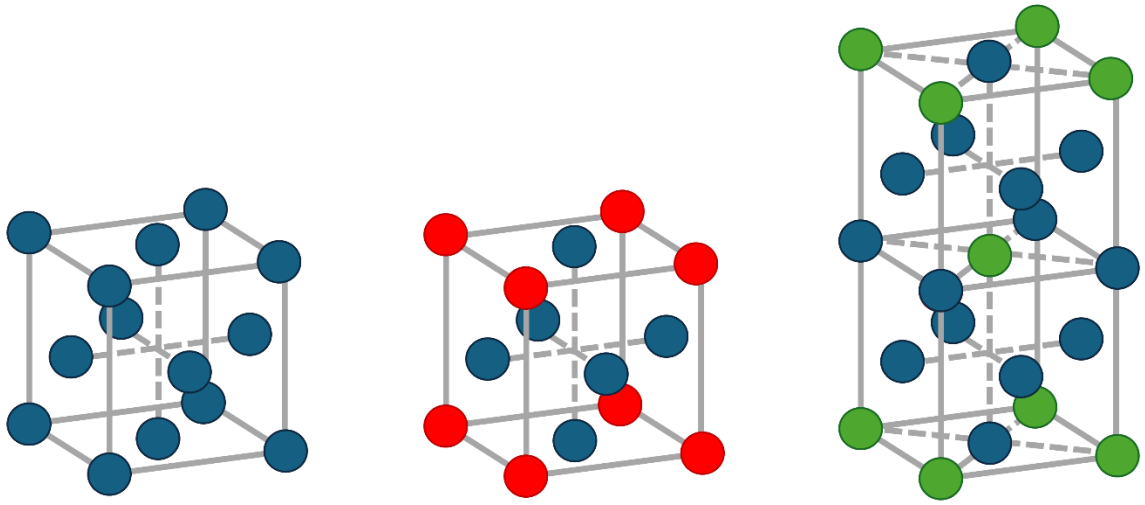


Figure 31: Crystal structures for (a) gamma phase (FCC), (b) gamma prime phase and (c) gamma double prime phase. Adapted from Watson [36].

2.6.4 Factors Affecting Nickel-based Superalloy Properties

The two main characteristics of the nickel-based superalloys which contribute to its mechanical properties are grain size and the phase composition (including the quantities and morphologies of these phases). Both can be tailored using specific processing methods and heat treatments which vary depending on both the material and its particular application.

The mechanical behaviour of nickel-based superalloys is strongly affected by the grain size in the material [161]; differences in grain sizes and distributions have a large impact on a material's creep-fatigue behaviour. The working conditions in different jet engine parts pose different demands on the mechanical properties – and hence the grain size requirements – of the superalloys used. Typically, the design of high-pressure turbine discs (such as those used in jet engines, shown in Figure 32, or gas turbines for electricity generation) are focussed on low cycle fatigue life and resistance against disc burst [162]; these properties are optimised by using alloys with a homogenous, small grain size. However, for use in high temperature disc and blade applications, damage mechanisms such as creep and creep-fatigue crack propagation could occur in the disc rim or blades. This means that larger grain sizes [163], or ideally single crystals, are required.

Creep behaviour can be divided into separate regions, as shown in Figure 33; there is an initial rapid transient (primary creep) which leads into a region of approximately constant creep strain rate (secondary creep). The final region, tertiary creep, is marked by a divergence from the steady-state creep behaviour, where the creep strain rate increases with strain until the material fails through fracture [119].



Figure 32: A turbine disc for an aerospace engine. [164]

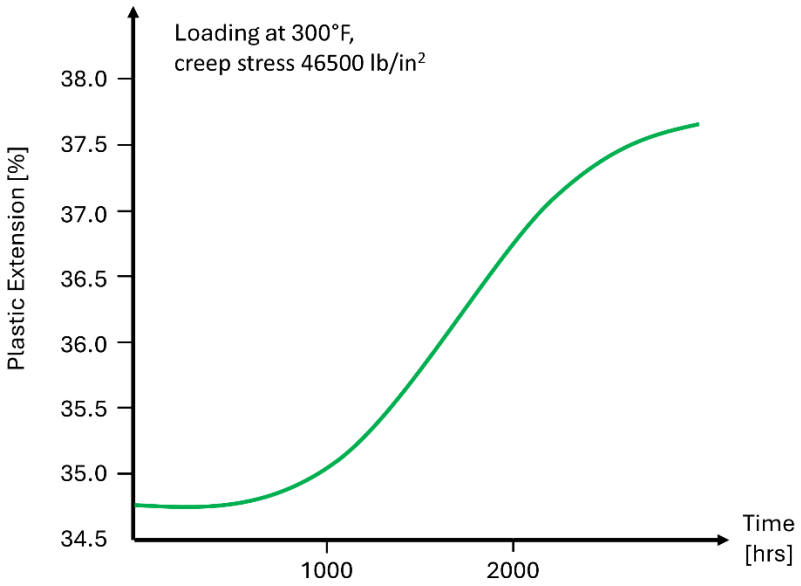


Figure 33: An example creep curve, for nominally pure nickel at 300°F with a creep stress of 46500 lb/in². Adapted from Jenkins et al [165].

In terms of phase composition, which is the other main influence on the material mechanical properties, the alloying additions as well as their quantities are tailored very carefully to generate the optimal amounts and morphologies of the required precipitates. Standard alloying additions include iron, titanium, chromium, aluminium, cobalt, niobium, molybdenum and boron [122]. These alloying elements can occupy one of three positions within a superalloy [12]; solid-solutionised in the main metal matrix, forming as intermetallic precipitates (or secondary phase particles), or forming precipitates at grain boundaries. Key solid solution strengtheners include cobalt, chromium, iron and molybdenum, whereas aluminium, titanium and niobium contribute to the formation of matrix-coherent hardening precipitates; elements such as chromium, hafnium and boron combine with carbon to form carbides which sit on grain boundaries [122].

In addition to these three strengthening mechanisms, the various alloying elements can have further benefits; iron, for example, can help to increase the weldability and formability of the material. This is not only a benefit for the manufacturing process, but also means that expensive parts can be repaired much more easily post-service [166]. Cobalt is also an excellent addition, as it reduces the solubility of aluminium and titanium in the metal matrix, resulting in the formation of greater volume fractions of the γ' precipitate [167]; indeed, nickel-based superalloys tend to have higher operating temperatures with the presence of cobalt [36]. However, it does have the drawback of being expensive, as well as being very difficult to form and machine. Other elements with beneficial effects are hafnium, boron, carbon and zirconium, which contribute to improved creep rupture life [168] and are crucial for single crystal or directionally solidified blades and vanes.

Of the three mechanisms described, the two key to the strengthening of nickel-based superalloys are solid solution strengthening [169] and precipitation hardening; the latter is where the UWS method could be deployed, in terms of determining the amount of precipitate present in a material. The process of precipitation hardening will be discussed in the following section.

2.6.5 Heat Treatment Processing: Precipitation Hardening

A typical heat-treatment process of nickel-based superalloys (to facilitate precipitation hardening) involves holding the material at an elevated temperature (the 'solid-solutioning' temperature) for several hours (usually ranging between 4 to 16 hours [118]) before cooling, or 'quenching', the material, either in air or oil. The faster the cooling rate, the lower the likelihood that undesirable precipitates will come back out of solution. Most heat treatments also include a further 'ageing'

process, where the material is held at an elevated temperature after being quenched, which helps to ensure that the key phases can be precipitated to their full extent, and required size. The determination of an optimal heat treatment is a compromise between achieving a balance between the best possible material properties without expensive and time-consuming heat-treatment schedules. Heat treatments can be tailored by altering the cooling rate, hold temperature and hold time, which will all impact the amount and size of the strengthening phase (such as γ'' for Inconel 718) precipitated in the material.

The rate of cooling in particular has a strong effect on the microstructure of the heat-treated material; the size and morphology of the γ' precipitate in Udimet 720Li, for example, varies depending on how slowly the material has been cooled (where in general, the slower the cooling rate, the larger the γ' precipitate [170]). Similarly, a slower cooling rate in Inconel 718 can allow precipitates other than the strengthening γ'' and γ' to form, such as the δ phase, as shown in Figure 34 – where the slower cooling rate has clearly allowed for a larger amount of this δ phase to form. Another consideration is the fact that high cooling rates (achieved with oil-quenching) can result in large internal thermal gradients and residual stresses, leading to cracking [171]. Hence a slower cooling rate is generally beneficial to the alloy (other manufacturing constraints permitting).

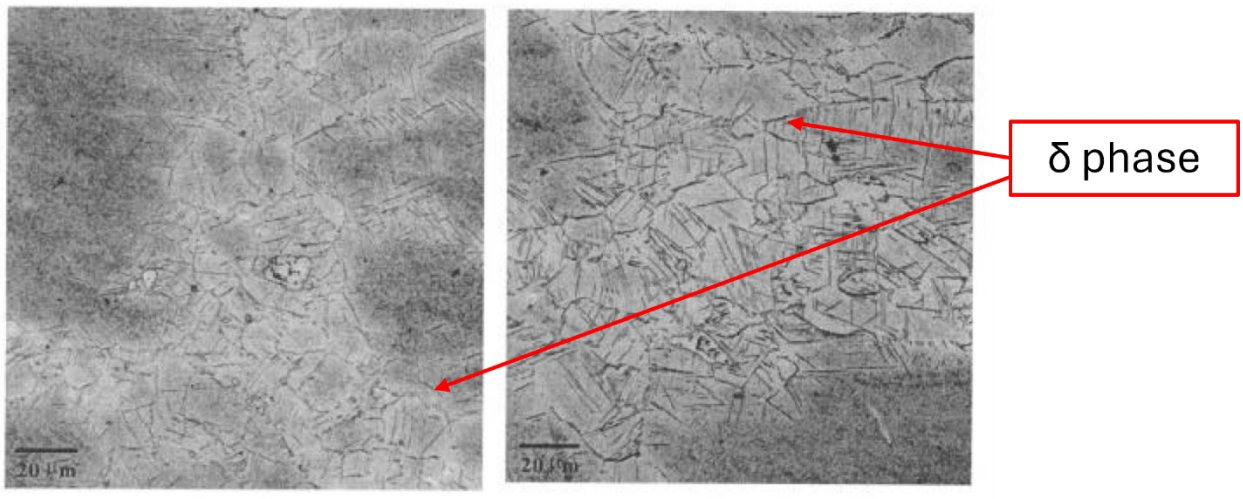


Figure 34: Micrographs of Inconel 718 after a solution heat treatment and over-aging at 732°C for 100 hours, where (a) is cooled at 11°C/minute and (b) at 28°C/minute. [172]

The hold temperature also has an effect – higher solution temperatures will result in improved creep resistance, but will compromise the tensile and fatigue strength of the material [173]. There is also a compromise between good yield strength/resistance to fatigue crack initiation (which

improves with decreasing grain size) and creep strength/resistance to fatigue crack growth (which improves with increasing grain size) [119]. Finally, when determining the appropriate heat treatment to use, it should also be kept in mind that uniform precipitate distribution should be achieved [119].

The extent of precipitation strengthening is determined by the selected heat treatment, but the effectiveness of such strengthening can also degrade during service. The UWS method could potentially be used for applications such as inspecting in-service components, as well as raw materials prior to component fabrication. Through understanding how each stage of the heat treatment process – temperature, cooling rate and ageing conditions – affects the key precipitates' morphology and distribution, the production of materials used for jet engine applications can be optimised [170] and the degradation of in-service components could be routinely checked; it would therefore be beneficial to have a quick, easy and non-destructive method to be able to accurately and reliably analyse the material's microstructure. However, as previously mentioned, there are slight variations in the microstructure (particularly in terms of the precipitates which form) within different nickel-based superalloys, and thus it was necessary to carry out experiments on different materials to verify that the ultrasonic wave speed method was applicable to different materials.

However, it was first important to carry out a feasibility study, to verify whether the technique could successfully detect microstructural changes which had taken place; Inconel 718 was utilised for these investigations, as it was the most accessible and, at the time, it was considered that the microstructure would be representative of other nickel-based superalloys, and could easily be manipulated via heat treatment. The following chapter of this thesis will discuss this first stage of experimental work.

3. Feasibility Study: Inconel 718

3.1 Introduction

This chapter focusses on the first stage of experimental work – namely the determination of whether or not the zeroth coefficient of velocity, V00, is sensitive to microstructural changes occurring within nickel-based superalloys. Inconel 718 was selected as a representative nickel-based superalloy; an overview is given of the material's characteristics and properties, followed by detailing the microstructural properties of the specific samples used for the study. The results from the experimental work, including both microscopy examinations as well as the first complete set of UWS data for Inconel 718, are then summarised and discussed, thus laying the foundations for the work carried out over the course of this EngD. The work in this chapter has been published in the peer-reviewed journal 'NDT&E International' [37].

3.2 Microstructure, Manufacture and Properties of Inconel 718

The first nickel-based superalloy to be investigated during this project was Inconel 718. This material is widely used for disc rotor applications in the compressor and turbine of aircraft engines [31], including heat shielding, bolts and fasteners [36], as well as the disc itself, due to its high strength, fracture toughness and resistance to corrosion and oxidation [174]. Historically it was used for first row engine discs, where the hottest temperatures are seen, but as superalloys with higher temperature capabilities have been developed the components using Inconel 718 have been pushed further back in the engine [175]. Its enduring success, despite the development of more capable superalloys, can be attributed to its ease and cost of manufacture (and relative ease of repair [36]), a low rate of melt anomalies from primary and remelting practices [176], as well as its excellent material properties which can be obtained from forging and either a conventional heat treatment, or a direct age [177]. It is also a good material for additive layer manufacturing [178] [179], which has seen an increase in popularity due to the reduction in material wastage when manufacturing components.

The samples of Inconel 718 used for this project had the designation AMS 5662, meaning that the chemical composition is as detailed in Table 2. If fully conforming to specification, the material will have undergone solution annealing at 968°C, followed by rapid cooling (usually in water), and precipitation hardening at 718°C for 8 hours followed by a furnace cool [180].

Table 2: Chemical composition of Inconel 718, AMS 5662. [180]

Element	Percentage
Nickel (Ni)	52.5
Chromium (Cr)	19.0
Molybdenum (Mo)	3.0
Niobium (Nb)[4]	5.1
Titanium (Ti)	0.90
Aluminium (Al)	0.50
Iron (Fe)	18.0

The main phase present in Inconel 718 is the gamma matrix, with secondary phases including gamma prime (γ'), gamma double prime (γ''), and delta (δ, also known as beta, β), which form coherently within the γ matrix. The strengthening of the material is via age hardening heat treatments which precipitate mainly the γ'' phase, with the γ' also forming but to a lesser extent. There are also minor phases, such as the carbide and Laves phases.

The composition of Inconel 718 provides a relatively low volume fraction (around 22%) of both γ'' and γ', with further thermomechanical processing producing a fine grain matrix (ASTM 10-13) and extremely small γ'' and γ' precipitates (less than 50nm) [31]. The relatively high iron content is beneficial as it acts not only as a solid solution strengthener, but also catalyses the γ'' precipitate formation [122]. It also makes the material easier to form and weld, in comparison to superalloys containing higher quantities of cobalt [166]. Chromium is key to increasing corrosion resistance, particularly against sulphur which tends to be found in fuels [181]. Aluminium and titanium are strong γ' formers, niobium constitutes the γ'' phase, and molybdenum is key for the solid solution strengthening of Inconel 718 [166].

The Time Temperature Transformation (TTT) diagram provides information on what phases can be expected in Inconel 718 depending on the temperature conditions. These diagrams essentially illustrate the isothermal transformation behaviour, and are generated using results from testing materials at different holding times and temperatures, before carrying out hardness testing and metallurgical imaging [182]. Since the initial conception of Inconel 718, the TTT diagrams in the

[4] Also known as Columbium.

literature have undergone minor modifications; the original was proposed by Eiselstein [182] in 1965, shown in Figure 30 in Section 2.6.3. More recent iterations, such as by Brooks and Bridges [128] as shown Figure 35 and that of Slama and Cizeron [183] in Figure 36, omit the Laves phase and suggest that this is more likely to be the δ phase. Similarly, Oradei-Basile and Radavich [182] proposed a diagram without the Laves phase (shown in Figure 37), suggesting that the improvement in metal processing techniques reduced the amount of carbon present [128]. These latter two TTT diagrams also contain the alpha-chromium (α-Cr) and sigma phases, which tend to form following long term exposure to temperatures and stress [36] [182]. Figure 38 shows a modification of this diagram proposed by Ranhof et al., which also includes the behaviour of Inconel 718 subjected to high strain rates. An alternative representation to these TTT diagrams is a schematic of the solidification and precipitation sequence during cooling of each of the phases (Figure 39).

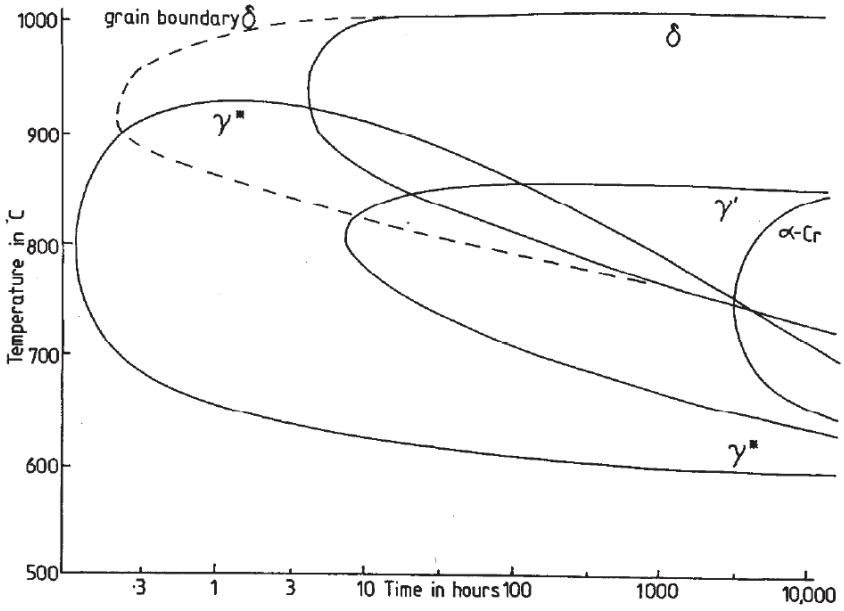


Figure 35: A modified TTT diagram proposed by Brooks and Bridges, omitting the Laves phase. [128]

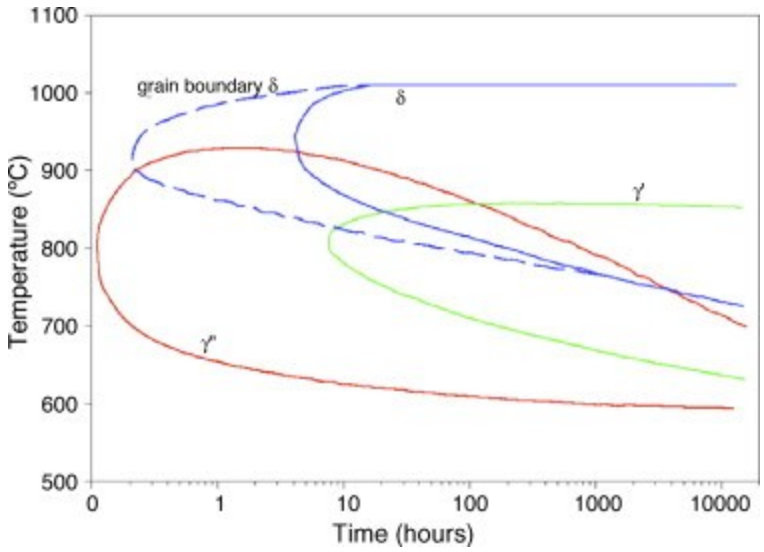


Figure 36: Slama and Cizeron's TTT diagram for Inconel 718. [183]

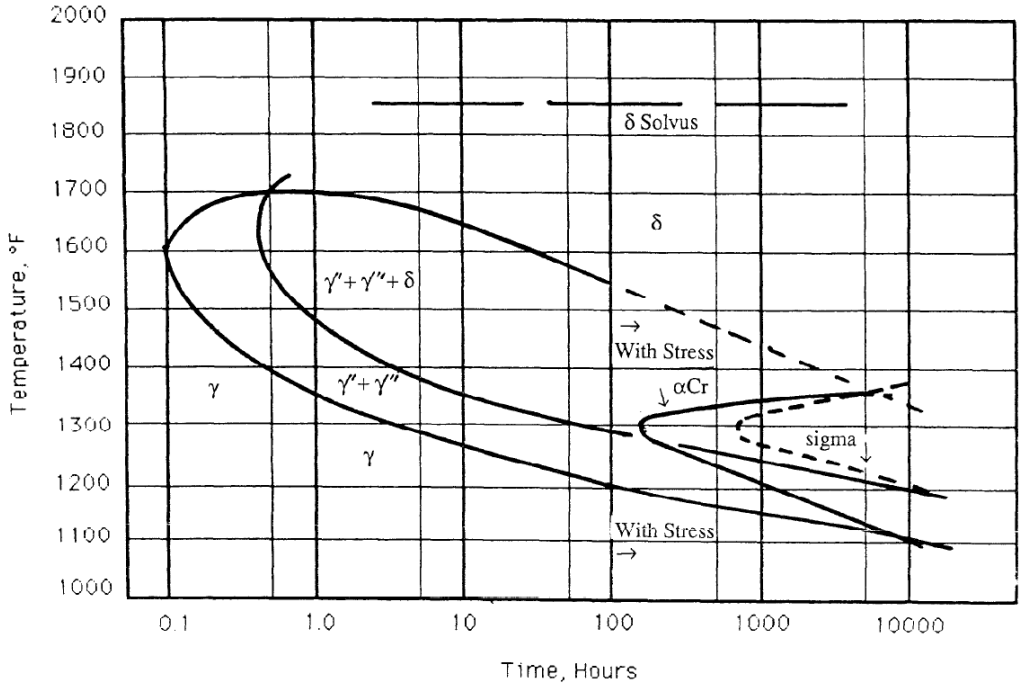


Figure 37: An updated TTT diagram proposed by Oradei-Basile, also omitting the Laves phase but with the inclusion of alpha-chromium and sigma phases. [182]

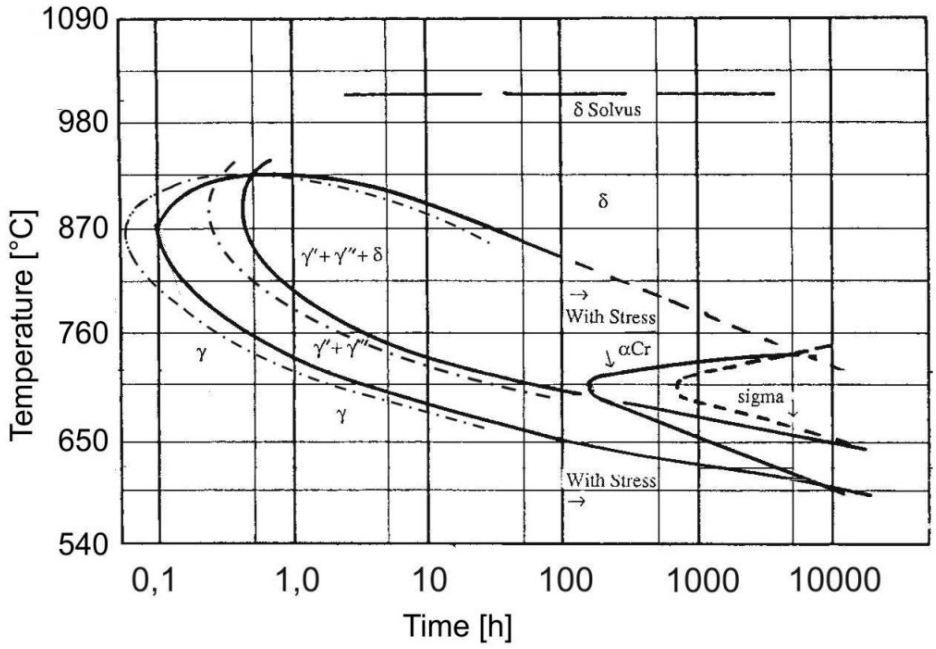


Figure 38: TTT Diagram for Inconel 718 [182], with dotted lines showing modified boundaries for Inconel 718 forged at high strain rates. [184]

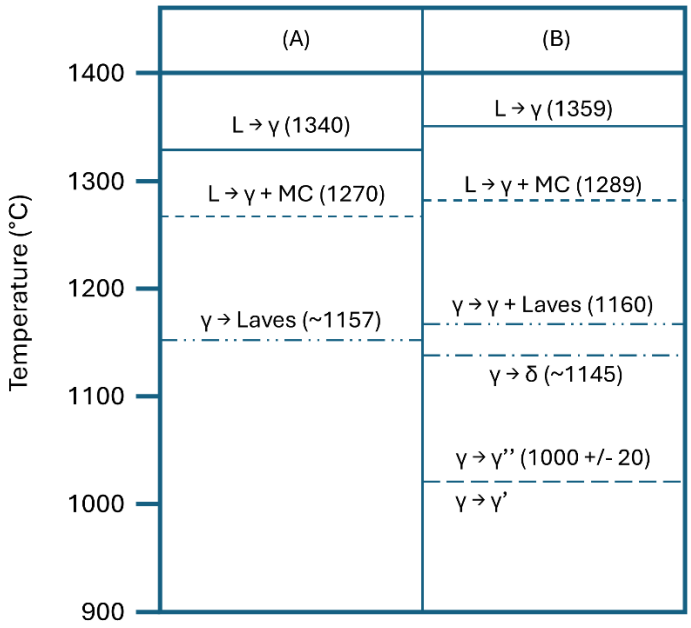


Figure 39: Solidification and precipitation sequence of phases in Inconel 718, adapted from Murata et al [185]. Data from (A) is sourced from Ballantyne and Mitchell [186], and (B) from studies by Murata et al [185].

The fact that there are many variants of these TTT diagrams is an excellent demonstration of the fact that the microstructure of superalloys can be far from straightforward, and also subjective; an advantage of a bulk measurement technique using ultrasonics would be its provision of more straightforward (albeit higher level) deductions regarding the microstructure and composition of the material. Despite their differences, the presence of the γ matrix, and the γ', γ'' and δ precipitates, is not disputed between the TTT diagrams. The aim of the UWS experiments is to investigate whether the method is suitable for detecting changes in phase composition in nickel-based superalloys, through changes in the calculated zeroth coefficient V00 (which is an average of all wave speeds in all 3D directions); the theory is that the change in mechanical properties caused by a change in the amount of these γ', γ'' and/or δ precipitates present would impact the wave speeds through the material (for example, a stiffer material would mean faster wave speeds and hence cause an increase in the zeroth coefficient value). These individual precipitates within Inconel 718 will be discussed in more detail in following sections.

3.2.1 Gamma, Gamma Prime and Gamma Double Prime

Figure 40 shows images taken using Transmission Electron Microscopy (TEM) of Inconel 718, which illustrate the morphologies of the gamma, gamma prime and gamma double-prime phases.

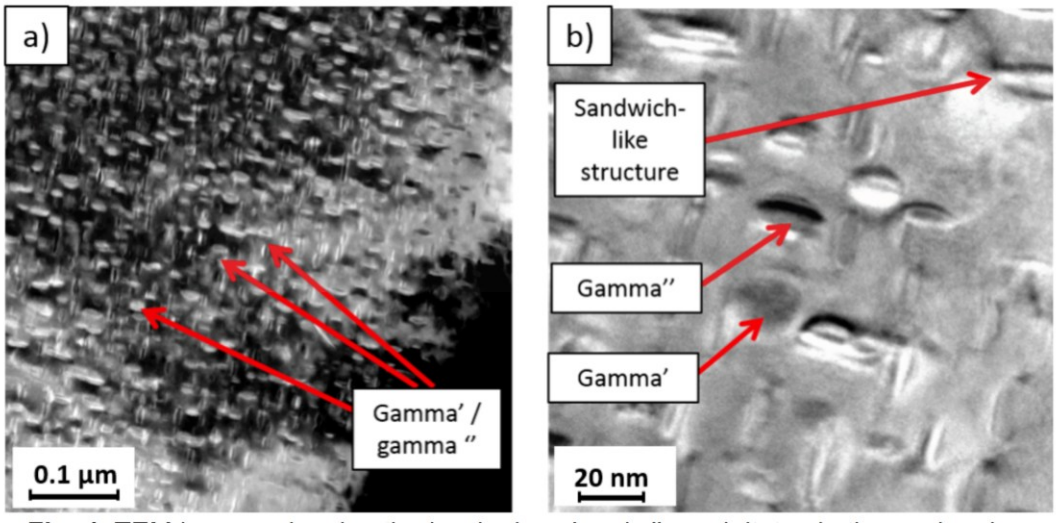


Figure 40: TEM images of Inconel 718 at different magnifications [187]. The γ'' precipitates have an elongated disc shape, whereas those for γ' are almost spheroidal, though both have an average size of 20nm. Note the presence of some more complex precipitates comprising of a combination of half-spheroidal γ' sandwiching a γ'' precipitate.

The main matrix phase in Inconel 718 is the gamma (γ) phase, formed of nickel and chromium crystallising in an FCC structure [188] – these are two of the main elements contributing to the corrosion resistance of the material. Niobium is added to form the major precipitation-strengthening component, which is the gamma double prime (γ'') phase [188]; this is a meta-stable phase, and has a body-centred tetragonal (BCT, or $D0_{22}$) structure, and chemical composition Ni_3Nb [157]. These γ'' precipitates exhibit a large coherency strain along the tetragonal axis with the γ matrix, and hence usually have a long disk-shaped morphology with 3 variants along the cubic axes [189]. As the strengthening effect of these γ'' precipitates is relatively high, only a small volume fraction is needed to make the material a high strength superalloy [189]. The γ'' phase tends to be homogenously nucleated, and coherent with the main γ matrix [190]. The size of the γ'' particles is the main factor in controlling the tensile and creep properties [191] [192]; there is also a strong relation between fatigue softening and the dislocation shearing mechanism at elevated temperatures [193]. In fact, the strengthening mechanism of γ'' has been attributed mainly due to the coherency strains between its particles and the matrix [194] [195].

Titanium and aluminium are added to the superalloy melt in order to form the gamma prime (γ') precipitate, an intermetallic precipitate with chemical composition $Ni_3(Ti,Al)$ [188]. The γ' has a simple cubic crystal structure ($L1_2$ ordered [156]), and a lower hardening and strengthening effect compared to the γ'' particles – this is due to the volume fraction of this phase being typically less than 5% [196], compared to ~15% of γ'' [197]), though there is still a small degree of strengthening [183]. The γ' phase precipitates also form coherently with the main γ matrix, as a fine dispersion of quasi-spherical particles [183].

The volume fractions of γ' and γ'' can be affected by both chemical composition and temperature conditions – for example, there have been studies indicating that increasing the total content of aluminium and titanium (with respect to the niobium content) can cause γ' precipitation to be favoured over the γ'' phase [190]. In terms of thermal conditions, the solvus temperature of the γ'' phase is higher than the γ' (with the γ'' being a more stable phase), and therefore is still present in samples of Inconel 718 which have been exposed to higher temperatures of around 1173K where the γ' phase is noticeably absent [190]. TEM observations have shown that the precipitations are also strongly dependent on ageing time; for example, at longer thermal exposure times, the γ'' platelets will coarsen and then progressively dissolve, while the delta phase begins to materialise [183].

3.2.2 Delta Phase

The delta (δ) phase, sometimes known as the beta (β) phase, is an intermetallic compound with formula Ni_3Nb and an orthorhombic structure [188]; it generally forms as a long needle-like, or plate-like, shape along the γ phase grain boundaries [198], as illustrated in Figure 41. It is the equilibrium phase of the γ'' precipitate [199], and is thermodynamically more stable [183]; however, despite this stability, the sluggishness of the δ phase precipitation means that its formation up to around 900°C is almost always preceded by γ'' precipitation [156]. When it does form, however, it is unlike the γ'' phase in its formation incoherently in the γ matrix [36]. Given that both of these phases are niobium-based, this implies that the growth of the δ phase corresponds to a loss of the γ'' phase (though this does not occur above the limit of γ'' formation, around 900°C [156]; indeed, the δ phase solvus is higher than the γ'' phase as it sits around 1000°C).

The proportion and morphology of the δ phase can alter during forging; if it takes place sub-solvus then any δ phase that is present tends to become spherical [200]. Conversely, if the strain is carried out in a temperature range where the δ phase is precipitating, the growth is discontinuous with the formation of short, lath-type structures which emanate from grain boundaries [36], and if there is only heating without strain in this same region then the δ phase tends to form as long, thin precipitates [123]. It is this latter morphology which tends to have a detrimental effect on the fracture toughness [201], and can also provide a preferential site for crack growth [159].

Both its morphology and its incoherency with the γ matrix means that the δ phase does not contribute significantly to the hardening or strengthening of the alloy, and indeed its presence implies loss of hardenability due to the depletion of the γ'' phase; it has also been associated with causing increased susceptibility to hot cracking [202], and increased plasticity [199]. However, it does have some benefits – it has been found that, if the δ precipitate has a suitable (more rounded) morphology, it can help to provide resistance to stress rupture ductility [183] or grain boundary creep fracture [203] [204]. This is due to the precipitates forming along the grain boundaries of the γ matrix, which increases the intergranular flow resistance of the alloy [188]. In this way, moderate amounts of the δ phase can also be effective in limiting grain growth[5] during solution treatment[6]

[5] Coarsening of the precipitates is generally a negative effect, as it can result in a decreased hardness [11].
[6] Note that a full heat treatment process usually involves a solution treatment and a precipitation treatment phase – the solution treatment refers to taking the geometrically close packed, or GCP, phases (i.e. the γ' and γ'', whereas the precipitation treatments are to nucleate and grow these precipitates under controlled conditions in order to develop the optimal properties required [35].

and thermomechanical processing [123] [156], and control the overall grain size of the material [159] – using the δ phase to control the grain size, such as through the 'Minigrain' process [205], can result in a material with improved ultrasonic inspectability and a more uniform microstructure [206] in the final forging. However, in its absence, other precipitate particles, such as the carbides, can also provide the same effect.

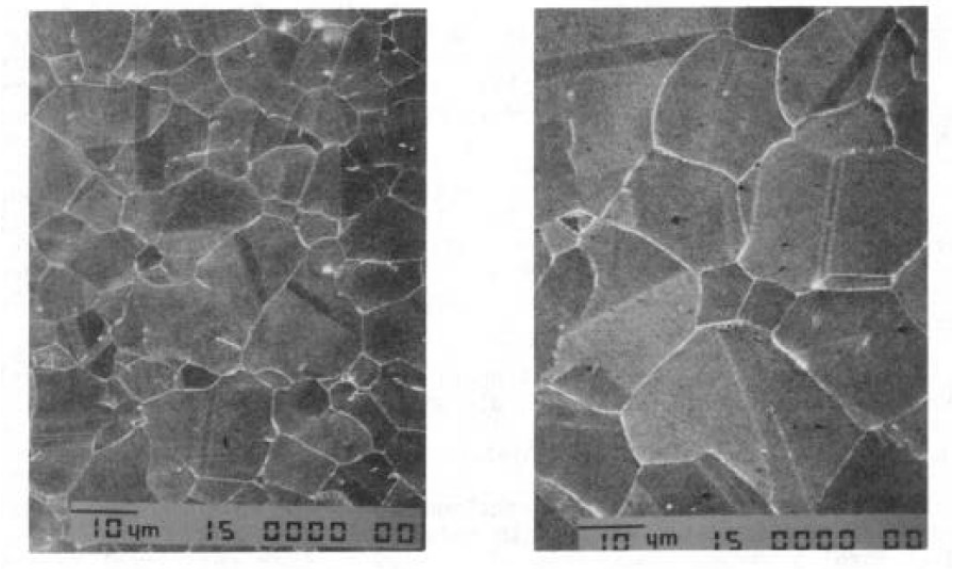


Figure 41: Micrographs showing the delta phase (white precipitates on the boundaries) at the surface (left) and centre (right) of an Inconel 718 bar. [207]

3.2.3 The Carbide Phases

The addition of carbon to the superalloy melt during Inconel 718 fabrication results in the formation of precipitates of the form MC, where M denotes a metal (in this case, titanium or niobium) [188] and the ratio of metal to carbon is 1:1. The carbon content must be low enough to ensure that these metal elements are able to precipitate in the form of γ' and γ'' particles [188]. The carbides generally form relatively early on in the cooling process, and will also develop with all conditions of heat treatment [160]. These are insoluble segregates, and tend to reduce strength and ductility; they can be identified as freckles on etched cross-sections, as illustrated in Figure 42. Due to the fact that the carbide phases are slightly more difficult to reveal during the etching process for microscopy, these precipitates can often be masked and confused with those of the Laves phase [160].

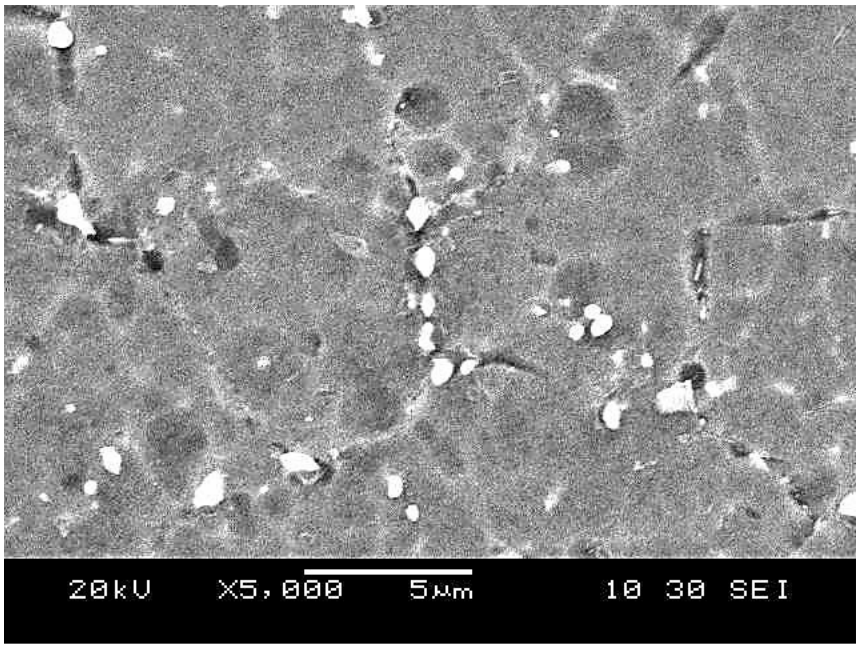


Figure 42: Metallic carbides in Inconel 718 (where the white globular precipitates at the grain boundaries are (Ti, Nb)C particles. [208]

3.2.4 The Laves Phase

The Laves phase is a minor phase in Inconel 718, and is typically high in niobium, molybdenum and nickel, with smaller quantities of iron, chromium and titanium also present. Its structure is isomorphous[7] with Fe_2Ti [160], and the precipitates tend to form as flat, irregular shapes. Previous studies have shown that there are two main kinds of the Laves phase, with compositions Fe_2Nb and Cr_2Nb [185]. Typically the Laves phase is only found where the volume fraction of niobium is 4.42% or above [160]. Similar to the δ phase, the Laves phase has also been found to affect the ageing response of Inconel 718 [160], and there has been some debate as to whether the Laves is in fact an alternative manifestation of this phase [128] [182] – as demonstrated through its omission in more modern TTT diagrams.

Although each of the phases present – whether γ', γ'', δ or Laves – have different chemistries, structures and impacts on the material, these are not only dependent on the solution treatment temperatures of the material, but can also be impacted by the thermo-mechanical processing; this is also an important factor in the final microstructure of the material.

[7] Isomorphous crystals have essentially identical cell dimensions and atomic arrangements, but with variations in the types of one or more of the atoms present [36].

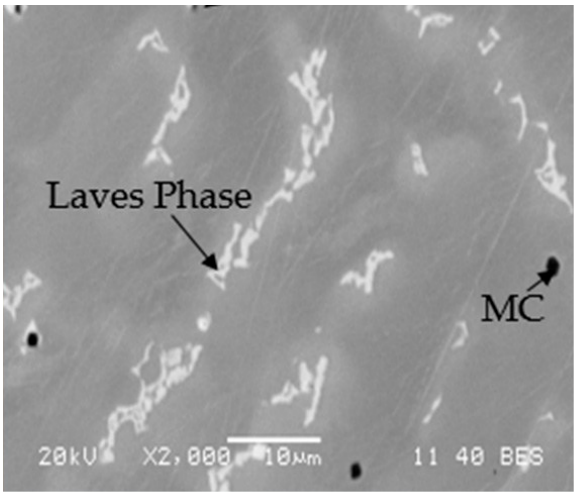


Figure 43: The Laves phase and a carbide labelled in a micrograph of a wire-arc additive manufactured sample of Inconel 718. [209]

3.2.5 Thermo-mechanical processing (TMP) of Inconel 718

The thermo-mechanical processing, or TMP, has an impact on the final microstructure of the material [188], affecting important properties including tensile strength [210], ductility, fatigue and creep resistance, and fracture toughness [36]. Generally, the forging must be carried out in at least two steps to reach the required grain size of ASTM 10 (corresponding to 11µm) [36]; it is during these steps that the full dynamic and meta-dynamic recrystallisation discussed previously must take place. The final forging step is conducted below the δ phase solvus in Inconel 718, to avoid its grain pinning effect being reduced [159].

For Inconel 718, the forging temperature is relatively low with respect to other superalloys, and tends to be in the range of 980 to 1040°C [36]. This forging temperature is chosen based on the starting microstructure of the billet, the solvus temperatures of the key individual precipitates (in this case, γ', γ'' and δ), as well as taking into account the grain coarsening characteristics of the material [123]. It is following this forging process that the heat treatment, conforming to AMS 5662 as mentioned previously, is carried out.

3.2.6 Summary

It is clear that the microstructure of Inconel 718 is far from straightforward – a fact very apparent from the variations in the TTT diagrams in Figure 30, and Figure 35 to Figure 38 – with many different precipitates able to form within the main material. However, it would be most useful and

straightforward to have a nickel-based superalloy in a dual phase form. Across all of the TTT diagrams shown, there is a large region where the only other phase present aside from the γ matrix should be the δ phase, and thus with more tailored heat treatments and processing there is the possibility of manipulating the microstructure into this dual-phase form. However, for the feasibility study, a heat treatment generating the maximum amount of contrast between the microstructures was used, as it would be immediately apparent that the V00 was not capable of detecting phase changes between any materials if the most extreme cases could not be differentiated. The following section will discuss the materials and experimental design of the feasibility study.

3.3 Feasibility Study Materials and Methods

The first set of four samples were machined off a billet acquired from Bibus Alloys, conforming to specification AMS 5662, which involves solution annealing at 968°C followed by a rapid cool, usually in water as previously stated [180][8]. These samples were machined into dodecagons (to simplify the rotation of the samples during test to acquire ultrasonic wave speeds in the correct orientations), each with a thickness of around 5mm. Electrical discharge machining (EDM) was used, to ensure that there were no alterations to the microstructure as the cutting took place – which could be the case if using standard mechanical cutting techniques. Having tested these all using the water tank, two of the samples were then sent off for a heat treatment which had the aim of simulating heat damage – the most extreme conditions that the material could sustain – which involved a hold at 1100°C for 4 hours, followed by an oil quench. A schematic of this heat treatment programme is shown in Figure 44 [37]. It was thought that this would create the most extreme difference between the microstructures, and thus if there was no change in V00 observable then it could immediately be concluded that the technique was not applicable for nickel-based superalloys. The heat treatment was carried out externally by Special Steels, with a certificate of conformity provided for reference. Following these heat treatments, the samples were then denoted OG1, OG2, and OG3HD and OG4HD (with HD representing 'heat damage'). Specimens were machined off each dodecagon to be prepared for examination using microscopy, in order to verify that the required microstructural changes had taken place, and to validate the UWS results obtained.

[8]The fact that this material it hadn't been fully aged according to this specification was not discovered until carrying out hardness tests, having completed the UWS experiments. This will be discussed further in later sections of this chapter.

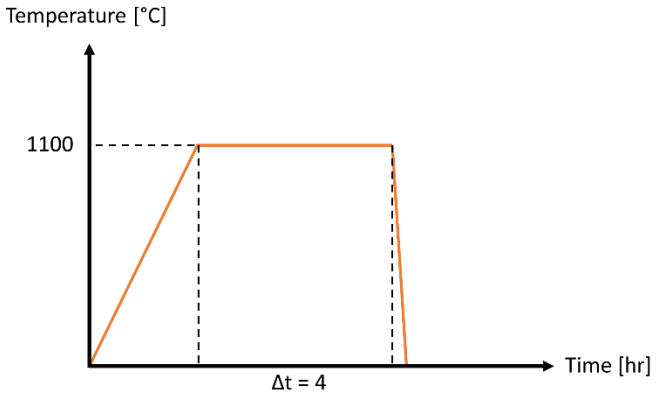


Figure 44: Schematic of heat treatment simulating 'Heat Damage' heat treatment. [37]

The UWS rig underwent a significant amount of changes (both in the hardware and software) during the testing carried out over the course of the EngD; the hardware modifications to the rig included replacing some components to increase the automation of the rotation and alignment of the samples. This had mixed results – some of the new components tended to corrode easily, causing jamming during the rotation of the sample, and thus needed to be replaced. It was found that a compromise of automating the tilting, but keeping the rotation a manual procedure, was the optimal setup. In terms of software, the code was rewritten in Python to aid with version control, and after some initial debugging did speed up the data acquisition. Unfortunately, the data acquired from the OG1HD and OG2HD samples before their heat damage have been lost during the course of these equipment modifications; however, it has been assumed for the purposes of the feasibility study (to verify whether the V00 is sensitive to changes in microstructure in nickel-based superalloys) that the billet microstructure was uniform, and so the material characteristics would have been very similar for each of the dodecagons which had been machined from it.

3.4 Microscopy Examinations

After extensive trial and error to find the optimal preparation method for carrying out scanning electron microscopy on the samples of Inconel 718, the final steps comprised the following –

- Grinding using silicon carbide papers with increasing fineness – 500, 800, 1200, 2000, 4000, around a minute on each stage (and done manually);
- Polishing using 6μm, 3μm and 1μm diamond suspension – around 100 counter-clockwise rotations on the pad spinning clockwise at 1500U/m;
- Automated polishing using a preset programme nickel preparation on the Struers Tegrapol-35 machine, including a final 2 minute polish using OPS suspension.

Having completed the preparation, the samples were then examined using optical microscopy, as well as scanning electron microscopy (SEM).

3.4.1 Optical Micrographs

Figure 45 to Figure 48 show representative optical micrographs of one OG sample and one OGHD sample at increasing magnifications, where both parts (a) and (b) in each figure have the same length scales (printed in part (a) only). The differences in colour are a result of varying lighting conditions while using the optical microscope. It is immediately apparent that the 1100°C heat treatment has been very effective, not only in terms of taking the precipitates back into solution, but in increasing the grain size by several times. For clarity, one grain in the micrographs of the heat damaged samples has been outlined in red; it is not as easy to determine where the grain boundaries are for these samples as the δ phase, which would ordinarily delineate the grain boundaries, have been taken back into solution. However, the preferential polishing of the grains (depending on their orientation) has allowed for some distinction to be made. At 200x magnification (Figure 47), the quality of the image obtained for the heat damaged samples has deteriorated and there was not sufficient brightness to be able to image these with a good resolution; the large grain sizes also mean that there was not a great deal to be seen. However, higher magnification images of an as-received sample have been included in order to show the δ phase in a higher magnitude.

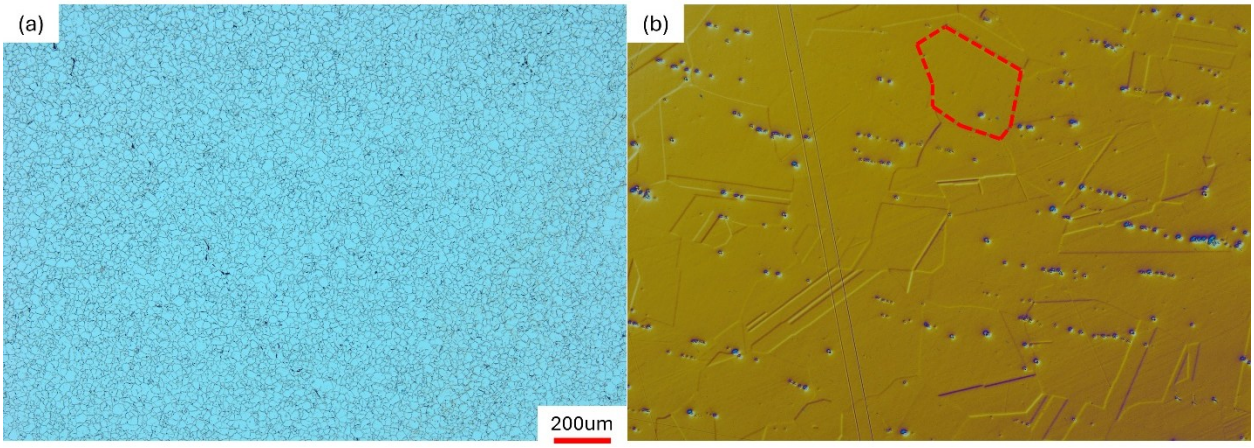


Figure 45: Optical micrographs of OG sample in (a) as-received condition and (b) heat damaged condition respectively, at 50x magnification.

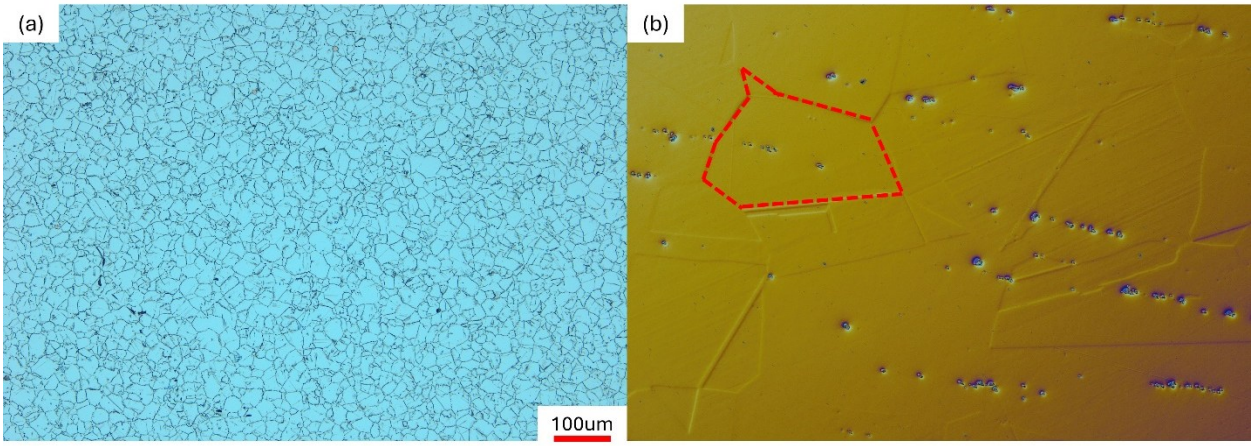


Figure 46: Optical micrographs of OG sample in (a) as-received condition and (b) heat damaged condition respectively, at 100x magnification.

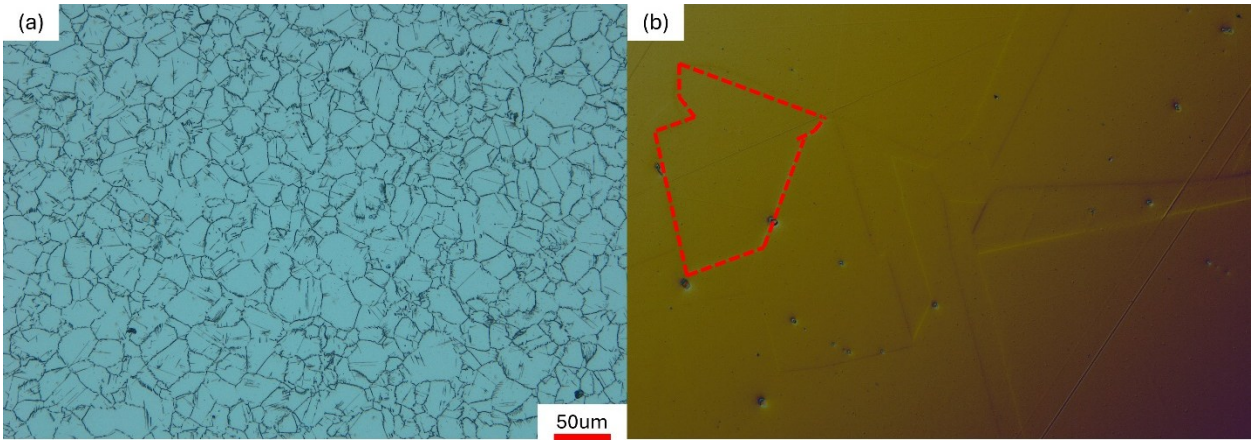


Figure 47: Optical micrographs of OG sample in (a) as-received condition and (b) heat damaged condition respectively, at 200x magnification.

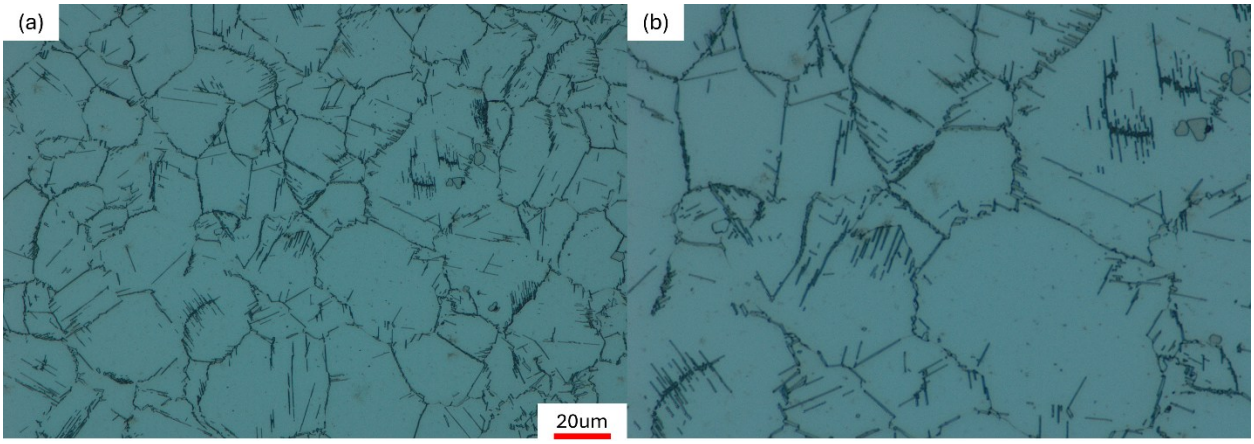


Figure 48: Optical micrographs of OG sample in as-received condition at (a) 500x and (b) 1000x magnifications respectively.

3.4.2 SEM Micrographs

Although the optical micrographs show the microstructure (particularly the carbide and δ phases) in good detail, the resolution is not sufficient in being able to image the smaller γ' and γ'' precipitates. The presence (or absence) of these are key to verifying that the microstructure has changed as intended (i.e. removing these phases), and that the V00 measurements being obtained are representative of these changes. The samples were therefore also examined using SEM using a variety of different detector combinations to investigate the microstructures at much higher magnifications.

The ThermoFisher Scios used is a state-of-the-art Scanning Electron Microscope, fully equipped with all of the detectors which were available (including optional modules), and thus enabling the best possible micrographs to be acquired. The various detectors included the Everhart-Thornley (ETD), the ion conversion and electron detector (ICE), as well as the in-column detectors T1, T2 and T3. These are shown in the schematics in Figure 49, with Figure 50 giving a view of the in-column detectors. Each detector has its own advantages; the ETD is optimal for general purpose, high resolution topographic imagery, as it works as an outboard secondary electron detector, and the ICE is the same but giving a different perspective as it is in front of the pole piece (whereas the ETD is behind). In the case of the in-column detectors, the T1, as an in-lens, high-angle backscatter electron (BSE) detector, is suitable for imaging material and compositional contrast, where the T2 is an improved topographical imaging and edge contrast as it detects mid-angle secondary electrons and energies [211]. The T3 similarly detects these same electrons but with lower energies, and thus tends to have better surface sensitivity than T1 and T2 [211].

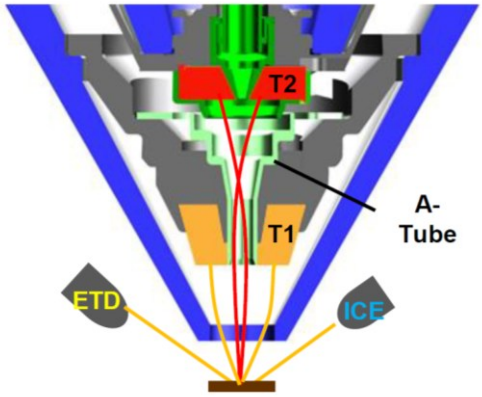


Figure 49: Schematic of detectors in Scios SEM [212]. 'A-tube' refers to the accelerating tube.

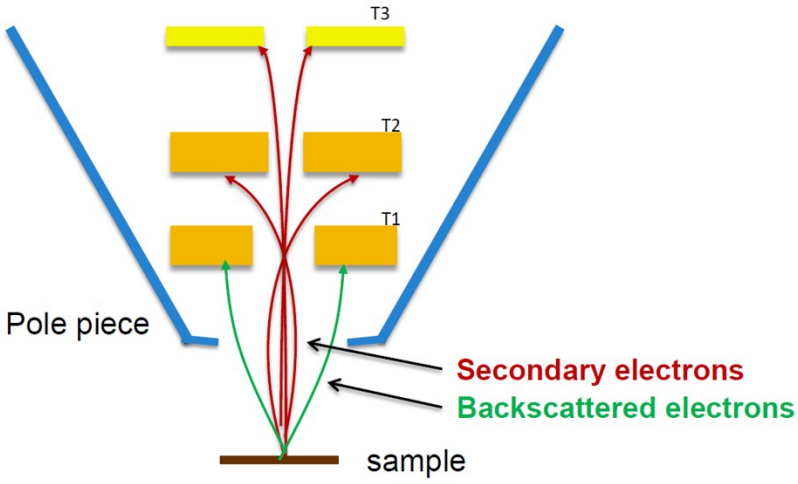


Figure 50: In-column detectors in Scios SEM. [211]

The differences in detector modes are shown in Figure 51; it can be seen that certain features appear much clearer in certain modes than others; for example, the background mottling effect (which is thought to be the γ'/γ'' precipitates) is barely resolved in the T1 mode, whereas it is much better seen in T2 mode. However, the δ phase almost being embedded in the main matrix is best shown in the T3 mode. There was therefore some compromise when trying to determine the most appropriate mode to image certain features of the materials.

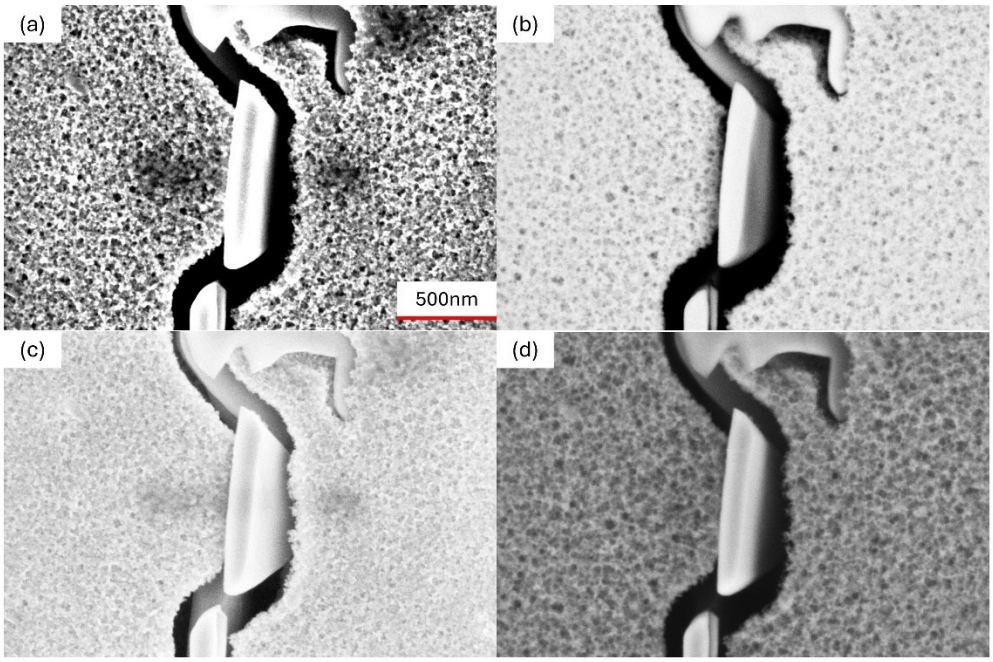


Figure 51: SEM micrographs of δ precipitate in as-received OG sample, illustrating the differences in images using detectors (a) T2, (b) T1, (c) T3 and (d) ETD.

As previously mentioned, the purpose of using SEM was to be able to obtain high quality images with large magnification to identify the presence of the γ'/γ'' phases within the material. Figure 52 clearly shows the stark contrast between the micrographs obtained for the as-received and the heat damaged samples; the precipitates are noticeably absent after heat damage, and the grains can be observed much clearer than for the optical micrographs.

Figure 53 shows images of an as-received sample with increasing magnification values, from 40μm scale to 1μm; by the time the magnification is at 30,000x, the background mottling within the main γ matrix is visible, potentially showing the presence of γ' and γ''. However, when examining the heat damaged samples at these high levels of magnification, there were some unexpected results, shown in Figure 54. At 35000x magnification, there appeared to also be a background mottling effect not unlike that seen for the as-received samples, which implied that there may in fact still be either γ' or γ'' present in the material, despite best efforts to avoid it re-precipitating using an oil quench. (An oil quench was used, as it had been previously reported to give a sufficiently fast cooling rate to avoid γ'' precipitation occurring [197].) At 100,000x magnification, which was very much at the limit of the SEM resolution, it did appear that these were not just a surface effect but almost as if they were individual particles on the cusp of fully forming out of solution. As it was

difficult to attribute with certainty this effect to either particles or surface residue from SEM images, it was proposed that a different technique, high-speed atomic force microscopy (HS-AFM), was used to determine the exact nature of this effect. However, before the HS-AFM work, experiments to take ultrasonic wave speed measurements (and hence determine the V00 of the materials) were first carried out.

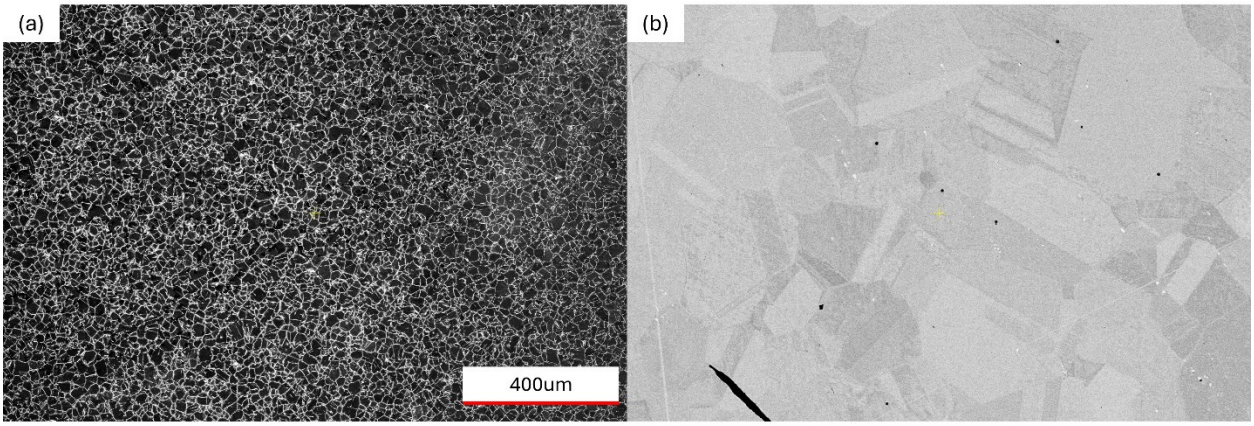


Figure 52: SEM micrographs of (a) as-received and (b) heat damaged OG samples respectively.

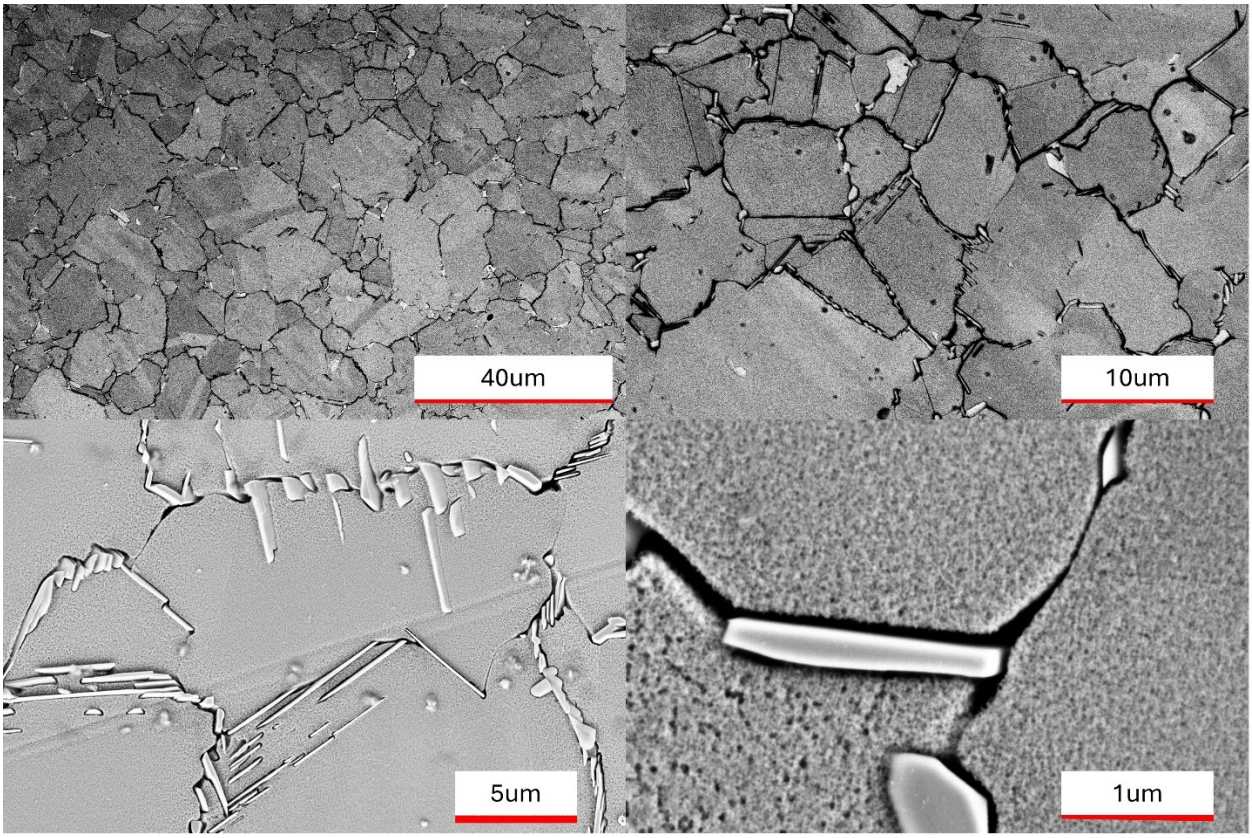


Figure 53: SEM micrographs at increasing magnification of as-received OG sample.

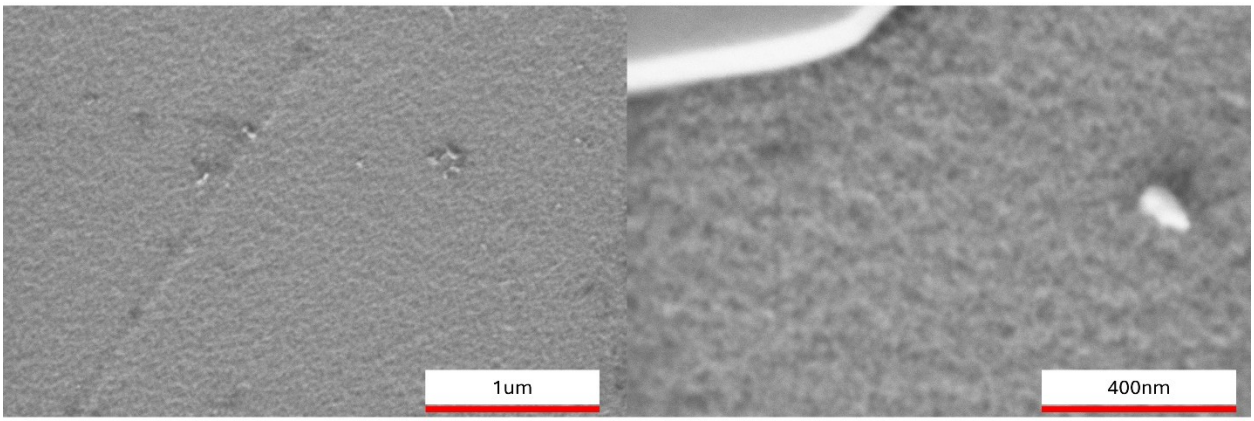


Figure 54: High magnification SEM micrographs of as-received OG sample showing background mottling effect, thought to be the γ'' precipitate.

3.5 UWS Testing Results

The ultrasonic wave speed measurements were acquired for samples OG1HD, OG2HD, OG3 and OG4 using the methodology outlined in Chapter 2. A total of 16 trials was carried out for each sample, with each 'trial' consisting of 3 separate runs of the experiment, from which an average value was taken. In between each trial, the sample was removed from the rig and the system reset before beginning the next set of experimental runs. Although it was hoped that in the future there would be fewer trials necessary (particularly with the experimental setup at the time of investigation requiring around an hour per trial), it was not initially known how many experiments would be required for the V00 value to converge to an accurate and representative mean value, and hence a large number of experiments was run for the initial investigations in order to establish this. Figure 55 shows the cumulative mean V00 value calculated for each of the samples following these 16 trials.

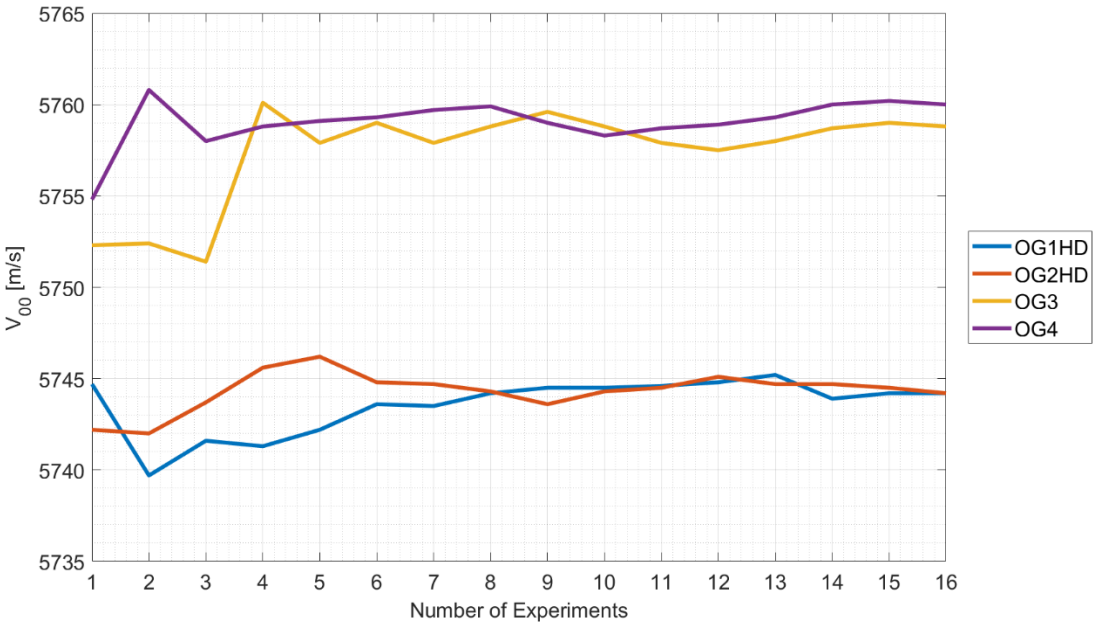


Figure 55: Cumulative mean of V00 measurements for OG samples.

There are several key observations which can be made from this plot; most importantly, there has been a good convergence to a cumulative mean for each sample, and the values between the as-received and heat damaged samples are noticeably different; both heat damaged samples have converged to 5744.2m/s, and the as-received samples to 5758.8m/s and 5760.0m/s, just 1.2m/s

apart. It should be noted that, although in percentage terms the difference in the zeroth coefficient of velocity is small, this is unavoidable as the ultrasonic wave speeds within nickel-based superalloys are 3 orders of magnitude larger than the error level of ultrasonic measurements; it is emphasised that the absolute wave speed measurements are key for this technique [37]. There has been a noticeable difference between the converged V00 values for each sample, where the difference between these two sets of sample conditions is around 15m/s; although the errors in measurement of ultrasonic waves speeds can vary between experimental configurations, it has been assumed that, given the similarity of apparatus used, the experimental error in this instance will be approximately that quantified by Bo Lan et al [104] of around 5-10m/s. It can therefore be concluded that, with cross-comparison of the micrographs obtained, the spherical harmonic zeroth coefficient of velocity is sensitive to microstructural changes within the material.

3.5.1 Velocity Surfaces

The deconvolution process can also be used to generate wave speed variation surfaces, or velocity surface plots, which give a visualisation of the 3D wave speeds through an average grain. These can be interpreted as visualising the grain to be spherical in shape, and taking a stereographic projection of the upper part onto the equator. The velocity surfaces for the 4 samples are shown in Figure 56.

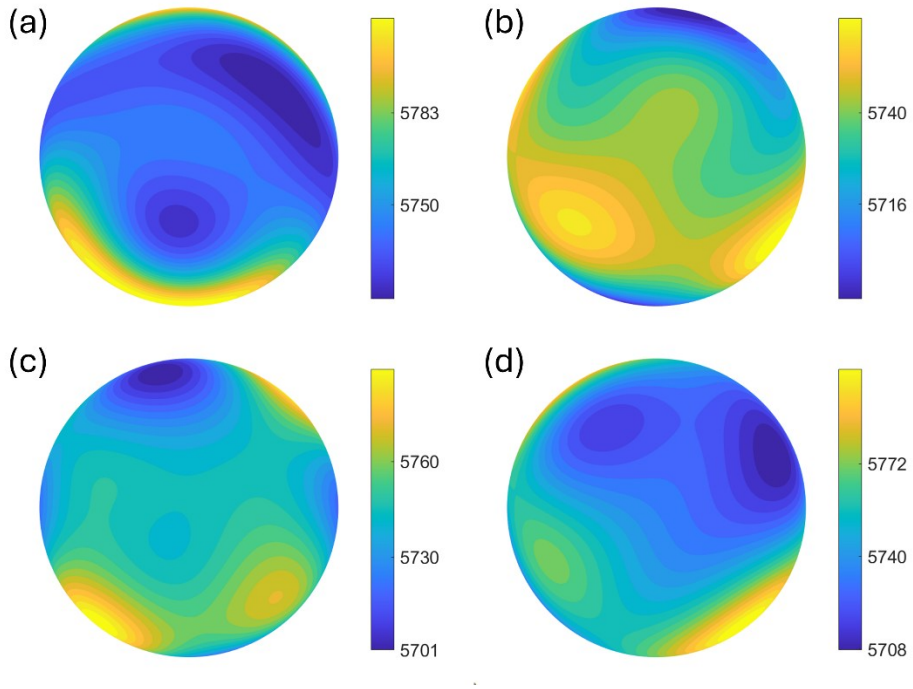


Figure 56: Velocity surface plots for (a) OG1HD, (b) OG2HD, (c) OG3 and (d) OG4.

3.5.2 Pole Figures

Although texture mapping is not the main point of interest for this study, the spherical deconvolution process can also be used to generate pole figures using the MTEX [213] extension in MATLAB, where the orientation of a selected plane normal (or pole) is shown with respect to the sample reference plane [214], and the intensities of the plots correspond to the prevalence of the preferred crystallographic orientations within the sample.

Figure 57 shows the pole figures for both the 111 and 200 orientations. It can be seen that each sample has a very different texture, but this difference has not affected the V00 measurements – particularly in the case of the heat damaged samples, which have converged to the same value. This validates the fact that it is purely phase changes within the material which would affect the zeroth coefficient [37]. An additional point to note is that, although the textures in the samples are relatively random (and as a result have low intensities), even if the inspection method was applied to a material with a strong texture (such as a forged component), the microstructural changes which had occurred would still be detectable using the V00 measurements with no influence from this stronger texture. V00 is related to the average bulk elasticity, and thus this zeroth spherical harmonic is perfectly isotropic; hence the texture has no effect on the polycrystal data [37].

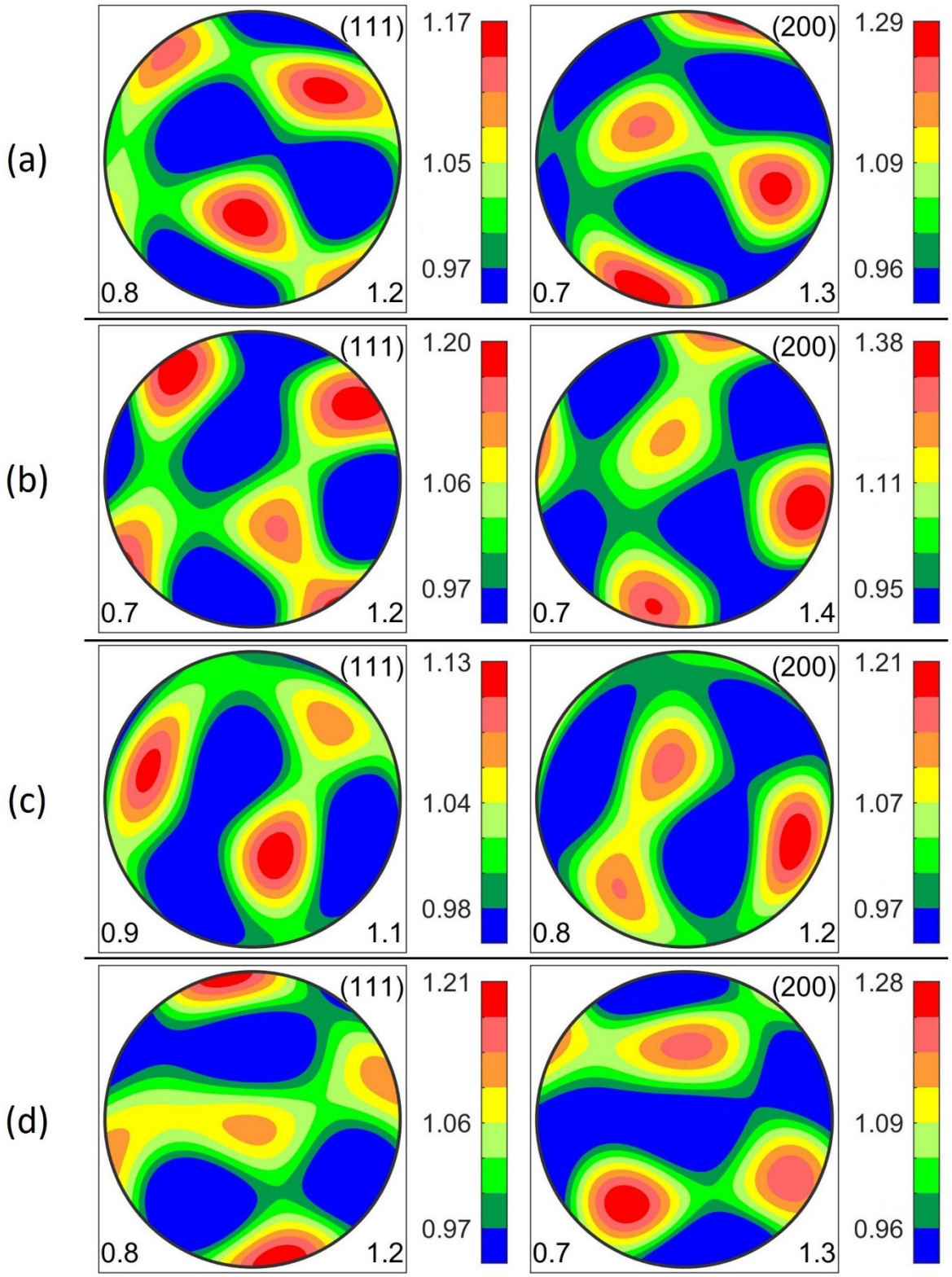


Figure 57: Pole figures in (111) and (200) orientations for samples (a) OG1HD, (b) OG2HD, (c) OG3 and (d) OG4. [37]

3.5.3 Error Analysis of Wave Speed Measurement Platform

Although the data from the ultrasonic wave speed measurements shows a clear convergence to different values for the as-received and heat damaged conditions, which can be robustly differentiated between, it is clear that there exists a level of experimental error which masks the true convergence at a lower number of tests, but averaged out as the number of tests increases [37]. As the differences in wave speeds between the samples in this case (around 15m/s) are relatively small and comparable to experimental error levels for this configuration, the averaging works well. Jobling et al. [37] present an error analysis using the convergence process to analyse both the real data required from the experiment as well as the associated errors of the experimental platform, which has been summarised here; this analysis method itself does not depend on the platform, and can therefore determine the number of tests required to achieve a certain confidence level. It was hoped that by establishing a lower number of tests (than the presently used 16 trials) which would be required to reach a reliable result, the overall time of data acquisition can be reduced for further experiments.

To attempt to quantify the convergence of the results and perform a statistical analysis, the experimental data for each sample was randomised ten times to vary the order in which the cumulative mean was calculated, to ensure that the number of trials after which convergence is reached was consistent. The 95% and 98% confidence intervals were calculated using the parameters from a fitted Gaussian distribution, which have been shown in Table 3 for each sample; these intervals describe the probability that any given measurement would fall between these ranges of values. Figure 58 shows an example of 3 randomised permutations of the dataset for V00 measurements of OG1HD to illustrate this process, with the 95% confidence intervals also shown in the dashed green lines. The fitted Gaussian distribution for each sample is shown in Figure 59, with the average number of trials required for each sample to reach the 95% and 98% confidence intervals for the ten permutations shown in Figure 60.

Table 3: 95% and 98% confidence intervals for each sample, calculated using a fitted Gaussian distribution.

Sample	95% Confidence Interval		98% Confidence Interval	
	Lower [m/s]	Upper [m/s]	Lower [m/s]	Upper [m/s]
OG1HD	5741.07	5757.30	5740.4	5748.0
OG2HD	5741.67	5746.66	5741.1	5747.2
OG3	5753.45	5764.21	5752.3	5765.4
OG4	5757.34	5762.7	5756.7	5763.3

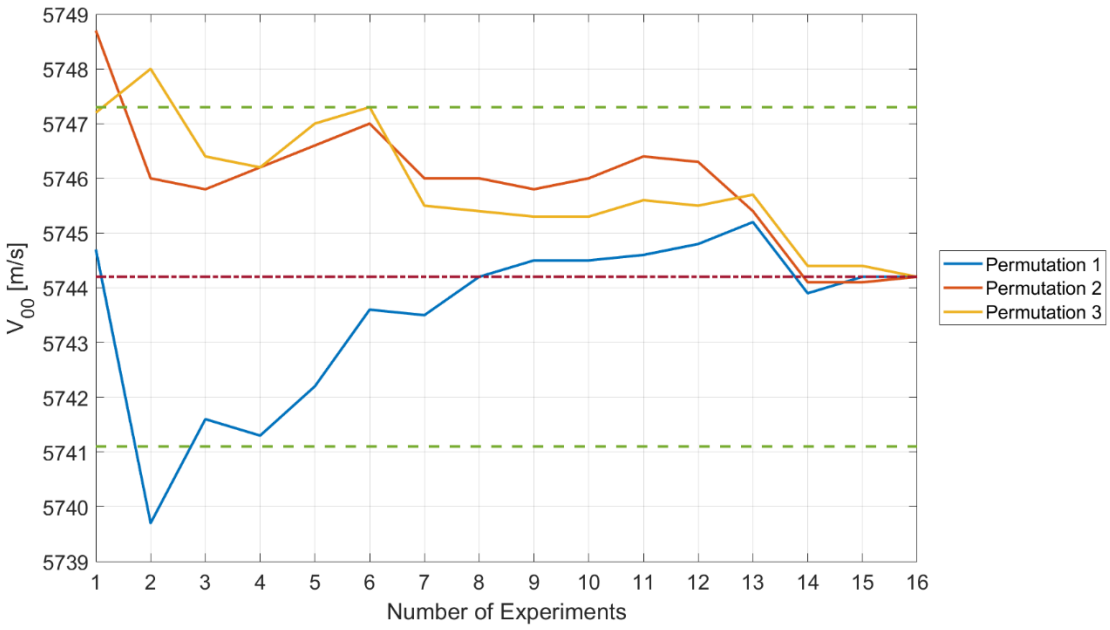


Figure 58: The cumulative mean V00 calculated using three randomised permutations of the dataset for sample OG1HD.

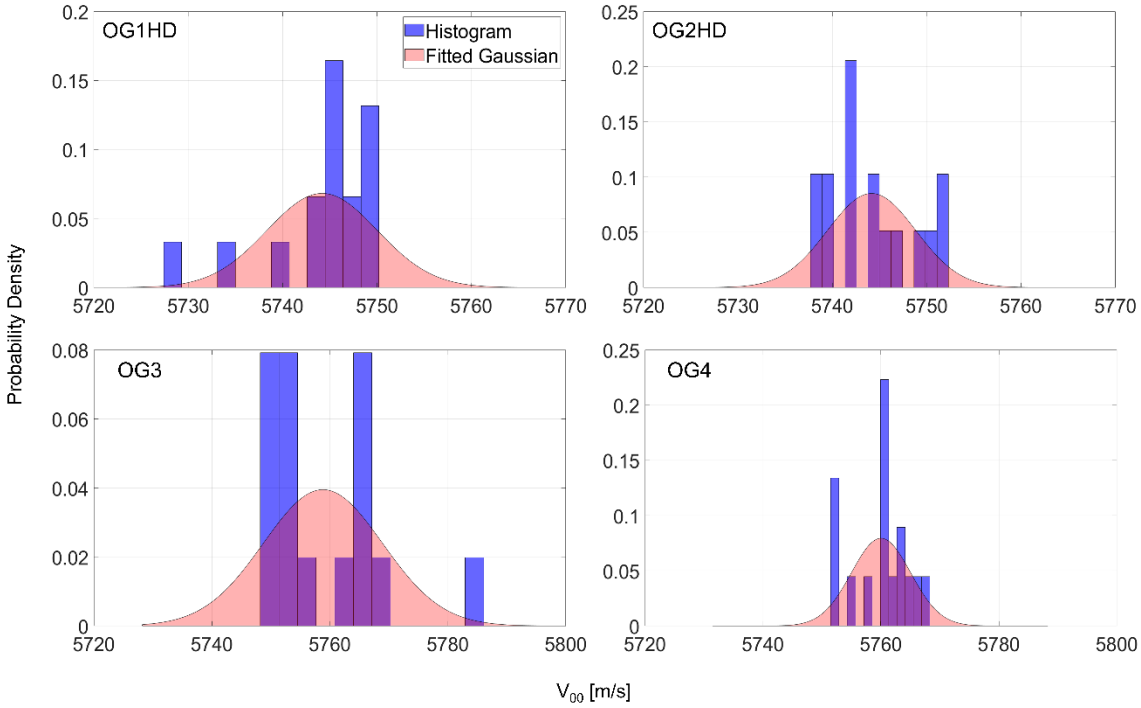


Figure 59: Fitted Gaussian distributions for each sample.

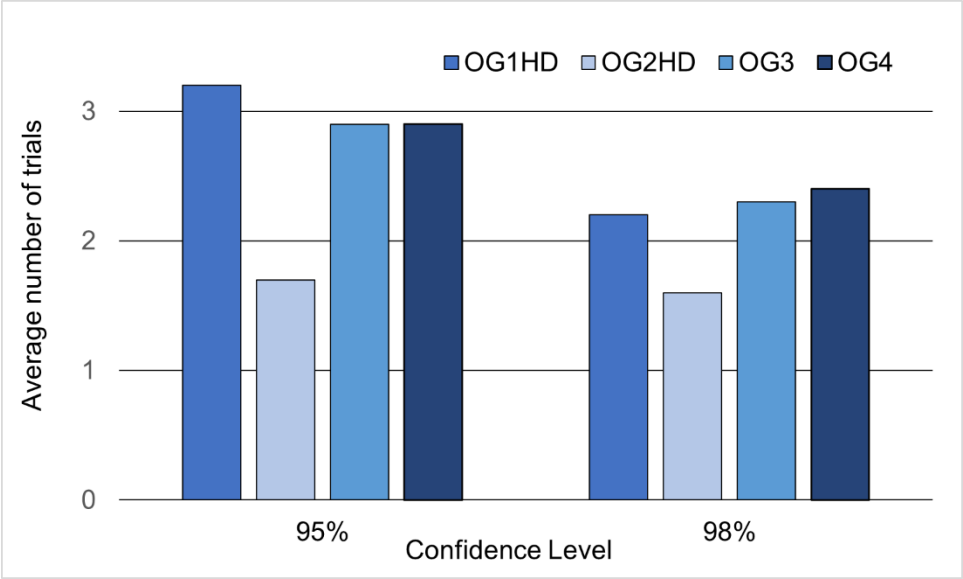


Figure 60: Average number of trials required for each sample to reach 95% and 98% confidence interval.

As discussed by Jobling et al., [37], the statistical analysis here has been carried out assuming that the experimental errors follow a Gaussian distribution, which is a well-accepted means for such analyses for a dataset with white noise, or random error [215] [216] [217]. Despite the fact that

there are some obvious outliers to the fitted distributions – particularly in the data for samples OG1HD and OG3 – the Gaussian distribution has still been considered to be the best method for approximating the measurement and instrumental errors for these results. The use of this distribution assumes that the experiments are a random process, and the issue may be that many more repeats of the experiments are required for this to sufficiently manifest in the data. Another possible explanation is that there may be other, more systematic errors occurring, but there was no evidence to suggest that there were any aside from white noise which contributed to the overall distribution of the results. Hence, despite the outliers, the Gaussian distribution was still used in order to estimate the confidence levels from the experimental data, and the deviation of these data from the standard model was attributed to the relatively small sample set. This was primarily due to time constraints; in an ideal scenario, the largest possible number of tests (with analysis of the averages following) would be carried out. Nevertheless, the statistical analysis has been carried out with the aim of determining at least a good estimate of the minimum number of experiments required to reach a suitable accuracy of the final V00 result.

From Figure 60, it can be seen that in the worst case, the cumulative mean reaches the 95% confidence interval after 4 trials. The plot of the cumulative mean V00 for each sample shows a good convergence (to within 2m/s of the mean value) after 8 experiments; these observations imply that a conclusive result with regards to the microstructure can be attained after this number of trials for this particular experimental configuration [37]. It is also noted that the confidence intervals vary in width between the samples; investigations into this could be continued in future studies.

There are a variety of different factors which could cause the errors in the measurements of V00 – as is the case with any experimental measurement acquisition – such as small vibrations of the equipment, and the water level of the tank, the latter of which has an impact due to it affecting the different reflections off the surfaces (i.e. the sample surface and the acoustic mirror surface); as the water surface is also an interface, its relative height with respect to the transducer, sample and acoustic mirror can cause variations in the reflections being observed. Despite these errors, it is important to emphasise that the differences in the ultrasonic wave speeds being detected in the samples of Inconel 718 are relatively small. As these unpreventable experimental errors which arise are themselves extremely small, they will eventually average out due to their being a random parameter; this is indeed what has been observed. It can therefore be concluded, despite these

experimental uncertainties, that a set of 8 trials per sample will be sufficient for this particular platform to reach a converged value of the zeroth coefficient, and allow for a reliable deduction to be made regarding the microstructural characteristics of the material [37].

Having established successfully that there is a noticeable variation in the V00 depending on microstructural changes in Inconel 718, the next stage in the experimental process was to create materials with contrasting microstructures where the only phases at play were the γ matrix and the δ precipitate. The δ precipitate was selected due to its ease of manipulation – in the TTT diagrams shown in Figure 30, and Figure 35 to Figure 38, there is a large region in the upper right where it should theoretically just be the δ phase present, in contrast to the γ' and γ'' phases which were not as simple to isolate in order to generate a dual phase material. It is also the easiest to observe using microscopy, which would theoretically enable a relatively straightforward comparison of the phase estimates calculated using V00 to the 'true' amount present. The following chapter will describe the materials and methods used for this second part of the investigation using Inconel 718.

4. Phase Estimation of Inconel 718

4.1 Introduction

The following chapter begins with a description of the processing regimes used for the second batch of Inconel 718 samples, with the aim of generating microstructures which could be used for the phase estimation process with UWS measurements; these are presented following the results of microscopy investigations, which were carried out to ensure the microstructures were indeed as intended following the heat treatments. Following more in-depth analysis of the samples, including Vickers hardness testing, further ageing heat treatments were carried out; these are described and presented together with the micrographs of these modified samples. There was also the opportunity to carry out some high-speed atomic force microscopy, a highly advanced technique imaging the topography of a material, rather than relying on the electron backscatter behaviour such as with SEM; this allowed for even more insight into the microstructure of the samples. The results of these investigations are also included, followed by a discussion of the various trials of phase estimations using the UWS method.

4.2 Inconel 718 'RR Furnace' Samples – Material Processing Methods

A further billet of Inconel 718 was acquired from NeoNickel, again conforming to AMS 5662 (but, similar to the Bibus alloy discs, in the solution annealed condition only – discovered later in the experimental investigations). Five circular discs were machined off this new billet, again using EDM. One was kept in the as-received condition, named the 'Datum' disc; two more were heat treated with specific heat treatment programmes with the aim of generating one sample with the maximum amount of δ phase, with no others present, and the other with a nominally precipitate free structure, but without the significant grain growth observed for the original set of samples (which tends to occur above 1000°C for Inconel 718). These heat treatment programmes were developed using the TTT diagram of Inconel 718 shown in Figure 30, and Figure 35 to Figure 38, where there is a region within which – theoretically – there should only be the γ matrix with solely the δ precipitates present. These heat treatments were a hold at 900°C for 50 hours followed by a water quench (rapid cool)[9] for maximum δ phase precipitation, and a hold at 1000°C for 10 hours, again followed by a

[9] For ageing times under 100 hours, the δ phase precipitates between around 700°C and its solvus temperature of 1000°C, with its rate of precipitation being highest at around 900°C [1].

water quench, for zero δ phase. The schematics for these heat treatments are shown in Figure 61. To save time and cost, these were carried out at Rolls-Royce's Materials Engineering department in Derby, with the assistance of Rolls-Royce engineers during the removal and quenching of these samples, and hence this batch of Inconel 718 was named the 'RR Furnace' set of samples. An image of the high temperature furnace used is shown in Figure 62, where the white hot disc can be seen.

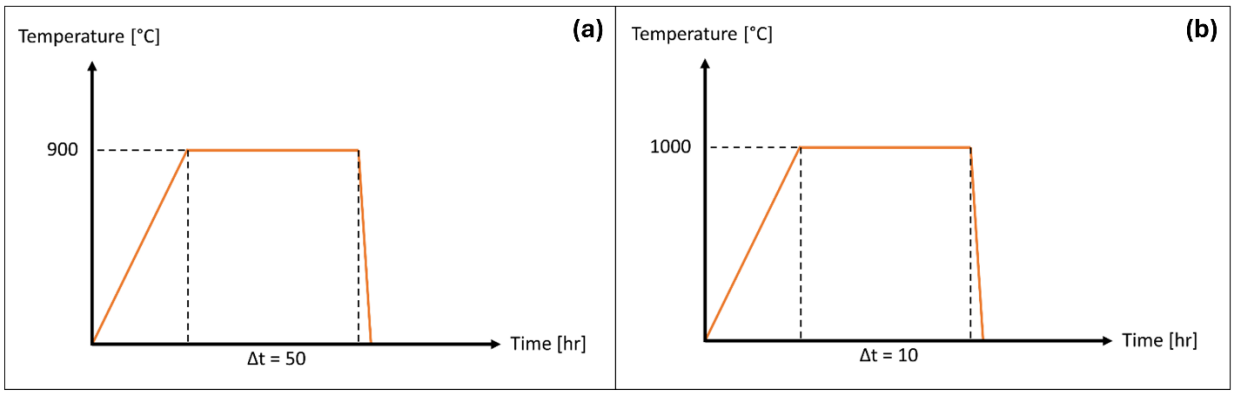


Figure 61: Schematics for heat treatment of (a) maximum delta phase precipitation, 900°C for 50 hours, and (b) nominally precipitate free microstructure, 1000°C for 10 hours. Both are water quenched.

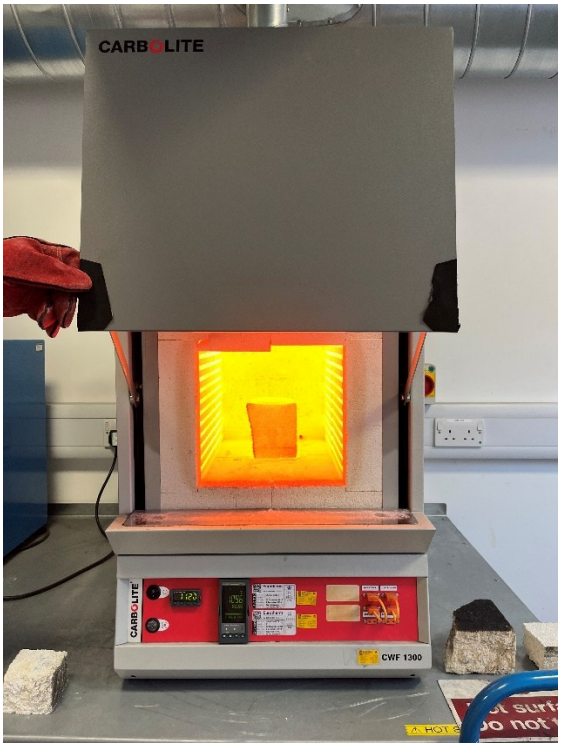


Figure 62: Inconel 718 at 1000°C being extracted from the high temperature furnace at Rolls-Royce, Derby.

Initially, the samples were erroneously furnace cooled instead of water quenched, and subsequently this slow cooling rate allowed the other precipitates to re-form. The heat treatments were thus repeated for the remaining two discs, leaving the total sample set of discs as WQ900, FC900 (where WQ represents water quenched, 900 is the furnace temperature, and FC is furnace cooled) as well as WQ1000 and FC1000. These furnace-cooled discs were still retained and used for experiments despite the unintended microstructures, as the slow cooling rate would have allowed all precipitates to return back out of solution, providing further samples in which to investigate the sensitivity of the V00 method in detecting phase changes. The microstructures of all discs were thus prepared for metallurgical examination, and observed as discussed in the following section.

4.3 Microscopy Results

As for the previous set of Inconel 718 samples, small specimens were machined off each disc and prepared for examination using optical and scanning electron microscopy using the method stated in Chapter 3. A selection of micrographs obtained at varying magnifications for each sample have been shown in here.

The Datum sample has much the same microstructure as the as-received dodecagons from the original, or 'OG', set of samples; the δ phase on the grain boundaries is clear from Figure 63, and at higher magnifications in Figure 64 there is the background mottling effect indicating the presence of the γ' and γ'' phases.

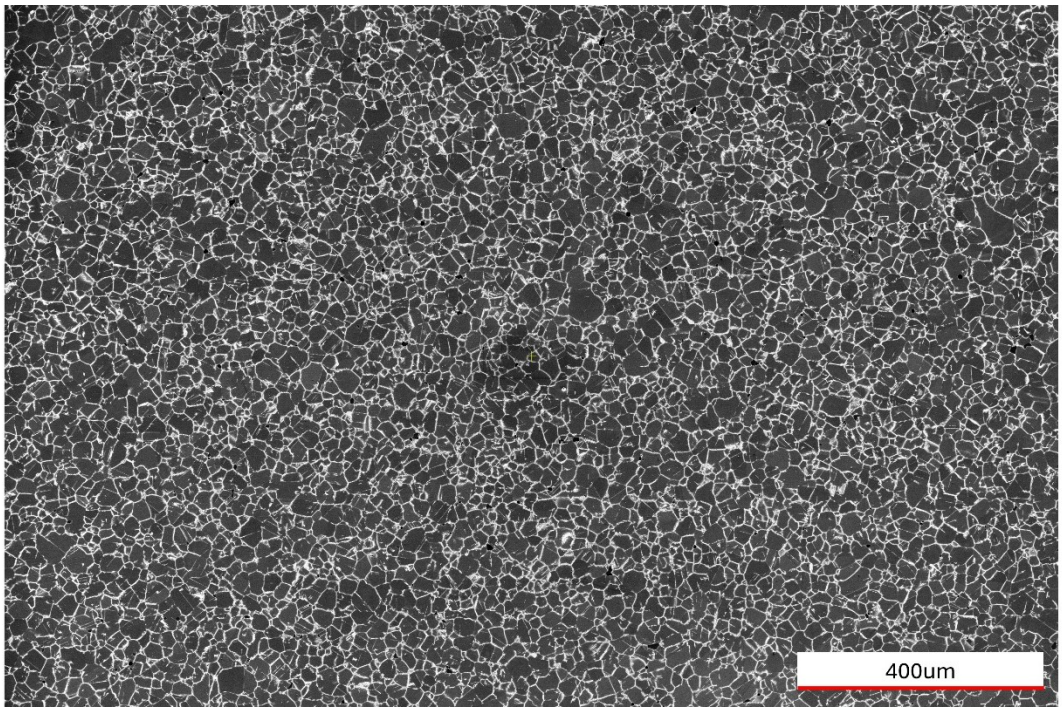


Figure 63: SEM Micrograph of Datum sample.

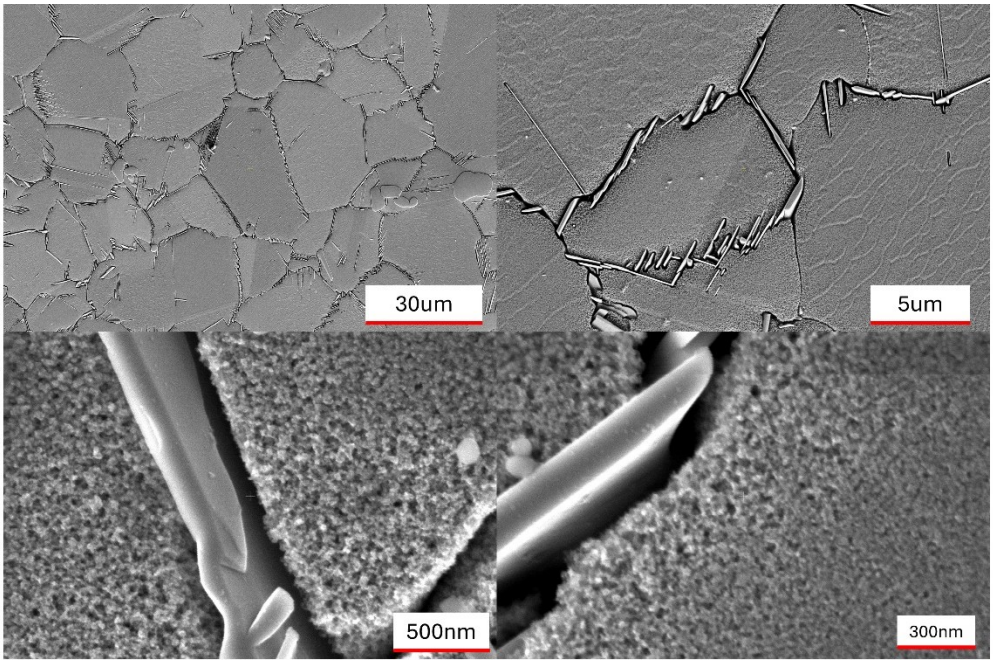


Figure 64: SEM micrographs of Datum sample at increased magnifications.

The microstructures of the two samples treated at 1000°C, FC1000 and WQ1000, are shown in Figure 65 to Figure 67. The presence of the δ phase, as well as the γ' and γ'' precipitates, is clear from the higher magnification images in Figure 65, a result of the slow cooling rate of this sample; they are noticeably absent in the water quenched sample, WQ1000, at a lower magnification (Figure 66). However, at higher magnifications (Figure 67), there are two key observations for WQ1000. The first concerns the wavy lines seen on the surface of the sample; these had not previously been observed, and the cause was unknown; it was uncertain whether they were surface effects or artefacts, or a result of another microstructural phenomenon that had not been considered. These wavy lines are also visible in Figure 64, of the Datum sample, and in fact across all of the samples from this billet; the cause of these would be investigated in later studies. The second, slightly unexpected feature seen in WQ1000 was the background mottling effect within the matrix (Figure 67), which suggested that there may still be γ' and/or the γ'' remaining in the sample, despite best efforts to avoid this precipitating. The SEM was not able to resolve beyond this magnification, so it was uncertain at this stage whether this was a surface effect or genuine precipitates being seen. As stated previously, further investigation using HS-AFM would be carried out to verify which was the case.

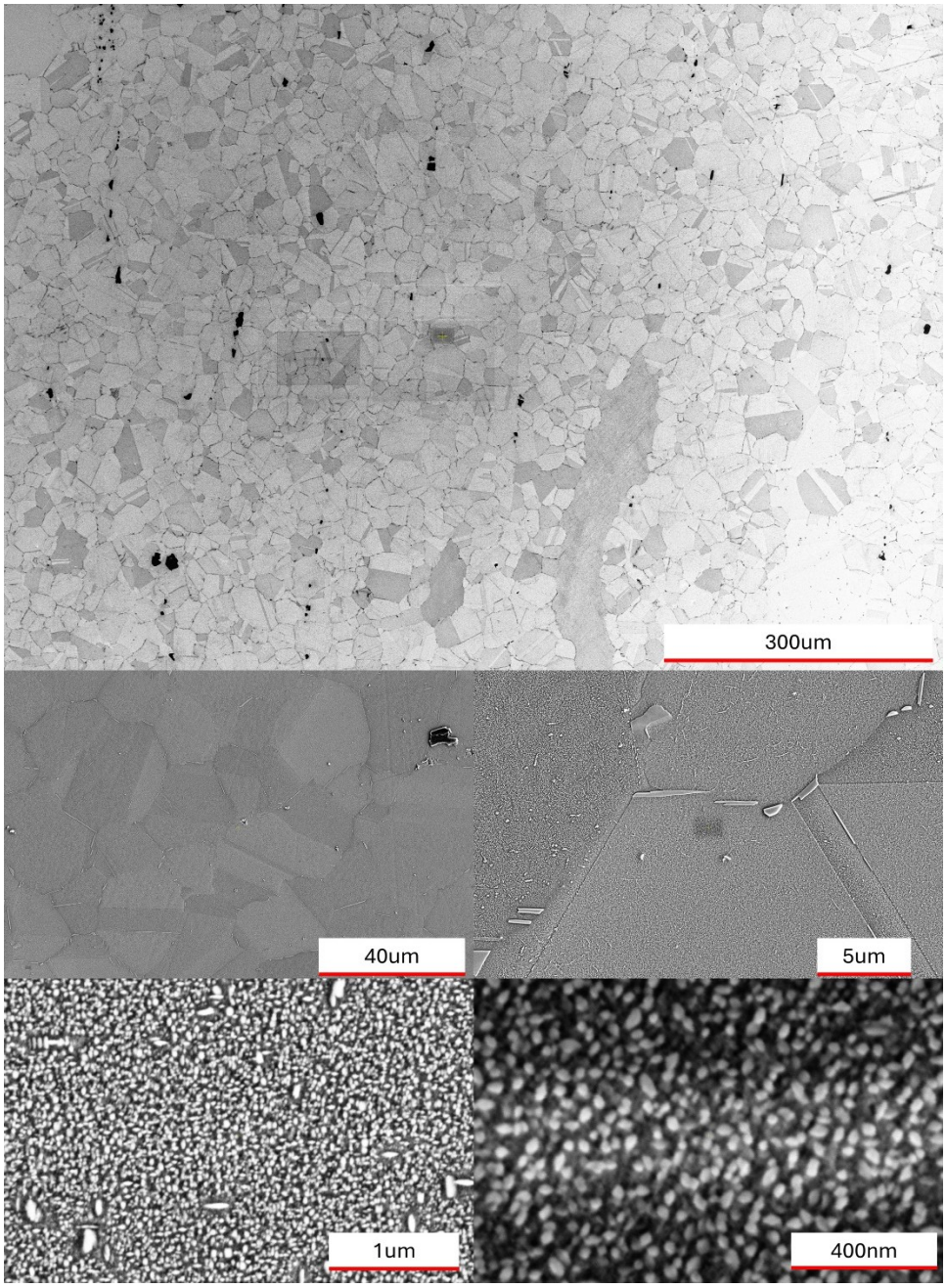


Figure 65: SEM Micrographs of FC1000 at increasing magnifications.

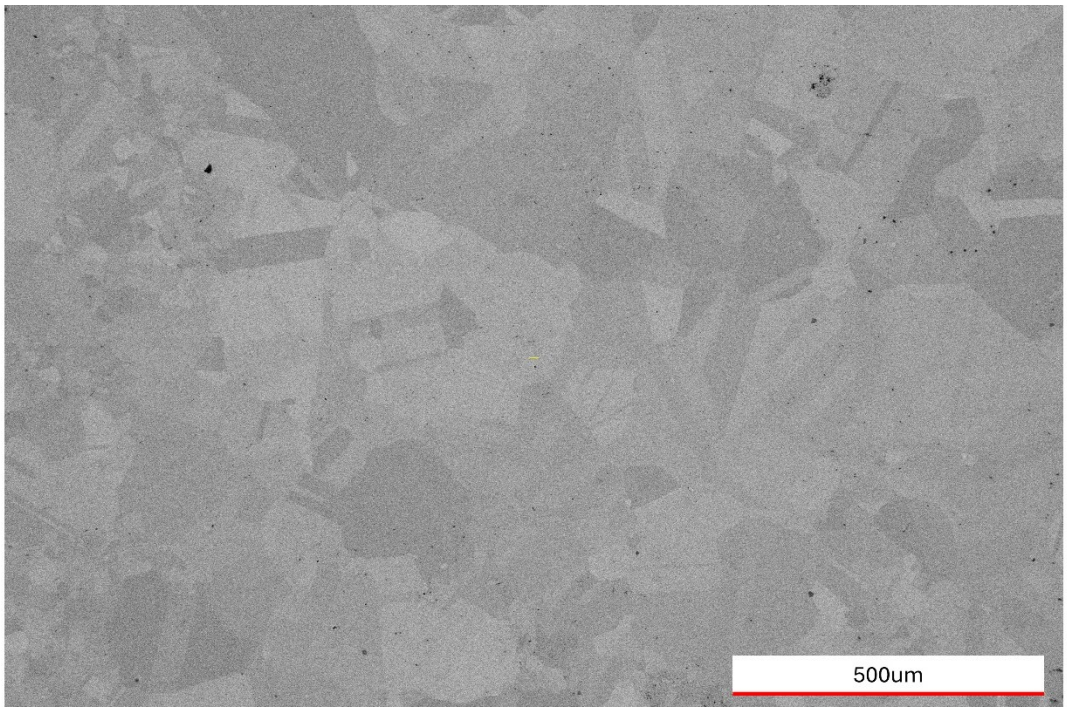


Figure 66: SEM Micrograph of WQ1000.

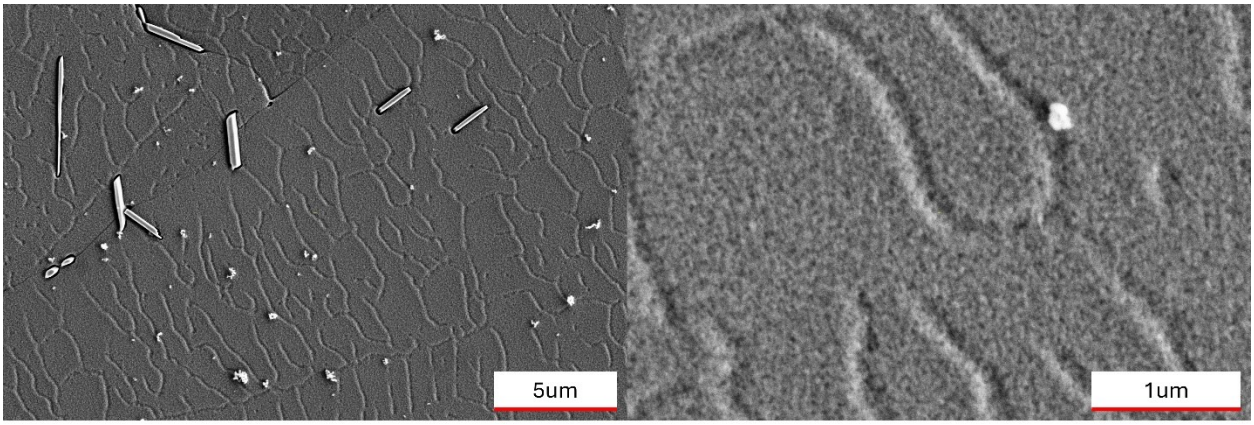


Figure 67: SEM micrographs of WQ1000 at higher magnifications.

SEM images of the samples which had undergone 900°C heat treatments (FC900 and WQ900) are shown in Figure 68 to Figure 70. From these, it was immediately apparent that this processing had been extremely effective in precipitating out large amounts of the δ phase in both samples; not only did it precipitate by nucleation at the grain boundaries as normal, but there were also growth of these thin plates extending into the grains themselves, as previously reported in the literature [156]. However, it was also noted from the literature that the intragranular nucleation observed here tends to occur in the presence of γ'' [156], which raised the question of whether this precipitate had

indeed been successfully removed. Further evidence to suggest that the γ'' phase may still be present is seen in Figure 71, depicting the edge of the WQ900 sample; in the bottom right corner of these images, there is a clear delineated region towards the surface of the sample, showing where the etchant has almost begun to 'over-etch'; the slight discolouration of this region implies the presence of the γ'' phase. There is also some background mottling visible at higher magnification images of WQ900 (Figure 70) which provides further evidence as to its presence.

The TTT diagrams for Inconel 718 shown in Chapter 3 all show that the 'nose', denoting the region of γ'' formation is quite close to the end of the diagram, and thus it was proposed that the water quenching cooling rate was perhaps not sufficient in preventing the γ'' from re-forming completely. Despite this unintended consequence, however, these heat treatments have not necessarily been unsuccessful and the samples were thought to still be suitable for phase estimation trials. Indeed, the aim of precipitating as much of the δ phase as possible for the 900°C samples has been highly effective and provided samples with dramatically contrasting microstructures. In addition, if there was γ'' present in the water quenched samples (as suspected from the micrographs), it would likely be the case for all of the Inconel 718 samples; indeed, even from micrographs of the OGHD samples, there was some uncertainty as to whether the mottling being observed were precipitates on the cusp of forming, rather than just surface residue. Thus it was theorised that the effect of the γ'' on the ultrasonic wave speed measurements could be assumed to be constant across all samples, and therefore negligible when investigating the link between V00 and phase composition; an alternative interpretation could be regarding the γ K00 coefficient as a 'homogenised' value, which also included these precipitates (where V00 is multiplied by $\sqrt{4\pi}$ to calculate K00, as illustrated in Equation 7).

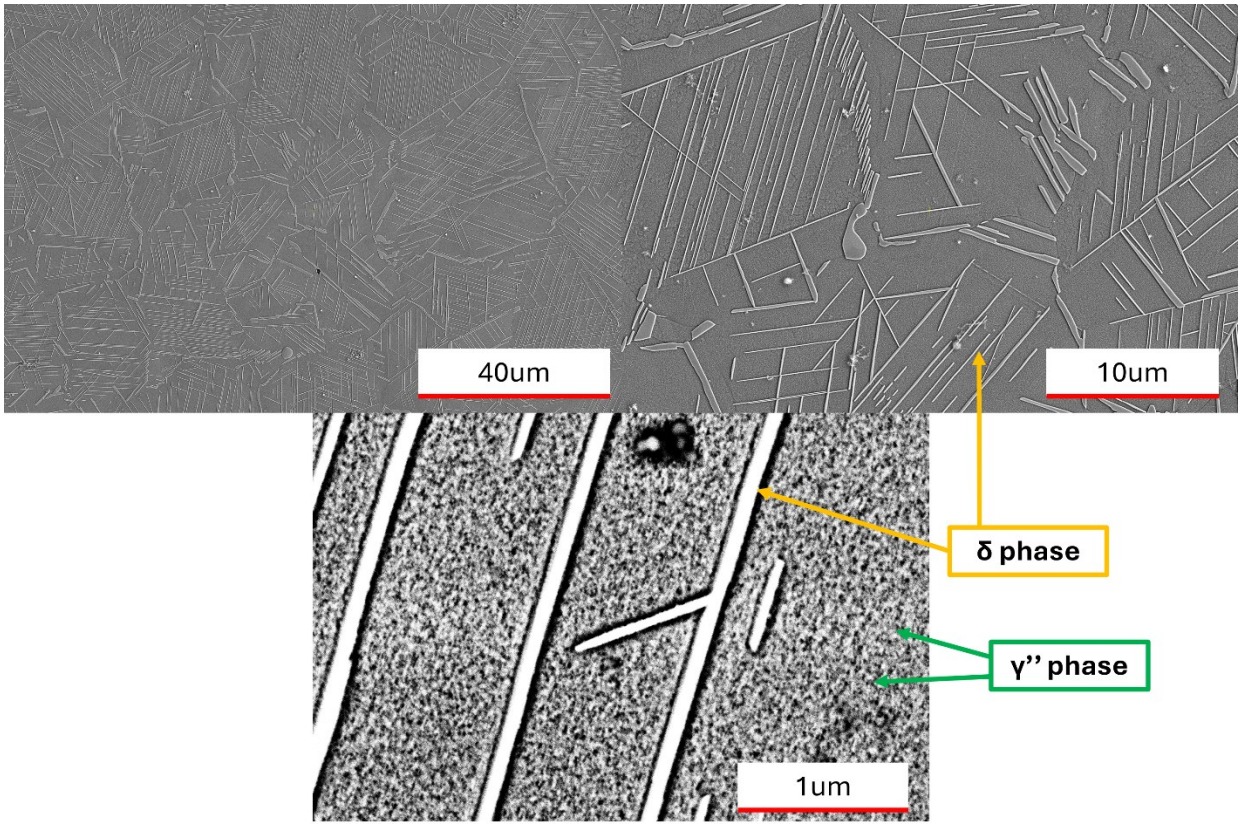


Figure 68: Micrographs of various magnifications of sample FC900.

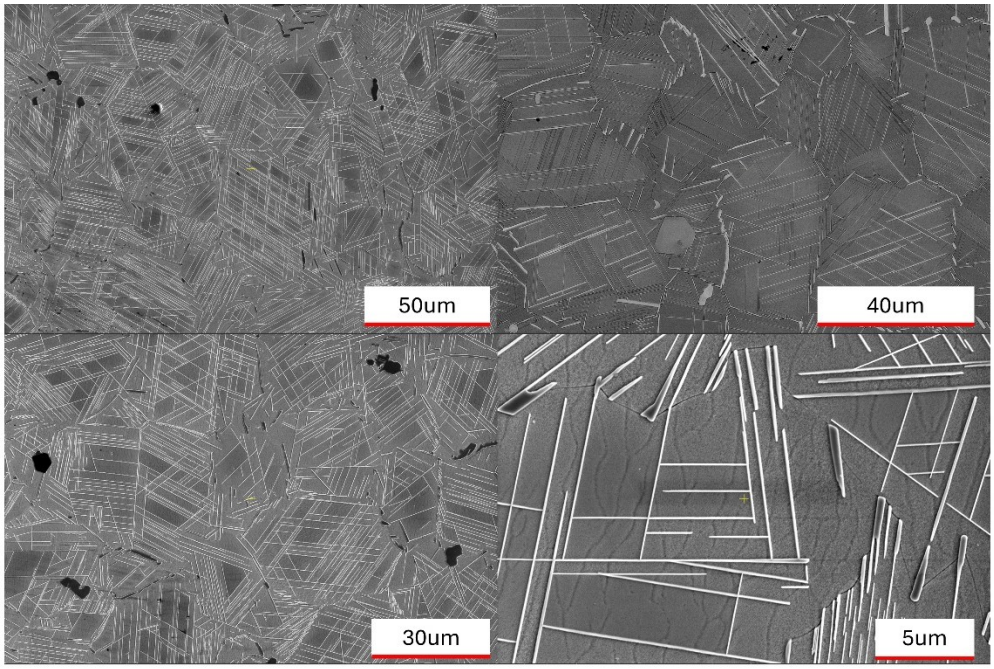


Figure 69: SEM micrographs of WQ900 at increasing magnifications.

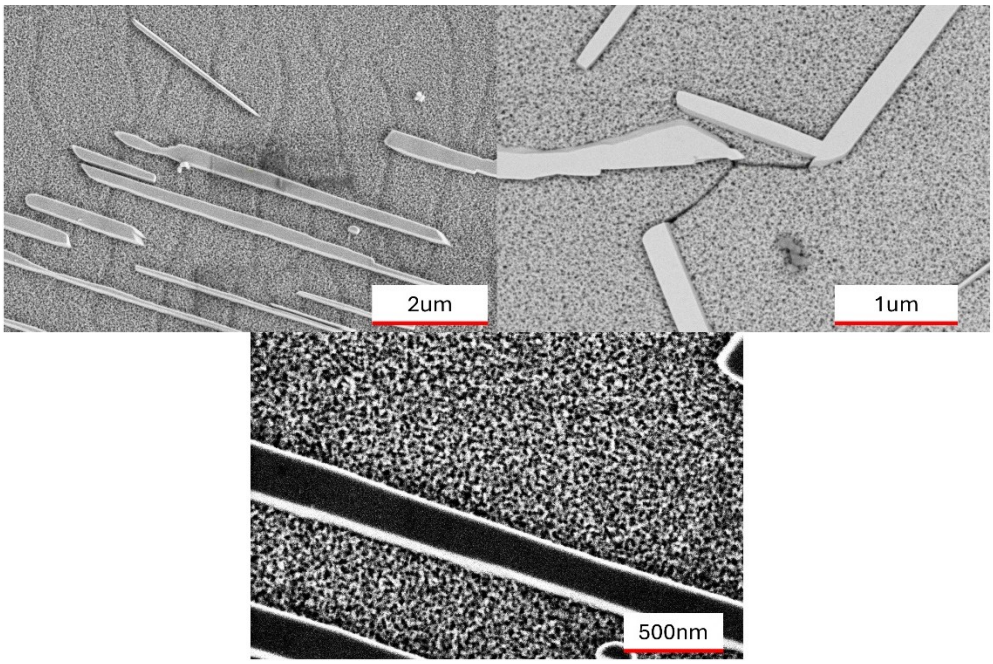


Figure 70: SEM micrographs of WQ900 at higher magnifications.

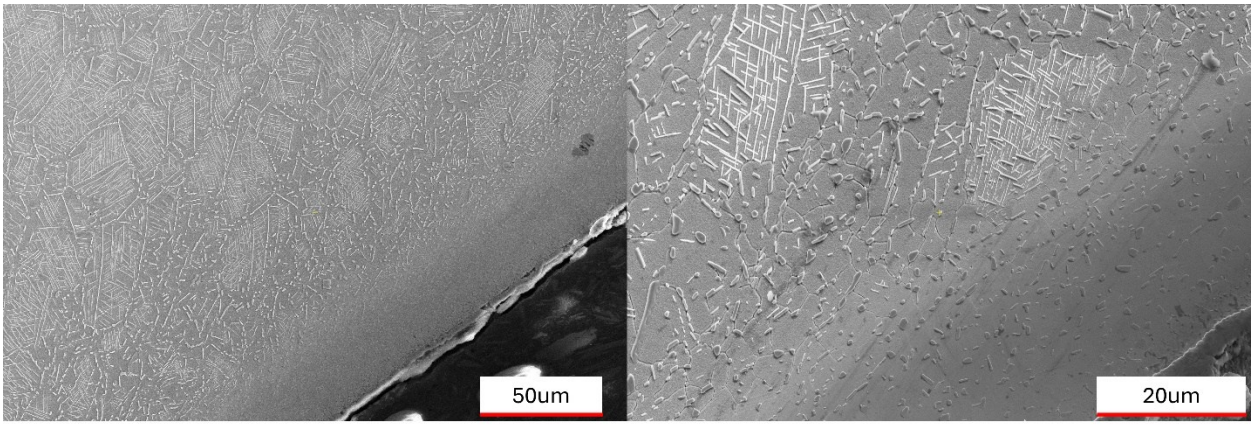


Figure 71: SEM micrographs of WQ900 showing the delineated regions at the edges.

Before progressing onto the V00 measurements, however, it was decided that EBSD would be used to investigate the kernel average misorientation, and associated pattern quality, within the samples, to attempt to determine the exact cause of the wavy lines seen in the water quenched samples. The main concern was that there were compositional differences that had taken place during heat treatments which had not previously been accounted for, but it was also theorised that these lines

may in fact be caused by differences in the amount of retained strain within the sample which the KAM and pattern quality maps would be able to identify.

4.3.1 Kernel Average Misorientation (KAM) and Pattern Quality

The Kernel Average Misorientation (KAM) and pattern quality maps are two individual metrics [218] [219] [220] which can be used when using the EBSD (or electron backscatter diffraction) mapping technique, which can be performed using a scanning electron microscope, and is a higher accuracy method of visualising grains within materials, particularly the individual grain orientations.

KAM is defined as the average misorientation between a kernel point and its neighbouring points, which reflect the local lattice curvature; this can be induced by elastic strain and defects including secondary phases and grain boundaries, but is primarily dominated by plastic deformation [218]. The pattern quality is a measurement of the contrast between the Kikuchi bands[10] against the background (essentially how sharp an analysed diffraction pattern is), where this data is generated from all points on the analysed surface, regardless of indexability and is independent of the EBSD indexing itself [220]; pattern quality maps can therefore be interpreted similar to microstructurally sensitive SEM images. This contrast arises from factors including phase density, crystallographic orientation and grain boundary location, as well as near-surface plastic strain [221]. Theoretically, the pattern quality will be lower for crystals with a higher number of crystal defects, such as dislocations (due to the patterns themselves being less sharp, and having a lower average band intensity) than those from a strain-free, but otherwise identical (in terms of phase and orientation), volume of crystal [220] – though the pattern quality does also depend on the level of sample preparation.

As KAM analysis is useful in understanding local lattice distortions, localised deformation and high dislocation density, it can be used to visualise stored strain energy within a grain; the KAM value tends to be high in deformed grains due to the higher dislocation density [222]. Similarly, the pattern quality can also indicate differing levels of strain within the material. One of the suggested causes of the wavy lines observed the RR Furnace batch of Inconel 718 samples was the presence of dislocations, or differences in the amount of retained strain, such as those reported by Stöcker et al [223] and Landau et al [224] (rather than compositional differences). It was therefore decided

[10] Kikuchi bands are patterns formed by scattered electrons in EBSD measurements. The positions of these bands are dependent on the crystal orientations within the sample, and hence can be used to calculate the orientation of a given diffracting crystal at the point where the beam interacts with the sample [398].

that an EBSD scan to generate KAM and pattern quality maps would be useful in confirming whether this was the case. The WQ900 sample was selected, and scanned at a medium-high resolution (as attempts to use high resolution resulted in too much drift). The KAM and pattern quality maps are shown in Figure 72 and Figure 73 respectively.

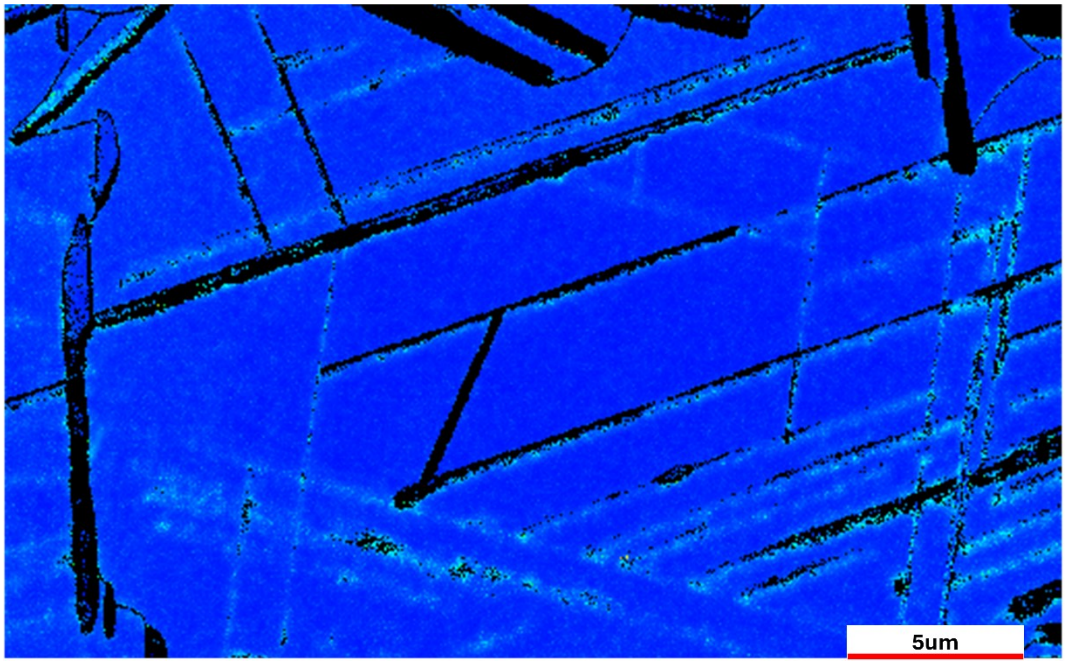


Figure 72: Kernel Average Misorientation map of WQ900.

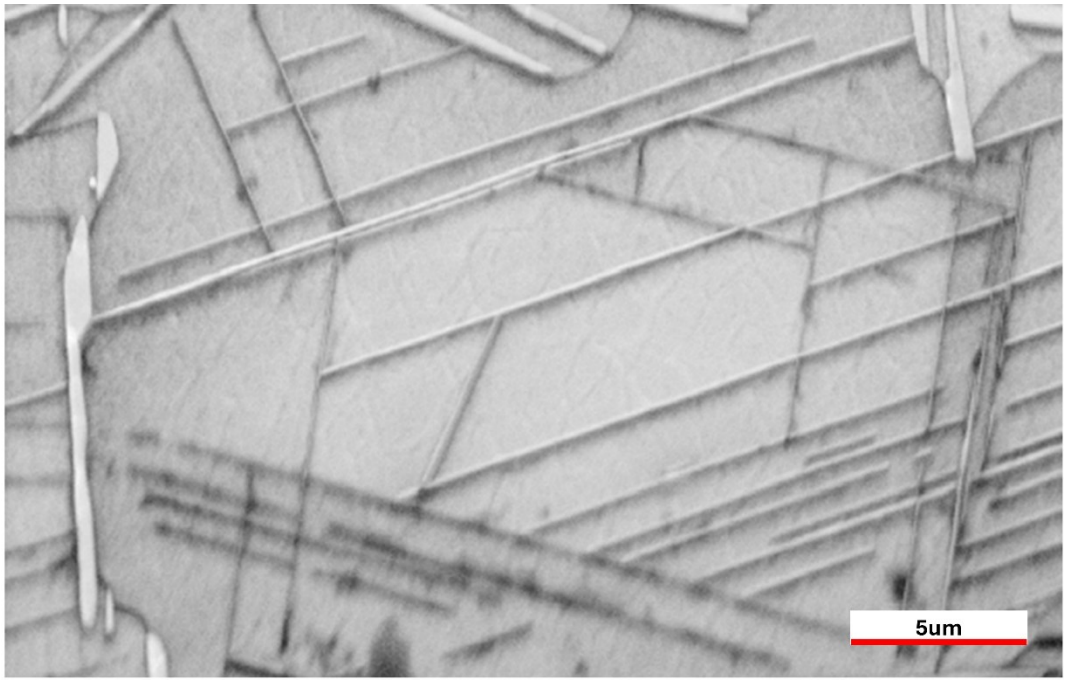


Figure 73: Pattern Quality map of WQ900.

The KAM map shown in Figure 72 shows that, although the main FCC matrix indexed well, only small amounts of the δ phase (which was specified as the Ni_3Nb crystal when performing the analysis) was well mapped, and only the strain associated with the δ phase and γ matrix boundaries are shown, with no noticeable variation caused by the wavy lines. The pattern quality map, on the other hand, does appear to show a subtle variation with respect to these lines, where the pattern quality does appear to drop slightly.

It is proposed that the combination of the KAM and pattern quality maps provide enough evidence to suggest these wavy lines, or 'loops', are in fact dislocation cells, or polygons, rather than any compositional variations. The KAM map failed to detect the presence of any unknown crystals or compositional variations, and the subtle variations in the pattern quality do correspond to the position of these loops. The observed pattern quality reduction at dislocation loops, or cells, is likely due to the slightly higher misorientation between the crystals (and is thus not as drastic a difference as shown at grain boundaries, where there is a near-amorphous structure).

These loops may be caused by there being a level of strain being retained in the billet, which means that the long exposure times at high temperature (or 'soaking' time) have allowed these dislocations to arrange themselves into walls to reduce overall lattice energy. This process is known as

polygonisation, and may be affected by various factors including the presence of vacancies and interstitials.

With these investigations suggesting that the cause of these wavy lines was retained strain, rather than differences in chemistry or phase composition, the ultrasonic wave speed measurement experiments could then be carried out with the assumption that these loops should not, in theory, affect the outcomes of these investigations.

4.4 RR Furnace Samples – UWS Results

Similarly to the first set of Inconel 718 samples, each of the new Inconel 718 discs was tested a total of 16 times, with the cumulative mean values of V00 plotted in Figure 74 below. As these were not in a dodecagon shape, some holders were 3D printed to simplify the 30 degree rotation of the samples in the required orientations for the V00 measurements. A statistical analysis was then carried out using this data to determine the confidence intervals, and verify the previous hypothesis that the 95% and 98% confidence intervals could be reached after 4 and 3 trials respectively. The histograms fitted to each sample's dataset have been shown in Figure 75, with the average number of trials (from ten randomised permutations) to reach the 95% and 98% confidence intervals shown in Figure 76. It can be seen that, much like with the OG sample set, in the worst case the 95% confidence interval can be reached after 4 trials, and the 98% after 3 trials.

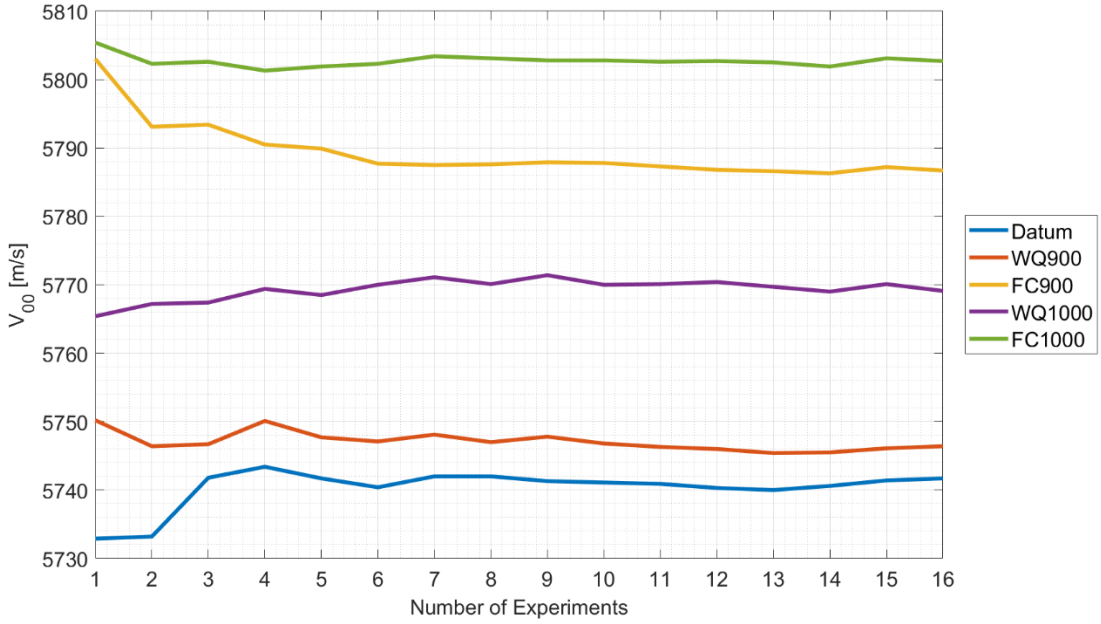


Figure 74: Cumulative mean V00 values for RR Furnaces batch of Inconel 718.

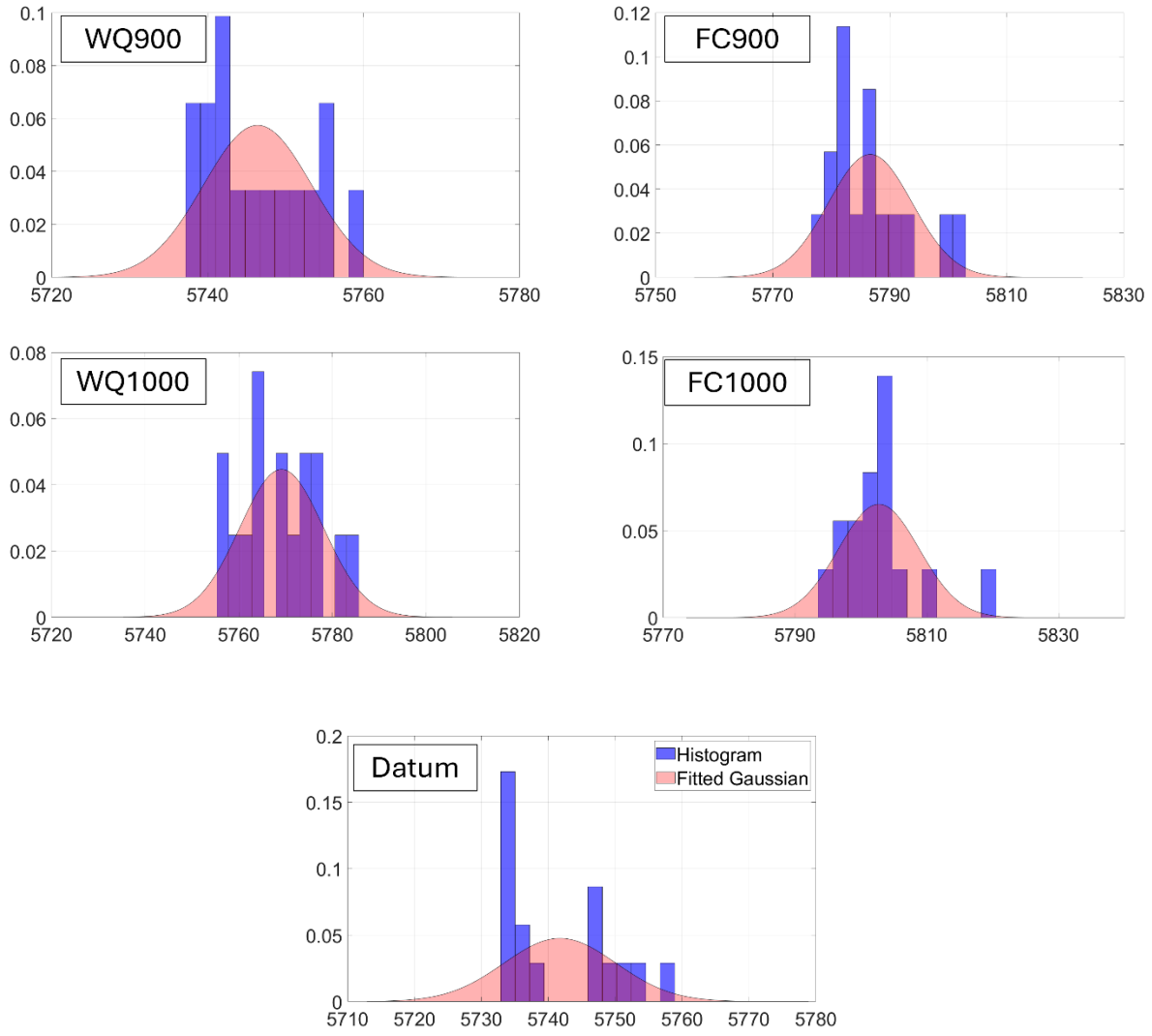


Figure 75: Fitted Gaussian distributions for each RR Furnace sample.

Table 4: 95% and 98% confidence intervals for each RR Furnace sample, calculated from fitted Gaussian distributions.

Sample	95% Confidence Interval		98% Confidence Interval	
	Lower [m/s]	Upper [m/s]	Lower [m/s]	Upper [m/s]
Datum	5737.3	5746.2	5736.3	5747.2
WQ900	5742.7	5750.1	5741.9	5750.9
WQ1000	5764.4	5773.9	5763.3	5775.0
FC900	5782.9	5790.5	5782.0	5791.3
FC1000	5799.5	5806.0	5798.7	5806.7

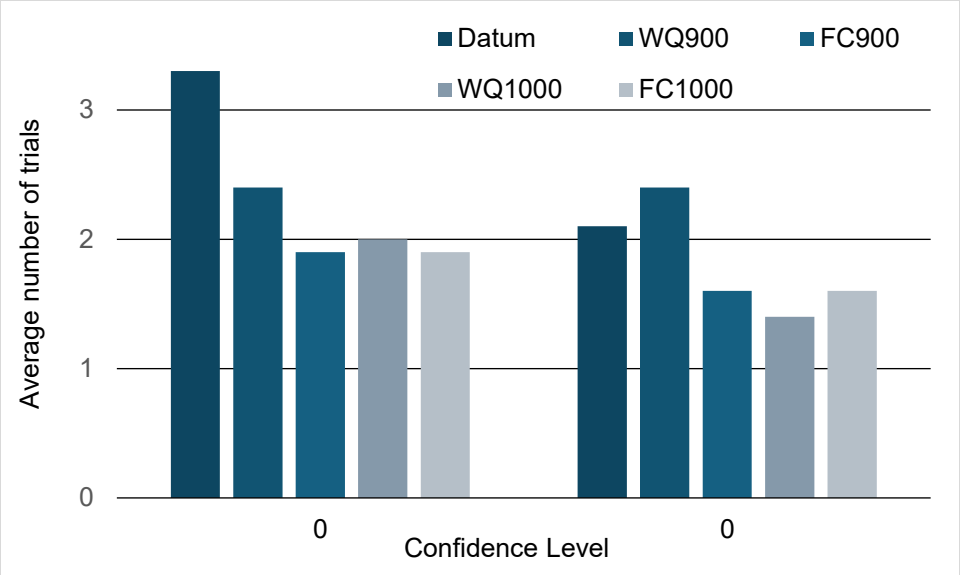


Figure 76: Average number of trials to reach 95% and 98% confidence intervals for each sample.

4.4.1 Discussion

It is promising to note that, much like the OG set of Inconel 718 dodecagons, there has been a good convergence to a distinct mean value of V00 for each sample condition, and this value is reached by the time 8 experiments have been carried out. The two highest values of V00, FC1000 followed by FC900, were as predicted; with the high hold temperature, followed by a slow cooling rate, this would have allowed for all of the precipitates to form back out of solution, and thus – in line with the theory that the more precipitates present, the stiffer the overall material – they would have the highest V00 measurements. The fact that FC1000 had a slightly greater overall wave speed than FC900 was also as predicted, due to its higher hold temperature, thus increasing the time allowed for the precipitates to form.

The V00 magnitudes of the remaining samples, however, was not quite as straightforward to interpret; not only was the Datum sample much lower than expected, but it was not that dissimilar from the converged V00 value for WQ900; this itself being lower than the WQ1000 sample was also not as expected. In the case of WQ1000, the fact that it was higher than expected could be explained from the micrographs, which showed evidence that there may be γ’ and γ’’ present, which could be the cause of it not having the lowest V00 of all samples as initially predicted. (It was also subsequently found from the literature that this heat treatment would likely result in a ~3% δ phase composition [225]; this will be revisited in later discussions.)

There are further uncertainties in the V00 results of WQ900. If keeping with the previously made assumptions that the presence of the precipitates (particularly the δ phase) would increase the overall stiffness of the material, this sample should have the highest V00 of these three samples, and be lower than only the furnace cooled samples which would have allowed for the γ'/γ'' phases to re-form in addition to the δ phase. Instead, it is second lowest, higher only than Datum[11].

There were two possible explanations proposed for this low V00 value; the first being that excessive precipitation within the grains of the δ phase may in fact be causing a retarding effect on the overall wave speeds, resulting in this lower than expected V00. This is, however, unlikely, given that the V00 measurements are theoretically only affected by the chemistry and subsequently the SCECs of the material; it is more likely that this precipitation mechanism is having an unexpected impact on the overall SCECs of the sample, the second explanation for the low V00. It may be the case that the way (and amount) in which the δ phase has formed is hindering the overall stiffness of the matrix via its morphology – perhaps the fact it is intra-, as well as intergranular, or its orientation, is causing a weakening effect – or its excessive precipitation has depleted the γ matrix of solid solution strengthening Niobium to such an extent that the overall SCEC has dropped drastically. (Indeed, the unintentional presence of the γ'/γ'' precipitates may also be contributing to this effect.)

Regardless of the cause, it has been demonstrated that, when being applied for the phase characterisation of materials where the morphology and precipitation mechanism can vary, the theory is not as straightforward as a direct positive correlation between V00 and amount of precipitate. However, the fact that V00 is sensitive to microstructural variations means that the technique could still be used – with the caveat that a lower velocity measurement was indicative of the presence of a greater amount of a precipitate for a given material, rather than the reverse as previously assumed.

Having acquired this set of results, two follow up experiments were planned; the first, hardness testing, to not only investigate whether there was any correlation between the V00 measurements and hardness tests, but also to see whether this alternative material property could provide any further explanation on the hierarchy of the V00 measurements. The second was use an alternative form of microscopy – high speed atomic force microscopy – to confirm the existence (or absence)

[11] In fact, the Datum V00 aligned more closely with the results from the OGHD samples; this implied that there may have been differences in processing histories. It was later discovered that there had been issues in the past with the material manufacturer in terms of nonconformance, which may explain this.

of the γ’/γ’’ precipitates in the heat treated samples where they were not intended to be present. The hardness testing was also carried out with the objective of beginning to compile a set of data for a materials characterisation framework, where in the future it would be possible to use the UWS technique and verify against hardness measurements in order to characterise a given material’s microstructure, and determine whether or not it was suitable for use in components. These hardness tests will be described in the following section.

4.5 Hardness Testing

The incorporation of hardness testing data into an overall materials characterisation framework was always of interest for this project, as the use of hardness tests is currently one of the most common techniques used in industry for inspecting components which have been subjected to abnormal loading conditions, such as overtemperature (and occasionally stress), to ensure that the material is still within specification – both in terms of tensile and fatigue properties. These hardness tests require a region of the material to be polished before an indentation is made, which can be time-consuming, and somewhat destructive, due to the need for an indentation. A set of hardness results alongside the UWS values would provide a demonstration of whether the technique could be deployed in industry for purposes other than phase composition estimates – i.e., to infer whether the microstructure of the material was still acceptable and with the required mechanical properties. In the future, it would be highly beneficial to have such a materials characterisation framework, where a combined V00 measurement and hardness value could be used to determine a material's microstructure, both in terms of phase composition as well as whether these tensile and fatigue properties were acceptable; if it is demonstrated that the UWS method can be used to accurately infer the state of the microstructure, the need for hardness testing could also be reduced. Indeed, there have been studies using ultrasonic backscattering to predict grain size, which in addition to the phase composition also affects the hardness of a material[12] [226]; the UWS technique developed here for estimating phase proportions could potentially be used to complement backscatter measurements to provide a holistic estimation of hardness, and therefore the state of the microstructure, for future metallurgy investigations.

However, the hardness values were now of particular interest having acquired the V00 data across all of the Inconel 718 samples and observed that the trends were not expected; it was thought that the use of hardness testing may be able to provide some insight into other microstructural effects which may be having an effect on the V00 results. Although the measurement of hardness and ultrasonic wave speed are quantifying different phenomena (where hardness testing is essentially a resistance to plastic deformation, and ultrasonic wave speeds are affected by elastic stiffness), in theory these values should align well, as the UWS measurements are only affected by changes in density and phase (where these differences will affect elastic stiffness and modulus, manifesting

[12] For the samples investigated in this study, the grain sizes are roughly the same – with the exception of the 'HD' samples – and it can be assumed that the grain size has a negligible effect on the hardness.

themselves in wave speed variations), much like the main factors influencing material hardness. However, it should also be noted that hardness tests can be affected by other factors, such as the γ’/γ’’ lattice parameter, spacing and mismatch, as well as grain orientation.

To carry out the hardness testing, the Vickers hardness tester pictured in Figure 77 was first calibrated using a control sample of nickel, before being used to make three indentations on each sample (in its ground, polished and etched condition), as shown in Figure 78. Each indent was at least 3 indentation widths away from each other and the sample edge. The average of the diagonal lengths (d) from each indent was then used to compare with HV30 charts to calculate the hardness value for each sample.

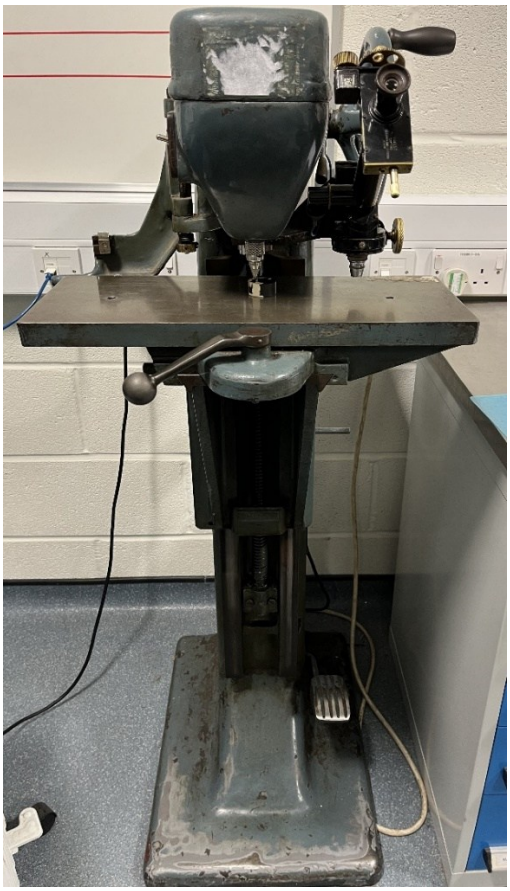


Figure 77: Vickers Hardness Tester.

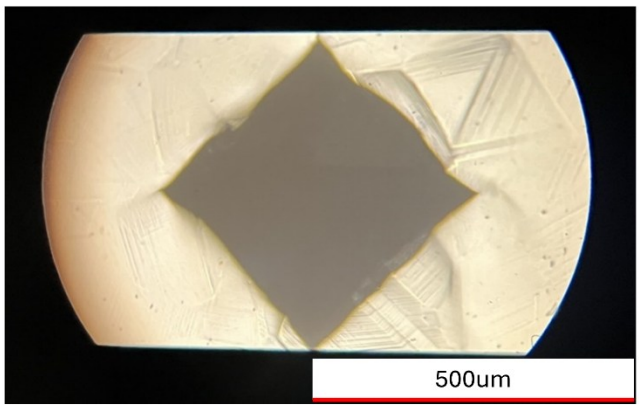


Figure 78: Example of an indentation made using the Vickers hardness tester.

4.5.1 Results

The HV30 values for each sample tested are shown in Table 5, with the diagonals of each indent denoted ‘d’ and the Vickers Hardness value ‘HV30’. For the second measurement of the Datum sample, only the average of the two diagonals had been recorded. Figure 79 illustrates the trend between the V00 measurements and the HV30 result for each of the samples tested. As previously mentioned, the two may not be directly comparable due to their quantifying different phenomena, but there is a overall a strong and positive correlation (with a Pearson coefficient *r* of 0.83) between the average ultrasonic wave speed and the hardness of the material.

Table 5: HV30 measurements for Inconel 718 samples.

Sample	d [µm]	HV30	d [µm]	HV30	d [µm]	HV30	d [µm]	HV30	Average HV30
Datum	521	205	516	209	507	216	530	198	207
	522	204			506	217	525	202	
OG	494	228	492	230	491	231	490	232	223
	492	230	495	227	494	228	492	230	
WQ900	470	252	474	248	473	249	471	251	249
	471	251	474	248	475	247	473	249	
WQ1000	576	168	573	169	553	182	567	173	173
	556	180	572	170	567	173	573	169	
FC900	406	338	406	338	407	336	406	338	336
	398	351	410	331	412	328	410	331	
FC1000	375	396	372	402	371	404	377	391	399
	372	402	368	411	378	389	373	400	
OGHD	598	156	592	159	592	159	599	155	155
	604	152	607	151	599	155	604	152	

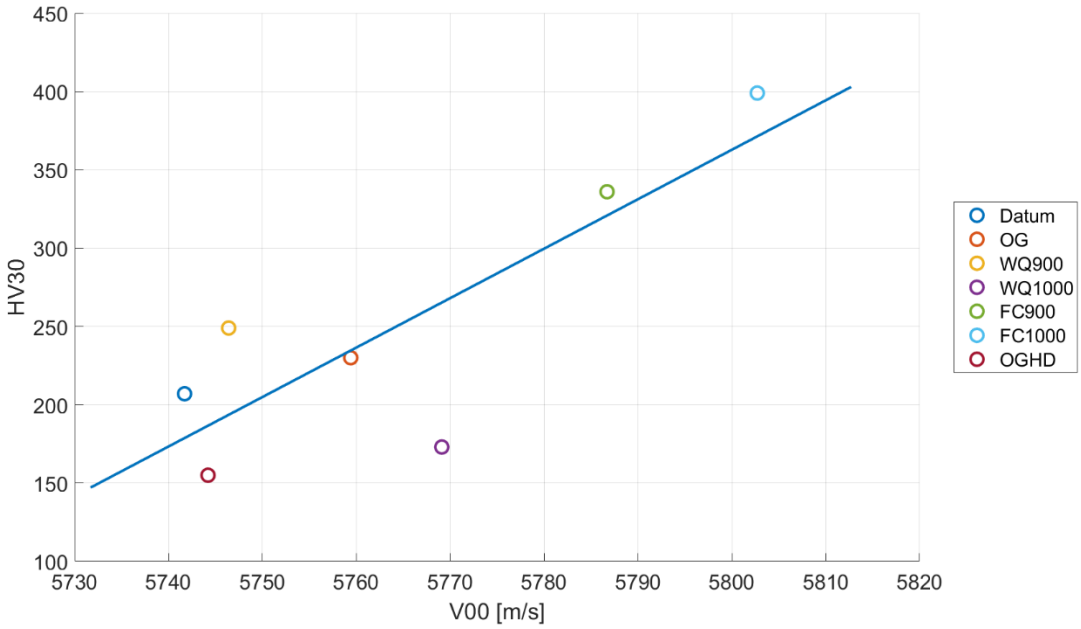


Figure 79: Plot showing correlation between V00 and HV30.

Despite the overall positive correlation between the Vickers hardness and the V00 measurements, there are however some noticeable outliers of this trend; these are the water quenched samples, WQ900 and WQ1000. It was theorised that the fact that they did not align well with the line of best fit could be explained by the effects of solid solution strengthening (or lack thereof), which had been previously proposed to explain the V00 trends not being as straightforward as initially expected.

In the case of WQ900, the V00 sits lower than the line of best fit which may be due to there being a lack of solid solution strengthening. The excessive precipitation of the δ phase may have resulted in a deficit of some of the elements (namely Nb, with the δ phase having the Ni_3Nb structure) which may otherwise have provided the matrix with elastic stiffness. Conversely, the fact that WQ1000 has a higher V00 than the trend would suggest could be due to the opposite effect; elements from other precipitates which have been taken back into solution (such as molybdenum and titanium [227] [228] as well as niobium, all of which are present in the γ'' phase [197]), may in turn have returned to the matrix to provide a solid solution strengthening effect to the matrix. This may contribute to an overall more elastically stiff structure – but with no change in the resistance to plastic deformation.

Although these hardness tests provided a potential explanation as to why the V00 results of these samples were not in the expected order, by providing further insight into the impact of solid solution strengthening on V00 measurements, a further key finding from these tests was the extremely low hardness of the Datum sample compared to the typical value of Inconel 718, which should sit around a HV30 value of 400 [229]. It has already been shown that this Datum sample had the lowest V00 of all the samples; the combination of these results posed the question of whether this sample did indeed have the expected microstructure of Inconel 718 in a service condition. If this were the case, the strengthening precipitates (γ' and γ'', as well as the δ phase) should be present to an extent where the V00 would be larger than the WQ1000 sample.

With both the V00 and the HV30 value for the Datum sample both being much lower than expected, the sample billet specification was further investigated; it was subsequently found that, although the material had been supplied in the AMS 5662 specification, it had not been prepared to both stages of this requirement. AMS 5662 consists of two parts – the first being solution treatment, followed by an ageing process, where the latter is crucial for ensuring that the strengthening precipitates were fully brought out of solution in the material. The combined experimental data from hardness and ultrasonic wave speed measurements were able to determine that the samples had been supplied in the solution annealed condition only, and not been aged.

This analysis proved to be an excellent demonstration of the potential place of V00 within a materials characterisation framework; the fact that the microstructure was unfit for purpose, and not conforming to specification, could be deduced from the combined experimental data from V00 and HV30 measurements. This was an excellent example of how the V00 technique could be deployed in industry – particularly as, during the course of the EngD, a significant amount of data for a given microstructural condition has been built up to form what could be a reference dataset for future experiments.

Having established that the Datum sample (and the as-received OG samples) were in fact not in the condition that Inconel 718 should be when being deployed in service, it was decided that these should be aged to be fully conformant to AMS 5662, as it would be useful for the V00 technique to be trialled on a sample which was relevant to industry and as close to its service-ready condition as possible. The ageing process was again carried out using furnaces at Rolls-Royce Materials Engineering, which comprised a hold of 720°C for 8 hours, followed by a furnace cool to 620°C at which there was a further hold for 8 hours, and finishing with an oil quench. The heat treatment

schematic is shown in Figure 80. This was carried out on both the Datum and one of the as-received OG samples, OG3. In addition, it was decided to carry out the 'heat damage' heat treatment (1100°C/4hr, but water quench instead of oil quench, due to health and safety regulations) on the remaining as-received sample OG4, to have a comparative dataset from the same sample before and after heat damage had occurred.

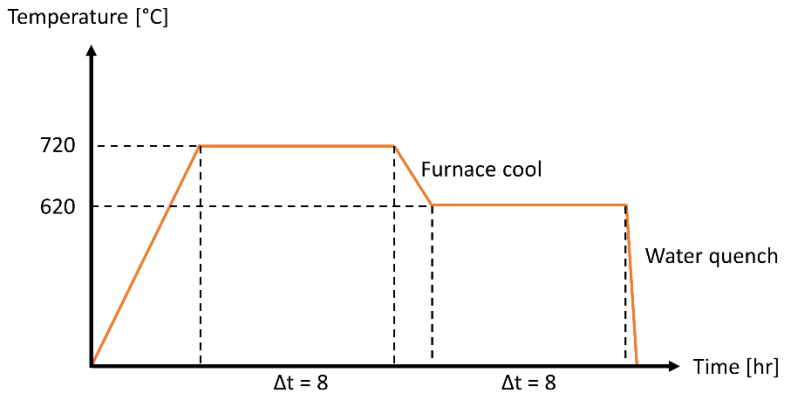


Figure 80: Schematic for heat treatment of ageing process according to AMS 5662.

4.6 Fully Aged Inconel 718 Samples

4.6.1 Microscopy

As for the previous samples, specimens were machined off each disc and prepared for observation using SEM. The microstructure of the OG3A and DatumA samples are shown in Figure 81 to Figure 84 below. It was not immediately clear that these microstructures were drastically different from the as-received, non-aged samples, but at higher magnifications (Figure 82 and Figure 84 for OG3A and DatumA respectively) the precipitation of the γ' and γ'' phases are very clearly visible.

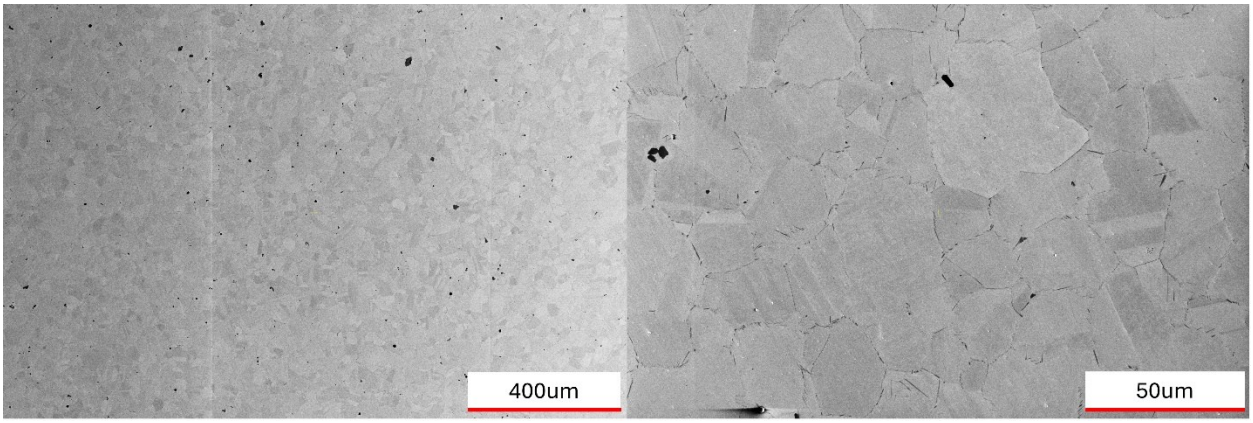


Figure 81: Low magnification micrographs of OG3A.

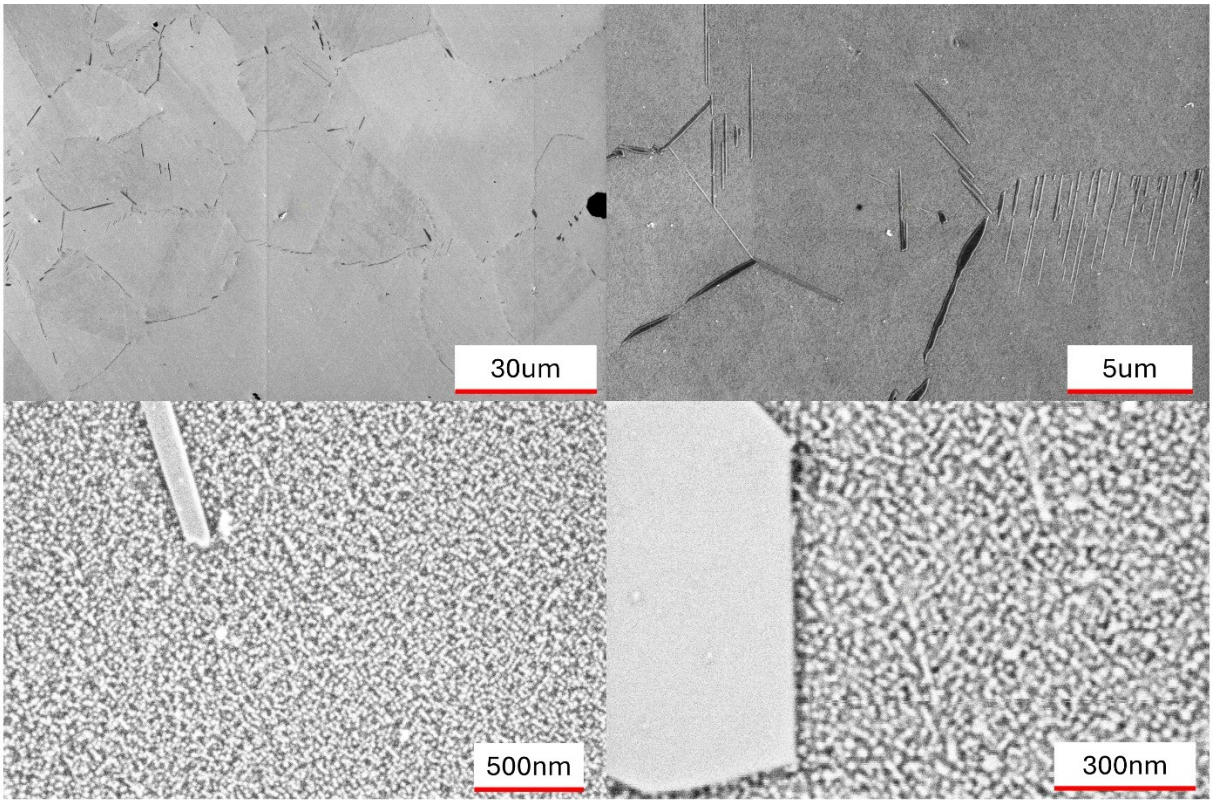


Figure 82: High magnification micrographs of OG3A.

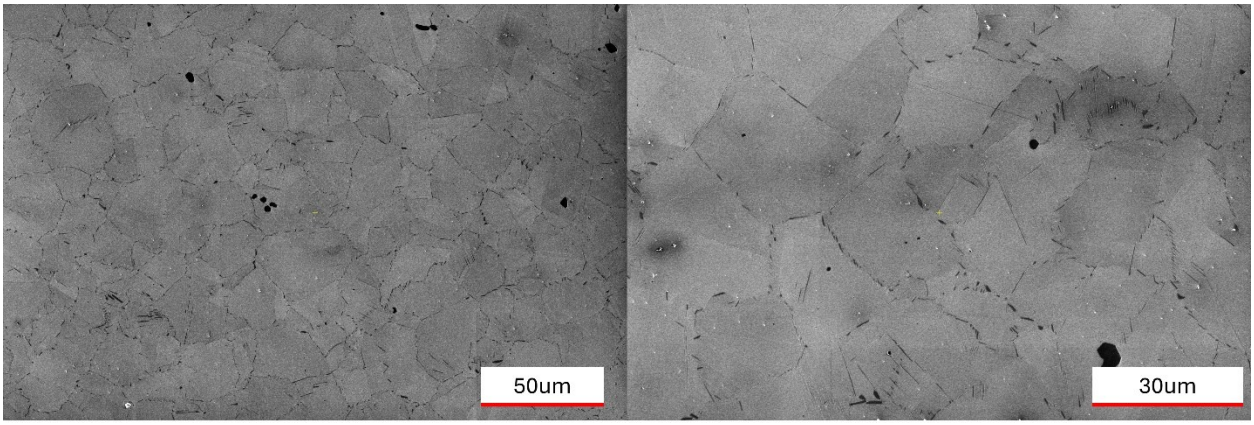


Figure 83: Low magnification micrographs of DatumA.

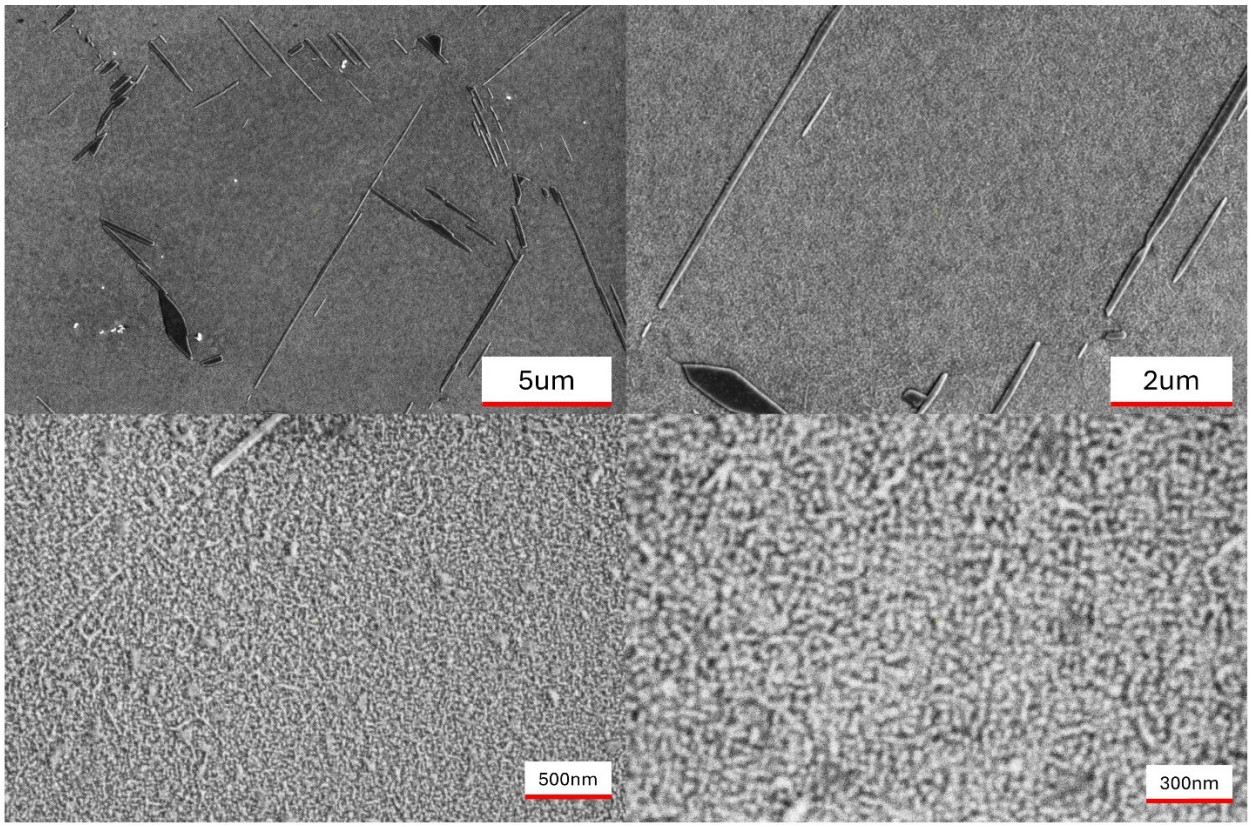


Figure 84: High magnification micrographs of DatumA.

4.6.2 UWS Results

For both sets of Inconel 718 samples, the V00 measurements from the aged discs (and the further heat damaged disc, in the case of the OG samples) were consolidated and the cumulative mean V00 values calculated, shown in Figure 85 and Figure 86 for the feasibility study discs and RR Furnace discs respectively. The V00 measurements from the additional heat damaged sample, OG4HD, have also been included in the set of results for the OG discs.

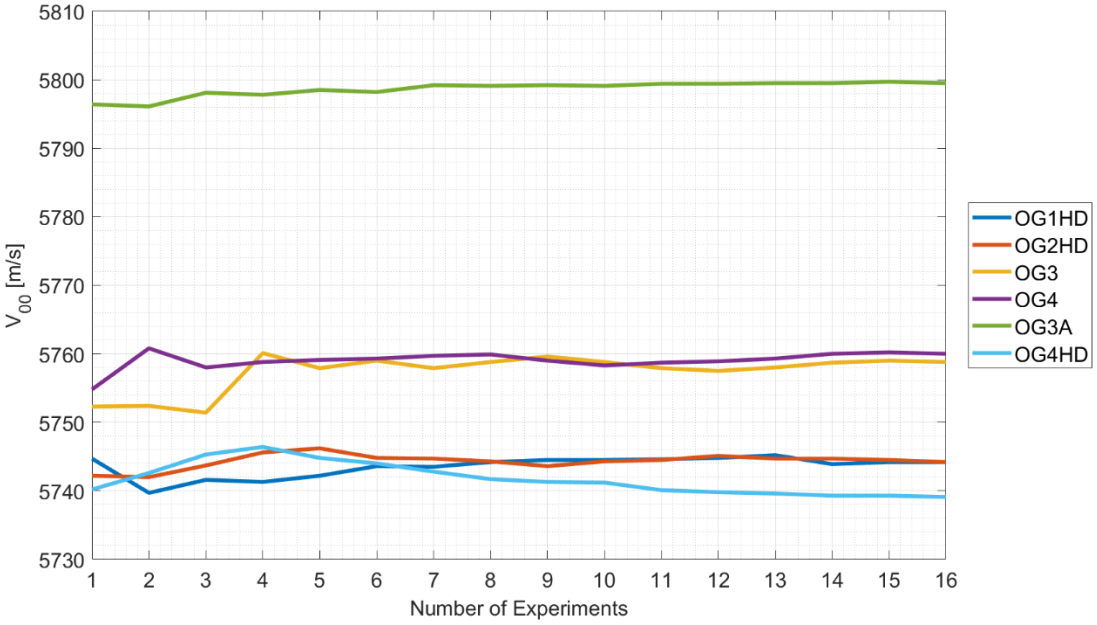


Figure 85: Cumulative mean of V00 measurements for all OG samples.

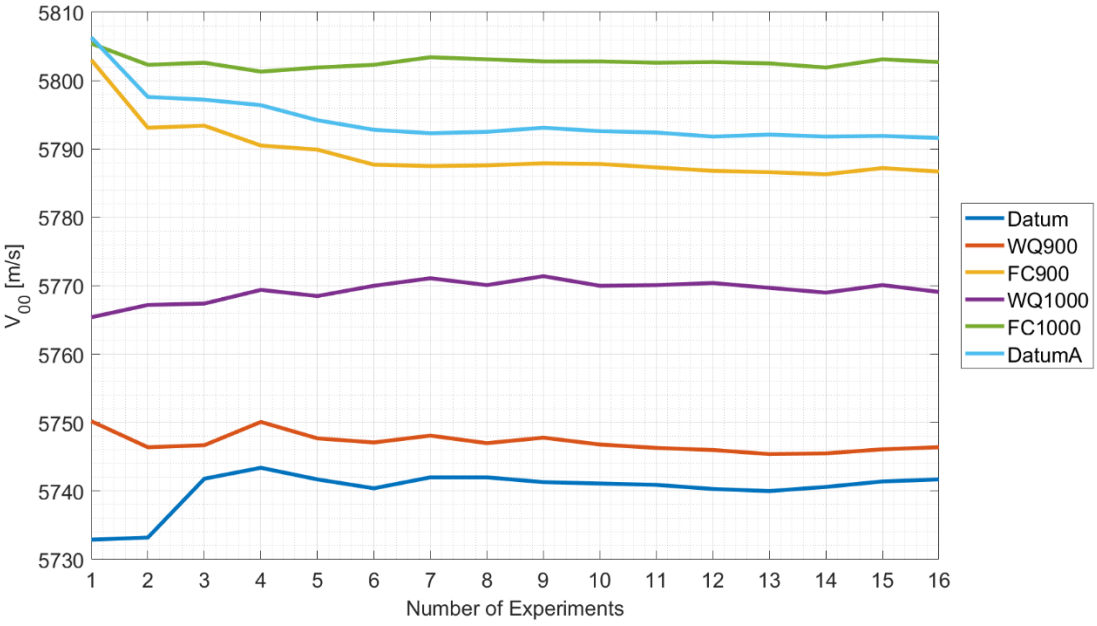


Figure 86: Cumulative mean of V00 measurements for all RR Furnace samples.

4.6.3 Discussion

For both sets of samples, it was immediately apparent that the ageing process had a marked effect on the V00 measurements; in the case of the OG samples, the mean V00 for OG3A is significantly higher than any of the other samples tested, and for the RR Furnace samples it is comparable to the two furnace cooled samples. This suggests (and indeed is verified with the micrographs) that the ageing process has been very effective in precipitating out γ' and γ'' phases to the extent that it can be clearly detected with V00 measurements. In addition, comparison of the V00 values for OG4 and OG4HD can be used to conclusively state that phase changes in the materials have been detectable between the aged (service condition) Inconel 718 and the heat damaged sample, with the difference of around 55m/s being well above the error levels of the ultrasonic wave speed measurements. It is also promising to note that the V00 values for the fully aged samples from both the OG and RR Furnace billets align well.

As previously discussed, the interpretation of the RR Furnace set of results is not straightforward, though it appears as if the microstructures fall into three 'bands'. The highest band is constituted by the DatumA, as well as the furnace cooled samples, followed by the region within which WQ1000 sits, and finally the lowest band formed by WQ900 and the Datum sample, in its original condition. These ranges of V00 could be useful as an initial rough estimation of the amount of the δ phase present in future inspections to establish the likely microstructure of a material, before proceeding with more experimental trials to more accurately determine and quantify the amount of δ phase present.

However, before proceeding onto the phase estimates, the opportunity arose to use HS-AFM to image a selection of the samples, in order to confirm whether the γ'/γ'' phases were indeed present in those samples in which it was not intended to be. It had been noted from the TTT diagrams of Inconel 718 (particularly more recent variations) that it may not have been possible to completely eliminate the γ'' phase from the samples, even though the heat treatments (both HD and WQ1000) were designed to do so. The cause of the mottling effect observed in SEM micrographs was still uncertain, as it was not clear whether this was a surface effect being observed or whether there were indeed precipitates present. It was thought that high-speed atomic force microscopy, or HS-AFM, would be able to help in conclusively determining whether or not the precipitates were present, as this would have an effect on the later phase estimation process.

As a highly sensitive topographical measurement technique, HS-AFM would be capable of imaging small-scale precipitates at a much higher resolution than electron microscopy (providing there was a detectable height difference between the precipitates and the material matrix itself, which there is for γ', γ'' and δ phases), without the risk of the sample being layered with carbon deposit if left under the microscope for prolonged periods of time. The use of topography to image the microstructure would essentially be able to eliminate any uncertainty of the cause of the mottling – if due to surface residue effects then there would be no change from the SEM micrographs, but there would be a detectable change if they were indeed precipitates. The following section gives a brief overview of the technique of HS-AFM, before presenting the results from the experiments.

4.7 High Speed Atomic Force Microscopy (HS-AFM)

4.7.1 Background

Atomic force microscopy, or AFM, is one of a group of experimental techniques known as scanning probe microscopy, or SPM [230], a field of research which emerged after the advent of the scanning tunnel microscope in 1982 by Binnig, Rohrer and Gerber [231] (which itself was based on Young's topografiner [232]). Other examples include scanning tunnelling microscopy [233] and scanning ion-conductance microscopy [234]. In general, SPMs obtain high spatial resolution measurements by raster-scanning a probe with a sharp detection tip (less than 10nm radius) across the surface of a flat sample [230], while changes in a parameter sensitive to the probe-sample separation (such as cantilever deflection, or tunnelling current) are measured [235]. A feedback loop is used to ensure the chosen parameter (i.e. contact force for AFM, or tunnelling current for STM) remains constant between the probe and the sample [235]. High resolution images can be obtained as the tip localises the interaction between the probe and the sample [236]; in the case of AFM, a three-dimensional map of the topography of the sample surface, with sub-nanometre lateral resolution and sub-angstrom height resolution, will be generated [230]. More details on HS-AFM, including various design considerations and applications, can be found in the Appendix.

4.7.1.1 Comparison to SEM and Limitations of HS-AFM

The reason for using HS-AFM in the present investigation to image Inconel 718 is primarily the increased resolution compared to SEM, as well as the technique being a topographical measurement method. Topographic contrast in SEM depends on the behaviour of electrons after they have entered the sample at the point of impact of the scanning beam, and their distribution can be defined in terms of an excitation volume – this is important in defining both the resolution and the contrast of the image [237]. An AFM uses applied forces which are small relative to the compressibility of the material, and hence the interaction volume is negligible on the nanoscale; however, the shape of the interacting surface is not negligible (as is necessary for imaging to be successful) and any topography on the surface will be convolved to an extent with the shape of the scanning tip [237]. Essentially, the images produced by both SEM and AFM are a result of a convolution of the investigated surface and a probe surface; in the case of AFM the tip surface is known, whereas in SEM it is a less well defined surface of the excitation volume; indeed, it is accepted that the point of origin of electrons which are being detected can be uncertain in depths

up to 10nm [237]. There can also be difficulty in separating topographic contrast generated from surfaces from those resulting from variations in the composition of crystallinity [237].

However, it is important to note that the HS-AFM technique is not without its limitations, and that it is more of a complementary technique to SEM rather than a superior imaging method. For example, if the sample surface is not sufficiently clean, the probe can be easily contaminated by loose material, picking up debris as it scans the surface; this has the effect of altering the effective radius of the tip and reducing the spatial resolution of the measurements [230]. Consequently, a variety of tip-shape-induced artefacts can be caused, known as double tip or tip convolution effects [238]; these effects are easily identifiable as an imaged feature tends to contain an identical substructure of an oval and an adjacent smaller circle, with the tip shape inducing an artificial preferential direction [239] . One example of this would be a circular precipitate appearing to be almost triangular in shape.

In addition, AFM cannot measure the shape of a sample obscured by overhangs, or down the sides of vertical structures, as the angle of the probe tip cannot be changed as it approaches the surface [230]. Samples with large changes in height are best imaged in an SEM, as AFM's strength lies in mapping a sample with a relatively flat surface (with features with a very low aspect ratio, in the order of 100s of nanometres height change per micron [230]). Hence, although ultimately the resolution of a state-of-the-art AFM could be said to exceed that of an equivalent SEM, the two techniques are very much complementary in nature, and obtaining micrographs of the selected Inconel 718 samples with both techniques would allow for a complete understanding of the microstructure of the material.

4.7.2 Experimental Methodology

The samples which were selected for HS-AFM were the aged Datum sample, DatumA; one heat damaged sample, OG3HD; and the maximum δ phase sample, WQ900 (all having being etched). The reasoning for these selections were to have a control sample (DatumA) to see how true γ'/γ'' would appear; a heat damaged sample to confirm whether there were γ'' precipitates on the cusp of forming, or whether the observed mottling was how the γ matrix appeared at the limit of the SEM resolution; and the WQ900 sample, to determine whether there were indeed the unintended γ'/γ'' precipitates present as suspected from SEM images. The HS-AFM used was at the University of Bristol's Nano-mapping Facility, supplied by Bristol Nanodynamics, with the HS-AFM in contact

mode and using a laser-doppler vibrometer (LDV) system to measure the cantilever tip displacement. The HS-AFM is shown in Figure 87 below.

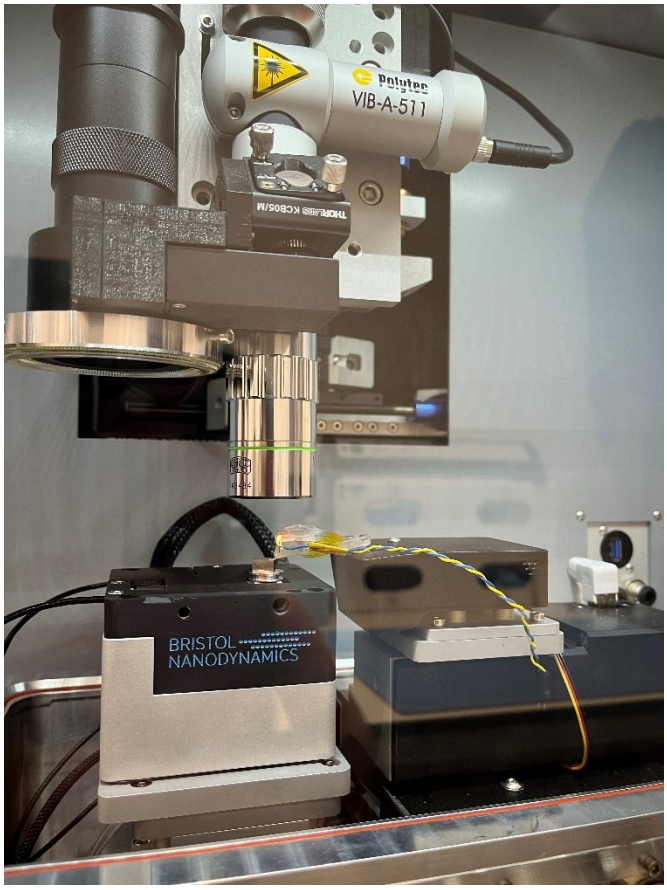


Figure 87: The HS-AFM manufactured by Bristol Nanodynamics, showing the cantilever (attached to the blue and yellow wire) resting on top of a sample, with the lens and laser suspended above.

On completion of the HS-AFM scanning, the post-processing procedure involved first mosaicking the individual frames acquired to form the complete (or composite) image, before importing the complete image into Gwyddion [240]. The plane subtraction tool was used to eliminate tilt, as well as 'correct horizontal scars' which helped to minimise the effect of loose debris. The Gaussian blur/2D CWT function within the integral transform set of tools was also used to minimize the 'salt and pepper' effect on the images (which is essentially the noise floor), a result of unavoidable electrical noise during the image acquisition process.

4.7.3 Results

4.7.3.1 Datum Aged

Figure 88 to Figure 90 show the composite images of the 'DatumA' sample, which was expected to have a microstructure containing all of the precipitates previously identified using SEM (including the γ', γ'' and δ phases, as well as the carbides). Figure 88 is a relatively low magnification image showing clearly the δ phase lying on the grain boundaries, though these pale in comparison to the carbide (the large white precipitate in the centre of the image) due to it being much more in relief than the other precipitates. The γ'/γ'' precipitates are also visible in the background, though much clearer in the images of Figure 89. The 3D representation shown of a single frame in Figure 90 shows the difference in topography between the γ'/γ'' and δ phases. These images, much like those obtained through SEM, all show conclusive evidence that the γ' and γ'' precipitates have been fully formed in the main γ matrix, and provided a good baseline microstructure against which to compare the other two samples which were examined.

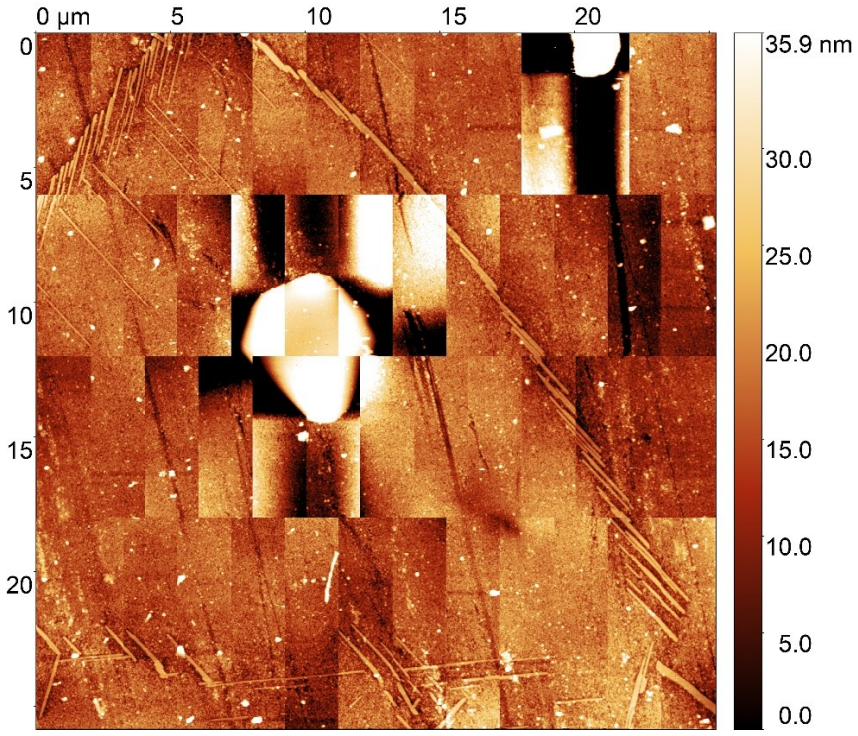


Figure 88: HS-AFM image of DatumA sample, clearly showing the δ phase (smaller needles) and the large carbide in image centre.

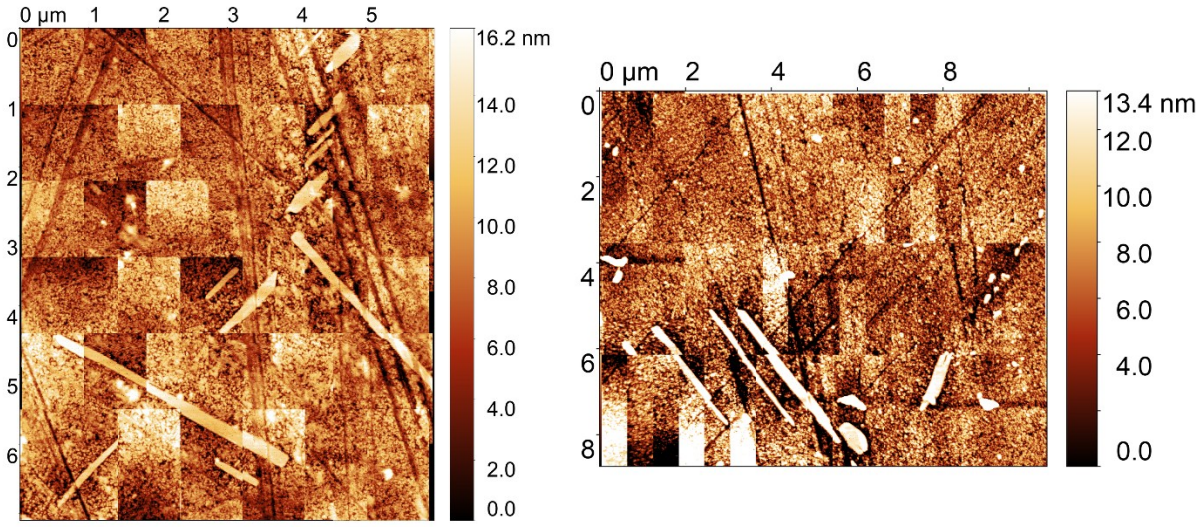


Figure 89: Higher magnification images of DatumA sample, showing the δ needles sitting in relief within the γ matrix saturated with γ' and γ'' precipitates.

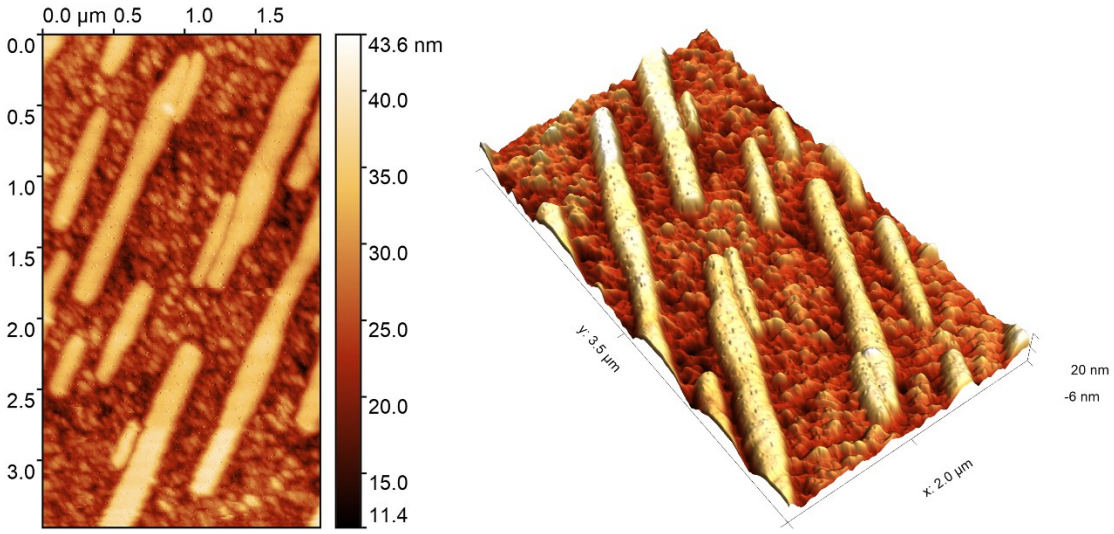


Figure 90: Single frame image of DatumA sample with 3D graphic, showing clearly the topographical difference between the γ' and γ'' precipitates with the δ phase.

4.7.3.2 Heat Damaged and WQ900 Samples

The main purpose of using HS-AFM for these two samples was to determine whether the samples, which theoretically should not contain any γ'/γ'' (critical for accurate phase estimation) were indeed free of these phases. Figure 91 and Figure 92 show the HD sample, where the wavy lines,

previously observed in SEM and established to be dislocation cells, are shown clearly here as topographical features, rather than surface residues. (These loops should not be mistaken for grain boundaries, which are shown as the regions indicated with the white arrows.) The main feature to note, however, is that the background mottling seen in SEM is shown much more clearly in these images as precipitates, although with slightly less relief than in the DatumA sample shown previously – almost as if the precipitate, which here is very likely the γ'', was not able to fully form. This microstructure is shown more clearly in Figure 92 at a slighly higher magnification. From these images, it can be concluded that, despite the high temperature hold and rapid cool, the microstructure of Inconel 718 in the heat damaged condition is still not free of the γ'' phase.

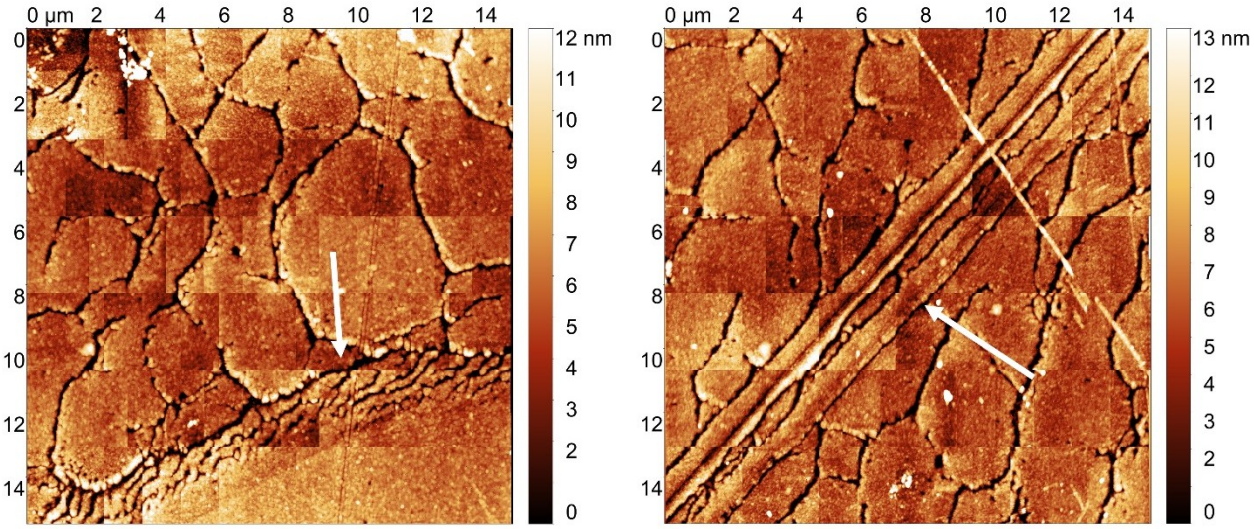


Figure 91: HS-AFM images of a sample in the HD condition. The wavy lines on the surface seen previously in SEM are visible, as well as a background mottling resembling the γ'' precipitate.

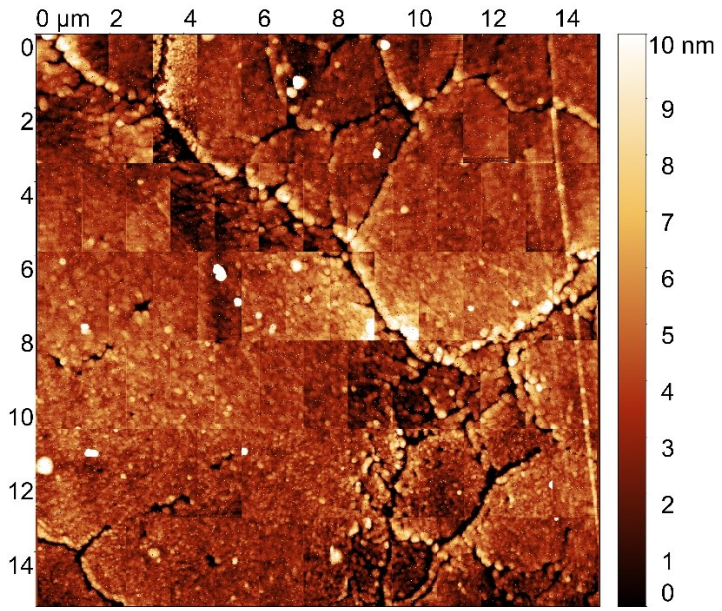


Figure 92: Higher magnification HS-AFM image of the HD sample, showing the γ'' precipitate.

Similar observations were made when examining the HS-AFM images acquired of the WQ900 sample in its etched condition, shown in Figure 93 and Figure 94. With this sample, however, there was the additional difficulty of the cantilever tips becoming blunt very rapidly after beginning the scanning of the surface; the effect of the blunt tip can clearly be seen in Figure 93b, where the particles which should be spherical have become triangular in shape, due to the previously described effect of tip convolution. However, it was possible to observe the presence of the spherical γ'' precipitate within the main matrix before the tip became blunt. Similarly, the spherical γ'' is identifiable in Figure 94, which – although is showing the effect of the blunt cantilever tip – also effectively shows the dislocation loops. Again, in the single frame image in Figure 94b, the γ'' is clearly shown, albeit with tip convolution affecting the perceived shape of the particles. It is thought that the excessive amount of the δ precipitate has had the effect of blunting the tip much more rapidly than in previously imaged samples, due to it having a much higher hardness that other phases present.

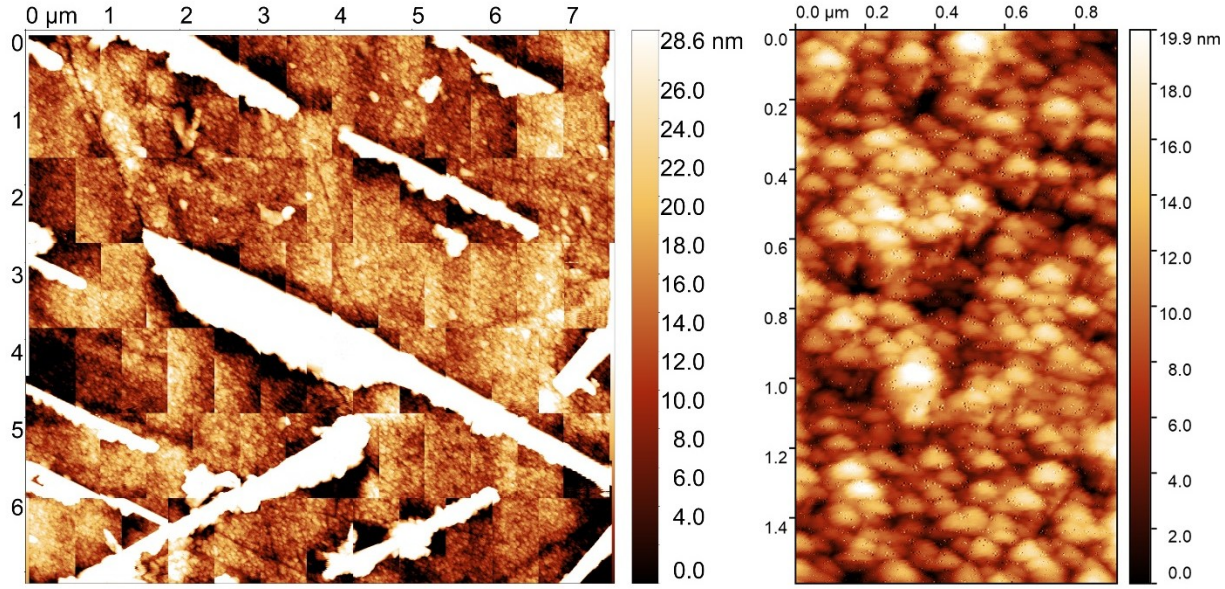


Figure 93: HS-AFM images of WQ900 sample, showing the γ'' precipitate in the background matrix as well as the δ phase needles.

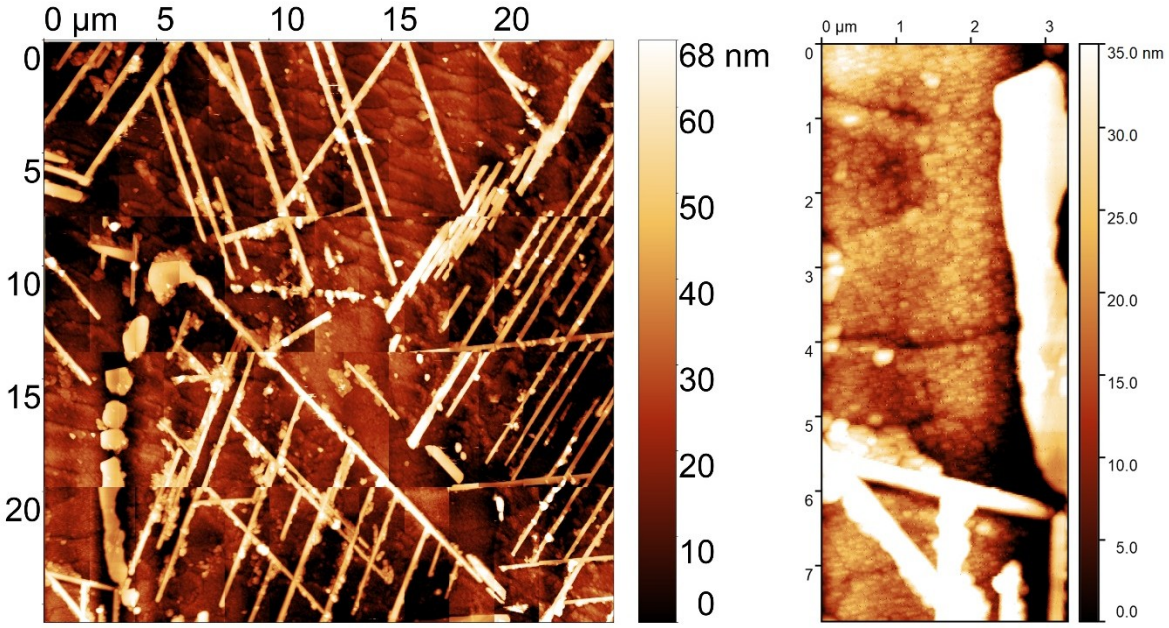


Figure 94: HS-AFM images of WQ900 showing the wavy lines previously observed in SEM images, as well as highlighting the effect of the blunt tip causing loss of edge definition of the δ phase needles.

4.7.4 Discussion

The technique of HS-AFM has been highly effective in producing nanoscale images of Inconel 718, especially with regards to imaging the smaller precipitates of γ' and γ''. Some key observations have been made, including the fact that γ'' is present across all of the samples, despite the HD and WQ900 heat treatments (or indeed both water quenching treatments) being designed to eliminate these. It was also possible to confirm that the wavy lines were indeed dislocation loops, rather than surface residue, as they were clearly shown to be topographical effects from HS-AFM images.

It has been assumed that it is the γ'' phase which is being observed from both the mottling effect as well as the nanometre-scale precipitates due to the line denoting its formation being the closest to zero on the temporal axis of the TTT diagrams; however, there may also be γ' present, but due to their small magnitudes, it is difficult to distinguish between their morphologies accurately, even with HS-AFM. Similarly, in the case of SEM, their similar masses mean that they have very little difference in electron contrast. In the future, atom probe measurements [241] could be used instead to determine whether both γ' and γ'' were present.

The fundamental conclusion which can be drawn from these investigations is the microstructure of Inconel 718 was much more complex, and difficult to manipulate, than expected from studying the TTT diagrams – both in terms of the variety of precipitates which can be present, as well as the differences which can be induced by even slight variations in processing conditions (taking the fact that the Datum V00 lines up more closely to the OGHD samples from the first batch of dodecagons). It may be the case that dual phase materials, such as Udimet 720Li and RR1000, may be more suitable for determining whether the V00 method will be able to quantify phase proportions within the family of nickel-based superalloys. Nevertheless, there was a definite microstructural contrast (especially in terms of the δ phase) generated between the samples, which was clearly manifested in the different measurements of V00. The consolidated micrographs from both SEM and HS-AFM, as well as data from the literature, were therefore compiled in order to investigate the effectiveness of the V00 technique for the phase estimation – specifically the δ phase proportion – present in Inconel 718.

4.8 Phase Estimation Trials of Inconel 718

The first step in estimating the amount of δ phase present involved finding the zeroth coefficient of the single crystal elastic constant, K00, of both the γ matrix as well as the δ phase. The main difficulty in terms of using these zeroth velocity coefficient results to estimate the phase proportions in the materials was the fact that, unlike those for the alpha and beta phase in titanium, the SCECs of each of the phases within Inconel 718 were not widely known, or available in the literature. It was therefore necessary to use the existing data acquired from the UWS experiments to attempt to estimate suitable values for both the γ and delta phases. Several different approaches were tested in estimating the amount of the δ phase present, which have been described in the following sections.

The various iterations of phase estimates were begun prior to the HS-AFM work taking place, and therefore without the knowledge that the γ'' phase was present; having confirmed this, the phase estimates were approached slightly differently (Trial 3 onwards), by assuming that this precipitate was present across all samples and therefore finding a homogenised K00 for the γ matrix – as well as any γ' and γ'' which were (or may be) present. The successful trials, which gave the most realistic proportions of the δ phase in the samples, are summarised at the end of this section.

4.8.1 SCECs of nickel for γ, and ImageJ estimates of δ

Initially, it was thought that the SCECs for nickel would be a suitable approximation for the main γ matrix. These were used, together with the density of nickel, in a code written in Wolfram (a symbolic computational language), which first utilised the Christoffel equation to find the wave speeds before using in the spherical convolution framework (in the forwards direction) to calculate the K00 value of nickel. The Christoffel equation for anisotropic media is given as follows [242]:

$$(\rho\omega^2\delta_{im} - C_{iklm}k_k k_l)u_m = 0 \tag{9}$$

The density of the material is represented by ρ, the k terms represent the wavevectors in the subscript axes directions, u is the displacement and ω the angular wave speed, δ_{im} is the Kronecker delta and the elastic stiffness tensor is represented as C_{iklm}. The derivation of this assumes homogeneous and pure anisotropic conditions [242]. The K00 of nickel was calculated to be 21056.7m/s.

This K00 of nickel was then used in conjunction with estimating the amount of the δ phase present in micrographs of the non-heat damaged 'OG' samples to back-calculate an estimate for the K00 of the δ phase. To estimate the amount of δ phase present, the image analysis software ImageJ [243] was used; after importing the micrograph, the image was 'smoothed' twice, set as a 32-bit type image, and then the colour threshold tool used to adjust the image such that the δ particles were shaded, as accurately as possible, with the background γ matrix being unshaded (or vice versa). The 'Analyse Particles' tool was then used to estimate the total amount of shaded (or unshaded) area. It was found that, for many of the micrographs, the precipitate area was overshaded (an example is shown in Figure 95 using the WQ900 sample), and thus the amount of the δ phase was being overestimated. It was also found that, even if the threshold image looked to have the correct amount of shading, the particle analysis did not necessarily correctly identify these areas, as shown for the Datum sample in Figure 96. Hence, to get as realistic a value as possible, the average of all values from the non-heat-damaged OG samples within a reasonable and realistic range (of only up to 5.1%, the maximum δ phase which may be expected after a standard ageing treatment [244]) was used.

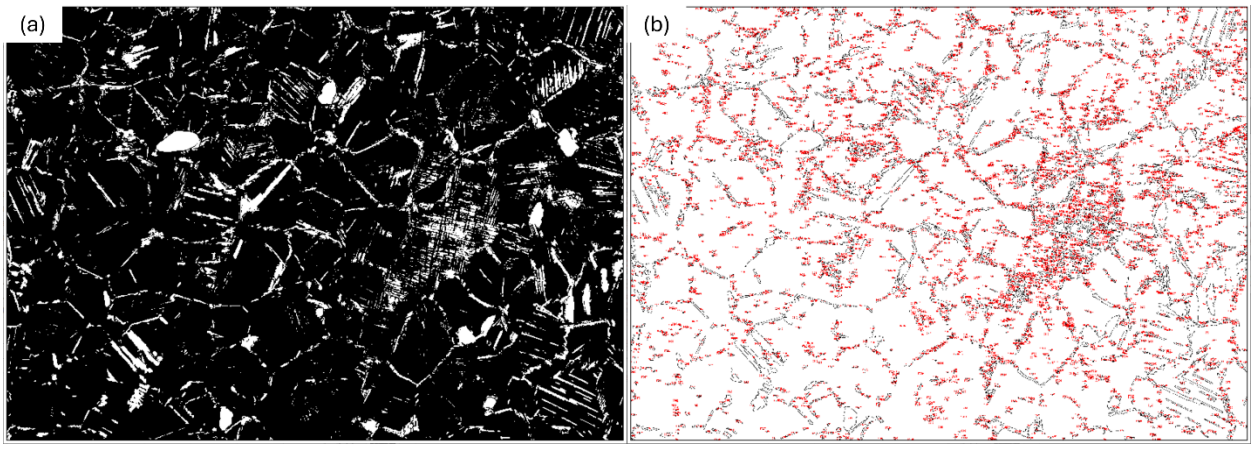


Figure 95: ImageJ analysis of a WQ900 micrograph, showing (a) the threshold adjusted image, and (b) the particles identified by ImageJ.

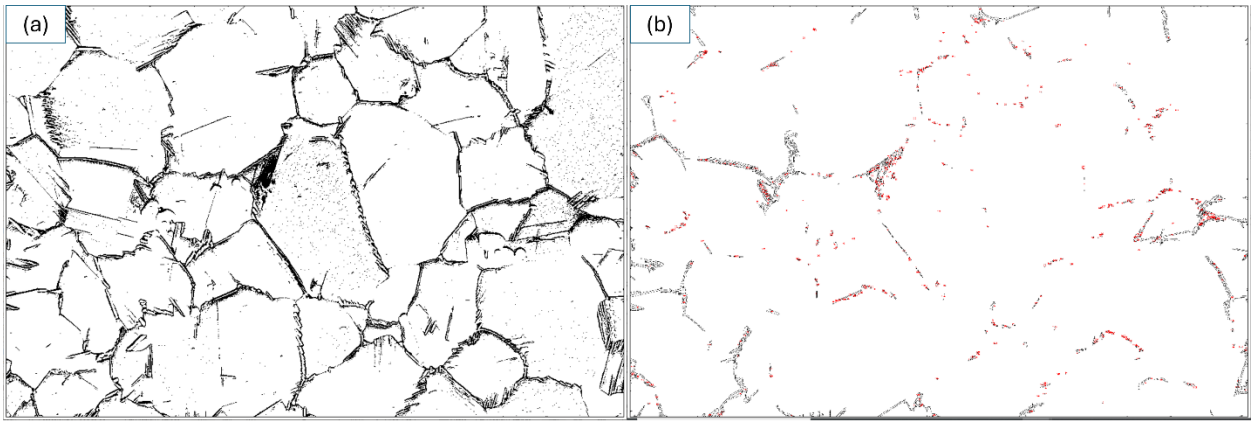


Figure 96: ImageJ analysis of a Datum micrograph, showing that the shading in the (a) colour threshold image has not been accurately analysed, where (b) shows the noticeable lack of many areas being identified as particles.

To determine if different tools within ImageJ could give more accurate results, an alternative method was trialled; the image was changed to a binary type micrograph, and setting the colour threshold (which in this case was done automatically) to attempt to obtain more accurate estimates of the percentage of δ phase present. However, the main drawback of using this method as opposed to the manual colour thresholding was that there was no control of the shading; if some images had the amount of δ phase over- or under-estimated, it could not be adjusted. Hence, despite the fact that there was a higher risk of inconsistency, the area fractions obtained using the manual thresholding technique were ultimately used.

Using an average of the δ phase proportion under 5.1% from across the OG (non HD) and Datum samples yielded 3.78%; this, in conjunction with Equation 7 and the K00 of nickel, was used to obtain the K00 value of 4210.42m/s for the δ phase. For reference the percentage of δ phase obtained are shown in Table 6 (with the data that were used to find the average in bold). Results from the binary method are included in the Appendix.

Even before attempting to predict the amount of δ phase in the RR Furnace set of samples, it was immediately apparent that the K00 values were erroneous; the δ phase K00 was significantly lower than the K00 of nickel, which was being used to represent the γ matrix. However, despite the ImageJ shading being inconsistent and therefore a source of error, it was the use of nickel to approximate the γ matrix which was incorrect in this instance. Although nickel did form the highest proportion of Inconel 718 in terms of chemical composition and had the same FCC crystal structure, the maximum amount of nickel and cobalt present should be no more than 50% [245], and therefore using the SCECs of nickel was in fact a poor representation of the single crystal elastic properties of

Inconel 718 (or indeed the γ matrix) itself. Hence the SCECs in the literature for Inconel 718 previously used for the deconvolution process [103] were used to estimate the K00 of the γ phase for the next trial.

Table 6: ImageJ estimates of delta phase percentages in Inconel 718 samples.

Sample	Micrograph	Predicted volume fraction of delta phase [%]
Aged	IN718_Datum_Aged_ETD_650x_03.tif	**3.042**
	IN718_Datum_Aged_ETD_1000x_04.tif	**5.008**
	IN718_Datum_Aged_ETD_1000x_05.tif	6.815
	IN718_Datum_Aged_ETD_5000x_06.tif	5.972
	IN718_OG3_Aged_ETD_500x_01.tif	8.961
	IN718_OG3_Aged_ETD_650x_02.tif	6.595
	IN718_OG3_Aged_ETD_650x_03.tif	10.309
	IN718_OG3_Aged_ETD_1000x_04.tif	8.442
Datum	Datum_5.00kV_0.10nA_5000x_ETD_04.tif	6.373
	Datum_5.00kV_0.10nA_5000x_T1_05.tif	8.247
	Datum_5.00kV_0.40nA_1000x_ETD_03.tif	7.499
	Datum_10.00kV_0.40nA_1000x_ETD_02.tif	6.342
FC900	900C_01_ETD.tif	16.41
	900C_02_ETD.tif	8.762
	900C_02_T1.tif	8.605
	900C_50h_500x_CA_BF.jpg	11.277
FC1000	1000C_10h_1000x_CA_DIC.jpg	3.803
WQ900	900C_ETD_SE_10.00kV_0.40nA_650x_01.tif	35.529
	900C_ETD_SE_10.00kV_0.40nA_1000x_02.tif	21.265
	900C_ETD_SE_10.00kV_0.40nA_5000x_03.tif	10.768
	900C_T1_A+B_5.00kV_0.40nA_1000x_01.tif	5.752

OG/Datum	AsReceived_04_ETD.tif	**4.838**
	AsReceived_04_T1.tif	**3.855**
	AsReceived_04_T2.tif	**4.825**
	AsReceived_05_ETD.tif	5.606
	AsReceived_05_T1.tif	11.703
	AsReceived_06_T1.tif	10.302
	AsReceived_ETD_SE_10.00kV_0.40nA_80x_01.tif	37.38
	AsReceived_ETD_SE_10.00kV_0.40nA_80x_02.tif	35.452
	NHT1_02_ETD_SE_1000x.tif	7.333
	NHT1_02_T1_A+B_1000x.tif	**3.906**
	NHT1_03_ETD_SE_1000x.tif	**2.93**
	NHT1_03_T1_A+B_1000x.tif	**3.231**
	NHT1_08_ETD_SE_500x.tif	**4.351**
	NHT1_08_T1_A+B_500x.tif	**4.156**
	NHT3_03_T1_A+B_500x.tif	**3.563**
	NHT3_04_T1_A+B_1000x.tif	**3.22**
	NHT4_03_ETD_SE_500x.tif	9.396
	NHT4_03_T1_A+B_500x.tif	**2.64**
	NHT4_04_ETD_SE_1000x.tif	8.549
	NHT4_04_T1_A+B_1000x.tif	**3.684**
	AsReceived_05_T2.tif	10.308
	NHT1_01_ETD_SE_1000x.tif	6.177
	NHT1_50x.tif	16.963
	NHT1_100x.tif	16.959
	NHT1_200x.tif	14.991
	NHT1_500x.tif	11.476
	NHT1_1000x.tif	12.508
	NHT3_50x.tif	22.23
	NHT3_100x.tif	13.794
	NHT3_200x.tif	12.665
	NHT3_500x.tif	12.307

	NHT3_1000x.tif	7.278
	NHT4_50x.tif	24.101
	NHT4_100x.tif	15.571
	NHT4_200x.tif	14.627
	NHT4_500x.tif	13.45
	NHT4_500x_2.tif	12.581
	NHT4_1000x.tif	7.597
	As_Received_500x_CA_BF.jpg	11.955
	As_Received_1000x_CA_BF.jpg	11.457
	NHD4.png	16.131

4.8.2 SCECs of Inconel 718 for γ, ImageJ estimates of δ

Having assumed that the K00 of Inconel 718 (20679.2m/s) represented that of the γ phase, together with the 3.78% estimate of δ phase gave a K00 of 17811.02m/s for the δ phase (where the K00 values are calculated by multiplying V00 by $\sqrt{4\pi}$, as previously shown in Equation 7). Although this K00 for δ was a significant improvement on the value predicted from Trial 1, it is still lower than the γ phase and hence still an incorrect estimate. It may be the case that the K00 of Inconel 718 was also an unsuitable approximation for the γ matrix; however, the fact that the ImageJ shading was highly inconsistent and inaccurate led to the decision to use an alternative approach which didn't involve the use of ImageJ area estimates. Instead, it was decided to use values reported in the literature of typical proportions of the δ phase for a given processing history, together with experimental data, to calculate the K00 of the individual phases.

4.8.3 Experimental V00 of HD and aged samples

For the third iteration of phase estimation trials, the prediction of K00 was attempted using a reverse approach, where first the HD samples would be used to estimate the K00 of the γ phase (as these should have 0% δ phase present) and then this used together with the average K00 value of the aged samples, to estimate the K00 of the δ phase, assuming a 4.2% percentage of δ phase (from average values reported in the literature for fully aged[13] Inconel 718 [244]). These K00 values

[13] Referred to in [3] as the standard ageing, or 'SA', process.

would then be used to estimate the amount of δ phase in the other samples. This approach has the additional advantage of giving essentially a 'homogenised' K00 value for the γ matrix which would include any γ' and γ'' particles present, as experimental data was used. The procedure and rationale for each step have been summarised in Table 7 for clarity.

Table 7: Phase estimation methodology and rationale.

Step	**Rationale**
Average of all OGHD sample V_{00} (OG1HD, OG2HD, OG4HD) to find K00 of γ phase	• WQ1000 still likely to have some γ' and γ'' present (and slightly higher K00 due to this) • Using K00 for nickel is unrealistic – according to AMS 5662, the %Ni + Co is maximum 50% • Values of K00 for γ using averages of OGHD samples are much better aligned with Inconel 718 K00 as calculated from Wolfram Alpha (as opposed to nickel)
Use V00 of aged samples' average, and assume a 4.2% delta to estimate a K00 of delta using above K00 of γ	• OG3A condition is likely to be closest to as-spec standard (as it has been solution treated and aged) as opposed to OG3, OG4 and Datum
Use the K00 of γ and delta found in this way to estimate % delta phases in other samples	

It was found that the K00 of the γ matrix found using this approach did align closely with that of Inconel 718 (as opposed to nickel alone). In addition, the K00 values of the γ and δ phase were much further apart, which was promising given that values further apart may result in more accurate phase estimations [104], and the K00 of the δ phase was higher than the γ phase was also as expected.

The final K00 values calculated for each phase are shown in Table 8, with the results of the phase estimates shown in Table 9; samples with clearly erroneous δ phase estimates are highlighted. The estimates for the amount of δ phase within those samples which had been used to find the K00 of

each phase in the first place have also been included, but the cells shaded, as a sanity check of these values (and investigating whether the K00 calculated for each phase worked well).

Table 8: K00 of gamma and delta phases (estimated using experimental data).

Variable	Value [m/s]	Method
K00 γ	20356.63	Average of V00 values from OG1HD, OG2HD, OG4HD
K00 δ	24834.98	Using above K00 γ, assuming 4.2% delta in both aged samples

Table 9: Estimates of δ phase proportion within samples, for Trial 3.

Sample	K00 [m/s]	% δ phase
OG3	20414.41	1.29
OG4	20418.67	1.39
OG3A	20558.74	4.51
Datum	20353.80	-0.06
DatumA	20530.71	3.89
FC900	20514.03	0.31
WQ900	20370.46	2.11
FC1000	20570.04	3.51
WQ1000	20450.93	4.77

The phase estimation trials carried out here highlighted a few limitations of the use of V00 to estimate the δ phase proportion in these Inconel 718 samples. Both WQ900 and FC900 had lower K00 values than would be expected from their high amount of the δ phase, and thus the proportion of this precipitate has been underestimated by a large extent. These samples have also clearly demonstrated that there is not a straightforward, positive correlation between the amount of a stiffening precipitate and the V00. WQ1000 is another sample with an erroneous amount of δ phase predicted, of 4.77% when it should theoretically be much nearer to zero. This sample may have been impacted by the fact that γ'' (and potentially γ') are still present, giving a slightly higher V00

than expected. The Datum sample result is also very clearly incorrect, due to its K00 being lower than that of the γ matrix; this meant that phase estimation would ultimately not be possible using these K00 values for the γ and δ phases (Table 8). A summary of these issues is presented in Table 10.

However, there still seemed to be good estimates of the proportion of δ phase present within the samples FC1000, OG3 and OG4. For FC1000, the amount of δ phase seemed reasonable, and corresponded to the δ phase having reprecipitated on the grain boundaries. For the samples OG3 and OG4, the results could be explained by their not being fully aged, and hence their lower percentages of the δ phase were due to their not being fully formed. The higher percentage of the delta phase in sample FC1000 could be rationalised by its being held at a higher temperature than the aged samples, potentially allowing more time for the δ phase (albeit in addition to other precipitates) to form in comparison to the OG samples.

Table 10: Summary of results and possible explanations for not meeting predicted values.

Sample	**Issue**	**Explanation**
Datum	Negative % delta	K00 is lower than γ phase
FC900, WQ900	Lower than expected % delta	Delta phase has formed within grain boundaries, resulting in a retarding effect on the wave speeds
WQ1000	Higher % delta than expected	Potentially γ' and γ'' present (as opposed to HD samples, much higher hold temperature + fast cool)

4.8.3.1 Variants of Trial 3

The method outlined in Trial 3 was investigated further with a number of variations; namely, through using the K00 values of individual samples in different combinations, to investigate whether any of these would give more realistic estimates for the amount of the δ phase present. Although it is typically good practice to use an average across several experimental values, in this case there were no reference data for the K00 of the individual γ and δ phases, and there was the possibility that a particular sample's K00 value was closer to the 'true' value of a phase (for example, it may be the case that the K00 of OG4HD alone is more accurate to represent the γ phase, rather than the

average across all HD values), especially with the 28m/s range in the calculated K00 from OGHD experimental data.

The various combinations of values trialled are summarised in Table 11 below, with the results following in Table 12; the variants generating realistic estimates have been highlighted.

Table 11: Trial 3 Variants.

Variant	**K00 γ**	**K00 δ**
(A)	OG4HD	Average of OG3A/DatumA
(B)	OG1HD	
(C)	Average of HD samples	OG3A
(D)		DatumA
(E)	OG1HD (=OG2HD)	OG3A
(F)		DatumA
(G)	OG4HD	OG3A
(H)		DatumA

Table 12: Results of Trial 3 Variants.

Variant	(A)	(B)	(C)	(D)	(E)	(F)	(G)	(H)
Sample	**% Delta**							
OG1HD	0.38	0.00	0.13	0.15	0.00	0.00	0.35	0.41
OG2HD	0.38	0.00	0.13	0.15	0.00	0.00	0.35	0.41
OG4HD	0.00	-0.42	-0.25	-0.29	-0.39	-0.45	0.00	0.00
OG3	1.47	1.19	1.20	1.39	1.11	1.29	1.37	1.58
OG4	1.55	1.29	1.29	1.50	1.20	1.40	1.45	1.67
OG3A	4.49	4.52	4.20	4.88	4.20	4.90	4.20	4.83
Datum	0.19	-0.20	-0.06	-0.07	-0.19	-0.22	0.18	0.21
DatumA	3.91	3.88	3.62	4.20	3.60	4.20	3.65	4.20
WQ900	0.54	0.18	0.29	0.33	0.17	0.19	0.51	0.58
WQ1000	2.23	2.04	1.96	2.28	1.89	2.21	2.09	2.40
FC900	3.56	3.49	3.27	3.80	3.24	3.78	3.32	3.82
FC1000	4.73	4.78	4.43	5.15	4.44	5.18	4.42	5.09

All of the variants generated erroneous results for the WQ900 sample, giving δ phase proportions much lower than observed in micrographs; however, this was not unexpected, as the V00 of this sample was significantly lower than expected (and indeed, lower than the OG samples before heat treatment). The variants (A), (G) and (H) are the only iterations without negative percentage of δ predicted – this was due to the V00 for OG1HD and OG2HD being higher than that of OG4HD and the Datum sample.

For all three of these realistic variants, the differences between the estimated proportions are of a very small order, and the aged samples both have predicted δ phase amounts which line up well with the average of 4.2% – for DatumA, between 3.65% and 3.91%, and for OG3A between 4.20% and 4.83% (though variant (G) did use OG3A as the K00 for δ phase, resulting in the exact value of 4.20%). In addition, the percentages of δ phase in the WQ1000 sample of between 2.09% and 2.40%, were originally thought to be erroneous; however, it was subsequently found that this in fact aligns well with the literature reported value of having around 3% δ phase [156] (despite this heat

treatment being given specifically to eliminate all precipitates). Azadian et al. [156] reported expected volume fractions of the δ phase given a specific heat treatment temperature and hold time, where it was predicted that processing similar to that of WQ1000 would result in a δ phase percentage composition of around 3%, rather than the 0% intended, as shown in Figure 97.

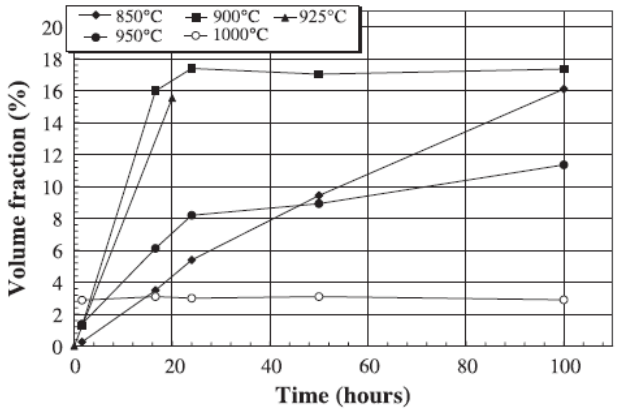


Figure 97: Expected amount of delta phase for various temperatures and times [156].

A further result from these three variants is lower proportion of the δ phase than expected for the Datum sample, though this was inevitable with the low value of V00 measurements; this may be indicative of incomplete or incorrect processing as to have not allowed the δ phase to fully precipitate. Finally, all three of these variants have predicted a δ phase proportion in the HD samples close to 0%. Overall, however, variant (A) seems to have the best compromise across the samples, with the aged samples being closest to 4.2%, a WQ1000 of close to 3%, and with OG1HD and OG2HD close to zero; it was concluded that the K00 values using this variant generated the most realistic results for the proportion of δ phase for this trial.

4.8.4 Simultaneous equations using experimental data and theoretical δ volume fraction

Having generated δ phase estimates which aligned well with the 3% δ phase for the WQ1000 sample as reported in the literature, this was taken into consideration when determining the process for the following (4th) trial, using a simultaneous equation with the K00 of both the WQ1000 and WQ900 samples, and 3% and 17% volume fractions of δ phase respectively [156], to solve a simultaneous equation for the K00 of both γ and δ phases. Again, this method would essentially be generating a homogenised K00 value for the γ phase which would account for any γ'' present across

all samples Although the K00 values for the phases themselves seemed reasonable, with K00 γ and K00 δ being 19889.79m/s and 20468.36m/s respectively, when used for predicting the amount of δ phase it was clear that these were erroneous, with some samples being predicted a proportion of over 100% (see Table 13). This was therefore deemed an unsuitable method for the prediction of K00 values, and subsequent δ phase proportions.

Table 13: Phase estimates from Trial 4.

Sample	**% δ**
OG1HD	81.73
OG2HD	81.73
OG3	90.68
OG4	91.41
OG3A	115.62
OG4HD	78.61
Datum	80.20
WQ900	83.08
WQ1000	96.99
FC900	107.89
FC1000	117.57
DatumA	110.78

4.8.5 Simultaneous equations using experimental data only

The next attempt was based on Trial 4, still using a 17% δ phase with the experimental V00 value of WQ900 but instead with a 0% δ phase together with the experimental value of WQ1000 – essentially meaning that the K00 of WQ1000 was assumed to be that of the γ phase. Although this was not the 3% volume fraction predicted from the literature [156], it was still investigated as the initial intention of the WQ1000 heat treatment was to eliminate the δ phase completely. In addition, it was thought that the WQ samples should have the most well-known microstructures due to the fact that the processing was done entirely internally, so the microstructures would be close to as intended. However, the fact that the WQ900 sample had a lower V00 than the WQ1000 sample

meant that the predicted K00 values for each phase would be unrealistic and incorrect; indeed, any technique which used the WQ900 sample to determine the K00 of the δ phase would not be successful, due to its extremely low K00. The results from this trial have been included here in Table 14 below, with the K00 for the γ and δ phase being 20450.93m/s and 19977.58m/s respectively; the fact that the K00 for the δ phase was found to be lower than that of the γ phase was an immediate indicator that the results from this trial would be unsuitable.

Table 14: Phase estimates from Trial 5.

Sample	**% δ**
OG1HD	18.65
OG2HD	18.65
OG3	7.71
OG4	6.81
OG3A	-22.78
OG4HD	22.47
Datum	20.52
WQ900	*17.00*
WQ1000	*0.00*
FC900	-13.33
FC1000	-25.16
DatumA	-16.85

4.8.6 Experimental data of WQ1000 and aged samples with theoretical δ volume fraction

Continuing with the use of WQ1000 and 0% δ phase to be the K00 of the γ phase, Trial 6 returned to the use of the aged samples with the 4.2% δ phase [244] to investigate whether the estimate of WQ1000 having 0% δ phase could be taken further. The variants (A) and (B) in this case were the use of each of the individual aged samples' K00 to calculate the K00 δ, as well as the average of the two. Table 15 shows the K00 of the individual phases found for this trial and its variants, with Table 16 showing the results of the phase proportion estimates themselves; this was ultimately an

unsuitable technique for estimating the amount of δ phase, as immediately apparent from the negative percentages predicted.

Table 15: K00 of delta phase from Trial 6 and variants.

Trial	**Sample(s) for K00 δ**	**K00 δ [m/s]**
Trial 6	Average of OG3A, DatumA	22684.17
Trial 6A	OG3A	23017.82
Trial 6B	DatumA	22350.51

Table 16: Estimates of delta phase proportions from Trial 6 and variants.

Trial	**6**	**6A**	**6B**
Sample	**% δ phase**		
OG1HD	-3.95	-3.44	-4.65
OG2HD	-3.95	-3.44	-4.65
OG4HD	-4.76	-4.14	-5.60
OG3	-1.63	-1.42	-1.92
OG4	-1.44	-1.26	-1.70
OG3A	4.83	4.20	5.68
Datum	-4.35	-3.78	-5.11
DatumA	3.57	3.11	4.20
WQ900	-3.60	-3.13	-4.24
WQ1000			
FC900	2.83	2.46	3.32
FC1000	5.33	4.64	6.27

4.8.7 OGHD sample(s) for γ, and WQ1000 with 3% δ phase for δ

Having used the WQ1000 sample with 0% δ phase for the previous two trials and not been successful, the final combination of results used for a trial reverted to using the reported 3% δ phase in WQ1000 to find the K00 of the δ phase, having used the OGHD sample(s) to first estimate

a K00 for the γ phase. The K00 values for each phase as well as the resulting δ phase proportions are shown in Table 17 and Table 18 respectively.

Table 17: K00 values from Trial 7 and variants.

Trial	Sample(s) for K00 γ	K00 γ [m/s]	K00 δ [m/s]
Trial 7	OG1HD, OG2HD, OG4HD	20356.63	23499.78
Trial 7A	OG1HD	20362.66	23304.93
Trial 7B	OG4HD	20344.58	23889.49

Table 18: Estimates of delta phase proportions in samples from Trial 7 and variants.

Trial	7	7A	7B
Sample	**% δ phase**		
OG1HD	0.19	0.00	0.51
OG2HD	0.19	0.00	0.51
OG4HD	-0.38	-0.61	0.00
OG3	1.84	1.76	1.97
OG4	1.97	1.90	2.09
OG3A	6.43	6.66	6.04
Datum	-0.99	-0.30	0.26
DatumA	5.54	5.71	5.25
WQ900	0.44	0.27	0.73
WQ1000	3.00	3.00	3.00
FC900	5.01	5.14	4.78
FC1000	6.79	7.05	6.36

Of the variants of Trial 7, it was found that variant (B), which used solely the OG4HD sample to estimate the K00 of the γ phase, yielded a realistic set of δ phase proportions, with no negative values – although, compared to those results from Trial 3A, G and H, the amount of δ phase in the HD samples as well as in the aged samples is slightly higher than what was expected.

4.8.8 Discussion and Summary

Of the various combinations of data and literature values attempted, there were four which were successful in that they gave realistic estimates of the δ phase across all samples (except for WQ900, as discussed), with no negative values. These have been summarised in Table 19 below. The K00 values for the γ and δ phase used for these trials are also shown in Table 20; despite there being no data in the literature for the SCECs of these individual phases, these trials have helped to identify a rough range of K00 values that these phases could be expected to have, which has been an additional useful outcome of this investigation.

Table 19: Trials with realistic estimates of delta phase in Inconel 718.

Variant	**3A**	**3G**	**3H**	**7B**
Sample	**% δ phase**			
OG1HD	0.38	0.35	0.41	0.51
OG2HD	0.38	0.35	0.41	0.51
OG4HD	0.00	0.00	0.00	0.00
OG3	1.47	1.37	1.58	1.97
OG4	1.55	1.45	1.67	2.09
OG3A	4.49	4.20	4.83	6.04
Datum	0.19	0.18	0.21	0.26
DatumA	3.91	3.65	4.20	5.25
WQ900	0.54	0.51	0.58	0.73
WQ1000	2.23	2.09	2.40	3.00
FC900	3.56	3.32	3.82	4.78
FC1000	4.73	4.42	5.09	6.36

Table 20: K00 values of each phase for the successful phase estimate trials.

K00 [m/s]	Trial			
	3A	3G	3H	7B
Gamma	20344.58	20344.58	20344.58	20344.58
Delta	25109.90	25443.55	24776.24	23889.49

Across the four successful trials of δ volume fraction estimations, the V00 of OG4HD was used for the γ phase. It was likely that this was the optimum value for the γ phase due to its being the lowest of all the HD samples, so there would be the maximum difference possible between the K00 of the γ and δ phases, and the least likely to result in negative phase proportion estimates. The HD heat treatment temperature was also above the δ solvus temperature of 1000°C [182] [246] so it was the most likely material condition to be free of the δ phase, and hence the best data to use to estimate a K00 for the γ matrix (or, as the case may be, a homogenised value for the γ matrix with any γ'' which may have remained or being on the cusp of formation).

The K00 values calculated for the δ phase ranged between 23889.49m/s and 25443.55m/s. Although the percentages of δ phase predicted only vary by small amounts across these trials, Trial 3A still appears to be the best compromise of all the values; the amount of δ phase in the HD samples is close to 0%, the aged samples close to the 4.2%, and WQ1000 sample predicted to be similar to the 3% as reported in the literature. The FC1000 sample is also predicted a similar value of the δ phase, which is also promising given the same hold temperature and time.

It should be noted, however, that these trials were ultimately estimates only, due to some uncertainties involved; for example, the OGHD samples had slightly different K00 values. (The fact that these were very different to WQ1000 was also a cause for concern, until it was subsequently found that WQ1000 would have around 3% δ phase.) It was also apparent that the technique may not be applicable in all conditions of Inconel 718, for example when there has been excessive precipitation of the δ phase; the WQ900 had such a low V00 that any phase estimate attempts for this sample were highly inaccurate. It is still the working theory that this is due to lack of solid solution strengthening, where the excessive δ phase is removing the solid solution strengthening atoms via its precipitating; there were no other microstructural properties or phenomena which were detected from SEM or HS-AFM which suggested alternative reasons due to microstructural

irregularities. This low V00 of WQ900 also meant that any trials using this sample to predict a K00 for the δ phase (such as Trial 4) would generate erroneous results across all of the samples, and thus ruled out one potential avenue of investigation for finding K00 of the phases themselves.

A further uncertainty was the fact that the percentages of δ phases used to find the K00 of this phase were from literature estimates, and it may be the case that the samples tested for this study had slightly different amounts of this precipitate present. The fact that it was not possible to use ImageJ in predicting the amount of δ phase present due to its inconsistency and inaccuracy meant that it was not possible to have a visual comparison or verification of the predicted amounts of the δ phase being calculated. High resolution EBSD scans were carried out to attempt to accurately quantify the proportions of the various phases present, but there were several issues encountered when attempted these scans; there appeared to be large amounts of drift when setting the scan to a high resolution, which meant that imaging was not successful; conversely, if lowering the resolution, there did not appear to be sufficient contrast to detect the δ phase. It was therefore decided that the use of EBSD would be revisited following investigations into the other nickel-based superalloys proposed for this project. Nevertheless, as there was no previously validated data on the K00 of the phases, it was useful to be able to calculate a range of values which could be used for future phase estimates on different samples of Inconel 718.

These investigations of Inconel 718 highlighted some interesting aspects regarding the use of V00 measurements for phase composition estimation, such as the effect that the extent of formation of a precipitate may have on the measurements; for example, the γ'' not being fully precipitated in the heat damaged samples clearly had a lower impact on the overall wave speeds, such that they were sufficiently removed from those of other materials which had been subjected to different processing. The δ phase in WQ900 did have a drastic effect on the wave speed measurements which was clearly observable, but its result was ultimately too low to be used for predicting the volume fraction of the δ phase present; it was clear that the more of a strengthening precipitate did not necessarily mean a higher V00, and the cause of this would be an interesting investigation to pursue in the future.

Throughout these experiments and investigations, it has become apparent that the microstructure of Inconel 718, and its behaviour depending on different processes it has undergone, is far from straightforward; it has transpired that even though there is a theoretical region of the TTT diagram where the δ phase is the only precipitate present, the WQ1000 treatment was not sufficient in

removing this precipitate completely. In addition, the quenching/cooling process may not be sufficient in preventing the γ'' phase from re-precipitating.

Indeed, there are aspects of the γ'' precipitate itself which add to complications; although it is generally assumed that these precipitates have a stoichiometric composition of Ni_3Nb, there are often differences in values quoted in literature of γ'' volume fractions [197] [247] [248] due to the fact that the γ'' does not only contain niobium but can also include other elements such as molybdenum and titanium [227] [228] as well as aluminium [249]. (This is also the case for the γ' phase, which can also contain iron and chromium [250].) Despite their differing morphologies (where the γ'' is disc-shaped, and the γ' more spherical), it can also be difficult to distinguish between γ' and γ'', and hence determine the exact ratio of volume fractions; although these were not the phases of focus in the estimates carried out here, it may be relevant for future investigations.

In summary, as this phase estimation technique can only be deployed effectively for dual phase materials, it has been the case that the more complex microstructural characteristics of Inconel 718 has made trials of the UWS phase characterisation technique more challenging than expected. Nevertheless, it was found that the phase estimates could be successfully deployed in some instances, and there have now been generated a set of K00 values for the γ and δ phase which could be used for rough δ phase approximations in the future. An additional point to note is that these variations could be detected even when they were so small (i.e. between 4.2% for the aged samples, compared to 0% in the heat damaged), which is a promising aspect of this technique which has been demonstrated.

However, it was decided that for further investigations, a purely dual phase material may be optimal in assessing the sensitivity and accuracy of using the UWS technique for phase estimation. Of the variety of nickel-based superalloy candidates, Udimet 720Li and RR1000 were chosen to be investigated next.

5. Application of UWS Technique to Udimet 720Li and RR1000

5.1 Introduction

This final chapter concerning the EngD research is divided into two sections; the first concerns the UWS experiments and concurrent microstructural investigations using discs of Udimet 720Li, and the latter details the research carried out using RR1000. Both of these nickel-based superalloys have dual phase microstructures, with purely the γ' phase present within the γ matrix, but have different chemistries and processing methods – and hence slight variations in mechanical properties. The samples of Udimet 720Li, originating from the same billet, were used to determine whether the UWS measurements could detect the minor microstructural variations typically found across a billet of this material; in the case of RR1000, three different discs subjected to different processing conditions (to create fine and coarse grain microstructures, as well as in its as-forged state) were used. It was also of interest to observe the differences in UWS measurements due to the microstructure's homogeneity resulting from the powder metallurgy processing of RR1000. For each material there is a brief summary of its chemistry and processing, followed by the experimental results and discussion to bring together the findings for each material.

5.2 Udimet 720Li – Microstructure, Processing and Properties

Udimet 720Li is a nickel-based superalloy developed in the late 1970s [251], and exhibits one of the highest temperature capabilities (around 730°C) amongst other Ni-based disk alloys [252], including high creep strength and resistance to low cycle fatigue [253]. It was developed as both a cast/wrought alloy and a powder metallurgy alloy [254] [255] [256] [257], though the cast/wrought manufacturing route is more advantageous in terms of cost. Unlike Inconel 718, it is a purely γ' strengthened alloy; it is one of the most successful alloys for high temperature applications (i.e. for temperatures above 650°C), where time dependent damage processes such as creep and creep-fatigue crack propagation may be encountered in the rim, hence requiring increased grain sizes [258]. It is for this reason that this superalloy has been chosen for a wide variety of industrial applications [259], despite being susceptible to quench cracking – a result of its relatively high γ'

content (one of the highest among wrought nickel-based superalloys [260]), of around 45% [261] [262].

Another key difference from Inconel 718 is the presence of a higher number of alloying elements [253]. The chemical composition of U720Li is shown in Table 21 [260], and is a slight modification of Udimet 720. Udimet 720 itself is also a γ' hardenable nickel-based superalloy, with high strength and corrosion resistance [251]. It was originally developed for land based gas turbine blades, and was one of the highest alloyed disk materials that could be processed along the traditional cast and wrought route [257]. It has many superior properties in comparison to other nickel-based superalloys – for instance, it demonstrated superior stress corrosion resistance in low temperature (of around 700°C) sulphate and chloride environments compared to IN738 [251], and retains a much higher percentage of its rupture life in saline environments than Udimet 710, U500, IN738 and IN939, due to its chemistry and resulting grain boundary precipitates [251]. This chemistry also gave the material enhanced impact resistance in long term service [251].

5.2.1 Chemistry and Heat Treatments

The main difference in chemical compositions of Udimet 720Li and Udimet 720 is the reduction in levels of chromium, carbon and boron [263]; it was found that Udimet 720 was susceptible to the formation of the detrimental sigma (σ) phase, which caused degradation during high temperature service [264], and hence the chromium content in Udimet 720Li was reduced to reduce the likelihood of this occurring [17]. There are also lower levels of carbon and boron, which facilitate the use of secondary melting techniques for ingot conversion prior to forging – hence avoiding the need for powder processing [17]. The 'Li' denotes 'low interstitial', referring to its improved phase stability as well as a reduced propensity to form TiN and TiCN inclusions [31] [252] [265], which can cause 'white spots' from which fatigue cracks can initiate, and cause catastrophic failure. An example of a carbonitride is shown in Figure 98 below.

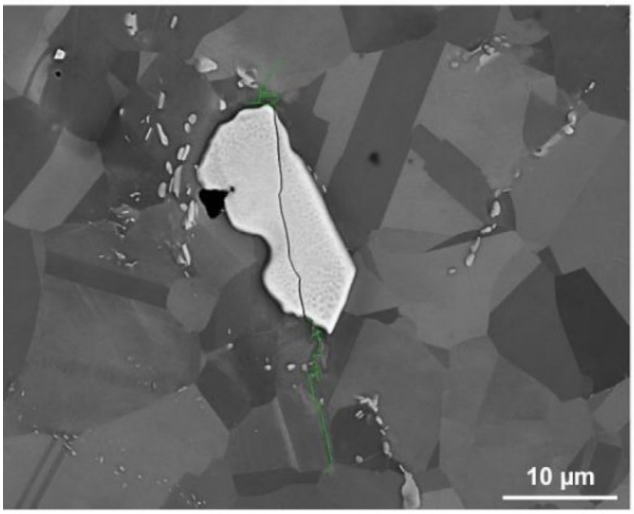


Figure 98: A carbonitride in a nickel-based superalloy, where the crack propagation path is shown in green running from the bottom of the particle. [266]

As well as a slight variation in chemical composition, the heat treatment of Udimet 720Li is slightly different to that of Udimet 720; the standard heat treatment for the latter [17] begins with a sub-solvus solution treatment at 1105°C for 4 hours (during which time the unsolutioned γ' prevents γ grain growth through Zener pinning [251], which is the phenomenon where a dispersion of fine particles affect grain size distribution through the influence of grain boundary movement [267]). This is followed by a quench to ambient temperature, typically in oil, the stage where it is claimed that the fine carbides and borides precipitate at the γ grain boundaries [268]. The process finishes with a 2-stage age of 24 hours at 650°C, followed by 16 hours at 760°C, concluding with an air cool.

Over the years, however, necessity of a dual stage ageing treatment for Udimet 720Li was questioned, as the microstructural response and changes in properties did not appear to warrant this – further studies showed that a modified heat treatment of 24 hours at 700°C gave tensile and hardness properties comparable to, or even better than, those exhibited by materials undergoing the 'standard' heat treatment, as well as improved creep properties at temperatures in the vicinity of 750°C [17]; the standard dual stage age also appeared to leave the tertiary γ' in the overaged condition for Udimet 720Li [17]. Thus the modified heat treatment has since been adopted, with the additional advantage that there is only one ageing step.

Table 21: Chemical composition of Udimet 720Li.

	Cr	Co	Mo	Ti	Al	B	Zr	Fe	Ni
720Li	16.0	14.4	3.02	5.07	2.70	0.016	0.04	0.013	Bal

The presence of Ti and Al among the alloying elements in Udimet 720Li (as seen in Table 21) allow the formation of the γ' phase, as its main constituents [260]; the contribution of this precipitate, as well as its various morphologies and characteristics, are discussed in the following section.

5.2.2 The gamma prime (γ') phase

Of the various high temperature, stable intermetallic phases such as the γ' ($Ni_3(Al,Ti)$), γ'' (Ni_3Nb) and eta, or η (Ni_3Ti) [269] (to which the superior high-temperature strength of wrought Ni-based superalloys is generally attributed, along with solid solution strengthening in the γ matrix [260]), the γ' phase has an advantage due to several reasons [119] [270] [271]; it can precipitate coherently with the γ matrix phase, and the solubility limit of its alloying elements is large (meaning that solid solution strengthening can be fully used). Much like the other nickel-based superalloys, the mechanical behaviour (including the plastic strain rate and ductility) of Udimet 720Li is greatly affected by the grain size and precipitation distribution within it [258].

5.1.2.1 Primary, Secondary and Tertiary γ'

The γ' phase is the dominant precipitate within Udimet 720Li, but its size and morphology varies depending on the processing it has undergone. These forms can be categorised into primary, secondary and tertiary, with the main differentiating factor being their size. The improvement of high-temperature strength of wrought Ni-based superalloys with a γ/γ' two phase microstructure depends strongly on the final precipitation microstructure of the γ' phase [260], and there has been much research conducted towards obtaining optimal microstructures which promote high temperature strength by tailoring the volume fraction, particle size and precipitation density of the γ' phase in its various forms [272] [273] [274].

Following a 'standard' heat treatment, the γ grain size is around 10um, and particles of γ' which have remained undissolved during the solutioning stage which delineate the grain boundaries are referred to as the primary γ' precipitation; this occurs when the solutioning temperature is below

the γ/(γ+γ') solvus, or the 'subsolvus' temperature [17] [260]. The primary γ' prevents γ-grain growth during solutioning [17].

Intragranular γ' precipitates form upon cooling, and exhibit a bimodal distribution; secondary γ' is intragranular, with diameters between 90 and 200nm, and tertiary γ' is similarly intragranular but with a particle diameter below 90nm. A schematic of the various γ' morphologies is shown in Figure 99 below.

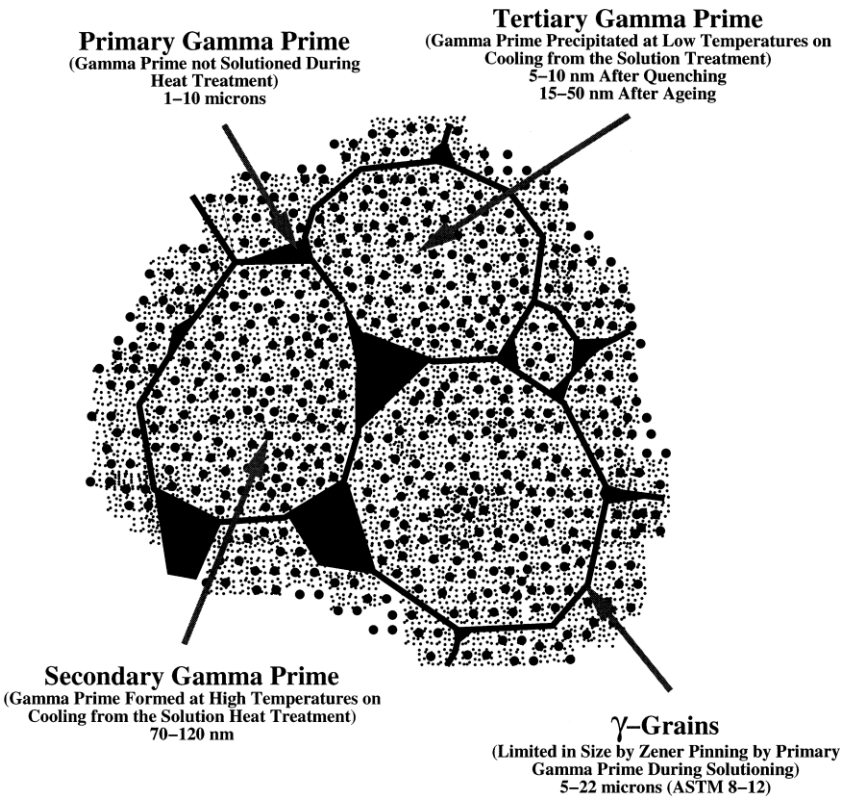


Figure 99: Size distributions of gamma prime precipitates in Udimet 720Li. The secondary γ' are the larger particles within the grains, with the tertiary being the smaller speckles of precipitate. [17]

The bimodal distributions of intragranular γ' is a result of the varying cooling rates during continuous cooling following the solutioning process [260] [17]; initially, during quenching from the solutioning temperature, the particles of secondary γ' nucleate in the supersaturate matrix of γ, but as the temperature decreases further the growth of secondary γ' occurs with partitioning of the solutes into the surrounding matrix. Eventually, the diffusion rates of the solute slow, and the γ' particles cannot grow fast enough to keep the matrix supersaturation low; at a critical undercooling, the driving force for nucleation is sufficient to allow the nucleation of tertiary γ' to occur. It can thus be deduced that solutioning a larger amount of primary γ' results in higher levels

of secondary and tertiary γ' being precipitated on cooling; this manifests itself as an increase in hardness [17].

The size of the secondary γ' precipitates depends strongly on the cooling rate from the solutioning temperature, and consequently this cooling rate strongly influences the hardness of the final material [17] (as it has been found that a smaller secondary γ' distribution – from a faster cooling rate – together with fine tertiary γ', hence giving a higher overall volume fraction of γ', improves the material's hardness [260]). Indeed, it appears that the cooling rate has the greatest impact on the size of the secondary γ' phase [260] – and for the very highest quench rate, it appears that the sizes of secondary and tertiary γ' are broadly similar [17]. However, the gain in properties which can be achieved with altering quench rates is limited by the increased risk of quench cracking, and generation of excessive residual stresses [17]; hence, despite the consensus that an increase in cooling rate improves the tensile strength [275], the severity of the cooling rate which can be used in reality is limited. An additional observation is that the secondary γ' size does not appear to be affected during ageing, whereas the tertiary γ' appears to coarsen (albeit selectively); it has been found that ageing at a temperature of 700°C for 24 hours leads to optimum properties [17].

It has also been found that the morphology of the secondary γ' phase can vary, depending on the cooling rate and the overall volume fraction of the γ' phase [260] – in general, the shapes after solution treatment and/or the subsequent ageing treatment are spherical, cuboidal or 'intermediate', but for nickel-based superalloys with high volume fractions of γ' (over 30%, such as the case with Udimet 720Li) there is an additional, more complex 'octodendritic' morphology which may be observed [170] [276], as shown in Figure 100. A specimen of Udimet 720Li cooled quickly (i.e. by oil quenching) showed secondary γ' with a spherical morphology, which evolved to a cuboidal and/or an octodendritic shape if the cooling rate was slowed (for example, through furnace cooling) [260].

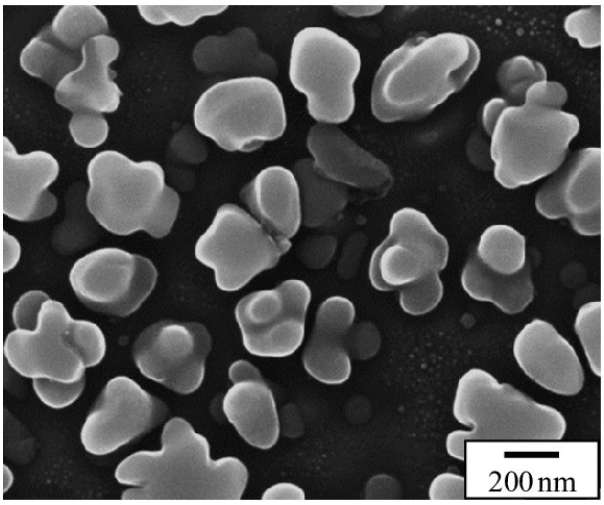


Figure 100: An example of the octodendritic morphology of γ' in Udimet 720Li. [277]

Although the γ' is the main strengthening property of Udimet 720Li, it should be noted that other microstructural characteristics, such as grain boundaries themselves, should not be neglected. Studies have shown that these grain boundaries can influence the creep-fatigue behaviour and damage processes at elevated temperatures, depending on the microstructure, as the crack initiation and the first propagation stages are intergranular [258].

5.2.3 Challenges for inspection

Udimet 720Li is one of the most difficult nickel-based superalloys to inspect; the microstructure can be widely variable, even within one billet; in hot-forged billets, it has been found that the microstructure near the surface generally differs from its inner regions [270] [278]. The microstructure of the material in the billet condition, particularly the γ' distribution, is particularly important for the final microstructure of a disc, as the forging is carried out below the γ' solvus temperature [253]. The nature of the criticality of the components that Udimet 720Li is used for (such as high pressure disks in both aerospace engines and land-based gas turbines [258]) warrants a robust inspection method, to ensure that the microstructure has not been altered during operation in a detrimental manner.

In contrast to Inconel 718 and other nickel-based superalloys, the microstructure of Udimet 720Li is much more sensitive to (and has a much greater dependence on) various processing parameters, such as temperature, strain rate and total strain [253]. As such, these must be controlled very carefully to obtain the desirable mechanical properties throughout any portion of a disk being

fabricated, which can be particularly difficult during a cast/wrought process [253]. An additional point to note is that the design of such components is mainly based on low cycle fatigue (LCF) criteria, and resistance against disk burst [119] [279]. Both the deformation resistance and microstructure behaviour are important for disk production, as the former restricts the disk size and shape, with the latter being related to the mechanical properties of the finished component [253] – hence it is often difficult to obtain the superior properties of nickel-based superalloys in the actual parts.

There are three more factors which makes Udimet 720Li a less straightforward nickel-based superalloy to work with than others within this material family. The first is regarding the stable γ phase; in Udimet 720Li, its mole fraction changes by about 10% between the γ prime solvus temperature and 40°C below it (in contrast to Waspaloy, where only around 4% change is estimated to occur [253]). Such a dramatic phase transition causes large changes in microstructure (including grain size and the extent of dynamic recrystallisation[14] which occurs), making it difficult to recognise the relationship between the microstructure and various parameters. Indeed, there are various types of recrystallisation which can occur during the hot working process, thus impacting the grain structure evolution [205]; dynamic recrystallisation occurs during the actual deformation process, with metadynamic recrystallisation, where the partially recrystallised grain structure, observed immediately after deformation, transforms to a more fully recrystallised structure through the growth of recrystallisation nuclei formed during deformation. There is also static recrystallisation, which occurs on reheating [205].

The second factor is the presence of relatively large amounts of aluminium and titanium; as previously mentioned, these are the major elements of γ' formation and essential in obtaining the high strength required, but both elements have the tendency to segregate in the billet [253]. This in turn reduces the temperature for incipient melting [205], an undesirable phenomenon where solute rich areas (such as grain boundaries) can melt before the rest of the material. An example of incipient melting is shown in Figure 101. It also makes it difficult to obtain complete uniform γ' distribution at the billet stage; often, two different types of region are observed, where one has a relatively high density of primary γ' particles (also known as γ' banding), where the grain size tends

[14] Dynamic recrystallisation is a phenomenon which occurs during the deformation process of hot working [31]. The dynamically recrystallized grain size is an important factor to predict accurately, due to its influence on the average grain size – where the average grain size is determined as a mixture of initial grain size and dynamically recrystallized grain size [29].

to be finer, than the other areas with a much lower density [253]. This γ' irregularity is also attributed to the differing extents of recrystallisation occurring; for example, the recrystallisation starts preferentially at grain boundaries, and at the surface, where the temperature is lower due to cooling, only a small amount of recrystallisation takes place [205]. The increase in volume fraction and solvus temperature of γ' also reduces the ductility of the material [205].

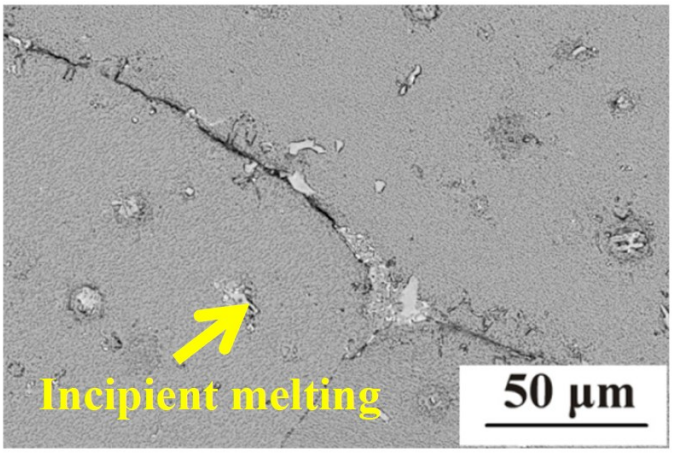


Figure 101: An example of incipient melting within a cast nickel-based superalloy. [280]

Finally, the presence of titanium also increases the likelihood of the aforementioned 'white spots', or TiCN inclusions, being formed, as titanium has the propensity to bond with nitrogen to form titanium nitride (and any titanium carbides will also include nitrogen; where carbon is present on an EDX image, these will almost certainly have nitrogen present). The previously described microstructural effects such as segregation and differences in extent of recrystallisation can hinder the ultrasonic detection of these white spots which can be so detrimental to the material performance.

It can be seen from the challenges outlined above that the development of a rapid, reliable (and additionally, non-destructive) method to detect and quantify any microstructural changes which had occurred would be highly advantageous for Udimet 720Li, with a great potential for industrial deployment if successful, and therefore making it an excellent candidate for investigation using the UWS method. For the following experiments, three different discs were machined from the same billet in its as-forged condition (i.e. no heat treatment) to be investigated, in order to determine whether the differences in microstructure could be distinguished with the zeroth coefficient technique. The results from these investigations are described in the following section.

5.4 Udimet 720Li – Experimental Materials

The three discs of Udimet 720Li which were investigated all originated from the same billet, of 9 inch diameter and 1 inch thickness and in its as-forged condition. The samples themselves were 72mm in diameter and extracted from various locations, as shown in Figure 102 below [281]; two were machined from the surface, with Part C from the centre and Part S from the outer edge, and a third disc from a subsurface location at the mid-radius point, Part MR.

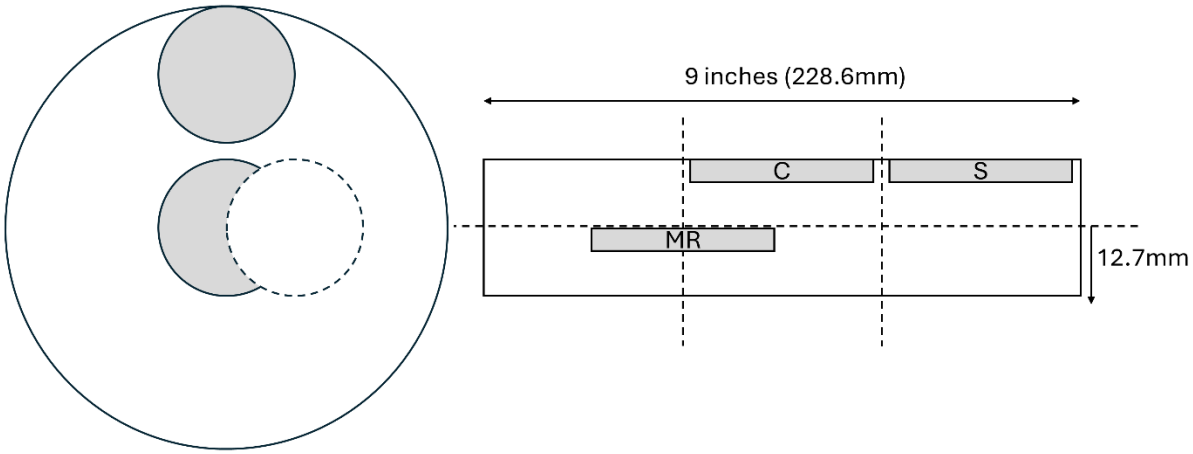


Figure 102: Locations of billet from which test discs of Udimet 720Li were machined.

The main purpose of the investigations using Udimet 720Li was to assess whether the zeroth coefficient method was able to detect microstructural changes within this particular superalloy. As previously discussed, this superalloy is notoriously difficult to inspect using ultrasonic methods as it is an incredibly noisy material, due to a combination of varying extents of recrystallisation, and differences in composition as well as grain size. Within one billet, the microstructure of the material can vary depending on its location – for example, there is a greater likelihood of retained strain at the surface where there tends to be finer grain size, which prevents grains from recrystallising completely. The grain size tends to be smaller and more uniform at the surface while 'ballooning' towards the centre and the edges, as the final preparation step in billet manufacture is radial forging, a surface specific process.

5.5 Udimet 720Li UWS Results

The cumulative mean value of V00 for the three different discs of Udimet 720Li are shown in Figure 103 below, with there being only 10 separate trials as opposed to the 16 used for Inconel 718; from these previous experiments, it was found that a good convergence was reached after 8 experimental runs. It was assumed that this would apply for Udimet 720Li, but a total of 10 trials was used, to ensure that the mean values did indeed converge.

The elastic stiffness kernel for use in the deconvolution process was calculated using the SCECs for RR1000, scaled down by 95% (based on the differences in γ' content, 46% to 44% respectively – further supported by the fact that the critical resolved shear stress, or CRSS, of 720Li is also 95% that of RR1000, from simulations [282]). These elastic constants are shown in Table 22, with those of RR1000, for reference.

Table 22: Density and SCECs used to calculate elastic stiffness kernels of Udimet 720Li and RR1000 for deconvolution.

Sample	Density [g.cm^{-3}]	Elastic Constant [GPa]		
		C_{11}	C_{12}	C_{44}
Udimet 720Li	8080 [283]	222.79	123.50	97.85
RR1000 [284]	8320 [285]	234.52	130.00	103.00

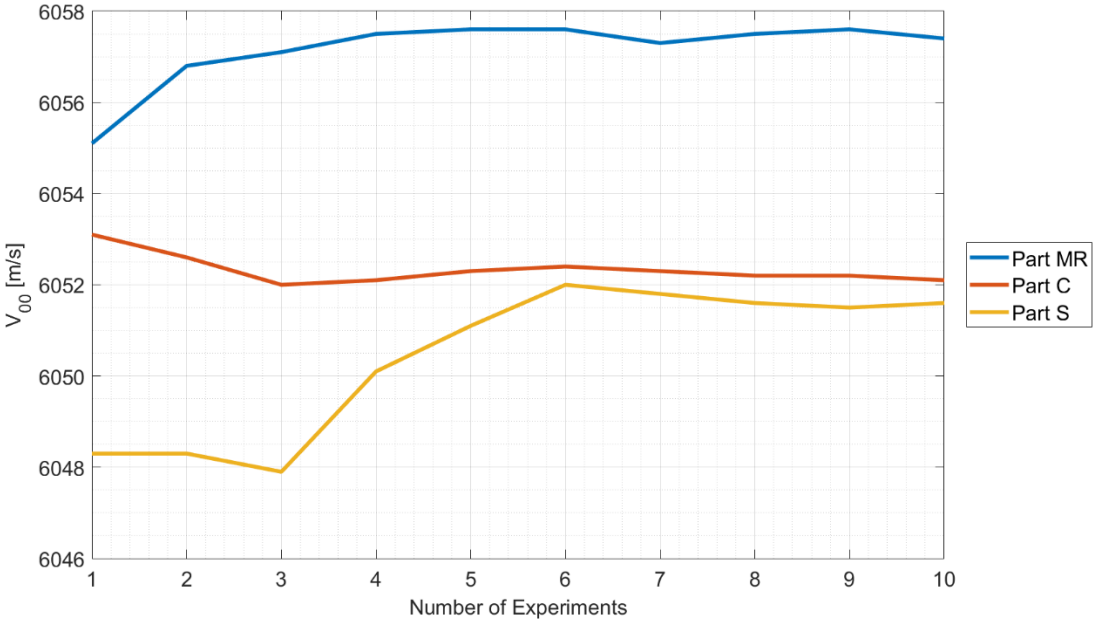


Figure 103: V00 measurements for Udimet 720Li samples.

The first observation from Figure 103 is that, despite the expectation that all three discs would have different microstructures, the V00 values have all converged to very similar values with a range of less than 10m/s; this is around the error margin associated with this experimental configuration, which has been estimated to be between 5-10m/s, as previously discussed in Section 3.5. However, this is a positive result in terms of demonstrating the UWS method; it is emphasised that the V00 measurement is indicative of variations purely in terms of the overall volume fraction of a precipitate, and phase composition changes. The fact that the values are all very closely aligned is promising, given that the overall amount of γ' within each disc should be consistent; it appears to have been unaffected by factors such as segregation and inhomogeneous recrystallisation, which typically impacts ultrasonic measurements. In addition, the fact that Part C and Part S have more similar V00 values to each other than Part MR may indicate a subtle difference in terms of the amount of γ', where perhaps the latter, with its higher V00, may have more of the precipitate present. (However it may not be as straightforward a relationship, as demonstrated by Inconel 718.)

In addition, it can be seen that the variability in individual V00 measurements of each of the samples is slightly different; Part S is the most variable, taking around 6 experiments to approach its final converged value, with Part C reaching its converged value comparatively quickly. This may be indicative of Part S having more microstructural effects which are increasing the noise, but is most likely to be caused by experimental errors. Nevertheless, the range in which the individual V00 measurements of Part S lies is still relatively small (under 5m/s), and it has not affected the number of trials required for the V00 to converge.

To investigate the link between the V00 measurements and the sample microstructures, metallurgical investigations, including optical and scanning electron microscopy as well as hardness tests, were used to determine the extent of microstructural variations within each disc.

5.6 Udimet 720Li Optical and SEM Micrographs

To prepare the samples for examination, the same initial process used for Inconel 718 was followed, where small specimens were machined off each disc of Udimet 720Li, and then ground and polished using the Struers Tegrapol-35, with a final OPS polish to finish. However, the samples were then swab etched for around 5 seconds using a solution of modified Kalling's reagent, before taking hardness measurements, and optical and SEM micrographs, of each sample.

The optical micrographs at increasing magnifications are shown in Figure 104 and Figure 105. These micrographs are an excellent demonstration of why as-forged structures are undesirable for use in disc applications; the inhomogeneity of the structure results in lower, and more variable, mechanical performance, and thus solution treatment and ageing processes are crucial in ensuring the microstructure is homogenised. The differences in microstructure between each disc are more subtle than observed in Inconel 718, but there are clear variations with regards to the precipitation behaviour of the γ' – particularly in terms of the distribution of these precipitates.

Even at lower magnifications (Figure 104), it is immediately apparent that Part S has more clusters – regions of higher density precipitation of γ' – than the other two samples; Part MR does have some present, though not as many, with Part C having the most uniform and homogeneous distribution. It is thought that these clusters are likely to be smaller primary γ' precipitates, rather than secondary γ', and are likely caused by segregation effects. This segregation may be a result of compositional differences, where there are variations in the amount of partitioning of elements such as Al and Ti, though it may also be caused by local variations in strain. It was difficult to determine at these lower magnifications whether Part MR appeared to have more high density precipitation regions than Part C, or whether the fact that there were also sparser areas made it seem that this was the case. Observations made at higher magnification (Figure 105) did appear to show that Part MR did have more of the clumps of finer γ' particles than Part C, with the latter having the most uniform microstructure in terms of the distribution of larger γ' particles. Again, Part S was the most inhomogeneous, with the differences in the density of γ' precipitation being very distinct.

The fact that the optical micrographs of the three samples are all very alike aligns well with the V00 values also being similar; it may well be the case that the overall γ' volume fraction is indeed similar across all three discs, in which case the V00 measurements have successfully verified this.

The slight difference from Part MR to the V00 of Part C and Part S may be caused by the compositional differences causing the aforementioned segregation effects (potentially responsible for the regions of varying precipitation density), or the fact that Part MR has a slightly higher amount of γ' overall. Indeed, it may be the case that Part S and Part C have a lower volume fraction of γ'; in the case of Part S, the presence of sparse, γ'-free regions are observed, as well as in Part C (though not to the same extent), which may be causing lower overall volume fractions of γ' than Part MR.

As it was not possible to distinguish the grain boundaries clearly, or use higher magnifications, using optical microscopy, the Scios SEM was used to examine the microstructures in more detail. These micrographs, at 500x and 1000x magnifications, are shown in Figure 106. It does seem to be the case, particularly at 1000x, that the γ' is slightly more sparsely precipitated in Part C, and that the overall volume fraction of γ' may be similar to Part S.

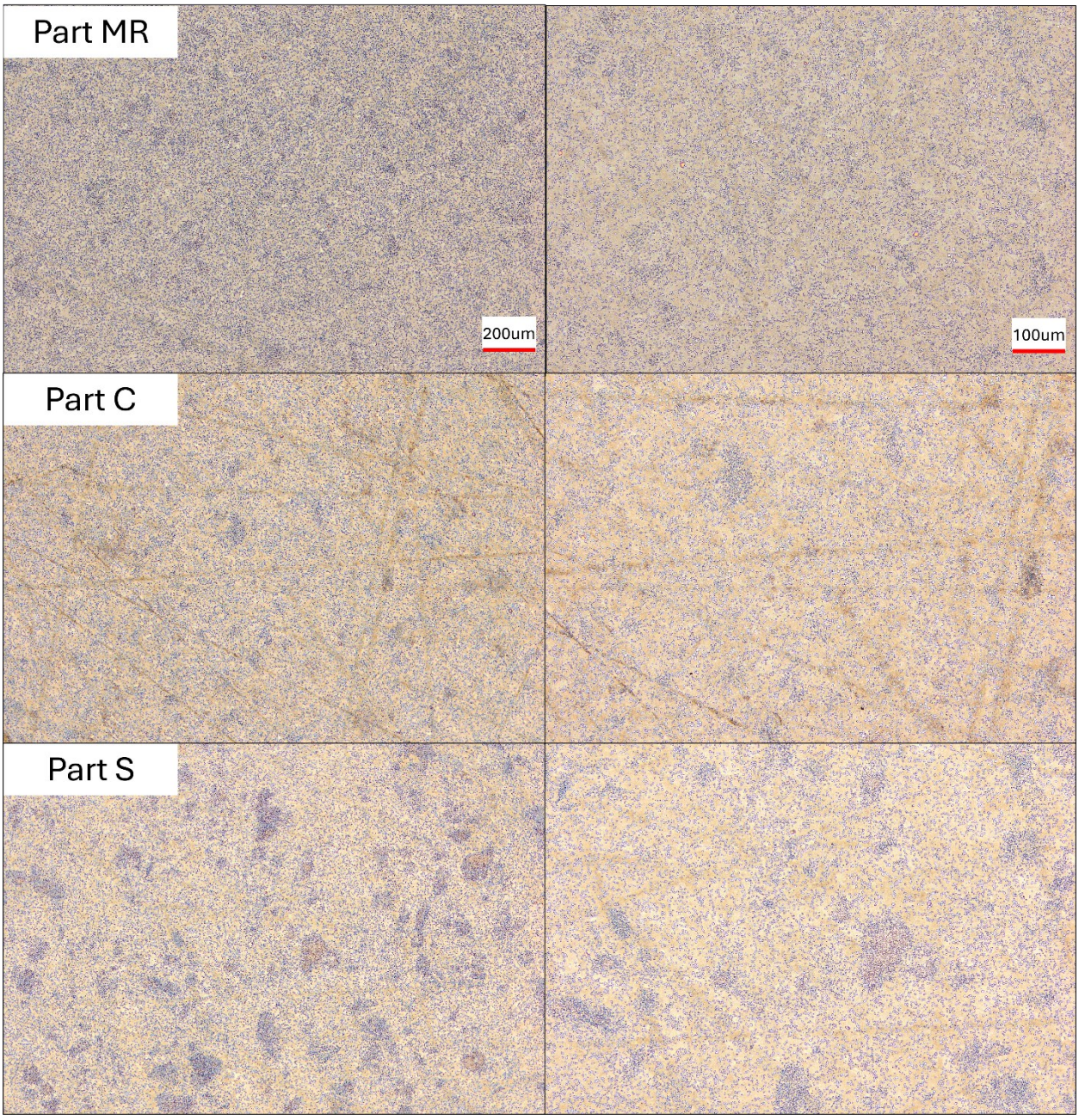


Figure 104: Low magnification images of Udimet 720Li samples.



Figure 105: High magnification images of Udimet 720Li samples.

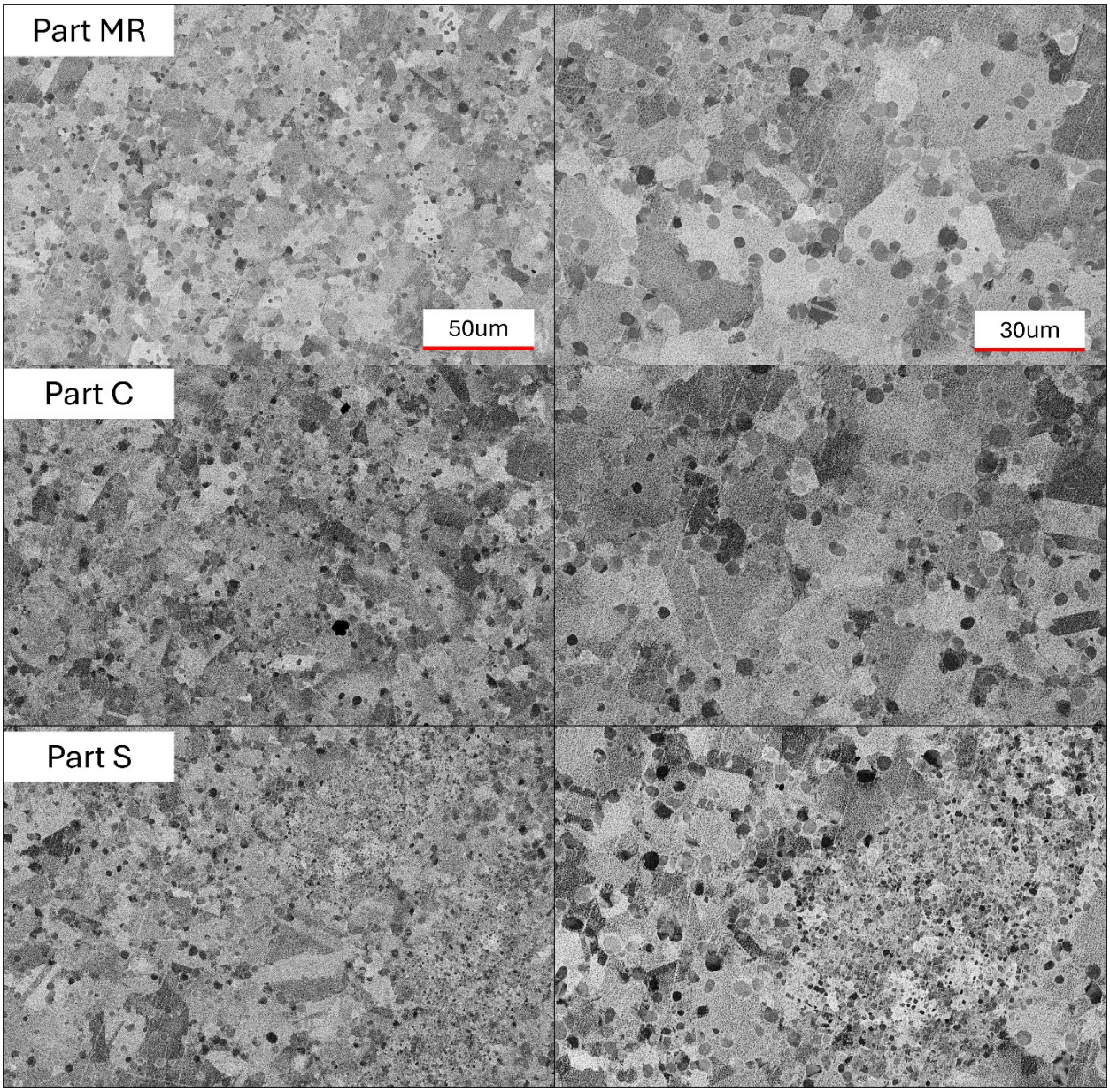


Figure 106: SEM micrographs of Udimet 720Li samples.

5.6.1 Further Analysis: EBSD and Hardness Tests

As the microstructural variations were quite subtle between these samples, further analysis using EBSD was carried out to ensure there were no further differences which the ultrasonic wave speed measurements may not have detected. The KAM maps in particular were of interest, as billets of as-forged Udimet 720Li are known for having varying levels of retained strain (which contributes to the inconsistencies in the microstructure depending on the location in the billet); these are shown in Figure 107. Hardness tests were also carried out to investigate whether there was any effect from the variable density of γ' precipitation, and the results given in Table 23.

From the KAM maps, there does not appear to be a discernible difference in the retained strain within each sample, and the vast majority of the highlighted regions are a result of scratches on the surface. There was no further evidence in the various EBSD scans to suggest the presence of other microstructural differences that had not been detected with SEM, or indeed the V00 measurements. The hardness values across the samples were also very similar, though the fact that Part S had the highest is consistent with studies suggesting that the outer periphery of billets tend to have an increased hardness [286].

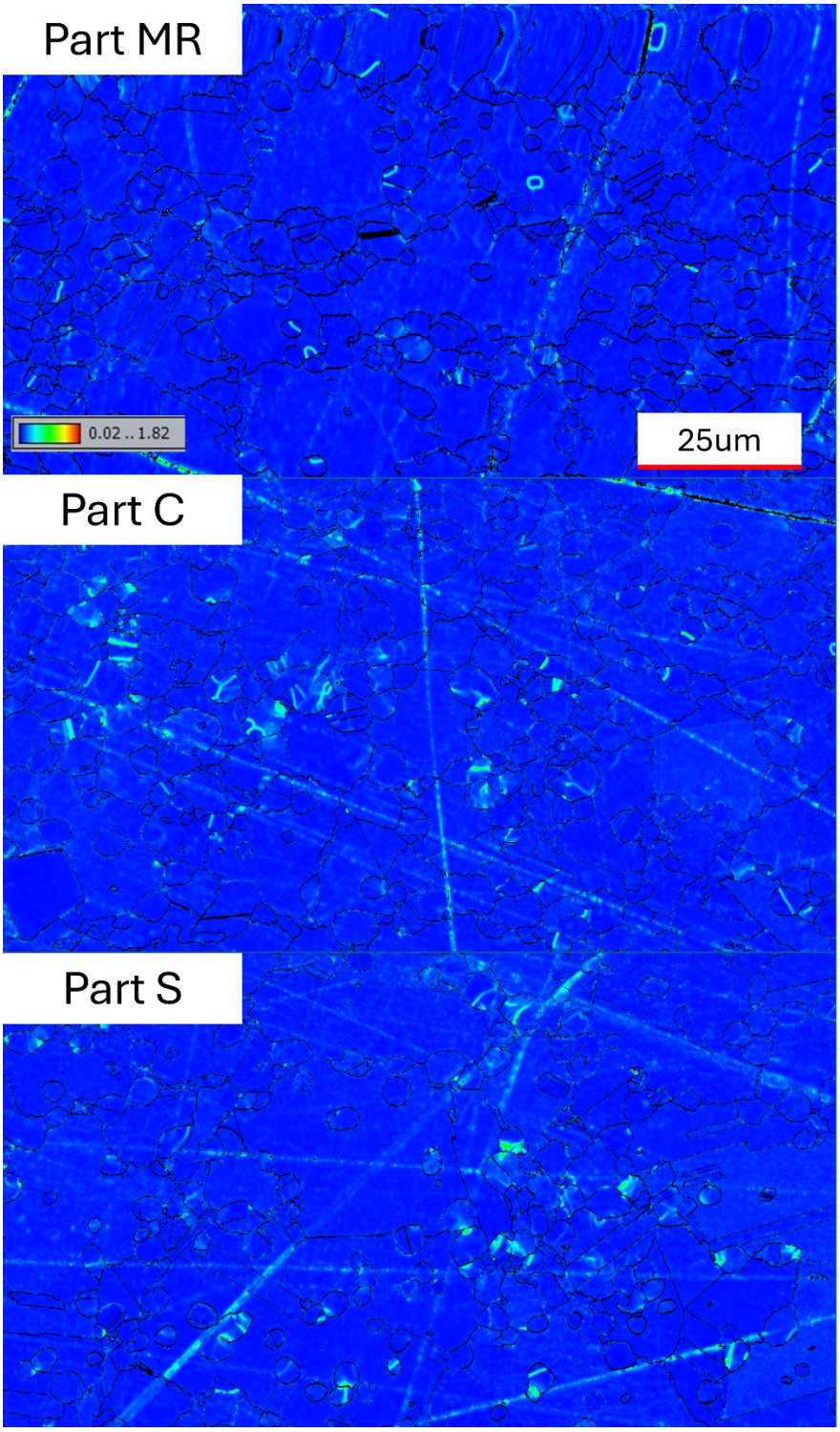


Figure 107: KAM maps of Udimet 720Li samples.

Table 23: Vickers Hardness test results for Udimet 720Li samples.

Sample	D [mm]	HV30	D [mm]	HV30	D [mm]	HV30	Average HV30
Part C	373	399	376	396	372	400	389
	374		374		374		
Part S	373	398	374	396	374	398	397
	375		376		374		
Part MR	375	394	374	396	374	396	396
	376		376		376		

5.7 ImageJ and Phase Estimation

It was previously found with Inconel 718 micrographs that ImageJ is not sufficiently accurate or consistent for the determination of the proportion of a precipitate present; indeed, any attempts to establish the total amount of γ' in these Udimet 720Li samples and comparing to the theoretical 45% were inaccurate due to the amount of over/under-shading, as previously discussed. It was also found here that the optical micrographs did not have sufficient contrast for ImageJ to detect differences between the γ' phase and the main γ matrix, and although some of the SEM micrographs did generate slightly more realistic results – within a reasonable range of 45% – the regions which were identified as particles to add to the total shaded area were often inaccurate. The full tabulated data can be found in the Appendix, with an example of a micrograph pre- and post-analysis.

However, ImageJ was still used for these samples to visualise how similar the amount of primary γ' there was present in each disc to verify that they lined up (albeit approximately) with the literature values of 19-20% [286] [287]. To best highlight the primary γ', the 'Ti K' maps were used, which were generated by overlaying the titanium composition maps generated from EDX onto forescatter data. The original maps, followed by the colour threshold-adjusted versions and then the area outlines which were counted as primary γ', are shown in Figure 108, with the primary γ' volume fractions estimated given in Table 24. Part S appears to have had slightly more particles 'identified', giving it the higher overall percentage, but it appears that the amount of primary γ' does not seem to differ drastically between each sample, and is fairly well aligned with the literature values.

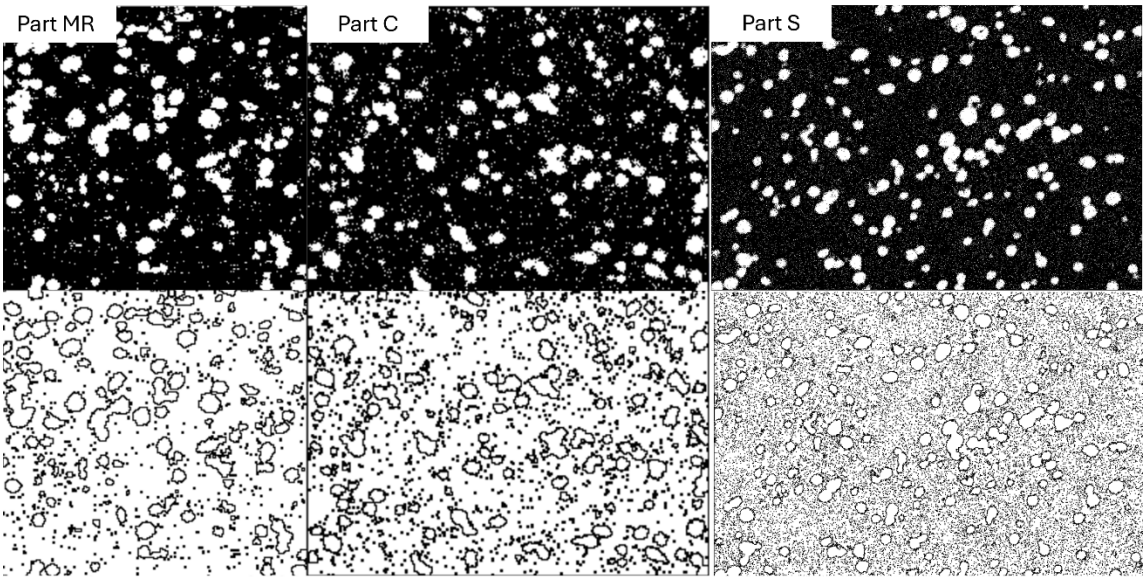


Figure 108: ImageJ analysis to estimate the amount of primary γ' in Udimet 720Li samples.

Table 24: Estimates of primary γ' volume fraction in Udimet 720Li samples.

Sample	Volume fraction of % primary γ'
Part MR	15.62
Part C	10.932
Part S	11.03

5.8 Attenuation Behaviour

With the V00 being a measure of the overall phase composition only, regardless of the uniformity of the precipitates (in terms of both size and density of formation), a brief investigation into the attenuation of the signals through the material was carried out to determine whether the clusters of γ' seen throughout Part S (and in Part C, though to a lesser extent) were having an effect on the ultrasonics, in terms of increased energy loss. Although the attenuation measurements are dependent on a different mechanism to the V00 measurements (where the former is related to scattering and absorption, and the latter being directly impacted by the material stiffnesses), it was of interest to investigate whether attenuation characteristics may offer some alternative insight into the microstructure of the samples.

The fact that the amplitude of the first arrival group of signals is closely linked to attenuation was used for this study; the same experimental setup as for the wave speed measurements was used, but with the sample in a stationary position at a fixed point from the transducer. Using the first arrival signals from each sample, the peaks of each reflection following the first arrival were first identified, as shown in Figure 109, and their amplitudes recorded for each sample as shown in Table 25. Part S appears to have the highest amount of attenuation – likely caused by the γ' clusters, and inhomogeneous microstructure. Conversely, Part MR has the lowest level of attenuation, as although the amplitude of its 9th peak is the same as Part C, its initial amplitude of the first reflection is slightly higher.

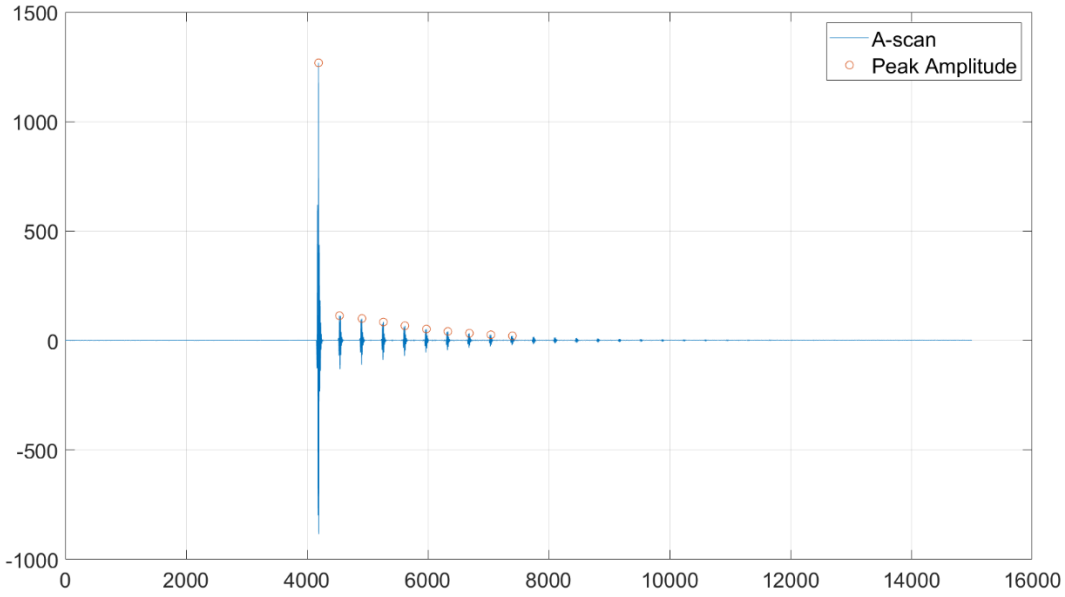


Figure 109: Illustration of the first arrival group of ultrasonic signals for a sample of Udimet 720Li.

Table 25: Amplitudes of peaks from ultrasonic wave reflections through each sample of Udimet 720Li.

Peak Number	Part C	Part MR	Part S
1	1375.4	1268.4	1297.5
2	120.4	113.4	114.5
3	107.4	100.4	96.5
4	86.4	84.4	78.5
5	70.4	67.4	62.5
6	55.4	52.4	49.5
7	44.4	41.4	38.5
8	34.4	33.4	30.5
9	26.4	26.4	23.5

5.9 Udimet 720Li: Discussion

Although the differences in V00 between Part MR to Part C and S are not as strongly pronounced as for the Inconel 718 samples, it is still possible to conclude that the V00 measurement technique has shown positive and promising results. There is a good convergence to a distinct mean V00 for each sample, indicating that the experimental errors are being minimised with each trial; in addition, the measurements appear to not have been affected by the inhomogeneity of the precipitates within the sample. The fact that the micrographs have not shown any drastic differences in the overall volume fraction of the γ' phase aligns well with the similarity the V00 measurements, from which it was predicted that the microstructures would indeed be similar in terms of overall volume fraction of γ'. Differences in terms of the distribution of γ' precipitation would not be detectable through the V00 coefficient, as this is a high-level statistical measure of phase composition in terms of the total amount of a given precipitate present; it was never the intention to use this measurement to infer more detailed spatial information, such as the distribution of particles. (This information could potentially be detected through other means, such as backscattering and attenuation studies.)

It is most likely that the slight difference between the V00 of Part MR, compared to Part C and Part S, is indicating a small variation in the amount of the γ' precipitate, where Part MR has more present

overall than Part C and Part S. Although it has not been possible to get an accurate, quantitative visual measure of this, the micrographs obtained appear to suggest that this is the case; Part S may have a lower amount due to the presence of sparse, γ'-deficient areas, also seen in Part C though to a lesser extent.

One aspect of the γ' precipitate which hasn't yet been considered is the impact which the proportion of each morphology present (primary, secondary and tertiary) could be having on the V00 measurements. The V00 is determined by the SCECs of the material, which are not determined solely by the single crystal itself but also the mechanism by which the material is stiffened. In this case, due to the presence of these various γ' morphologies, the morphology and size may be having an influence on the overall stiffening effect 'seen' by the ultrasonic waves as they propagate through the material, either via the chemistry or slightly more subtly by impacting the solid solution strengthening (perhaps in a similar manner to that proposed for Inconel 718). It could also be possible that there is one particular morphology of the γ' which has more of an effect than the others – though it is unlikely to be the tertiary γ', given that it forms in very small quantities with a very small size.

To further investigate whether the γ' morphology did have an effect on the V00 measurements, it was decided that RR1000 would be used, in the fine-grain, coarse-grain and as-forged conditions. This was due to the fact that the proportions of each morphology present in both the fine- and coarse-grain conditions were well known, and thus eliminate the need for ImageJ to estimate the amount present. There was the additional benefit with RR1000 that, due to it being a powder metallurgy superalloy, the microstructures would be more homogeneous and consistent, resulting in cleaner and less variable signals which would be more straightforward to analyse. The investigation of RR1000 will be discussed in the following section.

5.10 RR1000 – Microstructure, Processing and Properties

Despite the excellent mechanical properties demonstrated by Inconel 718, as well as other benefits – such as its relative ease and low cost of manufacture [31], a low rate of melt anomalies from primary and remelting practices [176] and the flexibility to use either a conventional heat treatment or direct age [177] – its temperature capability is limited to around 630°C, as the γ'' and γ' precipitates coarsen during prolonged exposures above 600°C (with the γ'' precipitates transforming to the delta phase above 700°C, further reducing strength [31]). There was therefore

the need for a material with temperature capability between Inconel 718 and the available powder metallurgy superalloys at the time. There were some potential candidates already in existence, including Waspaloy as well as the previously investigated Udimet 720Li; however, Waspaloy, with a γ' proportion of around 25%, show lower yield strength (particularly when coarse grained), and presents additional challenges in material and component manufacture (including recrystallisation, forge cracking, or twin cracking during machining [31]). In the case of Udimet 720Li, despite its successful deployment since the mid 1990s due to its fine grain microstructure and temperature capability around 650 to 700°C [257] [265], it did still require additional controls for successful remelting to minimise inclusion content [31].

Roll-Royce developed the powder metallurgy nickel-based superalloy RR1000 in the early 2000s to replace Udimet 720Li, the best of the nickel disc alloys available at the time [32]. It is a third generation γ' strengthened superalloy [288] [289] [290], designed to achieve the high levels of creep resistance and damage tolerance at extremely high temperatures, as required for modern civil jet engine components [288], where there are greater demands on the materials used to achieve better efficiency and reduce pollutants [23] but with reduced size and weight, to allow for faster shaft speeds [31]. The development process itself was also novel, as rather than the traditional, empirical and often iterative approach to the design of materials, analytical methods were used instead. Rolls-Royce extended existing thermodynamic modelling techniques (which allowed the accurate prediction of complex phase equilibria) for application to nickel-based superalloys, in order to predict the existence of stable phases both at fabrication and operating temperatures, as well as enabling much more accurate predictions of conditions deviating from equilibrium [291] [292] [293] [294].

The challenge in designing RR1000 was in satisfying superalloy design principles which appeared to conflict, where disc applications require low temperature strength which is also maintained at temperatures of 650°C and above [32]; the principles in alloy design indicate a large misfit between coherent γ' precipitates and the γ matrix is beneficial for low temperature strength, but low misfit is generally preferred for high temperature creep resistance [295]. Hence the objective in designing RR1000 was to develop a large enough misfit to give required strength properties, but to ensure that the γ' phase did remain coherent [32]; a minimal coherency strain is important to minimise coarsening of γ' precipitates during exposures to temperatures above 700°C [28].

The resulting fine grain microstructure, together with the carefully tailored chemistry of the material, resulted in a superalloy with at least a 35°C increase in temperature capability over Udimet 720Li, as well as an equivalent resistance to crack growth as coarse grain Waspaloy [32]. Although it was initially developed as manufacturable using both the cast/wrought and powder metallurgy routes [31], ultimately the latter was selected, in order to minimise elemental segregation to sub-micron length scales – a necessity for such complex, multi-component alloys with high levels of reactive elements including aluminium, titanium and tantalum) [296] [297] [298], as observed in billets of Udimet 720Li as discussed previously.

5.10.1 Precipitation Considerations for RR1000

RR1000 is more similar to Udimet 720Li than Inconel 718, in that the main strengthening precipitate is the γ' phase, which is present in various morphologies and sizes. Much like Udimet 720Li, this strengthening precipitate is present in primary, secondary and tertiary forms.

The primary γ' is conventionally defined as the precipitates occurring at grain boundaries; these tend to be irregular in shape and up to 1.5um in size [299] [300] [301], and goes on to determine the extent of the intragranular secondary and tertiary precipitate populations [302], as well as the grain size via Zener pinning. The secondary and tertiary sizes range between 100 to 400nm, and 5-50nm respectively [303] [304] [305] [306], with the particles being stabilised during post-forging heat treatment. The superior mechanical properties of this superalloy are a result of optimising the distribution of these latter precipitates [302]; it was understood from the literature at the time of design [307] [308] [309] [310] [311] that a larger number of (preferably smaller) γ' particles in comparison to existing superalloys was required to provide a higher level of precipitation hardening [28].

In addition to the optimisation of the γ' distribution, there was also the need to avoid the precipitation of deleterious topologically close packed (or TCP) phases, such as σ, μ, χ, P and R, due to the degradation in mechanical properties they cause (though the coarsening of tertiary γ' could have an equally damaging effect [293]). The detrimental effect is a result of these TCP phases depriving the matrix of elements used for solid solution strengthening, such as chromium [312], degrading the creep properties of nickel disc alloys [313] [314] and reducing oxidation resistance [315] as well as becoming crack initiation sites [31]. These phases tend to precipitate during long exposures to temperatures in excess of 700°C [31] [292]; the phase stability of the alloy (i.e. the

avoidance of these TCP phases precipitating) is key to the material having an extended service life [31], and is a characteristic that can be predicted using phase diagram modelling techniques [316] [317] – although experimental verifications are the only reliable method of determining the precipitation behaviour of these phases.

The precipitation behaviour is influenced significantly by the chemistry of the material, which is described in the following section. The amount of each element present in RR1000 was tailored carefully to give the best possible balance of properties, such as high strength and resistance to deformation and corrosion.

The chemistry of RR1000 is given in Table 26 [318], and the role of each of the alloying elements is described briefly below.

Table 26: Nominal composition of RR1000 [318].

	Ni	Co	Cr	Mo	Ti	Al	Ta	Hf	Zr	C	B
Weight %	Bal	18.5	15.0	5.0	3.6	3.0	2.0	0.5	0.06	0.02	0.03
Atomic %	Bal	17.9	16.5	3.0	4.3	6.35	0.63	0.16	0.04	0.14	0.10

5.10.2 Chemistry of RR1000

In keeping with the aim of designing a material with high strength but with a reduced volume fraction of γ' (in comparison to materials such as IN100 and Rene 95, which have the γ' phase present in amounts as high as 50-60% but suffer from very fast rates of crack growth), the tantalum was limited to 2.15wt% as it increases strength, but also crack growth rate [32]. Similarly, aluminium was limited to 3.1wt%, as any additional amount would increase the volume fraction of γ' and lead to chromium enrichment of the γ matrix, thus increasing the risk of TCP formation [32]. The titanium content was adjusted accordingly with these levels, resulting in a 45wt% of the γ' phase at 725°C [32], but there was also a further consideration in reducing the titanium content to increase the chromium to titanium ratio and thus enhance the resistance to environmental damage [28]. The presence of zirconium plays a similar role to manganese [319] where it can 'scavenge' O and sulphur from the material, thus reducing the availability of these elements for the formation of low melting point compounds and resulting in high temperature grain boundary embrittlement [259] [320] [321].

The cobalt content was optimised to produce a minimum stacking fault energy (SFE) to promote planar slip and encourage low crack growth rates [32], as well as minimising the propensity for σ phase formation [322] to improve resistance to hot corrosion damage; it also reduces the solubility of aluminium and titanium in the γ matrix, thus maximising these elements in the formation of γ' and reducing the γ' solvus temperature[15]. Cobalt also reduces the stacking fault energy [119] [322], and has the additional effect of producing more annealing twins [323]; this reduces the effective grain size, which is important for fatigue crack nucleation life in coarse grain microstructures at lower operating temperatures (below 650°C) [28]. The amount of chromium was ultimately limited to 15.0wt%, as despite its reducing the rate of crack propagation at high temperatures, it has been found to cause excessive precipitation of σ and μ phases in Udimet 720, even after relatively short exposure times [292] [324]. This amount of chromium was possible by, in turn, limiting the molybdenum content, at the expense of potential gains in high temperature strength and creep resistance [32]. Also limited were the levels of boron, carbon and zirconium, of which minimal levels were included required for enhanced high temperature creep resistance (although boron is also beneficial to the fatigue performance of the material) [32]. Finally, the presence of hafnium enables improvements in both the crack growth [325] and creep resistance of RR1000, producing a slight increase in tensile strength due to its partitioning to γ' [32]. Hafnium also forms a primary carbide that remains stable at low temperatures, which is beneficial in preventing excessive $M_{23}C_6$ carbide formation at grain boundaries (which are the types that remove chromium from the γ matrix).

Alongside the careful balancing of the elemental composition of RR1000 during design, there was also the practical limitation of the volume fraction of γ' and the amount of aluminium, titanium, niobium and tantalum that could be added to improve strength – the higher the volume fraction of γ', the greater the difficulty in manufacturing of billets and forgings, as well as finished components [31]. It also has a detrimental effect on the resistance to time-dependent crack growth [31]. Aluminium and titanium in particular can raise the γ' solvus temperature sufficiently such that incipient melting can occur at grain boundaries during super-solvus solution heat treatment [31], much like Udimet 720Li.

[15] A low γ' solvus temperature is favourable to minimise the risk of incipient melting at grain boundaries and quench cracking, following a super-solvus solution heat treatment (required for coarse grain microstructures) [39].

5.10.3 Heat Treatments of RR1000

In addition to tailoring the chemical composition of RR1000, the appropriate heat treatment procedure to obtain a material with the best possible mechanical properties was also required; as demonstrated for Udimet 720Li, an amendment in one stage of the process could result in drastic changes to the material performance. Design considerations included the forging and solution treatment temperatures, quench rates from solution treatment, and ageing temperature and time [32]. Despite the optimisation of strength and resistance to low cycle fatigue via a sub solvus heat treatment followed by an oil quench (to maximise the cooling rate), there is the disadvantage of lower crack growth resistance that this process results in [32]; evidence suggests that this is due to the fast quenching leaving grain boundary regions free of both secondary and tertiary γ', thus increasing the risk of intergranular cracking and fast rates of crack growth under creep-fatigue conditions [326]. Slower rates of cooling yield a more homogeneous distribution of the γ' precipitate, and hence improved resistance to high temperature crack growth [326]. For superalloys with a high volume fraction of the γ' phase, there are additional concerns; rapid quenching in oil can cause quench cracking in thin sections, as well as the development of significant internal residual stresses [32]. Although the latter can be relieved by heat treatment, this must be higher than the ageing temperature, which also coarsens the tertiary γ' and leads to an adverse impact on mechanical properties [32]. Ultimately, it was decided that oil quenching would not be used, and hence the solution heat treatment of RR1000 is limited to temperatures below the γ' solvus; the proof strength is also slightly lower than for oil-quenched Udimet 720Li due to its reduced cooling rate [32].

For both Udimet 720Li and RR1000, it was found that an optimised resistance to creep is achieved via a unimodal size distribution of fine tertiary γ' precipitates with a volume fraction of at least 3%, and average size of 15nm [31]. This is generally achieved with a soak of between 4-24 hours between 650°C to 800°C, but does vary depending on the superalloy. For powder metallurgy superalloys, however, this is not as effective as shorter duration exposures to higher temperatures to relieve residual stresses; the initially fine tertiary γ' particles will coarsen during exposure at about 700°C, particularly rapidly above 800°C [31]. Instead, a 2-stage post-solution heat treatment is often preferred, with an initial short soak at temperatures above 800°C before undergoing the longer duration exposure between 650°C to 800°C that grows the very fine tertiary γ' precipitates (around 15nm), resulting in a bimodal size distribution [31]. This processing provides effective

stress relief from quenching, and any subsequent coarsening of these tertiary γ' precipitates at long exposures to temperatures of 700°C and below will not significantly degrade yield stress and tensile strength [31] (though long exposures above 750°C may coarsen secondary γ' sufficiently to reduce strength [327]).

There have also been additional efforts in developing industrially robust processes for the production of dual-microstructure components [290] [328] [329] [330] [331]; essentially, for the fine grain regions the grain growth is restricted through Zener pinning by the primary γ', and then solution treating regions above the γ' solvus removes this primary γ' to allow for grain growth. Figure 110(a) shows the time above the γ' solvus which each region of a forging was held for, with (b) showing the resulting average grain size (in microns).

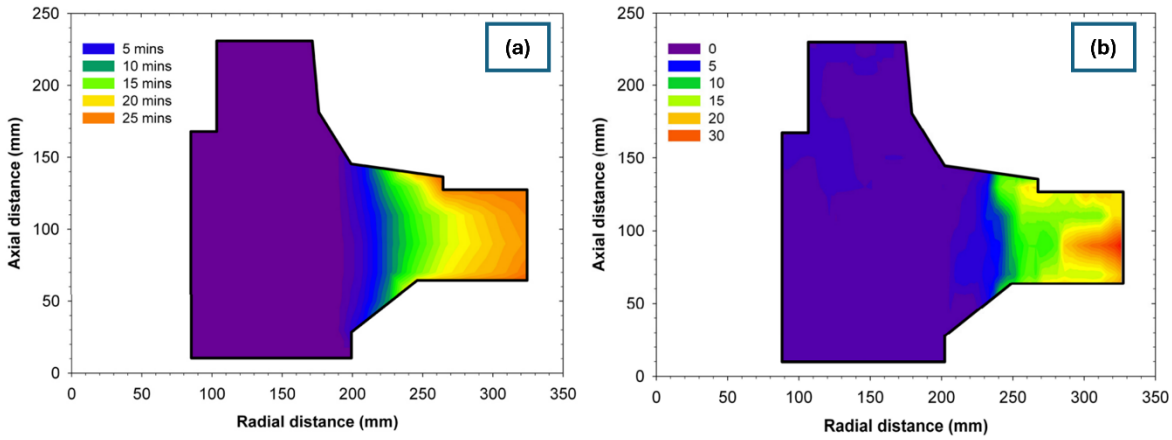


Figure 110: RR1000 components subjected to a dual microstructure heat treatment (DMHT) where (a) shows the time above gamma prime solvus and (b) the resulting grain size distribution in um. [290]

5.10.4 Summary

Much like Inconel 718 and Udimet 720Li, the design considerations for RR1000 are far from straightforward, and a variety of different heat treatments are available for generating varying microstructures, depending on requirements. However, for the UWS experiments, just three discs of different microstructure conditions were used; these were samples in the fine grain, coarse grain, and as-forged conditions. The sample processing conditions and their corresponding V00 results will be described in the following section.

5.11 RR1000: Experimental Materials

The processing of the fine and coarse grain samples are summarised in Table 28 below, together with the grain sizes. Table 27 shows the approximate proportions of each type of γ' morphology expected in the different conditions of RR1000. In the case of the as-forged sample, the exact proportions are not well known, but it is predicted that there should be approximately the same amount primary γ' as the fine grained, fully heat treated RR1000 condition (though towards the top end of the 10-15% range). In addition, there will likely be less secondary and tertiary γ' present; the forging temperature is below that where the secondary γ' is usually brought out, and there has not been an ageing process to nucleate the secondary γ' and precipitate the tertiary γ' to the same extent. There will also be γ' nuclei present, in contrast to the heat treated RR1000 samples, as the material has not been aged to allow for these precipitates to form fully.

The as-forged disc was machined from a RR1000 'centre drop' for a rim cover plate forging of a Trent 900 engine, of 475.7mm diameter, shown in Figure 111. (The name refers to the fact that, during the production process, there are two parts produced in one forging, with the first operation after forging being the removal of the centre.)

Table 27: Estimated proportions of each type of γ' morphology present.

Sample	Proportion of γ'		
	Primary	Secondary	Tertiary
Fine	10-15	25-30	<5
Coarse	0	40-42	<5
As Forged	~15		

Table 28: Heat treatment processes for RR1000 discs.

Sample	Heat Treatment	Grain Size
Fine	Solution treat 1125°C/1hr, air cool, age at 760°C/8hr	Ideally less than ASTM 12 (6um) [332]
Coarse	Solution treat at 1170°C/1hr, air cool, age at 760°C/16hr	7um [333] [334]

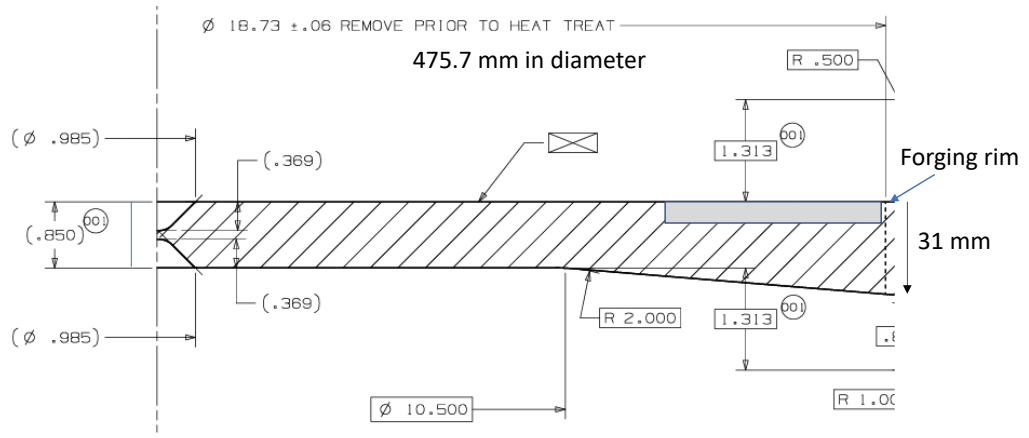


Figure 111: Origin of 'Centre-Drop' (as forged) RR1000 sample. [281]

5.12 RR1000: UWS Results

The cumulative mean value of V00 for each of the three different discs of RR1000 has been plotted in Figure 112 below, and similarly to Udimet 720Li there were only 10 total experiments carried out, having established that good convergence to the mean V00 would be reached after around 8 experiments, from the Inconel 718 investigations.

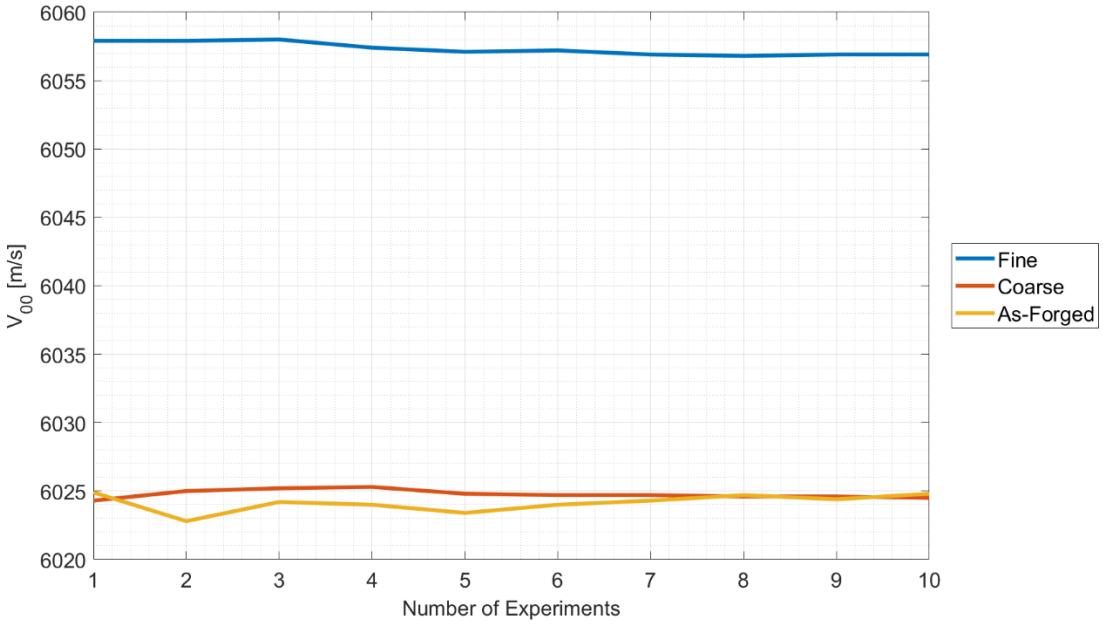


Figure 112: Cumulative mean of V00 measurements for RR1000 discs.

It is clear that powder metallurgy samples have a much cleaner ultrasonic response to forged billets, with less variability between the individual V00 measurements. In addition, it is immediately apparent that there is a very clear difference between the V00 value of the fine-grained RR1000, and the coarse grain and as-forged RR1000 discs.

Initially, these powder metallurgy samples were tested with the intention of carrying out a 'blind test'; the discs were not labelled so the fine- and coarse-grained samples were not identifiable, to investigate whether there would be a large enough difference between the V00 measurements to determine which disc had each microstructure. Figure 112 shows that there was a clearly detectable difference; although at the time it was not known how the V00 measurements would be ordered, it was predicted that the fine grain sample would have a higher V00 value. The reasoning was its having a lower heat treatment temperature, resulting in a greater proportion of the strengthening γ' phase being present (as less would be taken back into solution than the coarse-grain sample, treated at a higher temperature). Subsequent SEM showed that the fine grain was indeed the sample with the higher V00, though it was likely that the explanation for this was not quite as straightforward as simply having a greater proportion of the γ' phase. This will be discussed in more detail later in this chapter.

The optical and SEM micrographs obtained for each of the samples to verify the microstructures against the V00 results are discussed in the following section.

5.13 RR1000 Microstructure Investigations

The preparation method for the RR1000 samples involved use of the auto-polisher programme for nickel on the Struers Tegrapol-35 machine, finishing with a polish of 4 minutes using OPS solution, before rinsing and washing thoroughly with Teepol and submerging the samples in isopropyl until they were ready to be etched. The etching procedure used was a 5 second swab etch using modified Kalling's reagent. Before microscopy, hardness tests were carried out, the results of which are summarised in Table 29 below. These results are as expected, with the coarse grain having the lowest hardness due to the absence of primary γ', and the as-forged being less hard than the fine grain due to its lack of ageing to allow for the strengthening precipitates to fully form.

Table 29: Vickers Hardness tests for RR1000 samples.

Sample	D [mm]	HV30	D [mm]	HV30	D [mm]	HV30	Average HV30
Fine	351	452	351	449	351	451	450
	351		353		352		
Coarse	360	409	361	406	363	505	406
	378		380		379		
As Forged	361	425	360	427	360	429	427
	362		361		359		

5.13.1 Optical Micrographs

The optical micrographs obtained for the three RR1000 samples are shown in Figure 113 and Figure 114, with increasing magnifications. The differences between the fine- and coarse-grain samples are very apparent, and it could also be seen that the as-forged (AF) sample looked to be similar in terms of precipitation and grain size to the fine-grain disc. However, it was difficult to analyse these differences in detail, particularly as the grain boundaries did not show up particularly clearly in any of the samples. Nevertheless, some general comparisons and observations could be made using these optical micrographs; at 200x magnification, there was a noticeable difference between the AF and coarse grain samples, where the former had primary γ' present and the latter did not. The coarse grain did appear to have more of the secondary γ', with a more homogenous distribution (both in terms of the shape and size). However, it may be the case that the optical micrographs have not been able to image the secondary γ' in the AF sample, as some would be expected in this condition.

The AF and fine grain structures are very similar at lower magnifications, but observations at 500x begin to show some variations. From comparing the primary γ', the AF sample is much less uniform, both in terms of the size and the density of precipitation. The primary γ' is noticeably less evenly distributed across the sample, and there are clusters of precipitate present – similar to those observed in Udimet 720Li – which are likely to be smaller primary γ'. Increasing the magnification further to 1000x still did not show any secondary γ' phase in the AF condition, and hence the use of SEM was required (which would also better visualise the grain boundaries in the samples.)

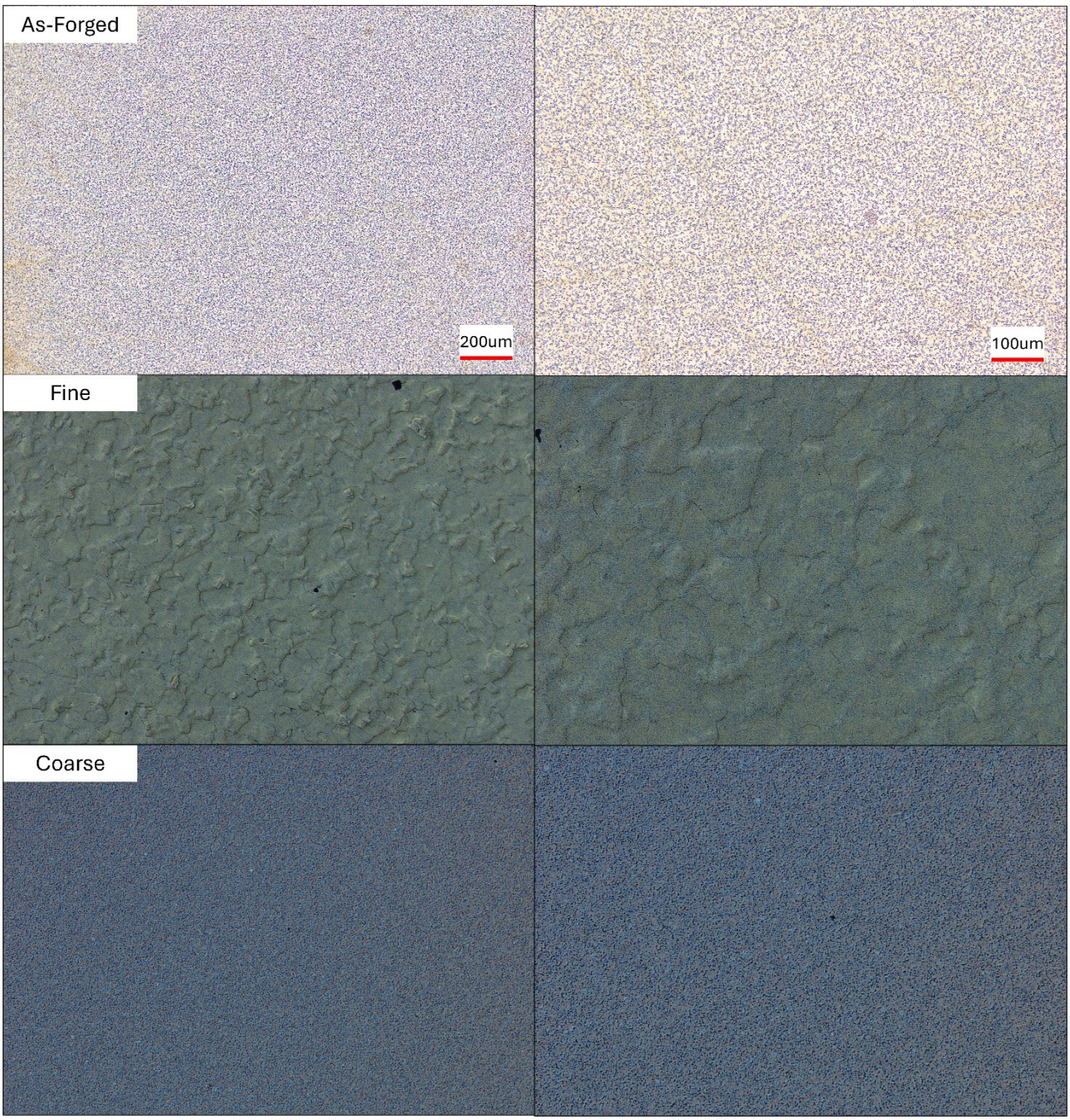


Figure 113: Low magnification optical micrographs of RR1000 samples.

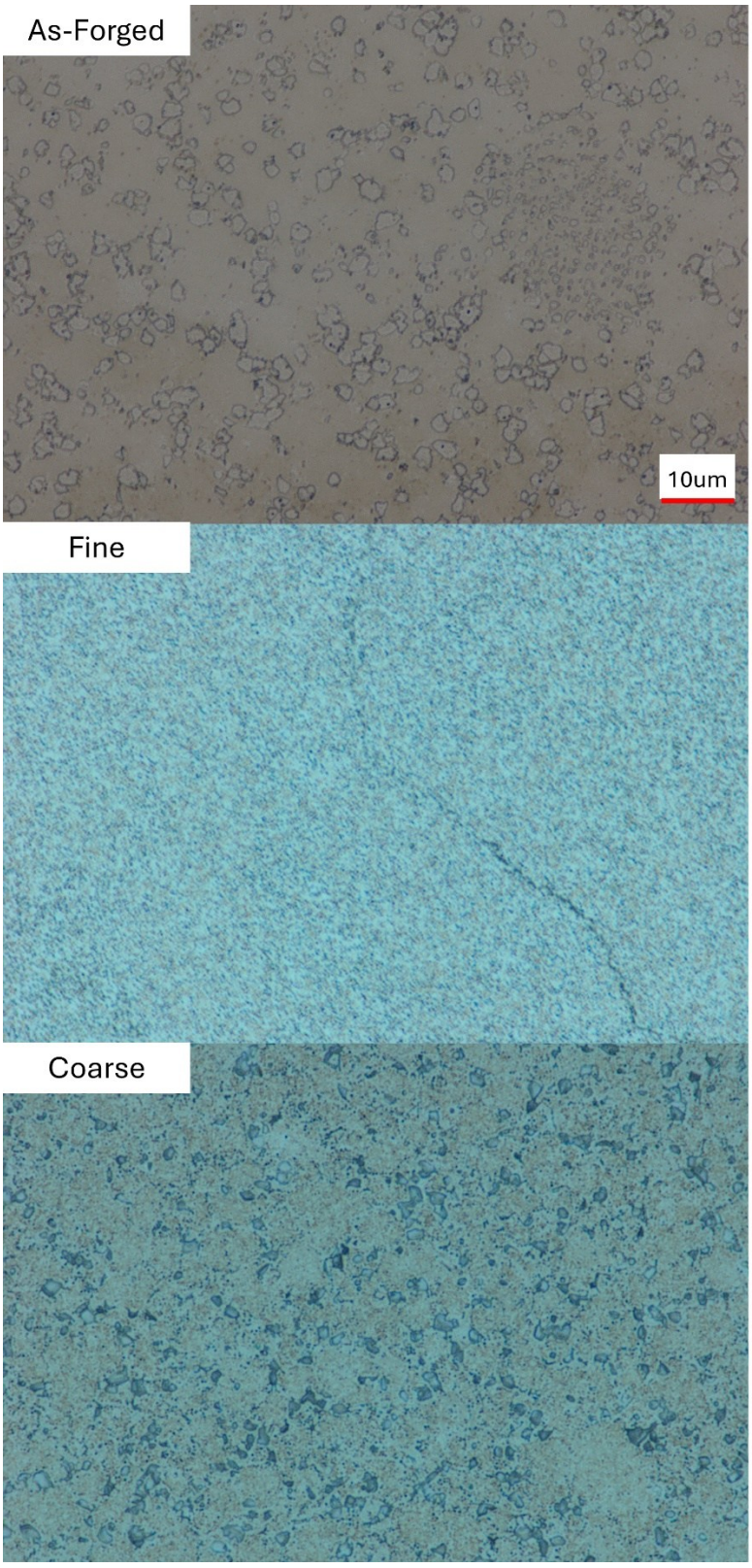


Figure 114: High magnification optical micrographs of RR1000 samples.

5.13.2 SEM Micrographs

The images obtained using SEM are shown in Figure 115 and Figure 116. The grain boundaries were much clearer, even at lower magnifications, but there was otherwise no observable difference compared to the optical micrographs. However, at 2000x magnification, the variations between the sample microstructures are more noticeable. The secondary γ' is indeed present in the AF sample, though it hadn't been visible in the optical images. There is also a more noticeable difference between the AF and fine grain samples, where the as-forged does less uniform size of primary γ' than the fine grain – and in general, it appears to be slightly larger. Indeed, the shape and size of the primary γ' in the as-forged sample is quite varied; some are smaller than those in the fine grain, others are of a comparable size, and a few appear on the cusp of breaking down into smaller particles (or could alternatively be γ' nuclei). The images at 10,000x magnification also appear to show the differences in the primary γ' morphology between the fine grain and as-forged, and that there are larger primary γ' particles present in the as-forged samples.

Observations in terms of the secondary γ' phase in the samples can also be made at this magnification. The as-forged sample in particular exhibits an interesting morphology of the secondary γ' compared to the fine grain – the particles seem smaller in general, which is consistent with the absence of the ageing process (which would result in a larger particle size and more uniform distribution). The secondary γ' precipitates themselves also seem to be rounder in the as-forged, and also have the tendency to merge into each other, almost as a ratcheting effect (which could potentially be for strain relief), rather than forming the petal-like morphology seen in the fine- and coarse-grain. Images at this magnification also confirms the absence of tertiary γ' in the as-forged sample, as expected.

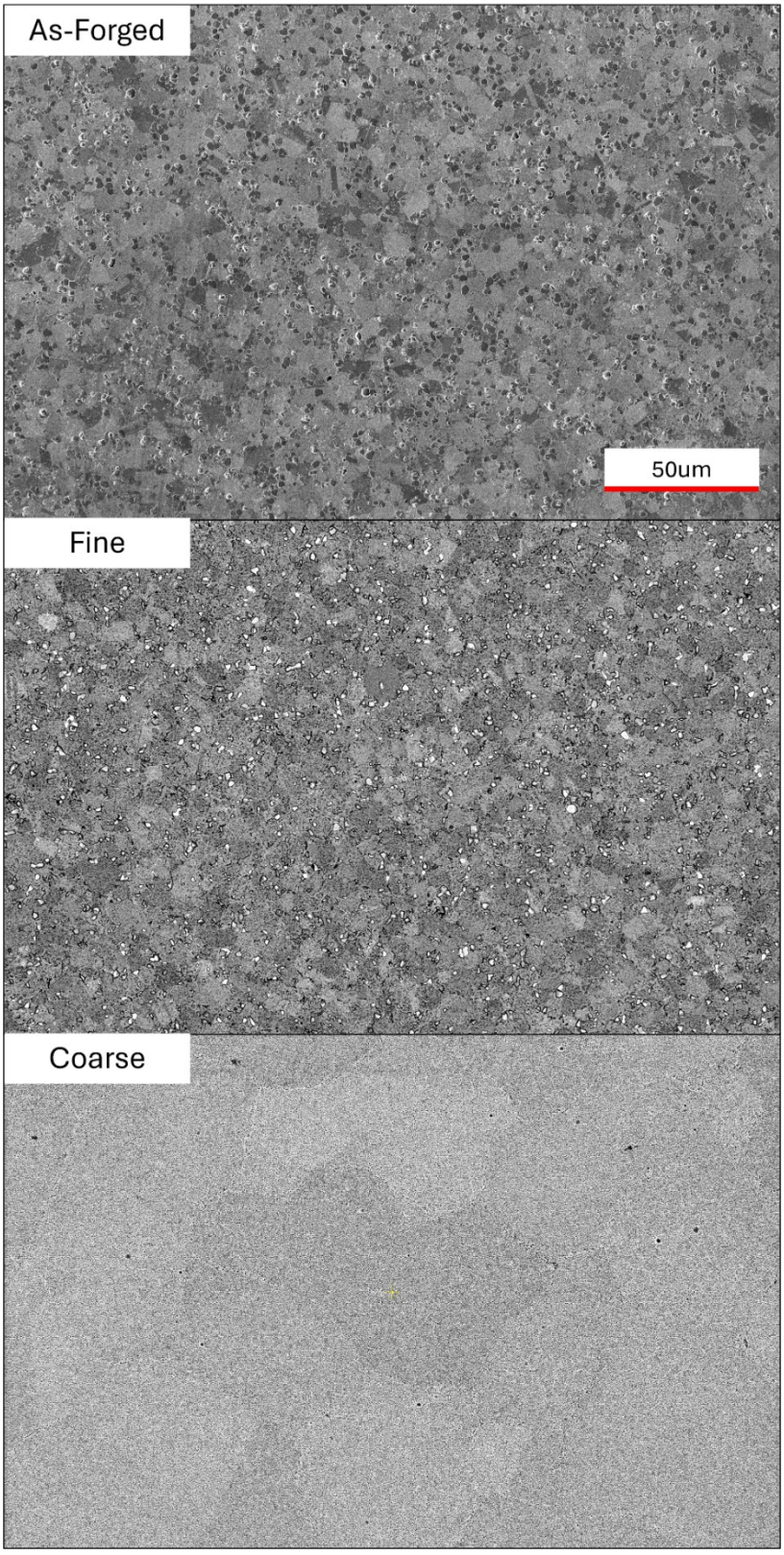


Figure 115: Low magnification SEM micrographs of RR1000 samples.

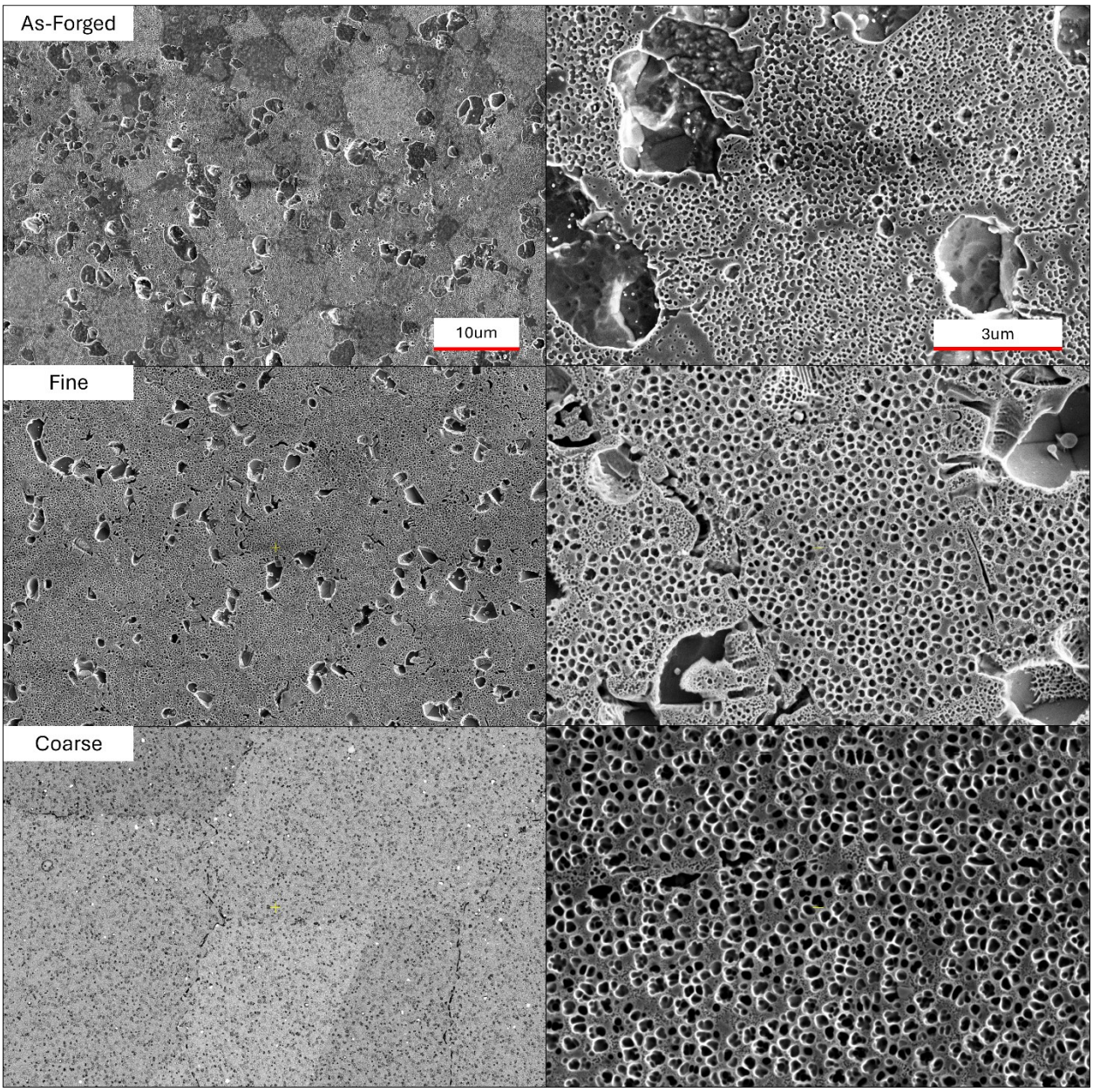


Figure 116: High magnification SEM micrographs of RR1000.

5.13.3 Attenuation Analysis

As the V00 measurements of the as-forged and coarse grain sample were so similar despite their clear differences in microstructure – with the as-forged having primary γ' and a finer grain size, compared to the latter having only secondary γ' – an analysis of the attenuation behaviours of these RR1000 samples was carried out, using the same methodology as for the Udimet 720Li samples. It was predicted that the coarse grain sample would have the highest level of attenuation, due to its larger grain size. This was indeed the case, as shown in Table 30 which shows the amplitudes of the successive reflections in the first arrival group of signals. The coarse grain signals decay rapidly, to the extent that no peak beyond the 5th reflection could be detected. It is also interesting to note that the fine grain sample is slightly less attenuative than the as-forged. This suggests that the non-uniformity of the precipitation does influence the ultrasonic wave propagation through the material; it may be that the presence of bigger and less regular shaped primary γ', such as in the as-forged condition, would be causing increased levels compared to the much more uniformly distributed precipitate in the fine grain structure. Despite the fact that the V00 values for the as-forged and coarse grain samples have converged to the same value, it has been demonstrated that these V00 measurements could be used in combination with quick attenuation analysis to determine, first, the grain size of the sample, before deducing whether the material was therefore fine grain, but in the as-forged condition (or similar), implying that further processing was required, or if it was coarse grain and had been manufactured and processed correctly.

Table 30: Amplitudes of successive first arrival signals for RR1000 samples.

Peak Number	As Forged	Fine	Coarse
1	1160.31	1216.35	1247.36
2	109.31	111.35	72.36
3	97.31	98.35	39.36
4	84.31	86.35	22.36
5	71.31	71.35	13.36
6	58.31	58.35	
7	48.31	47.35	
8	37.31	38.35	
9	31.31	32.35	
10	25.31	27.35	
11	20.31	22.35	

5.14 RR1000 Experiments: Discussion

The extensive metallurgical investigations have been conducted here in order to understand as fully as possible the microstructures of the materials being tested, and to link these observations to the trends and behaviours of the ultrasonic wave speed measurements. (ImageJ was again used for the micrographs to assess the amount of γ' phase present in each sample, but with the same inconsistent results seen for the previous superalloys with results for the total amount of γ' varying between around 14 to 50%; it was also not possible to distinguish accurately between the different morphologies of the γ' phase. These have therefore not been included here, but the full results are given in the Appendix.)

The V00 results for the RR1000 samples are not quite as straightforward to interpret as expected; the differences between the fine and coarse grain wave speeds could have been explained by the differences in amount of primary γ', but the additional data from the as-forged sample – and the fact it matches well with the coarse grain disc – means that it is not solely the primary γ' affecting these measurements (if at all). The V00 is indicative of changes in the phase composition of the material, via the effect of these changes on the elastic stiffness; these results show clearly that

there is a difference in the overall SCECs of the fine grain RR1000, compared to the coarse grain and as-forged conditions. However, the cause of the difference is uncertain; it may be caused by minor chemical compositional differences in the γ' phase, which can also contain iron and chromium [250] as mentioned in Chapter 4 (though its stoichiometric composition is $Ni_3(Ti,Al)$).

There is also the previously discussed possibility that some of these elements being removed from the matrix to form precipitates may be reducing the solid solution strengthening; in the case of the coarse grain RR1000, for example, the excessive formation of the secondary γ' could be causing this effect. The fact that the secondary γ' in the coarse grain RR1000 is relatively large implies that more of these elements are being drawn out from the matrix compared to the fine grain sample. Using a similar rationale, the as-forged RR1000 may be showing an overall lower V00 due to the presence of the much larger primary γ', as well as the smaller secondary γ', drawing out more of the elements of the matrix and hindering the overall stiffness of the material.

It may also be the case that the morphologies and structures of each type of γ' may be influencing the overall crystal structure and its stiffness – for example, a more complex shape such as the octodendritic morphology of the secondary γ' in the coarse grain RR1000 sample may be reducing the overall stiffness, in contrast to more regular spherical precipitates.

As stated previously for the δ phase in Inconel 718, it is unlikely that the precipitates are causing a retarding effect which is causing a reduction in overall wave speed, as the V00 measurements are only directly affected by phase composition and resultant effects on stiffness. Any retarding effect, or increase in scattering and energy loss, would be affecting the attenuation characteristics of the material, but comparisons between the peak amplitudes of the first arrival signals did not show any significant difference between the as-forged and fine grain samples.

Although the fundamental theoretical assumption of the UWS method, and the results, suggest that V00 measurements could be independent of grain size (from comparing as-forged and coarse samples), the differing contributions from other potential influences have not been unambiguously differentiated in their contributions; these include including grain size and grain boundary constraints, phase (both in terms of composition and morphology), and chemistry spatial variation. A key assumption which has been made involves the law of mixtures [335] in estimating the volume fraction of each phase within a dual phase material using the V00 measurements, as illustrated by Equation 6. However, this may not be applicable in all scenarios – for example, if there is a large

amount of precipitate present in one localised region, having a strong effect on the local stiffness (and hence V00). Similarly, if a precipitate has formed within a smaller grain, it may have a greater effect on the local stiffness than if it were within a much larger grain. The grain boundaries themselves may have differing amounts of influence on the elastic stiffness – within finer grains, where there are many more boundaries present than for coarser grains, which could increase the effect on the stiffness 'observed' by the ultrasonic waves [336]. Grain boundary constraints can also affect the morphology of the precipitates formed [337]; indeed, it may be the case that certain precipitate morphologies have a greater impact on the overall stiffness of the material than others – with the γ' within RR1000, a range of morphologies (including spherical and octodendritic) have been observed.

However, despite the underlying cause of the differences between the V00 being uncertain, these investigations suggest that the UWS technique can be used to detect variations – even subtle changes – between the microstructures of these three samples. It was interesting to find that, despite the overall volume fraction of the γ' precipitate being the same across all samples, there were distinct values of V00 for each of the sample conditions. The fact that the fine grain RR1000 and as-forged sample can be very clearly distinguished is a key result; it could be used in the future to determine whether, having been subjected to the solution treatment and ageing process, a fine-grain RR1000 sample does have the required microstructure (giving a much higher V00 than the original), or if there is further analysis and material modification required.

In the future, it is hoped that quasi-static simulations using Finite Element Analysis, combined with Euler angle data from EBSD scans, can be used to investigate the impact of various precipitate morphologies on the ultrasonic wave propagation through the material. This is just one of the exciting further areas of investigation which could be pursued in order to develop and refine the UWS technique for phase composition estimations in nickel-based superalloys. However, the investigations over the course of this EngD have also proved the effectiveness of the V00 technique in detecting microstructural variations in nickel-based superalloys even in its current configuration, with potential to be applied in a variety of industrial scenarios.

6. Industrial Relevance of EngD Research

When the scope of this EngD was originally proposed, the main application in mind was towards the microstructural characterisation of blisks, which are key jet engine components replacing individual blades and discs in compressor with a single part and which contribute to the overall reduction in weight of a jet engine. Over the course of this project, however, other areas in which the UWS measurements may be advantageous have emerged, including some more general applications. One example is the assessment of parts for concessions; for example, if there has been a slight manufacturing defect, it would be highly beneficial to assess rapidly (and non-destructively) whether the part was still fit for purpose, or if its mechanical properties no longer conformed to the standards required.

The fact that Udimet 720Li in particular was a notoriously difficult nickel-based superalloy to inspect was discussed in Chapter 5, due to various microstructural effects such as segregation, recrystallisation and the presence of white spots. Although the latter is more of an issue for defect detection due to its masking effect, the UWS experiments here appeared unaffected by these phenomena; indeed, it was found that the V00 measurements converged after only 10 trials, thus demonstrating that refinement of these measurements and further analysis into the link between phase composition and the V00 values could result in a rapid and reliable characterisation method of Udimet 720Li in the future. This could be particularly useful when assessing a large billet for γ' content across the section, and identifying optimal regions from which components could be machined.

A more general application where this technique could be deployed involves the assessment of rectilinear forgings, or 'Condition of Supply' (CoS) shapes, to investigate the quality of the forging with respect to the material inhomogeneity. These rectilinear forgings, from which critical parts (such as discs, shafts and spacers) are machined, are also known as ultrasonic shapes; this is due to their geometry being designed specifically for ultrasonic inspection, with low curvature (or rectilinear) contours to ensure that the transducer can be kept in uniform contact with the surface, and can be maintained close to normal to an ultrasonic beam during inspection prior to the machining of the part [338]. An example of such a forging is shown in Figure 117; the differences in phase proportions within these forgings could be detected through the V00 measurements, with the attenuation behaviour of the first arrival signals used to assess the grain size.

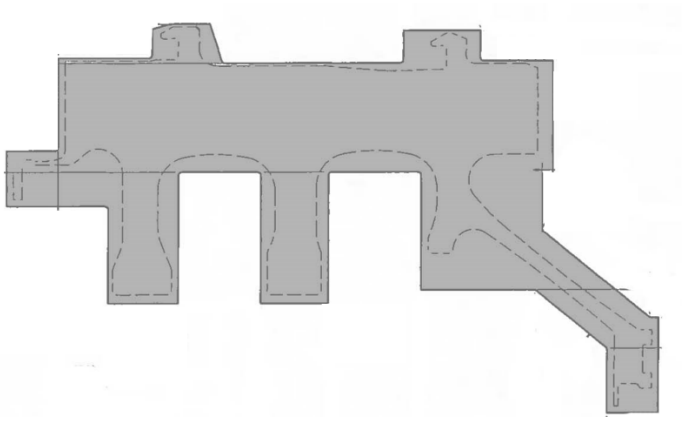


Figure 117: An example sketch (not to scale) of a rectilinear forging, where the dotted outline within the shape is that of the final component.

An additional application could be towards the inspection of components which have been exposed to overtemperature conditions, to investigate whether their microstructure has been damaged to the extent it is no longer fit for purpose, or whether the required precipitates and their morphology is still present for the required mechanical properties. Further work to pursue this particular use of the UWS technique could involve exposing samples with the same original microstructure to varying temperatures exceeding operational levels for different periods of time, and correlating these to V00 measurements to the microstructures revealed through metallurgical investigations (including microscopy and hardness).

A more recent development in the maintenance and repair of jet engines has been the emergence of additive repair of components, including the previously mentioned blisks; this has the benefit of reducing time and cost (compared to replacing the component entirely), as well as material wastage [339] [340] [341]. The use of this UWS technique could be used to inspect parts which had been additively repaired, to determine whether the correct microstructure had been developed in the newly added regions, and that there was good consistency between the existing, original areas of the blisk.

Finally, although this research has been predominantly focussed on nickel-based superalloys widely used within the aerospace industry, the UWS method could be deployed on a range of different materials within this family which are key to other industries; for example, Inconel 82, which is widely used for welds in nuclear reactors. Although the current experimental setup is limiting in terms of sample geometry where parallelism is required, the theoretical framework is not

constrained to this method of wave speed acquisition; if alternative ultrasonic wave speed measurement techniques were used instead of the immersion tank, such as diffuse ultrasound, there could be more complex geometries inspected (as is often the case with components in industry). Additionally, this could minimise the movement of the sample which would be required, if the wave speeds in multiple directions could be detected instead using multiple sensors rather than the rotation and tilting of the part. Alternative ultrasonic wave speed acquisition techniques are discussed further in the Future Work section.

7. Conclusions

Over the course of this EngD, three different nickel-based superalloys have been used to develop a non-destructive technique, using ultrasonic wave speed measurements, for the microstructural characterisation of this family of materials. More specifically, it was of interest to investigate whether the phase composition, in terms of the volume percentage of precipitates present, could be determined using a theoretical framework based on a spherical harmonic expansion, utilising the zeroth spherical harmonic coefficient of velocity (denoted V00) – an average of ultrasonic wave speeds through the material in all 3D propagation directions.

Having firstly carried out a feasibility study using Inconel 718, the fact that the V00 parameter was sensitive to phase changes within the material was clearly demonstrated; measurements taken from samples in the as-received condition showed a significantly higher V00 than those subjected to heat damage, which had none of the δ precipitate (the particle of interest) present.

Following this successful outcome, further samples of Inconel 718 were furnace treated with more specific heat treatment programmes to manipulate the microstructures, such that there were discs with none of the δ phase present, with others having the maximum possible. The different microstructures were immediately apparent from both conventional microscopy techniques, as well as high-speed atomic force microscopy, but the V00 outcomes were not as predicted; it was originally proposed that the larger amount of the δ phase, which is stiffer than the main γ matrix, would result in higher overall wave speeds through the material, but the opposite was observed. It was therefore concluded that there may be other microstructural phenomena contributing to these measurements, such as solid solution strengthening (or the reduction thereof), on the ultrasonic waves. These investigations highlighted the fact that the precipitation behaviour and morphology

could be having an impact previously not considered on the V00 measurements, via the fact that if the volume fraction of a precipitate was overly excessive it would deplete the matrix of solid solution strengthening elements, reducing the stiffness of the overall material.

A further observation from experiments using Inconel 718 showed that, despite using the TTT diagrams in the literature and best practices when heat treating and quenching the samples, the microstructure of Inconel 718 not straightforward to manipulate. Ultimately, it was not possible to generate samples with a purely dual phase microstructure (i.e. the δ phase and γ matrix only) due to the propensity of the γ'' phase to form on cooling, even when water quenched. As the proposed phase characterisation methodology is based on a dual phase microstructure, the further nickel-based superalloys to be investigated were selected specifically as they only had one major precipitate, the γ', in addition to the main γ matrix.

The first of these materials was Udimet 720Li, of which three discs in the as-forged condition were extracted from various locations of the same 9-inch diameter billet. Given that this superalloy was infamous for its microstructural inhomogeneity across and through the billet, it was of interest to investigate the extent of the V00 method sensitivity in detecting microstructural variations between each sample and whether the noisiness of the material, which impeded conventional ultrasonic inspection methods, would affect these measurements. Although it was found that the variation in V00 between each sample was still within the typical error bounds (~10m/s) of ultrasonic wave speed measurements, there were two samples which converged to more similar values (Part C and Part S) compared to the third, Part MR. Due to the good convergence of the V00 values over a relatively large number of experiments, it was unlikely that there would be large errors in these results. It could therefore be concluded that the UWS technique was able to detect even minor variations in the microstructure, in terms of overall chemical composition. It is likely that the variations in V00 was due to slight differences in the overall amount of γ' present, though it may also have been due to slight differences in chemistry of the γ' precipitates (though this is less likely). Indeed, despite a more quantitative approach not being possible, the micrographs obtained indicated that Part MR may have an overall slightly higher amount of γ' than the other two samples, resulting in overall higher wave speeds.

The V00 measurements appeared unaffected by the inhomogeneity in microstructure shown across the samples, where – particularly in Part S – there a large number of smaller γ' clusters of γ'. In addition, the fact that the V00 measurements were all quite similar was a positive indication that

the method was accurately indicating the phase characteristics, as, having originated from the same billet, the total amount of γ' should be around the same across the samples.

However, these experiments did result in a new direction to explore with respect to the UWS method – whether or not the morphology of a precipitate had an impact on the V00 measurements, in terms of its effect on the single crystal elastic constants, or SCECs. One scenario may be that a smaller volume fraction of γ', but in greater amounts may be drawing more of the Al and Ti out of the γ matrix which would otherwise contribute to solid solution strengthening, compared to the larger primary γ' particles present in lower numbers.

In order to investigate this, the final nickel-based superalloy selected for experiments was RR1000. Being a powder metallurgy nickel-based superalloy, this gave a much cleaner ultrasonic response compared to Udimet 720Li due to its homogeneous microstructure, and it would be possible to investigate solely the effect of the precipitate morphology on the V00 measurements. Three discs in different conditions were examined – fine- and coarse-grain, as well as in the as-forged conditions. Much like the three discs of Udimet 720Li, the total amount of the γ' precipitate is the same regardless of the condition (around 45%), with the breakdowns of each morphology being different depending on the processing history.

In the absence of the as-forged result, it appeared that the results were very straightforward to interpret, with the fine-grain having a significantly higher V00 than the coarse-grain; from two samples alone, it could have been concluded that the primary γ' had a significant effect on the measurements (comparing the 15% in fine-grain to the 0% in coarse-grain), and that the V00 method may not be suitable for detecting the overall volume fraction of a particular precipitate if it was present in various morphologies, but was effective in detecting differences in the amount of primary γ'. However, the fact that the as-forged V00 was almost identical to that of the coarse grain introduced some uncertainty into this conclusion, due to the fact that it had a similar volume fraction of primary γ' to the fine-grain sample, whereas the coarse grain sample had none; it was therefore not solely the amount of primary γ' (if at all) which was having an impact on the V00 results.

Having studied the microstructure of the samples of RR1000, including the expected proportions of each type of γ', it has been proposed that the morphology may be having an impact on the V00 measurements via affecting the different SCECs of the material that the amounts of each kind

result in. Although the exact reason is uncertain, it may be that their shape, as well as size, affects the stiffness of the overall matrix, either by the nature of its shape and fit within the matrix, or the amount and mechanism by which it extracts Al and Ti from the matrix. These V00 measurements could be used in conjunction with investigating the attenuation behaviour of the material – for example, to determine first whether a sample was fine or coarse grain, before proceeding to use V00 values to conclude whether it was in the correct condition for a coarse grain specification, or whether it was still closer to the as-forged condition and required some additional processing.

Ultimately, the microstructures of the nickel-based superalloys examined were far from trivial and the quantification of phase composition within these materials has not been straightforward; nevertheless, these investigations have been able to successfully demonstrate some key strengths and characteristics of the method, The V00 measurements are sensitive to variations in phase composition within nickel-based superalloys;

- These V00 measurements are independent of grain size – demonstrated clearly by the as-forged and fine grain samples of RR1000 – and texture;
- There is a good convergence to a mean value of V00 after 10 trials;
- The morphology and precipitation behaviour of a particular phase may have an impact – such as effects seen from the excessive δ phase in Inconel 718, and the various microstructures of both Udimet 720Li and RR1000.

In addition, it has been possible to begin the establishment of an expected range of V00 values for some various microstructures across these three nickel-based superalloys, which has been useful in working towards building up a database for a materials characterisation framework using a combination of techniques; the application of the UWS method, in conjunction with hardness tests and microscopy was demonstrated to form a very powerful materials characterisation framework when investigating the various microstructures of Inconel 718, as illustrated in Figure 118. The combination of these techniques were successfully deployed in discovering the fact that the original discs had not been fully aged, and therefore had microstructures not fit for purpose in industrial applications. In the case of RR1000, the addition of a brief attenuation analysis also contributed to this framework, and demonstrated its place in potential materials characterisation by establishing the grain size within the material.

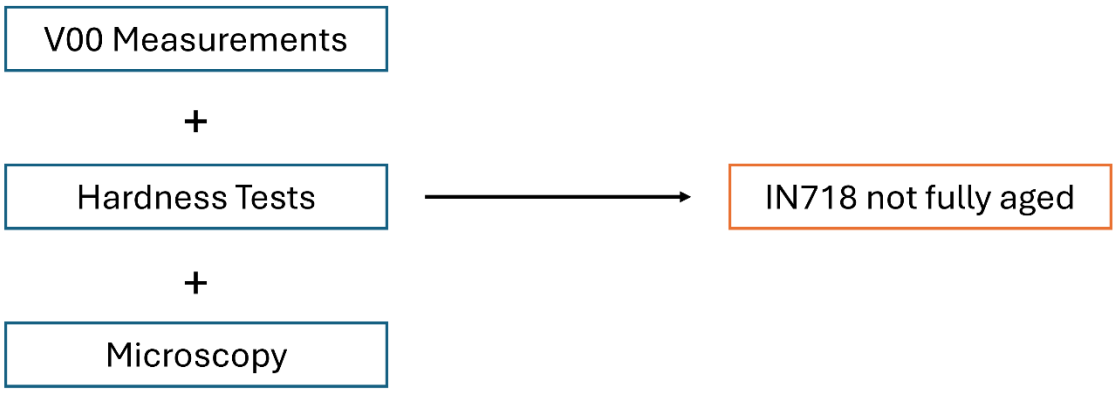


Figure 118: Illustration of a potential materials characterisation framework.

7.1 Future Work

Through carrying out these V00 investigations, there have also arisen some potential future developments to improve and refine the method –

- To what extent is the V00 sensitive to variations in phase composition? (I.e. in Udimet 720Li, were these subtle differences in V00 values sufficient in determining that there were microstructural variations?)
- To what extent does the morphology of a phase have an impact on the V00 measurements, and how is it affecting the SCECs of the material depending on its type?
- Is there a more accurate and objective technique to estimate the amount of precipitate present from a micrograph, given that ImageJ was somewhat subjective and often inconsistent and EBSD scans were not able to effectively detect the different phases? (Atom probe microscopy may be a suitable alternative to EBSD, if the access can be acquired.)

The use of modelling could also be extremely useful in investigating, and differentiating between, the effects caused by material influences on stiffness previously mentioned in Chapter 5, including grain size, grain boundary constraint, and phase content and morphology. One modelling simulation could be to determine how the size of the grain influences the local effect on stiffness of a precipitate present; another to model the theoretical effect of varying morphologies of a precipitate with a given stiffness within a grain.

If these further work areas could be pursued in more detail, this V00 technique has the potential to form a part of a powerful materials characterisation tool for industry; if, for example, it was used in conjunction with diffuse ultrasound, the limitation of sample geometry would be lifted. (The diffuse ultrasound theory is well described by Ahn et al [342] and Gao et al [343]; essentially, rather than directly measuring the ultrasonic wave speed, a finite time interval elapses which allows for the wave components to decompose into incoherent diffuse fields, which can then be analysed via correlation in either the time or frequency domains.) Indeed, even in its current form with the results and conclusions from investigations presented here, there is already evidence of potential applications within industry. It is hoped that, in the future, this framework will contribute to the field of non-destructive evaluation for materials characterisation, enabling faster, safer and more efficient design and monitoring of aerospace engine components for many years to come.

8. References

[1] S. L. Soo, R. Hood, D. K. Aspinwall, W. E. Voice and C. Sage, "Machinability and surface integrity of RR1000 nickel based superalloy," *CIRP Annals - Manufacturing Technology,* vol. 60, no. 1, pp. 89-92, 2011.

[2] K. Mahesh, J. T. Philip, S. N. Joshi and B. Kuriachen, "Machinability of Inconel 718: A critical review on the impact of cutting temperatures," *Materials and Manufacturing Processes,* vol. 36, no. 7, pp. 753-791, 2021.

[3] E. O. Ezugwu, "Key improvements in the machining of difficult-to-cut aerospace superalloys," *International Journal of Machine Tools and Manufacture,* vol. 45, pp. 1353-1367, 2005.

[4] D. Umbrello, "Investigation of surface integrity in dry machining of Inconel 718," *The International Journal of Advanced Manufacturing Technology,* vol. 69, pp. 2183-2190, 2013.

[5] K. C. Mills, Recommended Values of Thermophysical Properties for Selected Commercial Alloys, Sawston, UK: Woodhead Publishing, 2002.

[6] C. F. Yao, Q. C. Jin, X. C. Huang, D. X. Wu, J. X. Ren and D. H. Zhang, "Research on surface integrity of grinding Inconel718," *The International Journal of Advanced Manufacturing Technology,* vol. 65, pp. 1019-1030, 2013.

[7] R. Arunachalam and M. A. Mannan, "MACHINABILITY OF NICKEL-BASED HIGH TEMPERATURE ALLOYS," *Machining Science and Technology,* vol. 4, no. 1, pp. 127-168, 2000.

[8] J. J. Schirra and D. V. Viens, "Metallurgical Factors Influencing the Machinability of Inconel 718," *Superalloys 718, 625, 706 and Various Derivatives,* pp. 827-838, 1994.

[9] Z. F. Liu and S. M. He, "Experiment investigation of superfine deep hole drilling mechanism for high temperature alloy 718," *Materials Research Innovations,* vol. 17, pp. 229-233, 2013.

[10] R. Thirumalai, J. S. Senthilkumaar, P. Selvrarani, R. M. Arunachalam and K. M. Senthilkumaar, "Investigations of surface roughness and flank wear behaviour in machining of Inconel 718," *Australian Journal of Mechanical Engineering,* vol. 10, no. 2, pp. 157-168, 2012.

[11] F. Jafarian, M. Imaz Ciaran, D. Umbrello, P. J. Arrazola, L. Filice and H. Amirabadi, "Finite element simulation of machining Inconel 718 alloy including microstructure changes," *International Journal of Mechanical Sciences,* vol. 88, pp. 110-121, 2014.

[12] R. C. Reed, The Superalloys: Fundamentals And Applications, Cambridge: Cambridge University Press, 2008.

[13] A. Amiri, S. Bruschi, M. Hossein Sadeghi and P. Bariani, “Investigation on hot deformation behavior of Waspaloy,” *Materials Science and Engineering: A,* vol. 562, pp. 77-82, 2013.

[14] S. Utada, R. Sasaki, R. C. Reed and Y. T. Tang, “Overheating of Waspaloy: Effect of cooling rate on flow stress behavior,” *Materials & Design,* vol. 221, p. 110911, 2022.

[15] F. Liu, J. Chen, J. Dong, M. Zhang and Z. Yao, “The hot deformation behaviors of coarse, fine and mixed grain for Udimet 720Li superalloy,” *Materials Science and Engineering: A,* vol. 651, pp. 102-115, 2016.

[16] L. Chang, H. Jin and W. Sun, “Solidification behavior of Ni-base superalloy Udimet 720Li,” *Journal of Alloys and Compounds,* vol. 653, pp. 266-270, 2015.

[17] M. P. Jackson and R. C. Reed, “Heat treatment of UDIMET 720Li: the effect of microstructure on properties,” *Materials Science and Engineering: A,* vol. 259, no. 1, pp. 85-97, 1999.

[18] D. E. P. Klenam and W. O. Soboyejo, “Cyclic Loading and Fatigue,” in *Comprehensive Structural Integrity (Second Edition)*, The Netherlands, Elsevier, 2023, pp. 116-145.

[19] R. Viswanathan, J. F. Henry, J. Tanzosh, G. Stanko, J. Shingledecker, B. Vitalis and R. Purgert, “U.S. program on materials technology for ultra-supercritical coal power plants,” *Journal of Materials Engineering and Performance,* vol. 14, pp. 281-292, 2005.

[20] C. Jang, J. Lee, J. S. Kim and T. E. Jin, “Mechanical property variation within Inconel 82/182 dissimilar metal weld between low alloy steel and 316 stainless steel,” *International Journal of Pressure Vessels and Piping,* vol. 85, no. 9, pp. 635-646, 2008.

[21] G. Panneerselvam, S. Raju, R. Jose, K. Sivasubramanian, R. Divakar, E. Mohandas and M. P. Antony, “A study on the thermal expansion characteristics of Inconel-82® filler wire by high temperature X-ray diffraction,” *Materials Letters,* vol. 58, no. 1-2, pp. 216-221, 2004.

[22] M. Nur Dogu, K. Davut, M. Ahmed Bbeidi, M. Alp Yalcin, H. Gu, T. Song En Low, J. Ginn and D. Brabazon, “Recrystallization and grain growth kinetics of IN718 manufactured by laser powder bed fusion,” *Journal of Materials Research and Technlogy,* vol. 19, pp. 4242-4257, 2022.

[23] European Commission, “Flightpath 2050 – Europe’s vision for aviation – Maintaining global leadership and serving society’s needs,” Publications Office of the European Union, Luxembourg, 2011.

[24] K. W. Bushell, “Jet and Gas Turbine Engines,” in *Encyclopedia of Physical Science and Technology (Third Edition)*, Cambridge, MA, USA, Academic Press, 2003, pp. 127-152.

[25] L. S. Langston, “Turbines, Gas,” in *Reference Module in Earth Systems and Environmental Sciences*, Heidelberg, Elsevier, 2014, pp. 221-230.

[26] N. A. Cumpsty, Jet Propulsion: A Simple Guide to the Aerodynamic and Thermodynamic Design and Performance of Jet Engines, Cambridge: Cambridge University Press, 1997.

[27] C. L. Proctor II, "Internal Combustion Engines," in *Encyclopedia of Physical Science and Technology (Third Edition)*, Cambridge, MA, USA, Academic Press, 2003, pp. 33-44.

[28] M. C. e. a. Hardy, "Developing Alloy Compositions for Future High Temperature Disk Rotors," in *Superalloys 2020*, Warrendale, PA, TMS (The Minerals, Metals & Materials Society), 2020, pp. 19-30.

[29] D. Anderson, "Fuel Conservation - Operational Procedures for Environmental Performance," Boeing Commercial Airplanes, Seattle, WA, 2006.

[30] Rolls-Royce plc, "Trent XWB," Rolls-Royce plc, Derby, 2018.

[31] M. C. Hardy, M. Detrois, E. T. McDevitt, C. Argyrakis, V. Saraf, P. D. Jablonski, J. A. Hawk, R. C. Buckingham, H. S. Kitaguchi and S. Tin, "Solving Recent Challenges for Wrought Ni-Base Superalloys," *Metallurgical and Materials Transactions A,* vol. 51A, pp. 2626-2650, 2020.

[32] M. C. Hardy, B. Zirbel, G. Shen and R. Shankar, "Developing damage tolerance and creep resistance in a high strength nickel alloy for disc applications," in *Superalloys 2004*, Warrendale, PA, TMS (The Minerals, Metals & Materials Society), 2004, pp. 83-90.

[33] W. Voice, M. Hardy and D. Rugg, "Powder Prospects 'Set for Takeoff' as production methods change," *Metal Powder Report,* vol. 60, no. 4, pp. 8-12, 2005.

[34] Rolls-Royce plc, "Engine cutaway posters," Rolls-Royce plc, 2019. [Online]. Available: https://www.flickr.com/photos/rolls-royceplc/47510998232/in/album-72157679774812878/. [Accessed 8 July 2024].

[35] D. Furrer and H. Fecht, "Ni-based superalloys for turbine discs," *The Journal of The Minerals, Metals & Materials Society,* vol. 51, pp. 14-17, 1999.

[36] R. Watson, "Abnormal Grain Coarsening in Inconel 718 Aero-Engine Disc Forgings (PhD Thesis)," University of Manchester, Manchester, 2016.

[37] J. H. Jobling, E. A. Saunders, T. Barden, M. J. S. Lowe and B. Lan, "A feasibility study on phase characterisation of nickel-based superalloys using ultrasound," *NDT&E International,* vol. 145, p. 103120, 2024.

[38] Rolls-Royce plc, "Rolls-Royce ships 10,000th blisk from Oberursel," Rolls-Royce plc, 11 April 2019. [Online]. Available: https://www.rolls-royce.com/media/press-releases/2019/11-04-2019-ships-10000-blisk-from-oberursel.aspx. [Accessed 8 July 2024].

[39] O. Younossi, M. V. Arena, R. M. Moore, M. A. Lorell, J. Mason and J. C. Graser, Military Jet Engine Acquisition: Technology Basics and Cost-Estimating Methodology, Santa Monica, CA: RAND Corporation, 2003.

[40] A. J. Schwartz, M. Kumar, B. L. Adams and D. P. Field, Electron Backscatter Diffraction in Materials Science, Berlin: Springer, 2009.

[41] H. L. Eiselstein, "Metallurgy of Columbium-Hardened Nickel-Chromium-Iron Alloy," *Advances in the Technology of Stainless Steel and Related Alloys,* vol. 369, pp. 62-77, 1965.

[42] A. Szczotok, "Quantitative evaluation of carbides in nickel-base superalloy MAR-M247," *IOP Conference Series: Materials Science and Engineering,* vol. 22, p. 012007, 2011.

[43] M.-A. Charpagne, P. Vennegues, T. Billot, J.-M. Franchets and N. Bozzolo, "Evidence of multimicrometric coherentγ'precipitatesin a hot-forgedγ–γ'nickel-based superalloy," *Journal of Microscopy,* vol. 263, no. 1, pp. 106-112, 2016.

[44] J. Sharma, A. Nicolay, M. De Graef and N. Bozzolo, "Phase discrimination between δ and η phases in the new nickel-based superalloy VDM Alloy 780 using EBSD," *Materials Characterization,* vol. 176, p. 111105, 2021.

[45] A. B. Parsa, M. Ramsperger, A. Kostka, C. Somsen, C. Korner and G. Eggeler, "Transmission Electron Microscopy of a CMSX-4 Ni-Base Superalloy Produced by Selective Electron Beam Melting," *Metals,* vol. 6, no. 11, p. 258, 2016.

[46] B. Lan, T. Ben Britton, T.-S. Jun, W. Gan, M. Hofmann, F. P. Dunne and M. J. S. Lowe, "Direct volumetric measurement of crystallographic texture using acoustic waves," *Acta Materialia,* vol. 159, no. 1, pp. 384-394, 2018.

[47] M. P. Jackson and R. C. Reed, "Heat treatment of UDIMET 720Li: the effect of microstructure on properties," *Materials Science and Engineering: A,* vol. 259, no. 1, pp. 85-97, 1999.

[48] S. Sharples, M. Clark and M. G. Somekh, "Spatially resolved acoustic spectroscopy for fast noncontact imaging of material microstructure," *Optic Express,* vol. 14, pp. 10435-10440, 2006.

[49] M. Clark, S. D. Sharples and M. G. Somekh, "Fast, all-optical Rayleigh wave microscope imaging on isotropic and anisotropic materials," *IEEE Transactions on Ultrasonics Ferroelectrics and Frequency Control,* vol. 47, no. 1, pp. 65-74, 2000.

[50] W. Li, J. Coulson, J. W. Aveson, R. J. Smith, M. Clark, M. G. Somekh and S. D. Sharples, "Orientation Characterisation of Aerospace Materials by Spatially Resolved Acoustic Spectroscopy," *Journal of Physics: Conference Series,* vol. 520, p. 012017, 2014.

[51] P. Dryburgh, R. Patel, D. M. Pieris, M. Hirsch, W. Li, S. D. Sharples, R. J. Smith, A. T. Clare and M. Clark, "Spatially Resolved Acoustic Spectroscopy for Texture Imaging in Powder Bed Fusion Nickel Superalloys," *45th Annual Review of Progress in Quantitative Nondestructive Evaluation,* vol. 2102, p. 020004, 2019.

[52] R. Patel, M. Hirsch, P. Dryburgh, D. Pieris, S. Achamfuo-Yeboah, R. Smith, R. Light, S. Sharples, A. Clare and M. Clark, "Imaging Material Texture of As-Deposited Selective Laser

Melted Parts Using Spatially Resolved Acoustic Spectroscopy," *Applied Sciences,* vol. 8, no. 10, p. 1991, 2018.

[53] S. A. Croxall, M. C. Hardy, H. J. Stone and P. A. Midgely, "The Microstructure of RR1000 Nickel-Base Superalloy: The FIB-SEM Dual-Beam Approach," in *1st International Conference on 3D Materials Science*, Warrendale, PA, TMS (The Minerals, Metals & Materials Society), 2012, pp. 215-220.

[54] D. N. Dunn, A. J. Kubis and R. Hull, "Quantitative Three-Dimensional Analysis Using Focused Ion Beam Microscopy," in *Introduction to Focused Ion Beams*, New York, NY, Springer-Verlag US, 2005, pp. 281-300.

[55] M. A. Groeber, B. K. Haley, M. D. Uchic, D. M. Dimiduk and S. Ghosh, "3D reconstruction and characterization of polycrystalline microstructures using a FIB–SEM system," *Materials Characterization,* vol. 57, no. 1, pp. 259-273, 2006.

[56] J. MacSleyne, M. D. Uchic, J. P. Simmons and M. De Graef, "Three-dimensional analysis of secondary gamma prime precipitates in René-88 DT and UMF-20 superalloys," *Acta Materialia,* vol. 57, no. 20, pp. 6251-6267, 2009.

[57] T. Link, S. Zabler, A. Epishin, A. Haibel and T. X. Bansal, "Synchrotron tomography of porosity in single-crystal nickel-base superalloys," *Materials Science and Engineering: A,* vol. 425, no. 1-2, pp. 47-54, 2006.

[58] A. Epishin, B. Camin, L. Hansen, A. Chyrkin and G. Nolze, "Synchrotron Sub-μ X-ray Tomography of Kirkendall Porosity in a Diffusion Couple of Nickel-Base Superalloy and Nickel after Annealing at 1250C," *Advanced Engineering Materials,* vol. 23, p. 2001220, 2021.

[59] J.-B. le Graverend, A. Jacques, J. Cormier, O. Ferry, T. Schenk and J. Mendez, "Creep of a nickel-based single-crystal superalloy during very high-temperature jumps followed by synchrotron X-ray diffraction," *Acta Materialia,* vol. 84, pp. 65-79, 2015.

[60] R. P. Turner, C. Panwisawas, Y. Lu, I. Dhiman, H. C. Basoalto and J. W. Brooks, "Neutron tomography methods applied to a nickel-based superalloy additive manufacture build," *Materials Letters,* vol. 230, pp. 109-112, 2018.

[61] B. M. B. Grant, E. M. Francis, J. Quinta da Fonseca, M. R. Daymond and M. Preuss, "Deformation behaviour of an advanced nickel-based superalloy studied by neutron diffraction and electron microscopy," *Acta Materialia,* vol. 60, no. 19, pp. 6829-6841, 2012.

[62] N. C. Ferreri, S. C. Vogel and M. Knezevic, "Determining volume fractions of γ, γ0, γ00, δ, and MC-carbide phases in Inconel 718 as a function of its processing history using an advanced neutron diffraction procedure," *Materials Science & Engineering A,* vol. 781, p. 139228, 2020.

[63] E. H. Lehmann, P. Vontobel, G. Frei and C. Bronnimann, “Neutron imaging - detector options and practical results,” *Nuclear Instruments and Methods in Physics Research A,* vol. 531, pp. 228-237, 2004.

[64] NDT Resource Center, “Nondestructive Testing,” Iowa State University, 2012. [Online]. Available: https://www.nde-ed.org/EducationResources/CommunityCollege/NDTIntro/cc_intro001.php. [Accessed 27 January 2020].

[65] W. Alobaidi, E. Alkuam, H. Al-Rizzo and E. Sandgren, “Applications of Ultrasonic Techniques in Oil and Gas Pipeline Industries: A Review,” *American Journal of Operations Research,* vol. 5, no. 1, pp. 274-287, 2015.

[66] M. Budimir, A. Mohimi, C. Selcuk and T.-H. Gan, “High temperature NDE ultrasound transducers for condition monitoring of superheated steam pipes in nuclear power plants,” in *Nuclear Energy for New Europe 2011*, Bovec, Slovenia, 2011.

[67] D. Stubbs, R. Cook, D. Erdahl, I. Fiscus, D. Gasper, J. Hoeffel, W. Hoppe, V. Kramb, S. Kulhman, R. Martin, R. Olding, D. Petricola, N. Power and J. Sebastian, “An automated ultrasonic system for inspection of aircraft turbine engine components,” *Insight - Non-Destructive Testing and Condition Monitoring,* vol. 47, no. 3, pp. 157-162, 2005.

[68] G. Hübschen, “7 - Ultrasonic techniques for materials characterization,” in *Materials Characterization Using Nondestructive Evaluation (NDE) Methods*, Sawston, UK, Woodhead Publishing, 2016, pp. 177-224.

[69] F. Lionetto, “Ultrasound for Material Characterization and Processing,” *Materials,* vol. 14, no. 14, p. 3891, 2021.

[70] Victor Aviation, “C-Scan Ultrasonic Testing,” Victor Aviation Service, Inc., 2016. [Online]. Available: https://www.victor-aviation.com/NDT-Production-Services/Ultrasonic-Inspection.php. [Accessed 8 July 2024].

[71] B. Lan, M. A. Carpenter, W. Gan, M. Hofmann, F. P. Dunne and M. J. Lowe, “Rapid measurement of volumetric texture using resonant ultrasound spectroscopy,” *Scripta Materialia,* vol. 157, no. 1, pp. 44-48, 2018.

[72] C. Kim, C. Hyun, I. Park and K. Jhang, “Ultrasonic characterization for directional coarsening in a nickel-based superalloy during creep exposure,” *Journal of Nuclear Science and Technology,* vol. 49, no. 4, pp. 366-372, 2012.

[73] P. Haldipur, “Material characterization of nickel-based superalloys through ultrasonic inspection,” Iowa State University, Ames, Iowa, 2006.

[74] C. Kim, “Creep damage characterization of Ni-based superalloy by acoustic nonlinearity,” *Progress in Natural Science: Materials International,* vol. 22, no. 4, pp. 303-310, 2012.

[75] J.-Y. Kim, L. J. Jacobs, J. Qu and J. W. Littles, "Experimental characterization of fatigue damage in a nickel-base superalloy using nonlinear ultrasonic waves," *Journal of the Acoustical Society of America,* vol. 120, no. 3, pp. 1266-1273, 2006.

[76] K. Suzuki, H. Ito, T. Inoue and H. Miura, "Creep damage process of Ni-Base Superalloy caused by stress-induced anisotropic atomic diffusion," *Journal of Solid Mechanics and Materials Engineering,* vol. 3, no. 3, pp. 487-497, 2009.

[77] H. K. D. H. Bhadeshia, "Rafting in Nickel Based Superalloys," University of Cambridge, [Online]. Available: https://www.phase-trans.msm.cam.ac.uk/2003/Superalloys/rafting.html. [Accessed 8 July 2024].

[78] B. Lan, M. Lowe and F. Dunne, "A spherical harmonic approach for the determination of HCP texture from ultrasound: A solution to the inverse problem," *Journal of the Mechanics and Physics of Solids,* vol. 83, pp. 179-198, 2015.

[79] R. Klinman, G. Webster, F. Marsh and E. Stephenson, "Ultrasonic prediction of grain size, strength, and toughness in plain carbon steel," *Ultrasonic Materials Characterization,* vol. 596, no. 1, p. 83, 1980.

[80] J. Saniie and N. Bilgutay, "Quantitative grain size evaluation using ultrasonic backscattered echoes," *The Journal of the Acoustical Society of America,* vol. 80, no. 6, pp. 1816-1824, 1986.

[81] P. Palanichamy, C. Subramania, P. Barat and D. Bhattacharya, "An NDT method for grain size determination in austenitic stainless steel," *Transactions of the Indian Institute of Metals,* vol. 41, no. 5, pp. 485-488, 1988.

[82] E. Papadakis, "Physical acoustics and microstructure of iron alloys," *International Metals Review,* vol. 29, no. 1, pp. 1-24, 1984.

[83] M. Rosen, L. Ives, S. Ridder, F. Biancaniello and R. Mehrabian, "Correlation between ultrasonic and hardness measurements in aged aluminum alloy 2024," *Materials Science and Engineering,* vol. 74, no. 1, pp. 1-10, 1985.

[84] A. Bhattacharjee, A. Pilchak, O. Lobkis, J. Foltz, S. Rokhlin and J. Williams, "Correlating ultrasonic attenuation and microtexture in a near-alpha titanium alloy," *Metallurgical and Materials Transactions A - Physical Metallurgy and Materials Science,* vol. 42, no. 8, pp. 2358-2373, 2011.

[85] Y. Han and R. Thompson, "Ultrasonic backscattering in duplex microstructures: Theory and application to titanium alloys," *Metallurgical and Materials Transactions A,* vol. 28, no. 1, pp. 91-104, 1997.

[86] P. O. Tympel, T. C. Lindley, E. A. Saunders, M. Dixon and D. Dye, “Macrozones and dwell fatigue crack initiation in Ti-6Al-4V,” in *Proceedings of the 13th World Conference on Titanium*, San Diego, CA, USA, 2016.

[87] A. Battacharjee and S. Rokhlin, “Correlating Ultrasonic Attenuation and Microtexture in a Near-Alpha Titanium Alloy,” *Metallurgical and Materials Transactions A,* vol. 42, pp. 2358-2372, 2011.

[88] P. Palanichamy, A. Joseph, T. Jayakumar and B. Raj, “Ultrasonic velocity measurements for estimation of grain size in austenitic stainless steel,” *NDE&T International,* vol. 28, no. 3, pp. 179-185, 1995.

[89] M. Vasudevan and P. Palanichamy, “Characterization of microstructural changes during annealing of cold worked austenitic stainless steel using ultrasonic velocity measurements and correlation with mechanical properties,” *Journal of Materials Engineering and Performance,* vol. 11, no. 2, pp. 169-179, 2002.

[90] R. Thompson, J. Smith, S. Lee and G. Johnson, “A comparison of ultrasonic and X-ray determinations of texture in thin Cu and Al plates,” *Metallurgical Transactions A,* vol. 20, no. 11, pp. 2431-2447, 1989.

[91] B. Raj, T. Jayakumar and P. Palanichamy, “Testing and evaluation of weld cracking in ferrous alloys,” in *Weld Cracking in Ferrous Alloys*, Cambridge, Woodhead Publishing, 2009, pp. 222-313.

[92] A. Birks, R. Greene and P. McIntire, Nondestructive testing handbook, Volume 7: Ultrasonic Testing, Columbus, Ohio: American Society for Nondestructive Testing, 1991.

[93] H. Ledbetter and M. Austin, “Texture in stainless steel welds: an ultrasonic study,” *Journal of Materials Science,* vol. 20, no. 5, pp. 1720-1724, 1985.

[94] P. Shankar, P. Palanichamy, T. Jayakumar, B. Raj and S. Ranganathan, “Nitrogen redistribution, microstructure, and elastic constant evaluation using ultrasonics in aged 316LN stainless steels,” *Metallurgical and Materials Transactions A,* vol. 32A, no. 1, pp. 2959-2968, 2001.

[95] L. Ives, L. Swartzendruber, W. Boettinger, M. Rosen, S. Ridder, F. Biancaniello, R. Reno, D. Ballard and R. Mehrabian, “NBS: Processing/microstructure/property relationships in 2024 aluminum alloy plates,” National Bureau of Standards, Washington, DC, 1983.

[96] P. Palanichamy, M. Vasudevan, T. Jayakumar, B. Raj and S. Venugopal, “Ultrasonic velocity measurements for characterizing the annealing behavior of cold worked austenitic stainless steel,” *NDT&E International,* vol. 33, no. 4, pp. 253-259, 2000.

[97] P. Palanichamy, V. Srinivasa, T. Jayakumar and V. Rajendran, “Microstructural characterization of fatigue and creep-fatigue damaged 316L(N) stainless steel through

ultrasonic measurements," in *6th International Conference on Creep, Fatigue and Creep-Fatigue Interaction*, Kalpakkam, India, 2013.

[98] B. Lan, M. Lowe and F. P. E. Dunne, "Experimental and computational studies of ultrasound wave propagation in hexagonal close-packed polycrystals for texture detection," *Acta Materialia,* vol. 63, pp. 107-122, 2014.

[99] A. Moreau, L. Toubal, P. Bocher, M. Humbert, E. Uta and N. Gey, "Evaluation of macrozone dimensions by ultrasound and EBSD techniques," *Materials Charaterization,* vol. 75, no. 1, pp. 115-128, 2013.

[100] B. Lan, M. Lowe and F. Dunne, "A generalized spherical harmonic deconvolution to obtain texture of cubic materials from ultrasonic wave speed," *Journal of the Mechanics and Physics of Solids,* vol. 83, pp. 221-242, 2015.

[101] R. Roe, "Description of crystallite orientation in polycrystalline materials. 3. General solution to pole figure inversion.," *Journal of Applied Physics,* vol. 36, no. 6, pp. 2024-2031, 1965.

[102] F. Kocks, C. N. Tome and H.-R. Wenk, Texture and Anisotropy: Preferred orientations in polycrystals and their effect on material properties, Cambridge: Cambridge University Press, 2000.

[103] P. Haldipur, F. J. Margetan and R. B. Thompson, "Estimation of Single-Crystal Elastic Constants from Ultrasonic Measurements on Polycrystalline Specimens," *Review of Quantitative Nondestructive Evaluation,* vol. 23, pp. 1061-1068, 2004.

[104] B. Lan, T. B. Britton, T.-S. Jun, W. Gan, M. Hofmann, F. P. E. Dunne and M. J. S. Lowe, "Direct volumetric measurement of crystallographic texture using acoustic waves," *Acta Materialia,* vol. 159, pp. 384-394, 2018.

[105] E. W. Weisstein, "Spherical Harmonic," Wolfram Research, Inc., 2024. [Online]. Available: https://mathworld.wolfram.com/SphericalHarmonic.html. [Accessed 12 March 2024].

[106] P. Burnley, "Tensors: Stress, Strain and Elasticity," The Geological Society of America, 25 October 2019. [Online]. Available: https://serc.carleton.edu/NAGTWorkshops/mineralogy/mineral_physics/tensors.html. [Accessed 28 January 2020].

[107] K. Atkinson, "Numerical integration on the sphere," *Journal of the Australian Mathematical Society,* vol. 23, no. B, pp. 332-347, 1982.

[108] G. Lutjering and J. Williams, Titanium, 2nd ed., Springer, 2007.

[109] S. I. Rokhlin and W. Wang, "Double through-transmission bulk wave method for ultrasonic phase velocity measurement and determination of elastic constants of composite materials," *The Journal of the Acoustical Society of America,* vol. 91, pp. 3303-3212, 1992.

[110] M. F. Markham, “Measurement of the elastic constants of fibre composites by ultrasonics,” *Composites,* vol. 1, no. 3, pp. 145-149, 1970.

[111] S. Rokhlin and W. Wang, “Ultrasonic Evaluation of in-Plane and out-of-Plane Elastic Properties of Composite Materials,” in *Review of Progresss in QNDE*, New York, NY, USA, Plenum, 1989, pp. 1489-1496.

[112] S. I. Rokhlin and W. Wang, “Double through-transmission bulk wave method for ultrasonic phase velocity measurement and determination of elastic constants of composite materials,” *The Journal of the Acoustical Society of America,* vol. 91, no. 6, pp. 3303-3312, 1992.

[113] M. Hefetz and S. I. Rokhlin, “Thermal Shock Damage Assessment in Ceramics Using Ultrasonic Waves,” *Journal of the American Ceramic Society,* vol. 75, no. 7, pp. 1839-1845, 1992.

[114] Y. C. Chu and S. I. Rokhlin, “Determination of macro- and micromechanical and interfacial elastic properties of composites from ultrasonic data,” *The Journal of the Acoustical Society of America,* vol. 92, pp. 920-931, 1992.

[115] Y. C. Chu and S. I. Rokhlin, “Comparative analysis of through-transmission ultrasonic bulk wave methods for phase velocity measurements in anisotropic materials,” *The Journal of the Acoustical Society of America,* vol. 95, no. 6, pp. 3204-3212, 1994.

[116] N. Bilaniuk and G. S. K. Wong, “ Speed of sound in pure water as a function of temperature,” *The Journal of the Acoustical Society of America,* vol. 93, pp. 1609-1612, 1993.

[117] J. L. Rose, “Critical Angles and Mode Conversion,” in *Ultrasonic Waves in Solid Media*, Cambridge, Cambridge University Press, 1999, pp. 47-49.

[118] M. Jackson and R. Reed, “Heat treatment of Udimet 720Li: the effect of microstructure on properties,” *Materials Science and Engineering A,* vol. A259, no. 1, pp. 85-97, 1999.

[119] R. Reed, The Superalloys: Fundamentals and Applications, 1st ed., Cambridge: Cambridge University Press, 2006.

[120] E. Acka and A. Gursel, “A Review on Superalloys and IN718 Nickel-Based INCONEL Superalloy,” *Periodicals of Engineering and Natural Sciences,* vol. 1, p. 21533, 2015.

[121] M. G. Benz, “Preparation of clean superalloys,” in *Impurities in Engineering Materials: Impact, Reliability and Control*, New York, NY, USA, Marcel Dekker, 1999, pp. 31-47.

[122] M. J. Donachie and S. J. Donachie, Superalloys: A Technical Guide, Materials Park, OH, USA: ASM International, 2002.

[123] N. A. Wilkinson, “Forging of 718 - The Importance of T.M.P,” in *Superalloy 718 - Metallurgy and Applications*, Warrendale, PA, USA, The Minerals, Metals & Materials Society, 1989, pp. 119-133.

[124] R. J. Mitchell, J. A. Lemsky, R. Ramanathan, H. Y. Li, K. M. Perkins and L. D. Connor, “Process development & microstructure & mechanical property evaluation of a dual microstructure heat treated advanced nickel disc alloy,” in *Superalloys 2008*, Warrendale, PA, USA, TMS (The Minerals, Metals & Materials Society), 2008, pp. 347-356.

[125] Aeether, “What is VIM + ESR? Introducing the Smelting Method of Superalloys,” Aeether, 17 May 2022. [Online]. Available: https://www.aeether.com/AEETHER/media/media-52/media.html. [Accessed 27 August 2024].

[126] D. R. Nielsen, S. W. Thompson, C. J. Van Tyne and M. C. Mataya, “Grain Size Control in Ring-Rolled Alloy 718,” in *Superalloys 718, 625, 706 and Various Derivatives*, Pittsburgh, PA, USA, 1994.

[127] Y. A. Nozhnitsky, Y. A. Fedina, A. D. Rekin and N. I. Petrov, “Development and Investigation of Ceramic Parts for Gas-Turbine Engines,” in *International Gas Turbine & Aeroengine Congress & Exhibition*, Orlando, FL, USA, 1997.

[128] J. W. Brooks and P. J. Bridges, “Metallurgical Stability of Inconel Alloy 718,” in *Superalloys 1988: Proceedings of the Sixth International Symposium on Superalloys*, Champion, PA, USA, 1988.

[129] D. J. Tillack, J. M. Manning and J. R. Hensley, Heat Treating ASM Metals Handbook Volume 4, Materials Park, OH, USA: ASM International, 1991.

[130] R. D. Doherty, D. A. Hughes, F. J. Humphreys, J. J. Jonas, D. Juul Jensen, M. E. Kassner, W. E. King, T. R. McNelley, H. J. McQueen and A. D. Rollett, “Current issues in recrystallization: a review,” *Materials Science and Engineering: A,* vol. 238, no. 2, pp. 219-274, 1997.

[131] F. J. Humphreys and M. Hatherly, Recrystallization and Related Annealing Phenomena, London: Elsevier, 2004.

[132] J. E. Burke and D. Turnbull, “Recrystallization and grain growth,” *Progress in Metal Physics,* vol. 3, pp. 220-244, 1952.

[133] B. Verlinden, J. Driver, I. Samajdar and R. Doherty, Thermo-mechanical processing of metallic materials, London: Elsevier, 2007.

[134] F. J. Humphreys, “A unified theory of recovery, recrystallization and grain growth, based on the stability and growth of cellular microstructures—I. The basic model,” *Acta Materialia,* vol. 45, no. 10, pp. 4231-4240, 1997.

[135] Q. Guo-Zheng, “Characterization for Dynamic Recrystallization Kinetics Based on Stress-Strain Curves,” in *Recent Developments in the Study of Recrystallization*, London, InTechOpen, 2012, pp. 61-88.

[136] Y. Ikeda, B. Grabowski and F. Kormann, “Ab initio phase stabilities and mechanical properties of multicomponent alloys: A comprehensive review for high entropy alloys and compositionally complex alloys,” *Materials Characterization,* vol. 147, pp. 464-511, 2019.

[137] S. Dash and N. Brown, “An investigation of the origin and growth of annealing twins,” *Acta Metallurgica,* vol. 11, no. 9, pp. 1067-1075, 1963.

[138] U. Krupp, W. M. Kane, X. Liu, O. Dueber, C. Laird and C. J. McMahon Jr., “The effect of grain-boundary-engineering-type processing on oxygen-induced cracking of IN718,” *Materials Science and Engineering: A,* vol. 349, no. 1-2, pp. 213-217, 2003.

[139] S. H. Reichman and J. W. Smythe, “New Developments in Superalloy Powders,” in *Modern Developments in Powder Metallurgy*, Boston, MA, USA, 1971.

[140] A. Mostafaei, C. Zhao, Y. He, S. Reza Ghiaasiaan, B. Shi, S. Shao, N. Shamsaei, Z. Wu, N. Kouraytem, T. Sun, J. Pauza, J. V. Gordon, B. Webler, N. D. Parab, M. Asherloo, Q. Guo, L. Chen and A. Rollett, “Defects and anomalies in powder bed fusion metal additive manufacturing,” *Current Opinion in Solid State Materials Science,* vol. 26, no. 2, p. 100974, 2022.

[141] G. Kumari Salwan, R. Subbarao and S. Mondal, “Analysis on the Suitability of Powder Metallurgy Tehcniques for Making Nickel Based Superalloys,” in *International Conference on Materials Science and Engineering*, Paris, 2022.

[142] L. Yang, X. Ren, C. Ge and Q. Yan, “Status and developemtn of powder metallurgy nickel-based disk superalloys,” *International Journal of Materials Research,* vol. 110, no. 10, pp. 901-910, 2019.

[143] B. Sreenu, R. Sarkar, S. S. Satheesh Kumar, S. Chatterjee and G. Appa Rao, “Microstructure and mechanical behaviour of an advanced powder metallurgy nickel base superalloy processed through hot isostatic pressing route for aerospace applications,” *Materials Science and Engineering: A,* vol. 797, p. 140254, 2020.

[144] H. I. Sanderow, ASM Metlas Handbook Volume 7 - Powder Metal Technologies and Applications, Materials Park, OH, USA: ASM International, 1998.

[145] W. D. Callister, Materials Science and Engineering, 7th Edition, Hoboken, NJ, USA: Wiley, 2010.

[146] A. Mukherjee, J. Bird and J. Dorn, “Experimental correlations for high-temperature creep,” *Transactions of the American Society for Metals,* vol. 62, no. 1, pp. 155-179, 1969.

[147] Department of Materials Science & Metallurgy, “Ductile-brittle transition temperature,” University of Cambridge, 2004. [Online]. Available: https://www.doitpoms.ac.uk/tlplib/mechanical_properties/ductile.php. [Accessed 25 July 2024].

[148] W. Callister and D. Rethwisch, Materials Science and Engineering: An Introduction, New York: Wiley, 2007.

[149] Y. Fan, T. Wang, Z. Hao, X. Liu, S. Gao and R. Li, “Surface residual stress in high speed cutting of superalloy Inconel718 based on multiscale simulation,” *Journal of Manufacturing Processes,* vol. 31, pp. 480-493, 2019.

[150] E. O. Ezugwu, J. Bonney and Y. Yamane, “An overview of the machinability of aeroengine alloys,” *Journal of Materials Processing Technology,* vol. 134, no. 2, pp. 233-253, 2003.

[151] N. Corduan, T. Himbart, G. Poulachon, M. Dessoly, M. Lambertin, J. Vigneau and B. Payoux, “Wear Mechanisms of New Tool Materials for Ti-6Al-4V High Performance Machining,” *CIRP Annals,* vol. 52, no. 1, pp. 73-76, 2003.

[152] J. Williams and E. Starke, “Progress in structural materials for aerospace systems,” *Acta Materialia,* vol. 51, no. 1, pp. 5775-5799, 2003.

[153] M. Morinaga, A Quantum Approach to Alloy Design, 1st ed., Nagoya: Elsevier, 2019.

[154] M. Durand-Charre, The Microstructure of Superalloys, Amsterdam: Breach Science Publishers, 1997.

[155] University of Cambridge, “Precipitates from solid solution,” University of Cambridge, 2004. [Online]. Available: https://www.doitpoms.ac.uk/tlplib/solid-solutions/precipitates.php. [Accessed 23 July 2024].

[156] S. Azadian, L.-Y. Wei and R. Warren, “Delta phase precipitation in Inconel 718,” *Materials Characterisation,* vol. 53, pp. 7-16, 2004.

[157] D. F. Paulonis, J. M. Oblak and D. S. Duvall, “Precipitation in Nickel-Based Alloy 718,” *American Society of Metals,* vol. 62, pp. 611-622, 1969.

[158] T. Federova, J. Rosler, B. Gehrmann and J. Klower, “Invention of a new 718-type Ni-Co superalloy family for high temperature applications at 750C,” in *8th International Symposium on Superalloy 718 and Derivatives*, Pittsburgh, PA, USA, 2014.

[159] Y. Desvallees, M. Bouzidi, F. Bois and N. Beaude, “Delta phase in Inconel 718: mechanical properties and forging process requirements,” in *Superalloy 718 - metallurgy and applications*, Warrendale, PA, The Minerals, Metals and Materials Society, 1994, pp. 281-291.

[160] H. L. Eiselstein, “Metallurgy of Columbium-Hardened Nickel-Chromium-Iron Alloy,” *Advances in the Technology of Stainless Steel and Related Alloys,* vol. 369, pp. 62-77, 1965.

[161] P. Villechaise, J. Cormier, T. Billot and J. Mendez, “Mechanical Behavior and Damage Processes of Udimet 720Li: Influence of Localized Plasticity at Grain Boundaries,” in *Superalloys 2012*, Seven Springs, PA, USA, 2012.

[162] M. Maziere, J. Besson, S. Forest, B. Tanguy, H. Chalons and F. Vogel, “Overspeed burst of elastoviscoplastic rotating disks - Part I: Analytical and numerical stability analyses,” *European Journal of Mechanics A/Solids,* vol. 28, no. 1, pp. 36-44, 2009.

[163] P. Villechaise, J. Cormier, T. Billot and J. Mendez, “Mechanical behavior and damage processes of Udimet 720Li: Influence of localized plasticity at grain boundaries,” in *Superalloys 2012*, Seven Springs, PA, USA, 2012.

[164] Simuwu, “Superalloy Turbine Disc Casting and Forging,” Vacfurnace, 2021. [Online]. Available: https://www.vacfurnace.com/industry-news/superalloy-turbine-disc-casting-and-forging/. [Accessed 27 August 2024].

[165] W. Jenkins, T. Digges and C. Johnson, “Creep of high purity nickel,” *Journal of Research of the National Bureau of Standards,* vol. 53, no. 1, pp. 329-352, 1954.

[166] ASM Handbook Committee, Properties and Selection: Irons, Steels, and High-Performance Alloys, Materials Park, OH, USA: ASM International, 1990.

[167] J. Tien and R. Jarrett, “Effects of Cobalt in Nickel-Base Superalloys,” in *High Temperature Alloys for Gas Turbines*, Heidelberg, Germany, Springer, 1982, pp. 423-446.

[168] D. Shah and D. Duhl, “Effect of Minor Elements on the Deformation Behavior of Nickel-Base Superalloys,” in *Superalloys 1988*, Warrendale, PA, USA, TMS (The Minerals, Metals & Materials Society), 1988, pp. 693-702.

[169] J. Dennison, R. Llewellyn and B. Wilshire, “The creep and fracture properties of some nickel-chromium alloys at 600 degrees Celsius,” *Journal of the Institute of Metals,* vol. 95, no. 1, pp. 115-118, 1967.

[170] D. Furrer and H. Fecht, “Gamma prime formation in superalloy U720LI,” *Scripta Materialia,* vol. 40, no. 11, pp. 1215-1220, 1999.

[171] D. Furrer, R. Shankar and C. White, “Optimizing the heat treatment of Ni-Based Superalloy Turbine Discs,” *JOM,* vol. 55, no. 3, pp. 32-34, 2003.

[172] J. J. Schirra, “Effect of Heat Treatment Variations on the Hardness and Mechanical Properties of Wrought Inconel 718,” in *Superalloys 718, 625, 706 and Various Derivatives*, Warrendale, PA, USA, The Minerals, Metals & Materials Society, 1997, pp. 431-438.

[173] K. Bain, M. Gambone, J. Hyzak and M. Thomas, “Development of Damage Tolerant Microstructures in Udimet 720,” in *5th International Symposium on Superalloys*, Warrendale, PA, USA, 1988.

[174] K. Mert Doleker, A. Erdogan, T. Yener, A. Cahit Karaoglanli, O. Uzun, M. Sabri Gok and S. Zeytin, "Enhancing the wear and oxidation behaviors of the Inconel 718 by low temperature aluminizing," *Surface and Coatings Technology,* vol. 412, p. 127069, 2021.

[175] R. E. Schafrik, D. D. Ward and J. R. Groh, "Application of Alloy 718 in GE Aircraft Engines: Past, Present and Next Five Years," in *Fifth International Symposium on Superalloys 718, 625, 706, and Derivatives*, Pittsburgh, PA, USA, 2001.

[176] J. M. Moyer, L. A. Jackman, C. B. Adasczik, R. M. Davis and R. Forbes-Jones, "Advances in triple melting superalloys 718, 706, and 720," in *Superalloys 718, 625, 706 and Various Derivatives*, Warrendale, PA, USA, TMS (The Minerals, Metals & Materials Society), 1994, pp. 39-48.

[177] D. F. Paulonis and J. J. Schirra, "Alloy 718 at Pratt & Whitney - Historical Perspective and Future Challenges," in *Superalloys 718, 625, 706 and Various Derivatives*, Warrendale, PA, USA, TMS (The Minerals, Metals & Materials Society), 2001, pp. 13-23.

[178] C. Korner, H. Helmer, A. Bauereiß and R. F. Singer, "Tailoring the grain structure of IN718 during selective electron beam melting," in *EUROSUPERALLOYS 2014 – 2nd European Symposium on Superalloys and their Applications*, Giens, France, 2014.

[179] K. N. Amato, S. M. Gaytan, L. E. Murr, E. Martinez, P. W. Shindo, J. Hernandez, S. Collins and F. Medina, "Microstructures and mechanical behavior of Inconel 718 fabricated by selective laser melting," *Acta Materialia,* vol. 60, no. 5, pp. 2229-2239, 2012.

[180] Tech Steel & Materials, "Nickel Inconel 718 AMS 5662," Tech Steel & Materials, 2022. [Online]. Available: https://www.techsteel.net/alloy/nickel/inconel-718/ams-5662. [Accessed 23 May 2022].

[181] R. E. Santelli, E. P. Oliveira, M. d. F. Batista de Carvalho, M. A. Bezerra and A. S. Freire, "Total sulfur determination in gasoline, kerosene and diesel fuel using inductively coupled plasma optical emission spectrometry after direct sample introduction as detergent emulsions," *Spectrochimica Acta Part B: Atomic Spectroscopy,* vol. 63, no. 7, pp. 800-804, 2008.

[182] A. Oradei-Basile and J. F. Radavich, "A current T-T-T diagram for wrought alloy 718," in *Superalloys 718, 625 and Various Derivatives*, Warrendale, PA, The Minerals, Metals & Materials Society, 1991, 1991, pp. 325-335.

[183] C. Slama, C. Servant and G. J. Cizeron, "Aging of the Inconel 718 alloy between 500 and 750°C," *Journal of Materials Research,* vol. 12, pp. 2298-2316, 1997.

[184] L. Renhof, C. Krempaszky, E. Werner and M. Stockinger, "Analysis of microstructural properties of IN 718 after high speed forging," in *Superalloys 718, 625, 706 and Derivatives*, Warrendale, PA, USA, The Minerals, Metals & Materials Society, 2005, pp. 261-270.

[185] Y. Murata, M. Morinaga, N. Yukawa, H. Ogawa and M. Kato, “Solidification structures of Inconel 718 with microalloying elements,” in *Superalloys 718, 625, 706 and Various Derivatives*, Warrendale, PA, The Minerals, Metals & Materials Society, 1994, pp. 81-88.

[186] A. S. Ballantyne and A. Mitchell, “The Prediciton of Ingot Structure in VAR/ESR Inconel 718,” in *Sixth International Vacuum Metal Conference*, San Diego, CA, USA, 1979.

[187] A. Orozco-Caballero, C. Gutierrez, B. Gan and J. M. Molina-Aldareguia, “High-throughput nanoindentation mapping of cast IN718 nickel-based superalloys: influence of the Nb concentration,” *Journal of Materials Research,* vol. 36, pp. 2213-2222, 2021.

[188] A. Thomas, M. El-Wahabi, J. M. Cabrera and J. M. Prado, “High temperature deformation of Inconel 718,” *Journal of Materials Processing Technology,* vol. 177, pp. 469-472, 2006.

[189] L. Yang, K. M. Chang, S. Mannan and J. deBarbadillo, “A new DTA approach for verifying precipitate solvus in Inconel Alloy 718,” *Superalloys 718, 625, 706 and Various Derivatives,* pp. 353-365, 1997.

[190] M. Sundararaman, P. Mukhopadhyay and S. Banerjee, “Some aspects of the precipitation of metastable intermetallic phases in Inconel-718,” *Metallurgical Transactions A,* vol. 23, pp. 2015-2028, 1992.

[191] M. C. Chaturvedi and Y. Han, “Effect of particle size on the creep rate of superalloy Inconel 718,” *Materials Science and Engineering,* vol. 89, pp. L7-L10, 1987.

[192] Y. Han and M. C. Chaturvedi, “A study of back stress during creep deformation of a superalloy inconel 718,” *Materials Science and Engineering,* vol. 85, pp. 59-65, 1987.

[193] D. Fournier and A. Pineau, “Low cycle fatigue behavior of Inconel 718 at 298 K and 823 K,” *Metallurgical and Materials Transactions A,* vol. 8, no. 7, pp. 1095-1105, 1977.

[194] J. M. Oblak, D. S. Duvall and D. F. Paulonis, “An estimate of the strengthening arising from coherent, tetragonally-distorted particles,” *Materials Science and Engineering,* vol. 13, no. 1, pp. 51-56, 1974.

[195] M. C. Chaturvedi and Y. F. Han, “Strengthening mechanisms in Inconel 718 superalloy,” *Metal Science,* vol. 17, no. 3, pp. 145-149, 1983.

[196] Y. Huang and T. G. Langdon, “The evolution of delta-phase in a superplastic Inconel 718 alloy,” *Journal of Materials Science,* vol. 42, pp. 421-427, 2007.

[197] A. Devaux, L. Naze, R. Molins, A. Pineau, A. Organista, J. Y. Guedou, J. F. Uginet and P. Heritier, “Gamma double prime precipitation kinetic in Alloy 718,” *Materials Science & Engineering A,* vol. 486, pp. 117-122, 2008.

[198] E. J. Loria, “The status and prospects of Alloy 718,” *Journal of Metals,* vol. 40, pp. 36-41, 1988.

[199] Y. Ning, S. Huang, M. W. Fu and J. Dong, “Microstructural characterisation, formation mechanism and fracture behavior of the needle δ phase in Fe-Ni-Cr type superalloys with high Nb content,” *Materials Characterization,* vol. 109, no. 1, pp. 36-42, 2015.

[200] H. Y. Zhang, S. H. Zhang, M. Cheng and Z. X. Li, “Deformation characteristics of δ phase in the delta-processed Inconel 718 alloy,” *Materials Characterization,* vol. 61, no. 1, pp. 49-53, 2010.

[201] W. Mills, “Fracture Toughness Variations for Alloy 718 Base Metal and Welds,” in *Superalloy 718 - Metallurgy and Applications*, Pittsburgh, PA, USA, 1989.

[202] L. O, “HAZ Microstructural evolution in alloy 718 after multiple repair and PWHT cycles - PhD thesis,” Ohio State University, Ohio, 1999.

[203] J. Muller and M. Donachie, Superalloys - a technical guide, Materials Park, OH: ASM International, 1975.

[204] G. Sjoberg and N. Ingesten, “Grain boundary delta-phase morphology, carbides and notch rupture sensitivities of cast alloy 718,” in *Superalloy 718 - metallurgy and applications*, Warrendale, PA, Minerals, Metals & Materials Society, 1991, pp. 603-621.

[205] R. M. Forbes-Jones and L. A. Jackson, “The Structural Evolution of Superalloy Ingots during Hot Working,” *JOM,* vol. 51, pp. 27-31, 1999.

[206] A. W. Dix, J. M. Hyzak and R. P. Singh, “APPLICATION OF ULTRA FINE GRAIN ALLOY 718 FORGING BILLET,” in *Superalloys 1992*, Warrendale, PA, USA, The Minerals, Metals & Materials Society, 1992, pp. 23-32.

[207] L. A. Jackman, G. Smith, A. Dix and M. L. Lasonde, “Rotary Forge Processing of Direct Aged Inconel 718 for Aircraft Engine Shafts,” in *Superalloys 718, 625 and Various Derivatives*, Warrendale, PA, USA, The Minerals, Metals & Materials Society, 1991, pp. 125-132.

[208] T. Zaman, M. Farooque, S. A. Rizvi, I. Salam and M. Waseem, “Investigation of low stress rupture properties in Inconel-718 super alloy,” *14th International Symposium on Advanced Materials,* vol. 146, p. 012051, 2016.

[209] T. Bhujangrao, F. Veiga, A. Suarez, I. Edurne and F. Girot Mata, “High-Temperature Mechanical Properties of IN718 Alloy: Comparison of Additive Manufactured and Wrought Samples,” *Crystals,* vol. 10, p. 689, 2020.

[210] M. A. Meyers and R. Norman Orava, “Thermomechcmical processing of Inconel 718 by shock-wave deformation,” *Metallurgical Transactions A,* vol. 7, pp. 179-190, 1976.

[211] ThermoFisher Scientific, “Scios 2 - E-beam/NICol column,” ThermoFisher Scientific, Waltham, MA, USA, 2024.

[212] ThermoFisher Scientific, “Scios Detectors,” ThermoFisher Scientific, Waltham, MA, USA, 2024.

[213] R. Hielscher, “MTEX,” 2007.

[214] S. I. Wright, “Orientation Texture,” in *Encyclopedia of Condensed Matter Physics*, Amsterdam, The Netherlands, Elsevier, 2005, pp. 221-233.

[215] L. Hodges, “Common Univariate Distributions,” in *Statistical Methods for Physical Science*, San Diego, CA, Academic Press, 1994, pp. 35-61.

[216] W. R. Leo, Techniques for Nuclear and Particle Physics Experiments, Berlin: Springer, 1994.

[217] A. F. Siegel, Practical Business Statistics, Amsterdam: Academic Press, 2011.

[218] S. I. Wright, M. M. Nowell and D. P. Field, “A review of strain analysis using Electron backscatter diffraction,” *Microscopy and Microanalysis,* vol. 17, no. 3, pp. 316-329, 2011.

[219] N. C. K. Lassen, D. J. Jensen and K. J. S. M. Conradsen, “Image processing procedures for analysis of electron back scattering patterns,” *Scanning Microscopy,* vol. 6, no. 1, pp. 115-121, 1992.

[220] S. D. Stizman, G. Nolze and M. M. Nowell, “EBSD Pattern Quality and its Use in Evaluating Sample Surface Condition,” in *Microscopy and Microanalysis*, Portland, OR, USA, 2010.

[221] S. I. Wright and M. M. Nowell, “EBSD image quality mapping,” *Microscopy and Microanalysis,* vol. 12, no. 1, pp. 72-84, 2005.

[222] L. Saraf, “Kernel Average Misorientation Confidence Index Correlation from FIB Sliced Ni-Fe-Cr alloy Surface,” *Microscopy and Microanalysis,* vol. 17, no. S2, pp. 424-425, 2011.

[223] C. Stocker, M. Zimmerman and H.-J. Christ, “Localized cyclic deformation and corresponding dislocation arrangements of polycrystalline Ni-base superalloys and pure Nickel in the VHCF regime,” *International Journal of Fatigue,* vol. 33, no. 1, pp. 2-9, 2011.

[224] P. Landau, R. Z. Shneck, G. Makov and A. Venkert, “Evolution of dislocation patterns in fcc metals,” *IOP Conference Series: Materials Science and Engineering,* vol. 3, p. 012004, 2009.

[225] S. Azadian, L.-Y. Wei, F. Niklasson and R. Warren, “Precipitation in spray-formed IN718,” in *Superalloys 718, 625, 706 and Various Derivatives*, Warrendale, PA, USA, The Minerals, Metals and Materials Society, 2001, pp. 617-626.

[226] F. Singer and M. Kufner, “Model based laser-ultrasound determination of hardness gradients of gas-carburized steel,” *NDT&E International,* vol. 88, pp. 24-32, 2017.

[227] Y. C. Fayman, “Microstructural characterization and elemental partitioning in a direct-aged superalloy (DA 718),” *Materials Science and Engineering,* vol. 92, pp. 159-171, 1987.

[228] M. G. Burke and M. K. Miller, “Precipitation in alloy 718: a combined Al3M and apfim investigation,” in *Superalloys 718, 625 and Various Derivatives*, Warrendale, PA, USA, The Minerals, Metals & Materials Society, 1991, pp. 337-345.

[229] Y. S. Liao, H. M. Lin and J. H. Wang, “Behaviors of end milling Inconel 718 superalloy by cemented carbide tools,” *Journal of Materials Processing Technology,* vol. 201, no. 1-3, pp. 460-465, 2008.

[230] O. D. Payton, L. Picco and T. B. Scott, “High-speed atomic force microscopy for materials science,” *International Materials Reviews,* vol. 61, no. 8, pp. 473-494, 2016.

[231] G. Binnig, H. Rohrer, C. Gerber and E. Weibel, “Surface Studies by Scanning Tunneling Microscopy,” *Physical Review Letters,* vol. 49, no. 57, pp. 31-35, 1982.

[232] R. Young, J. Ward and F. Scire, “The Topografiner: An Instrument for Measuring Surface Microtopography,” *Review of Scientific Instruments,* vol. 43, pp. 999-1011, 1972.

[233] U. Durig, D. W. Pohl and R. Rohner, “Near-field optical-scanning microscopy,” *Journal of Applied Physics,* vol. 59, no. 1986, pp. 3318-3327, 1986.

[234] P. K. Hansma, B. Drake, O. Marti, S. A. Gould and C. B. Prater, “The scanning ion-conductance microscope,” *Science,* vol. 243, pp. 641-643, 1989.

[235] B. P. Brown, L. Picco, M. J. Miles and C. F. J. Faul, “Opportunities in High-Speed Atomic Force Microscopy,” *Small,* vol. 9, no. 19, pp. 3201-3211, 2013.

[236] L. Gross, F. Mohn, N. Moll, P. Liljeroth and G. Meyer, “The Chemical Structure of a Molecule Resolved by Atomic Force Microscopy,” *Science,* vol. 325, pp. 1110-1114, 2009.

[237] J. E. Castle and P. A. Zhdan, “Characterization of surface topography by SEM and SFM: problems and solutions,” *Journal of Physics D: Applied Physics,* vol. 30, no. 5, pp. 722-740, 1997.

[238] Y. Chen, J. Cai, M. Liu, G. Zeng, Q. Feng and Z. Chen, “Research on double-probe, double- and triple-tip effects during atomic force microscopy scanning,” *Scanning,* vol. 26, no. 4, pp. 155-161, 2004.

[239] U. D. Schwarz, H. Haefke, P. Reimann and H.-J. Guntherodt, “Tip artefacts in scanning force microscopy,” *Journal of Microscopy,* vol. 173, no. 3, pp. 183-197, 1994.

[240] P. Klapetek and D. Necsas, “Gwyddion,” Department of Nanometrology, Czech Metrology Institute, 2024. [Online]. Available: http://gwyddion.net/. [Accessed 28 June 2024].

[241] P. A. J. Bagot, O. B. W. Silk, J. O. Douglas, S. Pedrazzini, D. J. Crudden, T. L. Martin, M. C. Hardy, M. P. Moody and R. C. Reed, “An Atom Probe Tomography study of site preference and partitioning in a nickel-based superalloy,” *Acta Materialia,* vol. 125, pp. 156-165, 2017.

[242] J. L. Rose, “The Christoffel Equation for Anisotropic Media,” in *Ultrasonic Waves in Solid Media*, Cambridge, UK, Cambridge University Press, 1999, pp. 27-33.

[243] C. A. Schneider, W. S. Rasband and K. W. Eliceiri, “NIH Image to ImageJ: 25 years of image analysis,” *Nature Methods,* vol. 9, pp. 671-675, 2012.

[244] A. Nicolay, J.-M. Franchet, N. Bozzolo and J. Cormier, “Metallurgical Analysis of Direct Aging Effect on Tensile and Creep Properties in Inconel 718 Forgings,” in *Superalloys 2020*, Warrendale, PA, USA, The Minerals, Metals & Materials Society, 2020, pp. 559-569.

[245] NeoNickel, “Alloy 718 Datasheet,” NeoNickel, Milton Keynes, UK, 2024.

[246] H. Chandler, Heat Treater's Guide: Practices and Procedures for Nonferrous Alloys, Materials Park, OH, USA: ASM International, 1996.

[247] J. M. Oblak, D. F. Paulonis and D. S. Duvall, “Coherency strengthening in Ni base alloys hardened by DO22 γ' precipitates,” *Metallurgical Transactions,* vol. 5, pp. 143-153, 1974.

[248] J. P. Collier, A. O. Selius and J. K. Tien, “ON DEVELOPING A MICROSTRUCTURALLY AND THERMALLY STABLE IRON-NICKEL BASE SUPERALLOY,” in *Superalloys 1988*, Warrendale, PA, USA, The Minerals, Metals & Materials Society, 1988, pp. 43-52.

[249] Y.-f. Han, P. Deb and M. Chaturvedi, “Coarsening behaviour of γ''- and γ'-particles in Inconel alloy 718,” *Metal Science,* vol. 16, pp. 555-561, 1982.

[250] J. R. Mihalisin and D. L. Pasquine, “Phase Transformations in Nickel-Base Superalloys,” in *International Symposium on Structural Stability in Superalloys*, Seven Springs, PA, USA, 1968.

[251] F. E. Sczerzenie and G. E. Maurer, “Development of Udimet 720 for high strength disc applications,” in *Superalloys 1984*, Warrendale, PA, USA, TMS (The Minerals, Metals & Materials Society), 1984, pp. 573-582.

[252] D. Helm and O. Roder, “Influence of Long Term Exposure in Air on Microstructure, Surface Stability and Mechanical Properties of UDIMET 720LI,” in *Superalloys 2000*, Warrendale, PA, USA, TMS (The Minerals, Metals & Materials Society), 2000, pp. 487-493.

[253] T. Matsui, H. Takizawa, H. Kikuchi and S. Wakita, “The Microstructure Prediction of Alloy 720Li for Turbine Disk Applications,” in *Superalloys 2000*, Warrendale, PA, USA, TMS (The Minerals, Metals & Materials Society), 2000, pp. 127-133.

[254] P. W. Keefe, S. O. Mancuso and G. E. Maurer, “Effects of Heat Treatment and Chemistry on the Long-Term Phase Stability of a High Strength Nickel-Based Superalloy,” in *Superalloys 1992*, Warrendale, PA, USA, TMS (The Minerals, Metals & Materials Society), 1992, pp. 487-496.

[255] K. A. Green, J. A. Lemsky and R. M. Gasior, “Development of isothermally forged P/M Udimet 720 for turbine disk applications,” in *Superalloys 1996*, Warrendale, PA, USA, TMS (The Minerals, Metals & Materials Society), 1996, pp. 697-703.

[256] H. Hattori, M. Takekawa, D. Furrer and R. J. Noel, “Evaluation of P/M U720 for gas turbine engine disk application,” in *Superalloys 1996*, Warrendale, PA, USA, TMS (The Minerals, Metals & Materials Society), 1996, pp. 705-711.

[257] D. J. Bryant and G. McIntosh, “The Manufacture and Evaluation of a Large Turbine Disc in Cast and Wrought Alloy 720Li,” in *Superalloys 1996*, Warrendale, PA, TMS (The Minerals, Metals & Materials Society), 1996, pp. 713-722.

[258] P. Villechaise, J. Cormier, T. Billot and J. Mendez, “Mechanical Behavior and Damage Processes of Udimet 720Li: Influence of Localized Plasticity at Grain Boundaries,” in *Superalloys 2012*, Warrendale, PA, USA, TMS (The Minerals, Metals & Materials Society), 2012, pp. 15-24.

[259] S. K. Jain, B. A. Ewing and C. A. Yin, “The development of improved performance PM Udimet 720 Turbine Disks,” in *Superalloys 2000*, Warrendale, PA, TMS (The Minerals, Metals & Materials Society), 2000, pp. 785-794.

[260] Y. Yamaguchi, H. Hisazawa and Y. Terada, “Microstructure Quantification in Nickel-Based Superalloy Udimet 720Li,” *Materials Transactions,* vol. 60, no. 4, pp. 593-601, 2019.

[261] D. U. Furrer, R. Shankar and C. White, “Optimizing the Heat Treatment of Ni-Based Superalloy Turbine Discs,” *JOM,* vol. 55, pp. 32-34, 2003.

[262] J. Mao, K.-M. Chang, V. L. Keefer and D. Furrer, “An investigation on quench cracking behavior of superalloy udimet 720LI using a fracture mechanics approach,” *Journal of Materials Engineering and Performance ,* vol. 9, pp. 204-214, 2000.

[263] Q. Y. Yu, Z. H. Yao and J. X. Dong, “Deformation and recrystallization behavior of a coarse-grain, nickel-base superalloy Udimet 720Li ingot material,” *Materials Characterization,* vol. 107, pp. 398-410, 2015.

[264] R. C. Reed, M. P. Jackson and Y. S. Na, “Characterization and modeling of the precipitation of the sigma phase in UDIMET 720 and UDIMET 720Li,” *Metallurgical and Materials Transactions A,* vol. 30, pp. 521-533, 1999.

[265] P. W. Keefe, S. O. Mancuso and G. E. Maurer, “Effects of Heat Treatment and Chemistry on the Long-Term Phase Stability of a High Strength Nickel-Based Superalloy,” in *Superalloys 1992*, Warrendale, PA, USA, TMS (The Minerals, Metals & Materials Society), 1992, pp. 487-496.

[266] D. Texier, J.-C. Stinville, M. P. Echlin, S. Pierret, P. Villechaise, T. M. Pollock and J. Cormier, "Short crack propagation from cracked non-metallic inclusions in a Ni-based polycrystalline superalloy," *Acta Materialia,* vol. 165, pp. 241-258, 2019.

[267] S. Manna, H. Chan, A. Ghosh, T. Chakrabarti and S. K. R. S. Sankaranarayanan, "Understanding and control of Zener pinning via phase field and ensemble learning," *Computational Materials Science,* vol. 229, p. 112384, 2023.

[268] F. E. Sczerzenie, S. O. Mancuso, P. W. Keefe, G. E. Maurer and W. J. Boesch, "Udimet alloy 720," Special Metals Corporation, New Hartford, NY, USA, 1988.

[269] B. Geddes, H. Leon and X. Huang, Superalloys: Alloying and Performance, Ohio: ASM International, 2010.

[270] T. M. Pollock and S. Tin, "Nickel-Based Superalloys for Advanced Turbine Engines: Chemistry, Microstructure and Properties," *Journal of Propulsion and Power,* vol. 22, no. 2, pp. 361-374, 2006.

[271] D. Furrer and H. Fecht, "Ni-based superalloys for turbine discs," *JOM,* vol. 51, no. 1, pp. 14-17, 1999.

[272] W. Huther and B. Reppich, "Interaction of Dislocations With Coherent, Stress-Free, Ordered Particles," *International Journal of Materials Research,* vol. 69, no. 10, pp. 628-634, 1978.

[273] R. W. Kozar, A. Suzuki, W. W. Milligan, J. J. Schirra, M. F. Savage and T. M. Pollock, "Strengthening Mechanisms in Polycrystalline Multimodal Nickel-Base Superalloys," *Metallurgical and Materials Transactions A,* vol. 40, pp. 1588-1603, 2009.

[274] E. I. Galindo-Nava, L. D. Connor and C. M. F. Rae, "On the prediction of the yield stress of unimodal and multimodal γ' Nickel-base superalloys," *Acta Materialia,* vol. 98, pp. 377-390, 2015.

[275] J. J. Schirra and S. H. Goetschius, "Development of an analytical model predicting microstructure and properties resulting from the thermal processing of a wrought powder nickel-base superalloy component," in *Superalloys 1992*, Warrendale, PA, USA, TMS (The Minerals, Metals & Materials Society), 1992, pp. 437-446.

[276] T. Grosdidier, A. Hazote and A. Simon, "Precipitation and dissolution processes in γ/γ' single crystal nickel-based superalloys," *Materials Science and Engineering: A,* vol. 256, no. 1-2, pp. 183-196, 1998.

[277] Y. Yamaguchi, H. Hisazawa and Y. Terada, "Microstructure Quantification in Nickel-Based Superalloy Udimet 720Li," *Materials Transactions,* vol. 60, no. 4, pp. 593-601, 2019.

[278] Y. Tsuboi and K. Kakehi, "Effect of Heat Treatment on Tensile/Compressional Strenghts in U720Li," *Journal of the Japan Institute of Metals,* vol. 69, no. 2, pp. 202-205, 2005.

[279] M. Mazière, J. Besson, S. Forest, B. Tanguy, H. H. Chalons and F. Vogel, "Overspeed burst of elastoviscoplastic rotating disks – Part I: Analytical and numerical stability analyses," *European Journal of Mecahnics A/Solids,* vol. 28, pp. 36-44, 2009.

[280] H. Lu, M. Yang, L. Zhou, Z. Ma, F. Yin and D. Li, "Effects of Heat Treatment on the Microstructure and Properties of a Cast Nickel-Based High-Cr Superalloy," *Metals,* vol. 12, no. 12, p. 2176, 2022.

[281] M. C. Hardy, "Specification for manufacture of 4 off circular plates for ultra-sonic inspection," Rolls-Royce PLC, Derby, UK, 2024.

[282] C. Argyrakis, Interviewee, *RR1000 SX Elastic Coefficients.* [Interview]. 22 April 2024.

[283] Special Metals Corporation, "UDIMET alloy 720," Speical Metals Corporation, New Hartford, NY, USA, 2024.

[284] S. R. Yeratapally, M. G. Glavicic, M. Hardy and M. D. Sangid, "Microstructure based fatigue life prediction framework for polycrystalline nickel-base superalloys with emphasis on the role played by twin boundaries in crack initiation," *Acta Materialia,* vol. 107, pp. 152-167, 2016.

[285] G. Conduit, "Top Trumps: materials and alloys," The University of Cambridge, Cambridge, 2013.

[286] Y. Yamaguchi, H. Hisazawa and Y. Terada, "Microstructure Quantification in Nickel-Based Superalloy Udimet 720Li," *Materials Transactions,* vol. 60, no. 4, pp. 593-601, 2019.

[287] D. J. Child, G. D. West and R. C. Thomson, "The use of combined three-dimensional electron backscatter diffraction and energy dispersive X-ray analysis to assess the characteristics of the gamma/gamma-prime microstructure in alloy 720Li™," *Ultramicroscopy,* vol. 114, pp. 1-10, 2012.

[288] "Microstructure and Mechanical Properties of an Advanced Nickel-Based Superalloy in the as-HIP form," *Advanced Materials Research,* vol. 278, no. 1, pp. 265-270, 2011.

[289] M. C. Hardy, B. Zirbel, G. Shen and R. Shankar, "Developing damage tolerance and creep resistance in a high strength nickel alloy for disc applications," in *Superalloys 2004*, Warrendale, PA, TMS (The Minerals, Metals & Materials Society), 2004, pp. 83-90.

[290] R. J. Mitchell, J. A. Lemsky, R. Ramanathan, H. Y. Li, K. M. Perkins and L. D. Connor, "Process development & microstructure & mechanical property evaluation of a dual microstructure heat treated advanced nickel disc alloy," in *Superalloys 2008*, Warrendale, PA, TMS (The Minerals, Metals & Materials Society), 2008, pp. 347-356.

[291] N. Saunders and A. P. Miodownik, CALPHAD (Calculation of Phase Diagrams): A Comprehensive Guide, Oxford: Pergammon, 1998.

[292] N. Saunders, “Phase Diagram Calculations for Ni-Based Superalloys,” in *Superalloys 1996*, Warrendale, PA, TMS (The Minerals, Metals & Materials Society), 1996, pp. 101-110.

[293] D. W. Hunt, “The Stability and Mechanical Properties of a Nickel-Base Turbine Disc Alloy (PhD Thesis),” University of Cambridge, Cambridge, 2001.

[294] N. Saunders, M. Fahrmann and C. J. Small, “The Application of CALPHAD Calculations to Ni-Based Superalloys,” in *Superalloys 2000*, Warrendale, PA, TMS (The Minerals, Metals & Materials Society), 2000, pp. 803-811.

[295] C. T. Sims, N. S. Stoloff and W. C. Hagel, “Fundamental of Strengthening,” in *Superalloys II*, New York, NY, John Wiley & Sons, 1987, pp. 61-96.

[296] R. L. Dreshfield and H. R. Gray, “P/M Superalloys – a Troubled adolescent?,” NASA Lewis Research Center, Cleveland, OH, 1984.

[297] R. Anderson, “Powder Metallurgy at Pratt and Whitney,” *The International Journal of Powder Metallurgy,* vol. 26, no. 2, pp. 171-178, 1990.

[298] J. Smythe, “Superalloy Powders: An amazing history,” *Advanced Materials and Processes,* vol. 166, no. 11, pp. 52-55, 2008.

[299] I. M. D. Parr, T. J. Jackson, M. C. Hardy, D. J. Child, C. Argyrakis, K. Severes, V. Saraf and J. M. Stumpf, “Inhomogeneous Grain Coarsening Behavior in Supersolvus Heat Treated Nickel-Based Superalloy RR1000,” in *Superalloys 2016: Proceedings of the 13th International Symposium of Superalloys*, Warrendale, PA, TMS (The Minerals, Metals & Materials Society), 2016, pp. 447-56.

[300] M.-A. Charpagne, T. Billot, J.-M. Franchet and N. Bozzolo, “Heteroepitaxial recrystallization: A new mechanism discovered in a polycrystalline γ-γ’ nickel based superalloy,” *Journal of Alloys and Compounds,* vol. 688, pp. 685-694, 2016.

[301] D. M. Collins, B. D. Conduit, H. J. Stone, M. C. Hardy, G. J. Conduit and R. J. Mitchell, “Grain growth behaviour during near-γ' solvus thermal exposures in a polycrystalline nickel-base superalloy,” *Acta Materialia,* vol. 61, no. 9, pp. 3378-3391, 2013.

[302] “On the Evolution of Primary Gamma Prime Precipitates During High Temperature and High Strain Rate Deformation and Subsequent Heat Treatment in the Ni-Based Superalloy, RR1000,” *Metallurgical and Materials Transactions A,* vol. 50A, no. 1, p. 4205, 2019.

[303] Y. Q. Chen, T. J. A. Slater, E. A. Lewis, E. M. Francis, M. G. Burke, M. Preuss and S. J. Haigh, “Measurement of size-dependent composition variations for gamma prime (γ') precipitates in an advanced nickel-based superalloy,” *Ultramicroscopy,* vol. 144, pp. 1-8, 2014.

[304] A. R. P. Singh, S. Nag, S. Chattopadhyay, Y. Ren, J. Tiley, G. B. Viswanathan, H. L. Fraser and R. Banerjee, “Mechanisms related to different generations of γ' precipitation during

continuous cooling of a nickel base superalloy," *Acta Materialia,* vol. 61, no. 1, pp. 280-293, 2013.

[305] Y. Q. Chen, E. Francis, J. Robson, M. Preuss and S. J. Haigh, "Compositional variations for small-scale gamma prime (γ') precipitates formed at different cooling rates in an advanced Ni-based superalloy," *Acta Materialia,* vol. 85, pp. 199-206, 2015.

[306] C. Papadaki, W. Li and A. M. Korsunsky, "On the Dependence of γ' Precipitate Size in a Nickel-Based Superalloy on the Cooling Rate from Super-Solvus Temperature Heat Treatment," *Materials,* vol. 11, no. 9, p. 1528, 2018.

[307] B. Reppich, P. Schepp and G. Wehner, "Some new aspects concerning particle hardening mechanisms in γ' precipitating nickel-base alloys—II. Experiments," *Acta Metallurgica,* vol. 30, no. 1, pp. 95-104, 1982.

[308] T. A. Parthasaraty, S. I. Rao and D. M. Dimiduk, "A fast spreadsheet model for the yield strength of superalloys," in *Superalloys 2004*, Warrendale, PA, TMS (The Minerals, Metals & Materials Society), 2004, pp. 887-896.

[309] R. W. Kozar, A. Suzuki, W. W. Milligan, J. J. Schirra, M. F. Savage and T. M. Pollock, "Strengthening Mechanisms in Polycrystalline Multimodal Nickel-Base Superalloys," *Metallurgical and Materials Transactions A,* vol. 40, no. 1, pp. 1588-1603, 2009.

[310] D. J. Crudden, A. Mottura, N. Warnken, B. Raeisinia and R. C. Reed, "Modelling of the influence of alloy composition on flow stress in high-strength nickel-based superalloys," *Acta Materialia,* vol. 75, no. 1, pp. 356-370, 2014.

[311] E. I. Galindo-Nava, L. D. Connor and C. M. F. Rae, "On the prediction of the yield stress of unimodal and multimodal γ' Nickel-base superalloys," *Acta Materialia,* vol. 98, no. 1, pp. 377-390, 2015.

[312] H. E. Evans, "Cavity formation and metallurgical changes induced by growth of oxide scale," *Materials Science and Technology,* vol. 4, no. 12, pp. 1089-1098, 1988.

[313] S. Floreen, "Mechanical Behavior," in *Superalloys II*, New York, NY, John Wiley & Sons, 1987, pp. 241-262.

[314] C. T. Sims, "Prediction of Phase Composition," in *Superalloys II*, New York, NY, John Wiley & Sons, 1987, pp. 217-240.

[315] C. K. Sudbrack, L. J. Evans, A. Garg, D. E. Perea and D. K. Schreiber, "Characterization of grain boundaries and associated minor phases in disk alloy ME3 exposed at 815C," in *Superalloys 2016: Proceedings of the 13th International Symposium on Superalloys*, Warrendale, PA, TMS (The Minerals, Metals & Materials Society), 2016, pp. 927-936.

[316] R. C. Reed, M. P. Jackson and Y. S. Na, “Characterization and modeling of the precipitation of the sigma phase in UDIMET 720 and UDIMET 720Li,” *Metallurgical and Materials Transactions A,* vol. 30, pp. 521-533, 1999.

[317] A. S. Wilson, K. A. Christofidou, A. Evans, M. C. Hardy and H. J. Stone, “Comparison of methods for quantification of topologically close-packed phases in Ni-based superalloys,” *Metallurgical and Materials Transactions A,* vol. 50, no. 12, pp. 5925-5934, 2019.

[318] S. Cruchley, M. P. Taylor, H. E. Evans, P. Bowen, M. C. Hardy and S. Stekovic, “Microstructural characterisation of high temperature oxidation of nickel base superalloy RR1000 and the effect of shot-peening,” in *Superalloys 2012: 12th International Symposium on Superalloys*, Warrendale, PA, TMS (The Minerals, Metals & Materials Society), 2012, pp. 751-758.

[319] C. L. White, J. H. Schneibel and R. A. Padgett, “High temperature embrittlement of NI and Ni-Cr alloys by trace elements,” *Metallurgical Transactions A,* vol. 14, no. 1, pp. 595-610, 1983.

[320] T. J. Garosshen, T. D. Tillman and G. P. McCarthy, “Effects of B, C, and Zr on the structure and properties of a P/M nickel base superalloy,” *Metallurgical Transactions A,* vol. 18, no. 1, pp. 69-77, 1987.

[321] J. Gayda, T. P. Gabb and R. V. Miner, “Fatigue Crack Propagation of Nickel-Base Superalloys at 650C,” NASA Lewis Research Center, Cleveland, OH, 1985.

[322] J. K. Tien and R. N. Jarrett, “Effects of Cobalt in Nickel-Base Superalloys,” NASA Lewis Research Center, Cleveland, OH, 1983.

[323] V. Randle, “Mechanism of twinning-induced grain boundary engineering in low stacking-fault energy materials,” *Acta Materialia,* vol. 47, no. 15-16, pp. 4187-4196, 1999.

[324] “Effects of Heat Treatment and Chemistry on the Long-Term Phase Stability of a High Strength Nickel-Based Superalloy,” in *Superalloys 1992*, Warrendale, PA, TMS (The Minerals, Metals & Materials Society), 1992, pp. 487-496.

[325] H. Y. Li and P. Bowen, “Effect of Hafnium on the Creep-Fatigue Crack Growth resistance of Nickel Based Superalloy RR1000 at 725C,” University of Birmingham, Birmingham, UK, 2000.

[326] A. Pineau, “High Temperature Fatigue of Ni-Base Superalloys: Microstructural and Environmental Effects,” in *Engineering Against Fatigue*, Rotterdam, Netherlands, A. A. Balkema, 1999, pp. 557-565.

[327] A. Agnoli, C. Le Gall, J. Thebault, E. Marin and J. Cormier, “Mechanical Properties Evolution of γ'/γ" Nickel-Base Superalloys During Long-Term Thermal Over-Aging,” *Metallurgical and Materials Transactions A,* vol. 49, pp. 4290-4300, 2018.

[328] J. Gayda, T. P. Gabb and P. T. Katzos, “Heat Treatment Devices and Method Operation Thereof to Produce Dual Microstructure Superalloy Disks”. USA Patent 6660110, December 2003.

[329] J. e. a. Gayda, “Heat Treatment Technology for Production of Dual Microstructure Superalloy Disks”. USA Patent NASA TM 2002-211558, April 2002.

[330] D. P. Mourer and J. L. Williams, “Dual Heat Treat Process Development for Advanced Disk Applications,” in *Superalloys 2004*, Warrendale, PA, USA, TMS (The Minerals, Metals & Materials Society), 2004, pp. 401-408.

[331] G. F. Mathey, “Method of making superalloy turbine disks having graded coarse and fine grains”. USA Patent 5312497, 17 May 1994.

[332] M. C. Hardy, B. Zirbel, G. Shen and R. Shankar, “Developing damage tolerance and creep resistance in a high strength nickel alloy for disc applications,” in *Superalloys 2004*, Warrendale, PA, The Minerals, Metals & Materials Society, 2004, pp. 83-90.

[333] L. Connor, “Development of a dual microstructure heat treated Ni-base superalloy for turbine disc applications,” University of Cambridge, Cambridge, 2009.

[334] B. Engel, J. P. Rouse, C. J. Hyde, W. Lavie, D. Leidermark, S. Stekovic, S. J. Williams, S. J. Pattison, B. Grant, M. T. Whittaker, J. P. Jones, R. J. Lancaster and H. Y. Li, “The prediction of crack propagation in coarse grain RR1000 using a unified modelling approach,” *International Journal of Fatigue,* vol. 137, p. 105652, 2020.

[335] F. Delannay, “Thermal Stresses and Thermal Expansion in MMCs,” in *Comprehensive Composite Materials*, Amsterdam, Pergamon, 2000, pp. 341-369.

[336] K. Nishioka, T. Takai, Y. Arimistu and T. Ohashi, “A method of analyzing elastic constraints due to grain or interphase boundaries,” *Mechanics of Materials,* vol. 6, no. 2, pp. 139-145, 1987.

[337] S. Zhu, E. Borodin and A. P. Jivkov, “Topological characteristics of grain boundary networks during severe plastic deformations of copper alloys,” *Acta Materialia,* vol. 259, p. 119290, 2023.

[338] F. Simonetti, “Cryo-ultrasonic testing of curved components,” *NDT&E International,* vol. 137, p. 102835, 2023.

[339] R. Berger, G. Quaak, B. Hofmeister and C. G. Gebhardt, “Multiobjective Approach Toward Optimized Patch Repairs of Blisk Blades,” *AIAA Journal,* vol. 60, no. 2, pp. 1199-1210, 2022.

[340] L. Wang, Y. Li, L. Zhou, Y. Lou, S. Liu, D. Zheng and M. Yi, “Progress in additive manufacturing, additive repair and fatigue evaluation of aviation titanium alloy blades,” *Materials Research Letters,* vol. 11, no. 12, pp. 973-1012, 2023.

[341] R. Liu, Z. Wang, T. Sparks, F. Liou and J. Newkirk, “13 - Aerospace applications of laser additive manufacturing,” in *Woodhead Publishing Series in Electronic and Optical Materials*, Sawston, UK, Woodhead Publishing, 2017, pp. 351-371.

[342] E. Ahn, M. Shin, J. S. Popovics and R. E. Weaver, “Effectiveness of diffuse ultrasound for evaluation of micro-cracking damage in concrete,” *Cement and Concrete Research,* vol. 124, p. 105862, 2019.

[343] S. Gao, R. Zhang, Z. Fan, N. Li, Y. Yue and L. Xie, “Online monitoring of fatigue damage in welded joints using diffuse ultrasound,” *Ultrasonics,* vol. 138, p. 107181, 2024.

[344] A. Van Pamel, “Ultrasonic inspection of highly scattering materials,” Imperial College London, London, UK, 2006.

[345] J. J. Wang, Z. X. Wen, H. Q. Pei, S. N. Gu, C. J. Zhang and Z. F. Yue, “Thermal damage evaluation of nickel-based superalloys based on ultrasonic nondestructive testing,” *Applied Acoustics,* vol. 183, p. 108329, 2021.

[346] T. Ohtani, H. Ogi and M. Hirao, “Acoustic damping characterization and microstructure evolution in nickel-based superalloy during creep,” *International Journal of Solids and Structures,* vol. 42, no. 9-10, pp. 2911-2928, 2005.

[347] K. Barat, A. Metya, S. Sathpathy, S. Sivaprasad, S. Tarafder and S. K. Kar, “Ultrasonic quantification of high temperature cyclic damage in an advanced nickel based superalloy,” *Materials Science and Engineering: A,* vol. 625, pp. 194-204, 2015.

[348] H. K. Ann, C. S. Kim, Y. H. Shin, Y. C. Jeon and I. K. Park, “Nondestructive Evaluation of the Creep Damaged Ni-Based Superalloys using Ultrasonic Wave Method,” in *Asia-Pacific Conference on NDT*, Auckland, New Zealand, 2006.

[349] C. Kim, C. Hyun, I. Park and K. Jhang, “Ultrasonic characterization for directional coarsening in a nickel-based superalloy during creep exposure,” *Journal of Nuclear Science and Technlology,* vol. 49, no. 4, pp. 366-372, 2012.

[350] J.-Y. Kim, L. J. Jacobs, J. Qu and J. W. Littles, “Experimental characterization of fatigue damage in a nickel-base superalloy using nonlinear ultrasonic waves,” *The Journal of the Acoustical Society of America,* vol. 120, pp. 1266-1273, 2006.

[351] P. H. Rogers and A. L. Van Buren, “An exact expression for the Lommel-diffraction correction integral,” *The Journal of the Acoustical Society of America,* vol. 55, pp. 724-728, 1974.

[352] J. L. Bosse, S. Lee, A. S. Andersen, D. S. Sutehrland and B. D. Huey, “High Speed Friction Microscopy and Nanoscale Friction Coefficient Mapping,” *Measurement Science and Technology,* vol. 25, no. 11, pp. 115401-115409, 2014.

[353] Z. Wei, C. Wang and C. Bai, “Investigation of Nanoscale Frictional Contact by Friction Force Microscopy,” *Langmuir,* vol. 17, no. 13, pp. 3945-3951, 2001.

[354] N. S. Tambe, “Nanotribological investigations of materials, coatings and lubricants for nanotechnology applications at high sliding velocities,” Ohio State University, Columbus, OH, USA, 2005.

[355] J. J. Roa, G. Oncins, J. Diaz and X. G. Capdevila, “Study of the friction, adhesion and mechanical properties of single crystals, ceramics and ceramic coatings by AFM,” *Journal of the European Ceramic Society,* vol. 31, no. 4, pp. 429-449, 2011.

[356] K. O. van der Werf, C. A. J. Putman, B. G. de Grooth and J. Greve, “Adhesion force imaging in air and liquid by adhesion mode atomic force microscopy,” *Applied Physics Letters,* vol. 65, pp. 1195-1197, 1994.

[357] C. C. Dupont-Gillain and I. Jacquemart, “Patterned collagen layers on polystyrene: direct probing using AFM in the adhesion mapping mode,” *Surface Science,* vol. 539, no. 1-3, pp. 145-154, 2003.

[358] R. Garcia and E. T. Herruzo, “The emergence of multifrequency force microscopy,” *Nature Nanotechnology,* vol. 7, pp. 217-226, 2012.

[359] D. G. Yablon, A. Gannepalli, R. Proksch, J. Killgore, D. C. Hurley, J. Grabowski and A. H. Tsou, “Quantitative Viscoelastic Mapping of Polyolefin Blends with Contact Resonance Atomic Force Microscopy,” *Macromolecules,* vol. 45, pp. 4363-4370, 2012.

[360] A. Kumar, U. Rabe and W. Arnold, “Mapping of Elastic Stiffness in an α+β Titanium Alloy using Atomic Force Acoustic Microscopy,” *Japanese Journal of Applied Physics,* vol. 47, no. 7S2, pp. 6077-6080, 2008.

[361] G. Stan, S. W. King and R. F. Cook, “Nanoscale mapping of contact stiffness and damping by contact resonance atomic force microscopy,” *Nanotechnology,* vol. 23, no. 21, pp. 215703-215709, 2012.

[362] J. A. Turner and J. S. Wiehn, “Sensitivity of flexural and torsional vibration modes of atomic force microscope cantilevers to surface stiffness variations,” *Nanotechnology,* vol. 12, no. 3, pp. 322-330, 2001.

[363] A. Gannepalli, D. G. Yablon, A. H. Tsou and R. Proksch, “Mapping nanoscale elasticity and dissipation using dual frequency contact resonance AFM,” *Nanotechnology,* vol. 22, no. 35, p. 355705, 2011.

[364] X. Xu, J. Melcher and A. Raman, “Accurate force spectroscopy in tapping mode atomic force microscopy in liquids,” *Physical Review B,* vol. 81, p. 035407, 2010.

[365] X. Xu, J. Melcher, S. Basak, R. Reifenberger and A. Raman, “Compositional contrast of biological materials in liquids using the momentary excitation of higher eigenmodes in dynamic atomic force microscopy,” *Physical Review Letters,* vol. 102, no. 6, p. 060801, 2009.

[366] M. Kocun, A. Labuda, A. Gannepalli and R. Proksch, “Contact resonance atomic force microscopy imaging in air and water using photothermal excitation,” *Review of Scientific Instruments,* vol. 86, no. 8, p. 083706, 2015.

[367] A. Avila and B. Bhushan, “Electrical Measurement Techniques in Atomic Force Microscopy,” *Critical Reviews in Solid State and Materials Sciences,* vol. 35, no. 1, pp. 38-51, 2010.

[368] R. A. Oliver, “Advances in AFM for the electrical characterization of semiconductors,” *Reports on Progress in Physics,* vol. 71, pp. 076501-076537, 2008.

[369] P. Vettiger, G. Cross, M. Despont, U. Drechsler, U. Durig, B. Gotsmann, W. Haberle, M. A. Lantz, H. E. Rothuizen, R. Stutz and G. K. Binnig, “The "millipede" - nanotechnology entering data storage,” *IEEE Transactions on Nanotechnology,* vol. 1, no. 1, pp. 39-55, 2002.

[370] K. Edinger, T. Gotszalk and I. W. Rangelow, “Novel high resolution scanning thermal probe,” *Journal of Vacuum Science & Technology B,* vol. 19, pp. 2856-2860, 2001.

[371] O. D. Payton, L. Picco, T. Scott, A. Raman, J. E. Sader, J. Killgore and D. C. Hurley, “Development of a high-speed contact resonance force microscope,” Submitted to IOP Nanotechnology, 2016.

[372] N. J. Petch, “The influence of grain boundary carbide and grain size on the cleavage strength and impact transition temperature of steel,” *Acta Metallurgica,* vol. 34, no. 7, pp. 1387-1393, 1986.

[373] J. P. Killgore, D. G. Yablon, A. H. Tsou, A. Gannepalli, P. A. Yuya, J. A. Turner, R. Proksch and D. C. Hurley, “Viscoelastic property mapping with contact resonance force microscopy,” *Langmuir,* vol. 27, no. 23, pp. 13983-13987, 2011.

[374] J. P. Killgore and D. C. Hurley, “Low-force AFM nanomechanics with higher-eigenmode contact resonance spectroscopy,” *Nanotechnology,* vol. 23, no. 5, p. 055702, 2012.

[375] G. Stan and R. F. Cook, “Mapping the Elastic Properties of Granular Au Films by Contact Resonance Atomic Force Microscopy,” *Nanotechnology,* vol. 19, no. 23, p. 235701, 2008.

[376] I. Casuso, N. Kodera, C. Le Grimellec, T. Ando and S. Scheuring, “Contact-Mode High-Resolution High-Speed Atomic Force Microscopy Movies of the Purple Membrane,” *Biophysical Journal,* vol. 97, no. 5, pp. 1354-1361, 2009.

[377] P. A. Yuya, D. C. Hurley and J. A. Turner, “Contact-resonance atomic force microscopy for viscoelasticity,” *Journal of Applied Physics,* vol. 104, p. 074916, 2008.

[378] G. Meyer and N. M. Amer, “Novel optical approach to atomic force microscopy,” *Applied Physics Letters,* vol. 53, pp. 1045-1047, 1988.

[379] P. K. Hansma, J. P. Cleveland, M. Radmacher, D. A. Walters, P. E. Hillner, M. Bezanilla, M. Fritz, D. Vie, H. G. Hansma, C. B. Prater, J. Massie, L. Fukunaga, J. Gurley and V. Elings,

"Tapping mode atomic force microscopy in liquids," *Applied Physics Letters,* vol. 64, pp. 1738-1740, 1994.

[380] Q. Zhong, D. Inniss, K. Kjoller and V. B. Elings, "Fractured polymer/silica fiber surface studied by tapping mode atomic force microscopy," *Surface Science,* vol. 290, no. 1-2, pp. L688-L692, 1993.

[381] F. J. Giessibl, "Atomic Resolution of the Silicon (111)-(7×7) Surface by Atomic Force Microscopy," *Science,* vol. 267, no. 5194, pp. 68-71, 1995.

[382] G. Binnig, C. F. Quate and C. Gerber, "Atomic Force Microscope," *Physical Review Letters,* vol. 56, no. 9, pp. 930-933, 1986.

[383] S. Hosaka, K. Etoh, A. Kikukawa and H. Koyanagi, "Megahertz silicon atomic force microscopy (AFM) cantilever and high-speed readout in AFM-based recording," *Journal of Vacuum Science & Technology B,* vol. 18, pp. 94-99, 2000.

[384] G. T. Paloczi, B. L. Smith, P. K. Hansma, D. A. Walters and M. A. Wendman, "Rapid imaging of calcite crystal growth using atomic force microscopy with small cantilevers," *Applied Physics Letters,* vol. 73, pp. 1658-1660, 1998.

[385] T. Ando, "High-speed atomic force microscopy coming of age," *Nanotechnology,* vol. 23, no. 6, pp. 062001-062027, 2012.

[386] C. Braunsmann and T. E. Schaffer, "High-speed atomic force microscopy for large scan sizes using small cantilevers," *Nanotechnology,* vol. 21, pp. 225705-225707, 2010.

[387] T. Fukuma and S. P. Jarvis, "Development of liquid-environment frequency modulation atomic force microscope with low noise deflection sensor for cantilevers of various dimensions," *Review of Scientific Instruments,* vol. 77, no. 4, pp. 043701-043708, 2006.

[388] A. Labuda, T. Brastaviceanu, I. Pavlov, W. Paul and D. E. Rassier, "Optical detection system for probing cantilever deflections parallel to a sample surface," *Review of Scientific Instruments,* vol. 82, no. 1, pp. 59-62, 2011.

[389] G. Meyer and N. M. Amer, "Optical-beam-deflection atomic force microscopy: The NaCl (001) surface," *Applied Physics Letters,* vol. 56, pp. 2100-2101, 1990.

[390] O. D. Payton, L. Picco, M. J. Miles, M. E. Homer and A. R. Champneys, "Improving the signal-to-noise ratio of high-speed contact mode atomic force microscopy," *Review of Scientific Instruments,* vol. 83, no. 8, p. 083710, 2012.

[391] O. D. Payton, L. Picco, D. Robert, A. Raman, M. E. Homer, A. R. Champneys and M. J. Miles, "High-speed atomic force microscopy in slow motion-understanding cantilever behaviour at high scan velocities," *Nanotechnology,* vol. 23, no. 20, p. 205704, 2012.

[392] O. D. Payton, L. Picco, A. R. Champneys, M. E. Homer, A. Raman and M. J. Miles, "Experimental observation of contact mode cantilever dynamics with nanosecond resolution," *Review of Scientific Instruments,* vol. 82, no. 4, p. 043704, 2011.

[393] M. Spletzer, A. Raman and R. Reifenberger, "Spatio-temporal dynamics of microcantilevers tapping on samples observed under an atomic force microscope integrated with a scanning laser Doppler vibrometer: applications to proper orthogonal decomposition and model reduction," *Journal of Micromechanics and Microengineering,* vol. 20, p. 085204, 2010.

[394] Polytec GmbH, "Laser Doppler Vibrometry," Polytec, 2024. [Online]. Available: https://www.polytec.com/us/vibrometry/technology/laser-doppler-vibrometry. [Accessed 28 June 2024].

[395] I. S. Bozchalooi and K. Youcef-Toumi, "Multi-actuation and PI control: a simple recipe for high-speed and large-range atomic force microscopy," *Ultramicroscopy,* vol. 146, pp. 117-124, 2014.

[396] G. Schitter, R. W. Stark and A. Stemmer, "Fast contact-mode atomic force microscopy on biological specimen by model-based control," *Ultramicroscopy,* vol. 100, pp. 253-257, 2004.

[397] G. Schitter, F. Allgower and A. Stemmer, "A new control strategy for high-speed atomic force microscopy," *Nanotechnology,* vol. 15, no. 1, pp. 253-257, 2003.

[398] O. Payton, A. R. Champneys, M. E. Homer, L. Picco and M. J. Miles, "Feedback-induced instability in tapping mode atomic force microscopy: theory and experiment," *Proceedings of the Royal Society A: Mathematical, Physical and Engineering Sciences,* vol. 467, no. 2130, pp. 1801-1822, 2011.

[399] L. M. Picco, L. Bozec, A. Ulcinas, D. J. Engledew, M. Antognozzi, M. A. Horton and M. J. Miles, "Breaking the speed limit with atomic force microscopy," *Nanotechnology,* vol. 18, no. 4, pp. 044030-044033, 2006.

[400] P. Klapetek, L. Picco, O. Payton, A. Yacoot and M. Miles, "Error mapping of high-speed AFM systems," *Measurement Science and Technology,* vol. 24, no. 2, pp. 025006-025007, 2013.

[401] P. Klapetek, M. Valtr, L. Picco, O. D. Payton, J. Martinek, A. Yacoot and M. Miles, "Large area high-speed metrology SPM system," *Nanotechnology,* vol. 26, no. 6, pp. 056601-065509, 2015.

[402] Oxford Instruments, "Interpreting the Diffraction Pattern," Miramar Communications Ltd, 2025. [Online]. Available: https://www.ebsd.com/ebsd-explained/interpreting-the-diffraction-pattern. [Accessed 13 March 2025].

9. Appendices

9.1 ImageJ Binary Technique

Having had inconsistent results when attempting to analyse the total percentage of the δ phase in the micrographs of Inconel 718, alternative methods to estimate shaded areas from micrographs using ImageJ were investigated. One proposed technique, instead of using manual thresholding, involved smoothing the image, setting it to an 8-bit type before finally converting to binary format, before using the particle analysis tool. This generated an overall percentage of the shaded area (which generally corresponded to the δ precipitates, though in some instances the reverse was the case) as well as a breakdown of the individual particles it had detected and summed to calculate the final overall percentage. Much like the manual colour thresholding method, the results generated were inconsistent, as well as being highly inaccurate. Some examples of the drawings generated are shown in Figure 119 to Figure 121; in some cases, the individual δ precipitates were not detected and merged into much larger particles, (which still gave the same, albeit incorrect, overall area of the δ phase), whereas in other instances there were barely any δ particles identified (and in a couple of instances, none at all).

Table 31: Volume fraction estimates of the δ phase in Inconel 718 using binary image setting.

Sample	**Micrograph**	**% δ ImageJ (Binary)**
OG1 (pre-HD)	NHT1_01_ETD_SE_1000x	16.8
	NHT1_02_ETD_SE_1000x	17.34
	NHT1_02_T1_A+B_1000x	**2.46**
	NHT1_03_ETD_SE_1000x	**4.59**
	NHT1_03_T1_A+B_1000x	**4.35**
	NHT1_100X	20.02
	NHT1_200X	16.27
	NHT1_500X	12.56
	NHT1_1000X	12.46
	Average	**3.80**
OG3	NHT3_03_ETD_SE_500x	22.49

(pre-A)	NHT3_50X	30.33
	NHT3_100X	20.15
	NHT3_200X	14.74
	NHT3_500X	12.86
	Average	
OG4 (pre-HD)	NHT4_03_ETD_SE_500x	18.63
	NHT4_04_ETD_SE_1000x	13.91
	NHT4_50X	32.49
	NHT4_100X	23.1
	NHT4_200X	17.11
	NHT4_500X	13.9
	NHT4_500X_2	13.56
	NHD4	16.45
	Average	
Datum	As_Received_500x_CA_BF	13.53
	As_Received_1000x_CA_BF	11.28
	AsReceived_05_ETD	**4.08**
	AsReceived_05_T1	37.1
	AsReceived_05_T2	26.25
	AsReceived_06_T1	19.43
	AsReceived_ETD_SE_10.00kV_0.40nA_80x_01	41
	AsReceived_ETD_SE_10.00kV_0.40nA_80x_02	35.87
	Average	**4.08**
FC900	900C_01_ETD	16.95
	900C_02_ETD	9.00
	900C_02_T1	47.63
	900C_50h_500x_CA_BF	47.37
	Average	
FC1000	1000C_10h_1000x_CA_DIC	40.73
	Average	
WQ900	900C_ETD_SE_10.00kV_0.40nA_650x_01	29.45

	900C_ETD_SE_10.00kV_0.40nA_1000x_02	21.78
	900C_ETD_SE_10.00kV_0.40nA_5000x_03	10.15
	900C_T1_A+B_5.00kV_0.40nA_1000x_01	8.96
	Average	

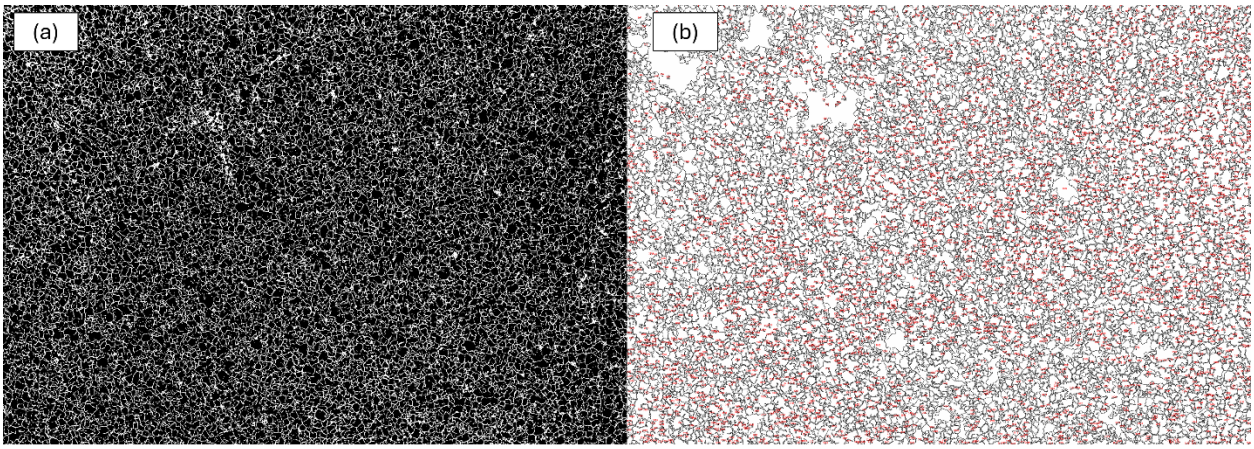


Figure 119: (a) A binary micrograph and (b) accompanying ImageJ drawing (with delta particles identified) for micrograph NHT4, 50x magnification.

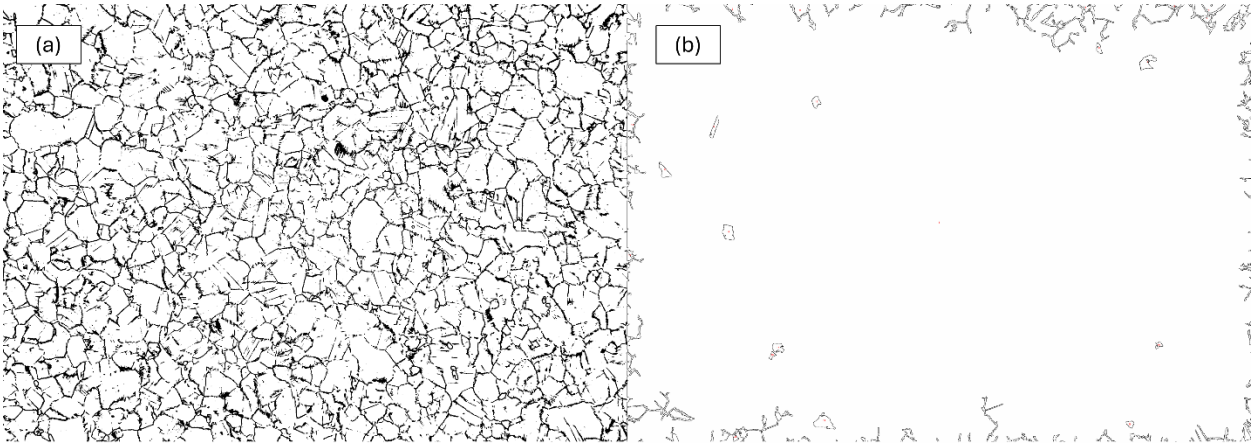


Figure 120: (a) A binary micrograph and (b) accompanying ImageJ drawing (with delta particles identified) for micrograph NHT4, 200x magnification.

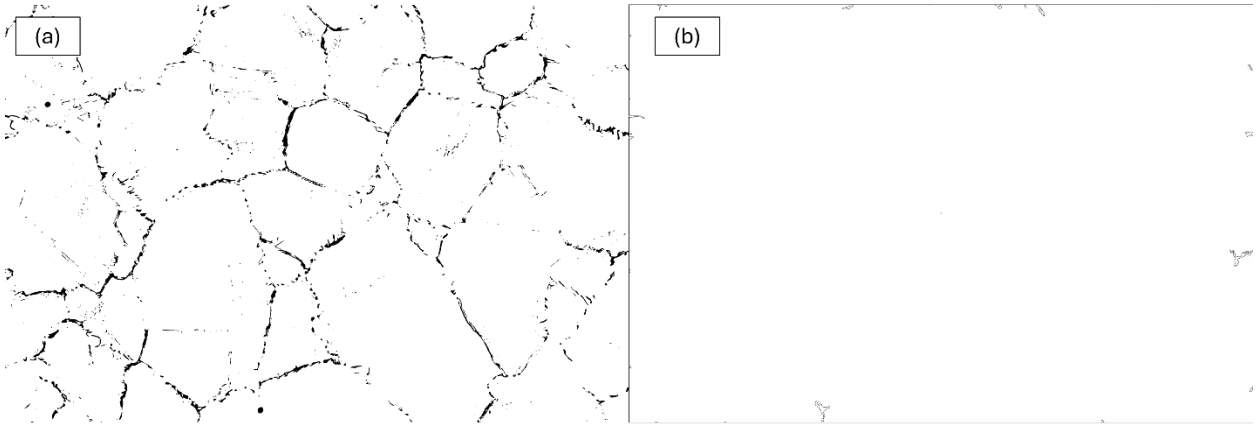


Figure 121: (a) A binary micrograph and (b) accompanying ImageJ drawing (with delta particles identified) for an SEM micrograph of sample NHT1, 1000x magnification.

9.2 Reduced Order UWS Investigations

It was noted from the UWS experiments for Inconel 718 that good convergence to the cumulative mean V00 value was reached after 8 trials, and thus for Udimet 720Li and RR1000 the number of experiments could be reduced from 16 to 10, enabling a reduction in the required experimental time. However, a further investigation was carried out regarding the required order of the spherical convolution theory; the currently used order, N, of 6 mean that measurements had to be taken in 6 different orientations in the x-y plane, but the use of a lower order would enable the V00 to be calculated with less measurement directions, meaning that a single experiment would require less time. Having acquired measurements in the 6 different directions, it was therefore possible to investigate orders 2 and 3 by using the first and fourth measurements, and every other measurement, respectively, when carrying out the deconvolution. The results for these studies, performed on the OG set of Inconel 718, have been presented here in Figure 122 and Figure 123. The 'true' value of V00 (found from using the full, 6th order deconvolution) have been plotted in dashed lines for each sample.

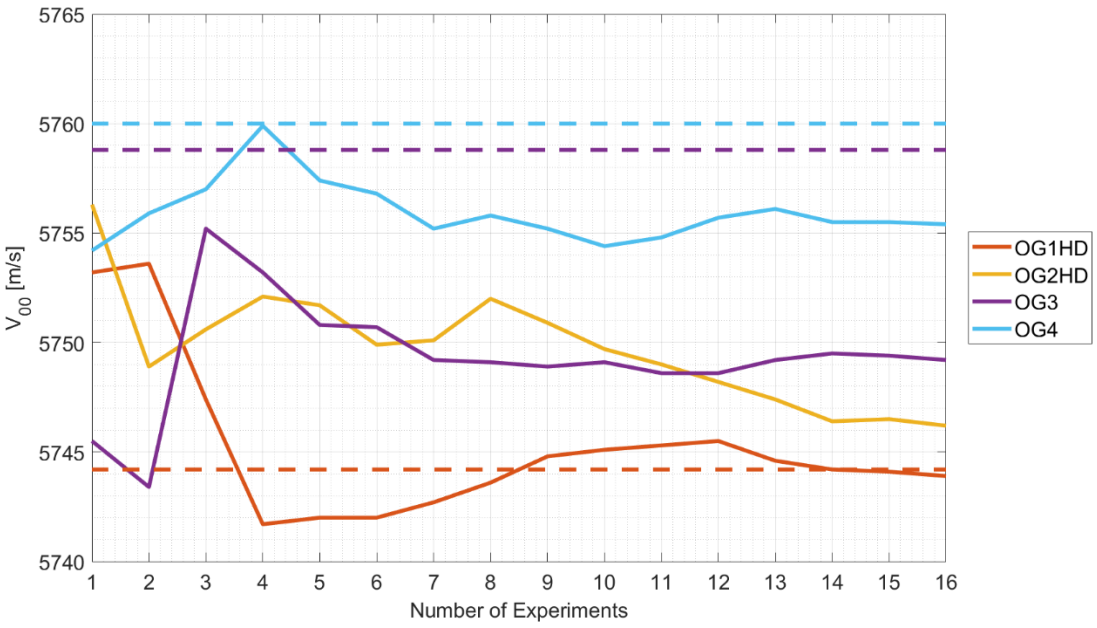


Figure 122: V00 results for OG samples using a second order deconvolution process.

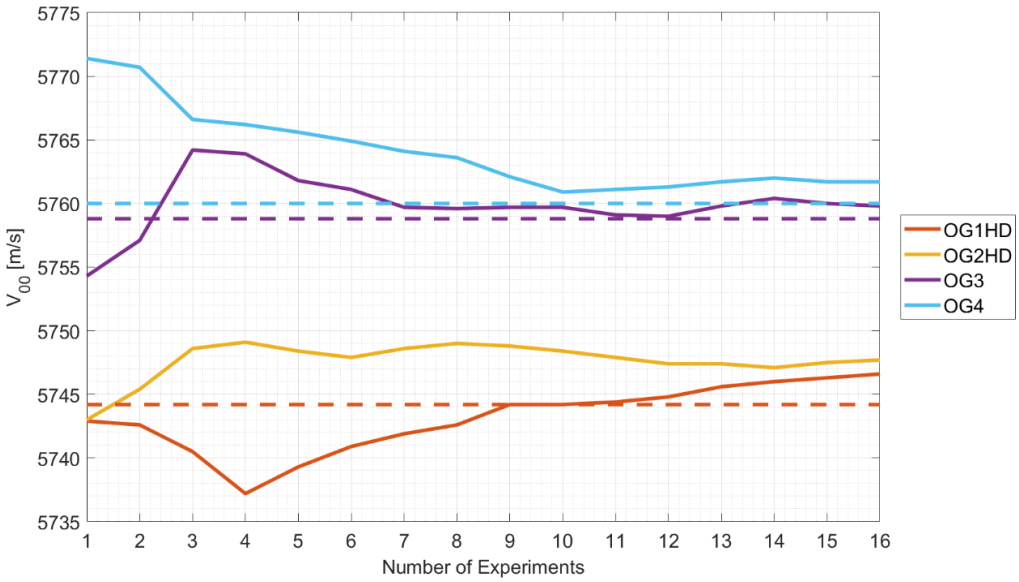


Figure 123: V00 results for OG samples using a third order deconvolution process.

It is immediately apparent from Figure 122, without a direct comparison to the real results from the deconvolution, that an order of 2 is insufficient to reach the required levels of accuracy for finding the V00. In the case of the as-received OG samples, the V00 values are significantly lower than they should be, and there is a much greater difference between those of OG3 and OG4 than for the sixth order deconvolution. It is interesting to note, however, that the heat damaged samples OG1HD and OG2HD have converged towards the true V00 value much more successfully – though there is still much more variability in the individual V00 measurements.

When using a third order deconvolution framework, not only do the values converge more closely to each other but they also approach the true mean values of V00 much better, with less variability in the individual measurements. The fact that they all samples have converged to within 5m/s of the mean value is promising; although, due to the nature of the deconvolution itself, the use of a third order is not possible, it may be the case that for future measurements an order of 4 may be sufficient, and thus only requiring the acquisition of angles in 4 different x-y plane orientations. However, the use of a reduce order may not be sufficient for samples with microstructures which cause V00 measurements to have a great deal of variability, such as the Udimet 720Li discs; thus, when using the UWS technique for phase characterisation for a new material, the full sixth order deconvolution should be used initially before establishing whether reducing the order will still result in the required levels of accuracy.

9.3 Attenuation Measurements

9.3.1 Overview

The idea of using of frequency-dependent attenuation as an alternative method of detecting microstructural changes within nickel-based superalloys arose from the greatly increased levels of attenuation observed while measuring wave speeds through the set of heat-damaged Inconel 718 samples (due to their significantly larger grain size, a consequence of the high hold temperature simulating extreme over-temperature conditions).

Attenuation is a phenomenon whereby the energy of an ultrasonic wave propagating through a material is dissipated, with the beam spreading and the wave amplitude itself decreasing (though the effect is not exclusively observed for ultrasonic waves – sound waves of all frequencies will display this effect, though the levels of attenuation observed depend on the frequency of the wave as well as the medium being travelled through). The energy dissipation is due to a number of different factors, including dispersion (beam spreading), diffraction (the spreading of waves around impurities and inclusions), absorption, and scattering – with the latter two being solely properties of the material [344]. There will also be energy loss at interfaces; in the case of the immersion tank used for these experiments, this occurs first when the wave hits the water, again when it encounters the sample, and as it continues its path through the sample. There is the additional complexity within polycrystalline materials of anisotropy, or macro-anisotropy – where there are stiffness variations on a macro-scale – can further affect wave propagation, causing deviations from the expected straight-line path (such as in an isotropic medium) [344].

It has been found in the literature that ultrasonic attenuation can be used for materials characterisation applications within nickel-based superalloys; for example, thermal damage evaluation [345], microstructure evolution during creep [346], the influence of plastic strain accumulation and surface crack density on attenuation [347], evaluating creep damage [348] as well as directional coarsening as a result of creep exposure [349] and characterisation of fatigue damage [350]. Although these are all phenomena based on grain size changes, rather than variations in phase composition, the literature studies do demonstrate the fact that the potential to quantify attenuation for materials characterisation purposes has been validated.

Although measurements of ultrasonic attenuation alone cannot be used as a quantitative measure of microstructural changes as it is also sensitive to textural variations, it was a potentially useful comparison measurement to the wave speed measurements; for example, attenuation values could be used as an initial assessment of a material, to see whether it was likely to require further detailed investigation as to its suitability for an application. It is a rapid way of detecting grain size changes, as larger grain sizes will manifest as increased levels of attenuation (as well as greater difficulty in detecting reflections of signals, particularly those occurring later temporally, such as the DTT signals). Combined with the ultrasonic wave speed measurement technique, it could form a powerful and rapid tool for characterising a material, with attenuation indicating the grain size and the UWS measurements the more detailed information pertaining to the phases present.

9.3.2 Theoretical Framework

The underlying theory for attenuation measurements is based on an approach derived in a previous doctoral thesis [344], using a pulse-echo immersion setup (almost identical to that used for the UWS measurements, without the moving sample platform; instead, the disc being tested can be supported by two bars of the same height, resting on the acoustic mirror). The following equation defines a wave of amplitude A_z propagating at a distance z from a finite source, with initial incident amplitude A_0. The attenuation coefficients for scattering and absorption are represented by α_s and α_a respectively, and are later combined into a single coefficient α. The attenuation resulting from diffraction is represented by the term D_z.

$$A_z = D_z A_0 e^{-(\alpha_s + \alpha_a)z} = D_z A_0 e^{-\alpha z} \tag{A1}$$

The first, second and third coherent reverberations, F, $B1$ and $B2$, are shown with the black, blue and orange arrows respectively in Figure 124, where '1' and '2' denote the media of water and the sample, required for the calculation of the reflection (R) and transmission (T) coefficients. These coefficients are independent of frequency, and calculated using a plane wave assumption, with the order of the subscripts denotes the direction of travel (e.g. '12' represents the wave travelling from water to sample).

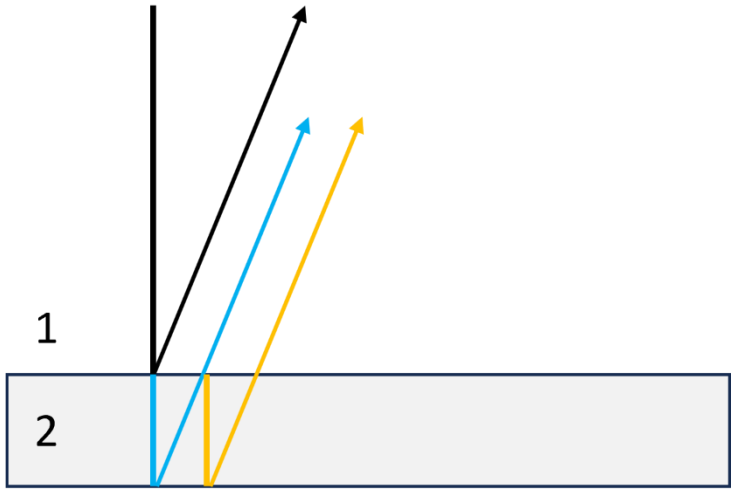


Figure 124: Schematic illustrating the reverberations F, B1 and B2 (black, blue and orange respectively). The reverberations are skewed for illustrative purposes.

The amplitudes of these signals can be found using the following equations:

$$F = D_0 A_0 e^{-\alpha z_0} R_{12} \tag{A2}$$

$$B1 = D_1 A_0 e^{-\alpha z_1} T_{21} R_{21} T_{12} \tag{A3}$$

$$B2 = D_2 A_0 e^{-\alpha z_2} T_{21} (R_{21})^3 T_{12} \tag{A4}$$

The diffraction coefficients of the respective signals depend on the propagation distance, denoted by z, which is the total axial distance travelled by the wave. In the case of the frontwall echo, this would be twice the distance between the transducer and the sample surface; for the first backwall echo B1, this would be summed with twice the thickness of the sample, and so on.

By dividing equation 10 by equation 9, and equation 11 by equation 10, two different expressions for the attenuation coefficient can be obtained. For highly attenuative materials, where the signal B2 may not be detectable, the first expression may be used; however, it is generally better experimental practice to use the first and second backwall echoes, as both signals would be affected by the surface roughness of the sample by the same amount, and therefore these are the echoes which have been used for these experiments (although the roughness should not pose too much of an issue in terms of accuracy, but just have the effect of a reduced signal amplitude).

$$\alpha_{FB} = \frac{1}{(z_1 - z_0)} \ln\left(\frac{F D_1 T_{12} R_{12} T_{21}}{B D_0 R_{21}}\right) \tag{A5}$$

$$\alpha_{B1B2} = \frac{1}{(z_2 - z_1)} \ln\left(\frac{B1 D_2 [R_{12}]^2}{B2 D_1}\right) \tag{A6}$$

Taking the Fourier transforms of F, B1 and B2, and introducing the angular frequency ω gives the final expression for calculating the frequency dependent attenuation from the measured first and second backwall signals, as below:

$$\alpha(\omega) = \frac{1}{(z_2 - z_1)} \ln \frac{B1'(\omega) D_2 [R_{12}]^2}{B2'(\omega) D_1} \tag{A7}$$

The calculation of the diffraction correction coefficient is a slightly more involved process; the widely accepted solution is derived from using the underlying assumption of a piston set in a rigid baffle, oscillating harmonically into a homogeneous fluid, and neglecting refraction effects by considering a normal beam [351]. The expression for the diffraction correction is as follows [344]:

$$D_i = 1 - e^{-i\left(\frac{2\pi}{s}\right)}\left[J_0\left(\frac{2\pi}{s}\right) + iJ_1\left(\frac{2\pi}{s}\right)\right] \tag{A8}$$

$$s = \frac{2\pi z_i}{k_i a^2} \tag{A9}$$

The transducer radius is denoted by a, with z_i being the total axial distance travelled by a signal, k_i the wavenumber in the medium which the signal is travelling through (i.e. the sample material, for signals $B1$ and $B2$), and J_0 the zeroth order Bessel function.

9.3.3 Experimental Setup

As previously mentioned, the experimental equipment is a pulse-echo immersion; this was much like the apparatus used for the ultrasonic wave speed measurements, but without the need for the moving sample platform. Instead, the sample was supported by blocks resting on the acoustic mirror (such that the sample rested parallel) and the transducer positioned directly above the centre of the sample, to ensure minimal interference from side wall reflections. An additional difference to the UWS measurement setup was the frequency of the transducer; in order to force higher levels of attenuation (and attempt to reduce fluctuations in the signal), a 15MHz non-focussed transducer was used. This allowed for the levels of attenuation to be increased enough such that the fluctuations diminished, but to such an extent that the backwall signals could still be detected. (A lower frequency probe would have made the attenuation profile more susceptible to experimental and other forms of errors, if both the attenuation and test specimen thickness are quite small, as in the case of these samples.) The code used to move the transducer was also slightly different; the gain, pulse width, voltage and signal windows set in the same manner, but in addition the start and end positions of the C scan (equivalent to top left and bottom right corner of the scan area, if looking top-down at the sample from above) were also inputs. The use of a C scan across an area, rather than an A-scan of a point on the sample, was used as the attenuation is likely to vary from point to point; the use of an average of points would therefore be more likely to give a better representation of the attenuation profile of the sample.

The setup is shown in Figure 125 below, and the wave velocity through water, as well as the densities of each material, are shown in Table 32. The amount of attenuation through the sample at each point was calculated during the data post-processing, the procedure of which is described in the following section.

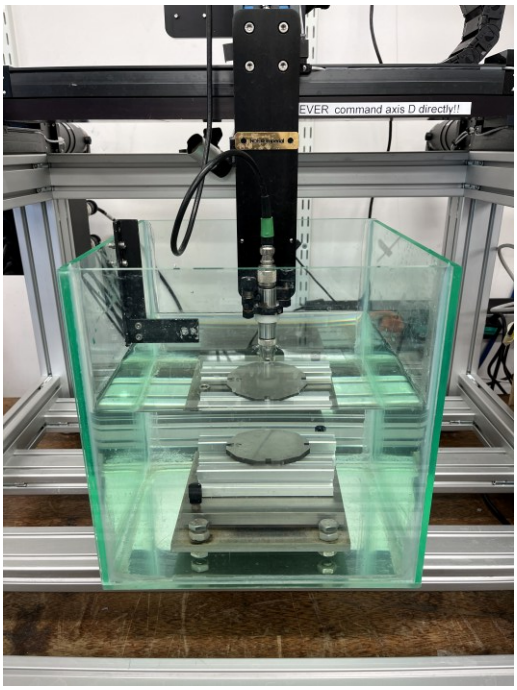


Figure 125: Pulse-echo immersion setup for attenuation measurements.

Table 32: Required variables for frequency-dependent attenuation calculations.

Sound velocity through water [m/s]	1.4967×10^3
Density of water [kg/m^3]	997
Density of Inconel 718 [245]	8193
Density of Udimet 720Li [283]	8080
Density of RR1000 [285]	8320

9.3.4 Post Processing

Having acquired the C scans for each sample, the following procedure was used in order to first extract the data, before calculating the frequency dependent attenuation through the samples.

Initially, each of the signals (F, B1, B2) was isolated using a Tukey window with 190 points, and cosine fraction 0.1. The number of points was determined by the minimum possible that could be used in order to encompass each signal fully (to create as smooth as a profile as possible, by minimising noise), and the Tukey window was chosen as opposed to a rectangular window such that it would have tapered edges, rather than a straight cutoff. Each signal was then normalised by subtracting the mean from all data points, in order to centre the signal on the x axis with zero offset.

The frequency vector was then established for the frequency domain analysis; using the sampling frequency from the experimental setup (200MHz), the time vector was set up using the following equation:

$$t = \left(0{:}\,1{:}\,size\left(B1_{sigWin}, 1\right) - 1\right).* \left(\frac{1}{f_{sampling}}\right) \tag{A10}$$

Having established the time vector, the sampling frequency required to carry out the Fourier transform was found:

$$f_s = \frac{1}{t(2) - t(1)} \tag{A11}$$

The number of points in the Fourier transform was set to be twice the length of the time array:

$$fft_{points} = 2 * length(t) \tag{A12}$$

Finally, the frequency vector for the plots of frequency-dependent attenuation was set up:

$$freq = f_s * \frac{\left(0{:}\left[\frac{fft_{pts}}{2} - 1\right]\right)}{fft_{pts}} \tag{A13}$$

The Fourier transform could then be performed on each of the windowed signals. The number of sampling points was increased to be double the length of the number of data points (from the default length, of the number of elements in the original dataset) in order to make the line smoother, and then padded with zeros. The frequency-dependent attenuation was calculated using the first and second backwall signals, B1 and B2, with the front-wall signal F used to find the FWHM of the transducer. This was required to establish the correct frequency range for plotting the frequency-dependent attenuation, as only data from within this bandwidth would be accurate. As the FFT produces a mirror of values for positive and negative frequencies, only the positive side of the spectrum is plotted for simplicity.

The steps required to calculate the frequency-dependent attenuation are as outlined in Equations 14 to 16, with the only additional step in the procedure being the calculation of the wave velocity

through the sample for each measured point in the C scan; this was found using the time lag between the first and second echoes, and twice the thickness of the sample.

The final step to plot the frequency-dependent attenuation for each of the samples involved finding the mean values from the C scan, before isolating the FWHM region of frequencies within which the attenuation data could be considered accurate (due to it being the ideal operating frequency of the transducer). In order to find the FWHM of the transducer, the front wall reflection was used, as it was likely to give a better representation of the main energy bandwidth of the transducer due to there being less attenuation than the subsequent echoes from the backwall. In addition, when plotting the mean values of attenuation, the natural logarithm of the absolute value was taken to ensure there were no imaginary components remaining.

9.3.5 Attenuation Results

9.3.5.1 Determining FWHM

Having acquired C scans of all of the samples and post-processed the data, the frequency-dependent attenuation in the FWHM range of the transducer, found to be approximately 8-15MHz (see Figure 126), was plotted (where possible) for each set of materials. The FWHM was determined using the front wall echo (F) of the C scans.

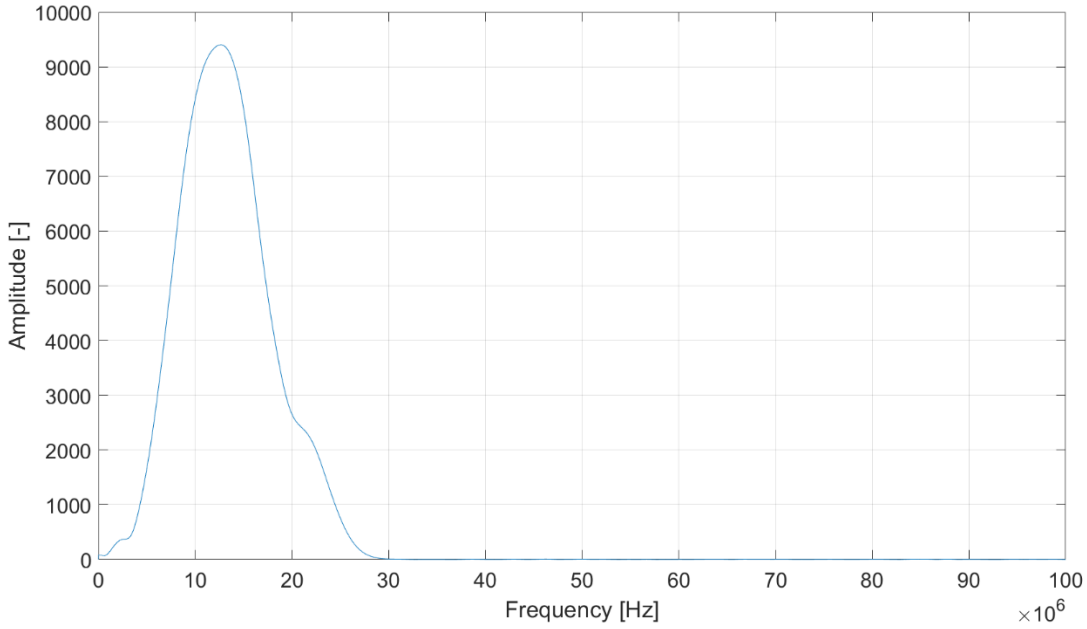


Figure 126: Frequency content of front wall echo (F) for sample OG3A.

There were, however, a few samples where the frequency plot of the front-wall echo was not as expected; one example was OG1HD, whose plot is shown in Figure 127, where there are two peaks present in the frequency transform. The exact reason for these double peaks could not be determined, but it was thought that there may be been an overlap of signals within some samples (due to their relatively small thickness) causing there to be multiple peaks. A possible reason that this did not occur across all samples may have been due to the differences in axial separation between the transducer and the sample when acquiring the C scans. One of the A-scans for the sample OG1HD is shown in Figure 128, where it can be seen that there may be multiple pulses within one signal packet. The first has a wider spacing (or wavelength), followed by a set of peaks where this becomes slightly narrower. As it was more likely that the bandwidth of the transducer

would be lower than the quoted central frequency of 15MHz (due to energy being lost from attenuation and scattering as the wave passes through the material), the FWHM was deduced by extrapolating the downwards curve of the first peak and determining the operating bandwidth using this range, neglecting the other peak. This also yielded a similar range to the 8-15MHz found from the single peak frequency transform in Figure 126. In the future, the double peak effect may be mitigated against by increasing the distance between the transducer and the top surface of the sample, as this may reduce the effect of signal overlap. (In fact, a similar adjustment was required when acquiring the V00 measurements, and ensuring the DTT signal was suitably isolated from any other reflections.)

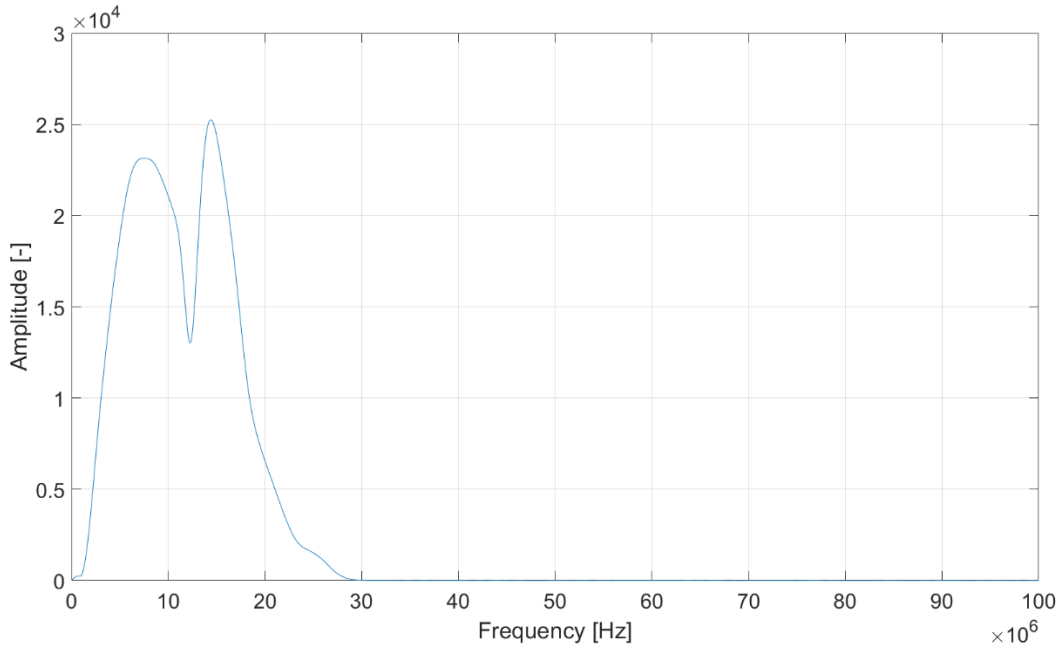


Figure 127: Frequency content of front wall echo (F) of sample OG1HD.

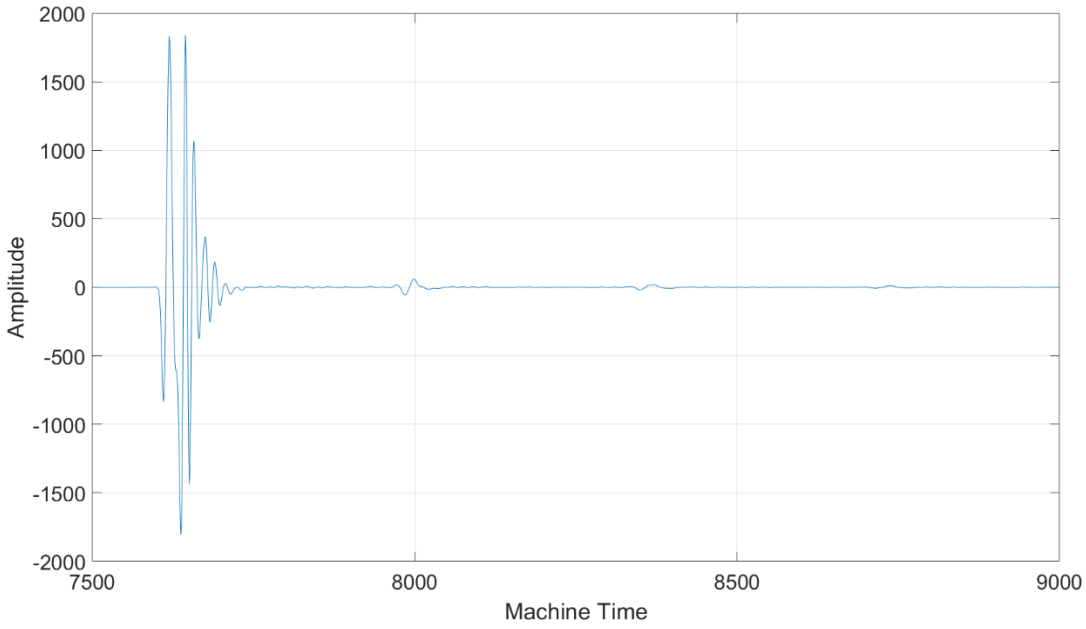


Figure 128: A-scan from OG1HD C-scan data.

For the 'OG' set of Inconel 718 samples, it was found that only the finer grain samples (OG3, OG3A and OG4) showed the expected trend of increasing attenuation with frequency in the FWHM region of the transducer bandwidth, albeit with some fluctuations. These results are shown in Figure 129, with the standard deviations plotted in Figure 130; there is not a great difference in the attenuation values between the individual samples.

In the case of the heat damaged discs, shown in Figure 131, the attenuation was drastically higher in the FWHM region of the transducer, but the extent of fluctuation was too great for there to be any discernible trend to be determined. The region where there was the expected increase in attenuation with was manifested at a much lower frequency range; this may be related to the double peak effect being seen in the FWHM of the front wall echo. (This double-peak was also observed when acquiring C scans for OG3 and OG4, but in the case of these samples the small grain sizes, meaning low levels of scattering and attenuation, may have meant that the attenuation profiles were not significantly affected by this double peak issue.) The double peak problem does mean that the results are not straightforward to interpret, but the fact that the HD samples all have similar trends and values (as well as a fairly consistent standard deviation, seen in Figure 132) means that it can at least be inferred that these samples all have very similar grain sizes.

The results for the lower bandwidth range for all OG samples have been shown in Figure 133 for comparison, with the standard deviations in Figure 134; the as-received and aged samples show a marked difference between the attenuation levels as expected, but whether this is a valid set of results to use due to the low frequency range with respect to the quoted transducer frequency is uncertain.

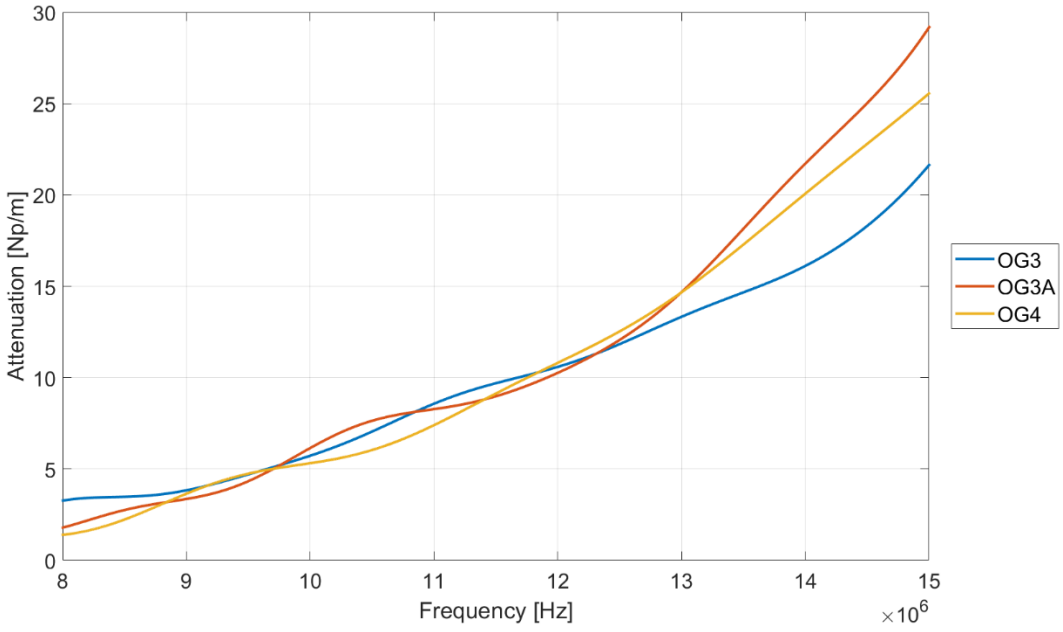


Figure 129: Frequency-dependent attenuation for finer grained OG samples.

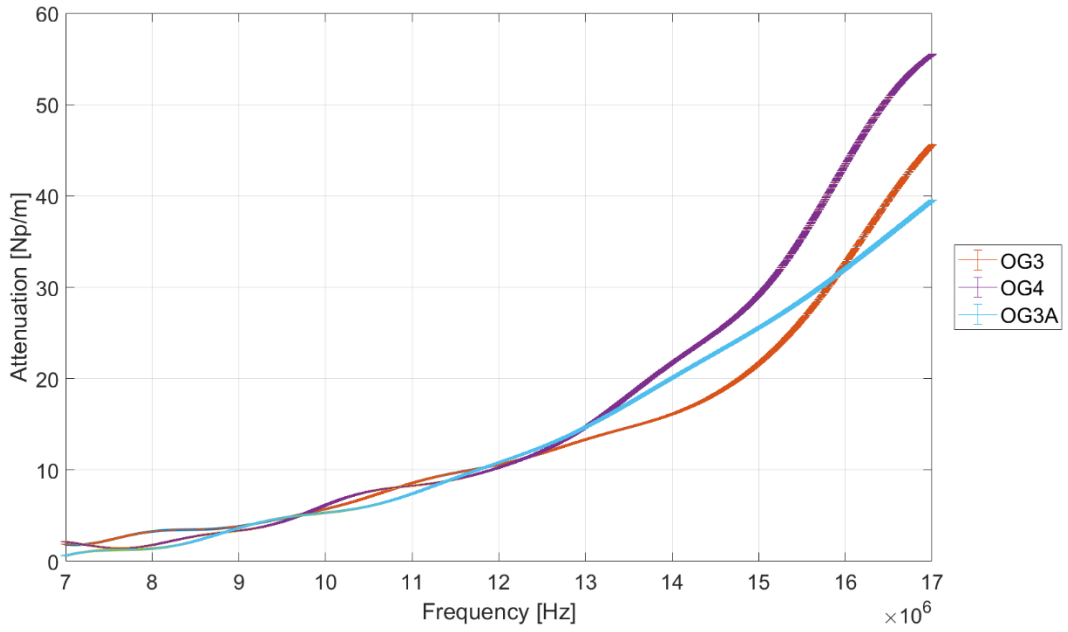


Figure 130: Frequency-dependent attenuation for finer grained OG samples, shown together with standard deviation error bars.

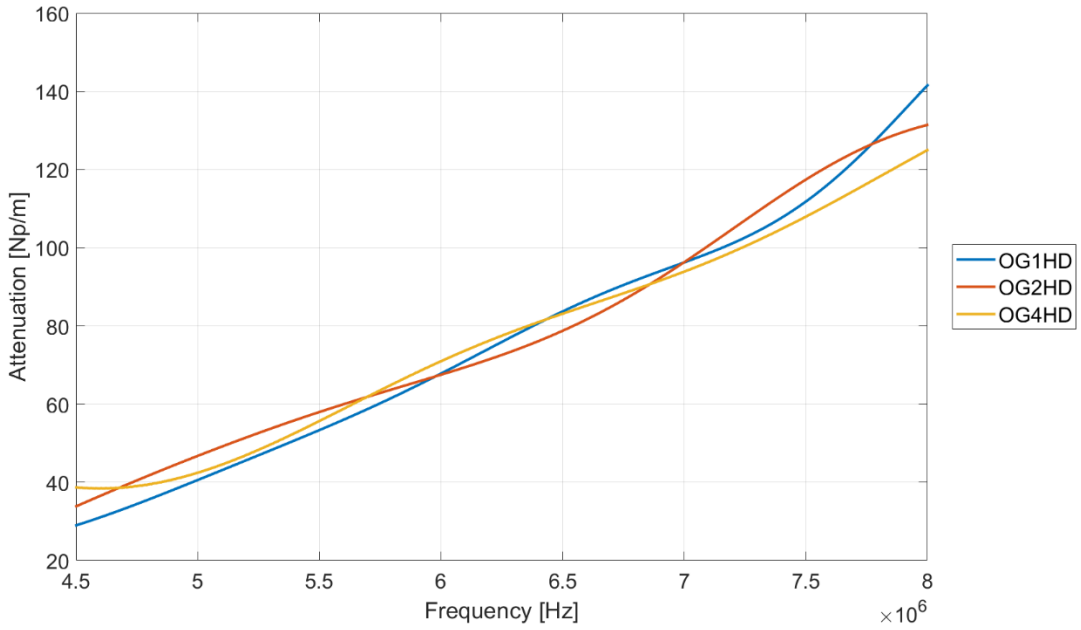


Figure 131: Frequency-dependent attenuation of heat damaged OG samples, with lower frequency range than FWHM.

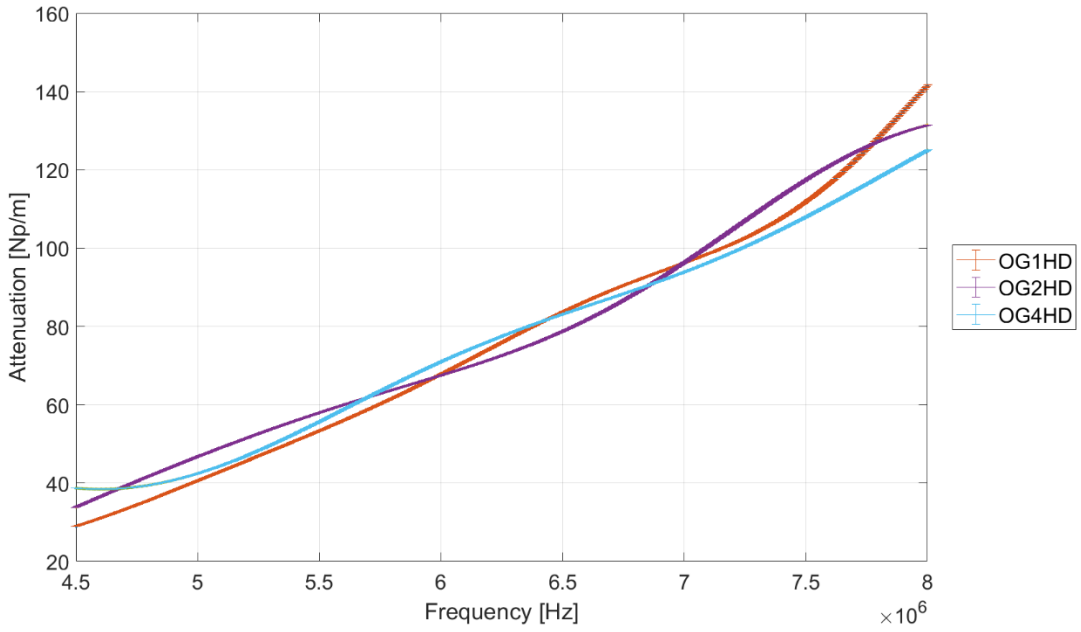


Figure 132: Frequency-dependent attenuation of heat damaged OG samples, with lower frequency range than FWHM, shown together with standard deviation error bars.

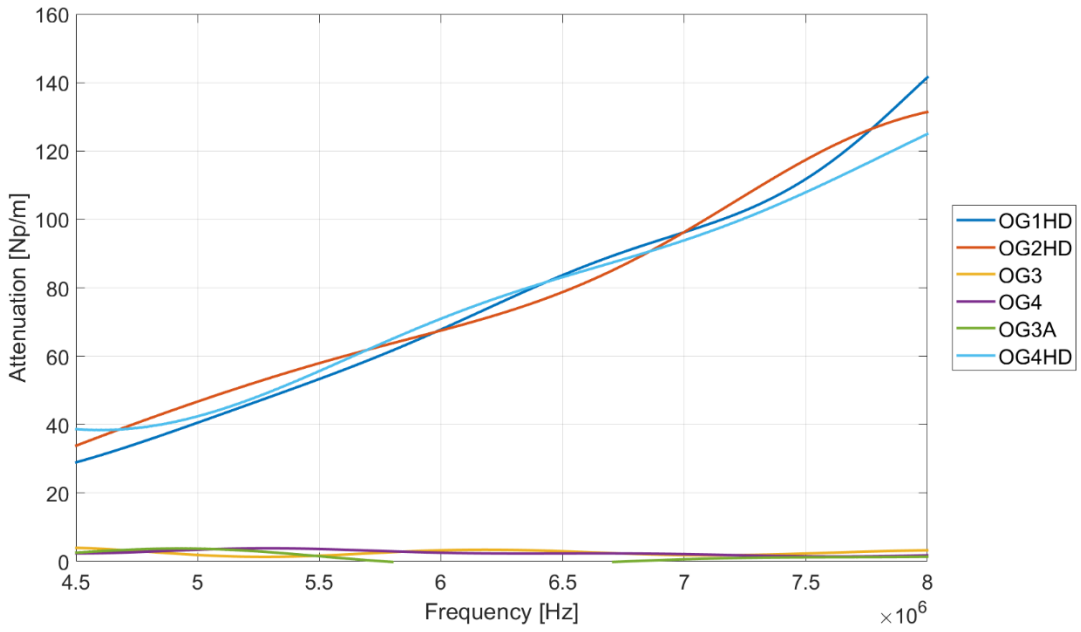


Figure 133: Comparison of frequency-dependent attenuation between heat damaged and fine grained OG samples at the lower frequency range.

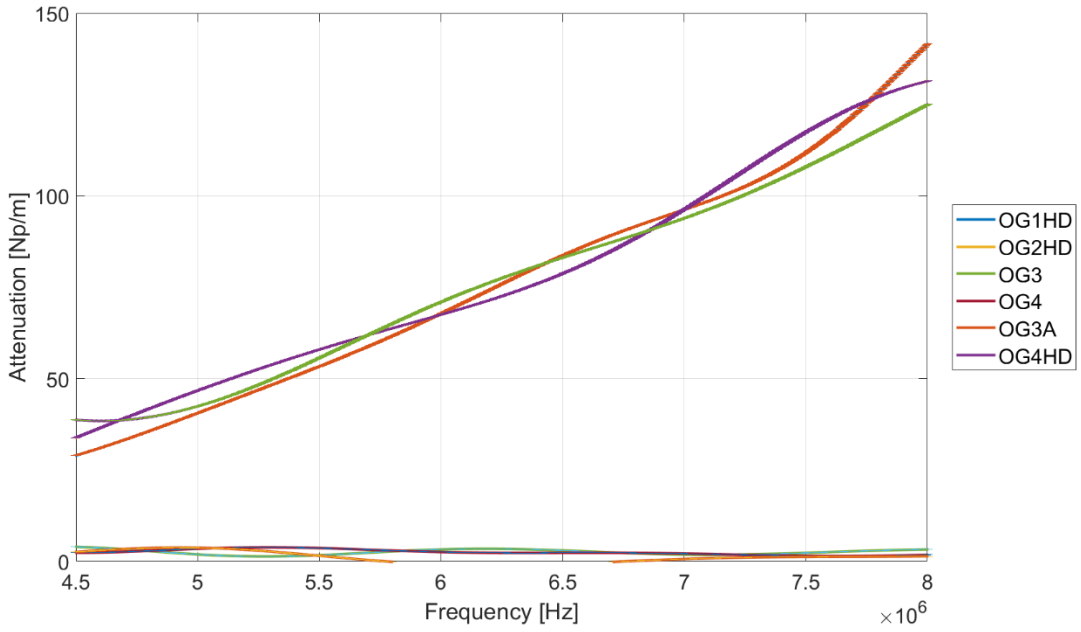


Figure 134: Comparison of frequency-dependent attenuation between heat damaged and fine grained OG samples at the lower frequency range. The standard deviation error bars have also been overlaid.

For the RR Furnace set of samples, whose profiles have been shown in Figure 135, there is again a clear trend exhibited with the attenuation increasing exponentially as the frequency increases. However, the contrast in attenuation levels shown in both sets of materials are not vastly different; in combination with the amount of fluctuation present, it is hard to determine quantitative microstructural information from these data. Figure 136 shows the frequency-dependent attenuation of the RR Furnace set of samples but with the error bars in measurements also shown (represented by the standard deviation calculated for each measurement point). The fact that the error bars are relatively small, and all of similar magnitudes, indicates that in this case also, the samples are relatively homogeneous across all of the points scanned and hence the microstructure is fairly consistent.

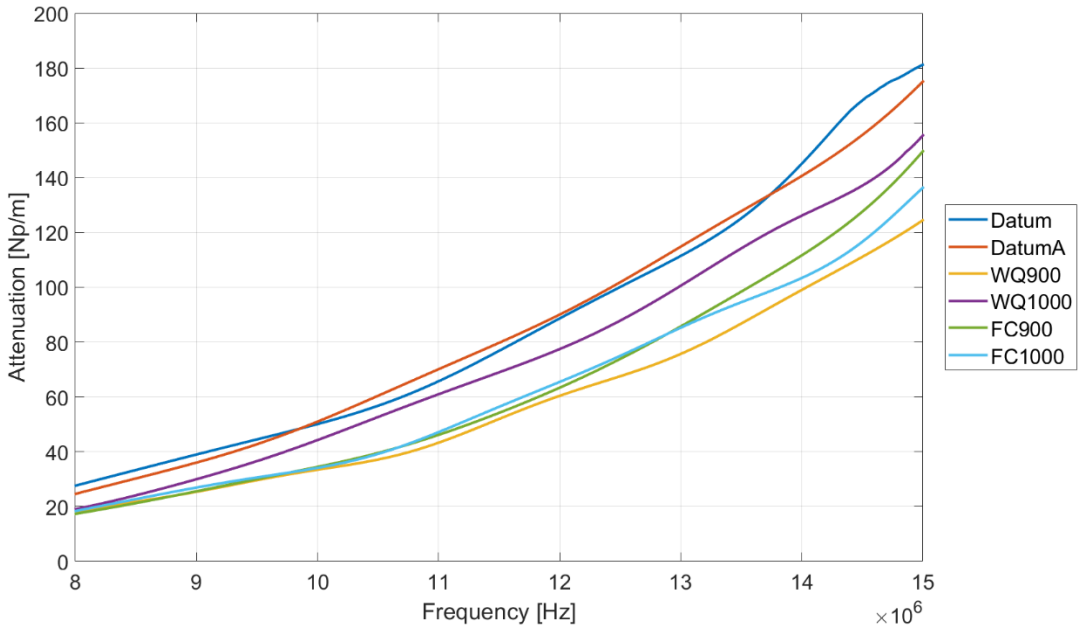


Figure 135: Frequency-dependent attenuation of RR Furnace samples.

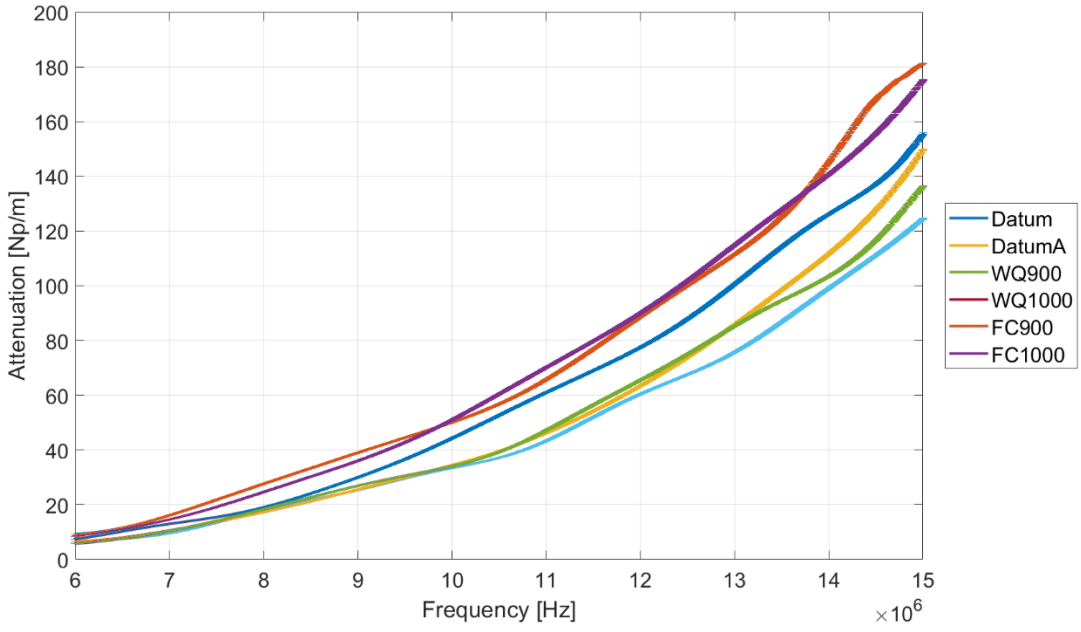


Figure 136: Frequency-dependent attenuation plots for RR Furnace samples, showing errors (represented by standard deviation bars).

9.3.6 Discussion

Although there is certainly a positive correlation between the frequency and attenuation, it is difficult to deduce much information in the way of microstructure from these results alone. It was shown that, despite large variations in microstructure (for example, between the WQ900 and WQ1000), these are not obviously manifested in attenuation value differences. In addition, the fact that the HD samples did not have attenuation data within a directly comparable frequency range rendered the use of frequency-dependent attenuation as a characterisation technique limited in its capability in this particular case. Nevertheless, the expected exponential increase in attenuation for the fine grained Inconel 718 samples was observed.

Due to the fact that attenuation is heavily dependent on grain size, it may be difficult to find a suitable transducer frequency which would give comparable data between the as-received and heat damaged samples of Inconel 718 (i.e. where the attenuation is within a suitable range where it is neither too low or too high and thus avoiding excessive levels of fluctuation). However, if further experiments were possible, it may be useful to trial a different range of transducer frequencies, as well as to modify the vertical distance between the sample and the transducer surface, to see at which point the frequency becomes too high for any echoes to be detected through the heat damaged, coarser grain samples, and to eliminate the issues caused by there being a double peak in the energy bandwidth of the transducers.

9.3.6.1 Comparison to UWS Measurements

When comparing these attenuation trends to the corresponding V00 measurements for the OG set of samples, it is difficult to draw any firm conclusions on how they can be linked to one another as there is only frequency response dataset within the expected transducer bandwidth, for the non-heat damaged OG samples as well as the RR Furnace samples. In addition, their attenuation values are all fairly similar, from which it can only really be inferred that their grain sizes are in the same order of magnitude – the differences in terms of precipitate proportions cannot really be detected. For the RR Furnace batch of Inconel 718 samples, all the sample profiles are within 60Np/m of each other at 15MHz, and for both the OG and RR Furnace data, the profiles of each sample overlap due to fluctuations. However, there does appear to be a slight hierarchy in the different samples; the Datum and DatumA (aged) samples have the highest levels of attenuation (with similar values), followed by WQ1000, FC900 and FC1000 and with WQ900 having the lowest level of attenuation. It had been expected that the samples which had been subjected to higher temperature heat

treatments (i.e. WQ1000 and FC1000) would have the slightly higher attenuation levels, as grain growth may have been more likely at these temperatures (as, though the aim was to avoid any grain growth occurring, it would have been impossible to prevent it completely). However, it may have been the case that the shorter hold time prevented this from occurring, or at least to a similar extent seen by FC900 – though it would have been expected that the δ phase would have caused a sufficient amount of pinning of the grain boundaries to prevent grain growth from occurring.

The fact that WQ900 has the lowest attenuation could call into question the working hypothesis that the excessive amount of δ phase is causing this sample condition to have a much lower V00 than predicted, due to it having a retarding effect on the ultrasonic waves; if this were the case, then the attenuation would be expected to be in a higher range, due to an increased amount of scatter. As it is highly unlikely that the phase composition of WQ900 is different to how it is expected – with both SEM and HS-AFM images in good agreement, and not highlighting any precipitates which should not be present – this difference in attenuation levels to what was expected is probably due to the fact that the attenuation values are not sufficiently accurate. Indeed, there is a notable amount of fluctuation, with some of the plots intertwining (such as Datum and DatumA), which calls into question how accurately any conclusions pertaining to the microstructure variations between the samples can be determined via attenuation measurements in this case. Hence it is still the working theory that the impact of solid solution strengthening is having the most impact in terms of the V00 values for the RR Furnace samples exhibiting a different trend to expectations.

9.3.6.2 Experimental Technique

As described in the Experimental Methodology section, there were various measures taken during the establishment of the post-processing steps in order to minimise errors in the experimental results; for example, using a higher frequency transducer in order to force greater levels of attenuation to reduce fluctuations, which can result where attenuation is very low, and using C-scans, rather than just a single A-scan, to obtain an effective average of multiple points across the sample surface. In addition, the number of sampling points was increased and then padded using zeros, to obtain as smooth a frequency profile as possible. However, despite these precautions, the frequency plots are still not completely smooth, and this is a result of parameters which are inevitable as part of the C-scan acquisition, such as the signals being of similar amplitudes to the background noise (particularly the backwall echoes). Despite using the minimum length window to encompass each individual error when they were being isolated before the Fourier transform, the

effect of background noise could not be completely eliminated. There was also the additional issue of the double peak in the FWHM of the front wall echo, which put into question the accuracy of the C-scan data being acquired; in the future, it would be beneficial to repeat the experiments using a different transducer (in case it was faulty) as well as trial different axial separations.

9.3.7 Conclusions

The experimental data from attenuation measurements for all of the nickel-based superalloys tested thus far have had mixed results; in the case of Inconel 718, it was found that only the finer grained samples could have attenuation quantified within the FWHM bandwidth of the transducer (8-15MHz), with the heat damaged, coarse grained samples exhibiting the trend of increased attenuation with frequency, but in a substantially lower frequency range than that which was realistic for a 15MHz transducer. In the case of the RR Furnace set of Inconel 718 discs, all samples did have the expected increasing attenuation with frequency within the FWHM of the transducer, but with the observed fluctuations and similarity in values, it is hard to determine whether these measurements would be able to detect any minor microstructural variations which had occurred in the material; even differences in grain size would be difficult to quantify. Indeed, the fact that attenuation is primarily affected by changes in grain size, rather than any differences in precipitate compositions, limits its ability to be deployed for the quantification of phase changes, and grain size variations will have a much more significant effect on the measurements of attenuation than any changes in phase composition itself.

For the samples of Udimet 720Li and RR1000, it was not possible to obtain useful data for all of the samples, meaning that the results acquired were limited in their use; in the case of Udimet 720Li, the attenuation levels appeared to be too low to accurately quantify the profile. It is well known that this material is particularly difficult to inspect using ultrasonics due to its high level of noise, which was clear from the excessive fluctuation seen in the full frequency plot of the attenuation calculations. For RR1000, the fine grained samples showed similar difficulties in having such high levels of fluctuations that it was impossible to isolate even a small region within the FWHM with good quality data. However, it was interesting to observe that the coarse grained RR1000 sample, which could have a frequency-dependent profile calculated, did have a slightly lower level of attenuation than Inconel 718.

Nevertheless, the frequency-dependent attenuation could still be used in combination with the UWS method and hardness testing as a materials characterisation framework, as it would be a rapid way to determine if there had been any undesirable grain growth; changes in phase composition could then be the role of the V00 measurements. There is further experimental work required to refine this technique – it would be beneficial to have several data sets for each sample, across a range of frequencies, in order for comparisons for real test pieces in industry for future use. It would be particularly useful to have a set of data where there was not a double peak being seen in the FWHM of the transducer, to ensure this effect was not having an adverse impact on the experimental data. An larger dataset would also help to verify whether the nature of the attenuation characteristics of the material is such that the values will always be very similar to each other, providing they have a similar grain size (such as for the RR Furnace samples), despite quite drastic variations in terms of the precipitate composition, and to attempt to get smoother profiles than those which have been acquired here. Despite its limited use, however, it has still been an interesting exercise in terms of investigating an alternative ultrasonic-based method to detect microstructural changes within these three nickel-based superalloys, and identify where there could be improvements to the experimental technique or indeed where there are instances where the method may not be usable for this particular transducer frequency (such as for extremely fine grained samples).

9.4 High Speed Atomic Force Microscopy (HS-AFM)

9.4.1 Applications of AFM

Historically, AFM has been primarily used for biological studies, due to its small sample size and slow data-collection time; it is also not limited to vacuum or low pressure conditions, and can be used in gaseous or liquid environments – making it optimal for measuring physiological phenomena in situ [230]. However, there have been many developments in advancing AFM hardware[16] in recent years, improving the bandwidth of components to allow a drastic increase in the pixel rate of the devices and thus much faster imaging speeds [230]. As a result, the technique is gaining popularity for use in materials science, due to its high spatial and temporal resolution. Some examples include, in addition to topography, the mapping of friction [352] [353] [354] and adhesion [355] [356] [357], as well as nano-mechanical properties such as local stiffness, [358] [359] [360] [361] [362] [363] [364] [365] [366] and both electrical [367] [368] and thermal [369] [370] conductivities. A particularly interesting application is the assessment of the carbide distribution within type 316 steels [371], by utilising the fact that an increased concentration of carbon (in the form of carbides) increases not only the hardness, but the brittleness of the steel [372]; a relative hardness map generated by AFM can therefore be used to determine regions of high carbide concentrations. One particular use for HS-AFM which may be of use in future studies is the ability to map stiffness variations with contact resonance force microscopy, or CR-FM [373] [374] [375]; using this with a contact mode HS-AFM makes it possible to measure the relative stiffness at each pixel, at the same time as the sample's topography [230]. The CR-FM measures the stiffness of the sample by observing the frequency shift of a deflection mode resonance peak of the probe, as the tip moves between the different types of material present in the sample [376] [363] [374] [377]. With the assumption that the cantilever properties remain constant, a frequency shift in the coupled cantilever-local sample system is assumed to be due to changes in the local sample stiffness, and thus a relative stiffness can be inferred [359] [373]; the stiffer the local sample, the higher the resonant frequency of the particular system.

[16] Such developments in hardware include a vast improvement in the frequency of the detection system (from 2MHz in standard contact mode AFM [34] to 25MHz in HS-AFM [35]) and the speed of the XY stage movement (from 10 lines per second [34] to between 1~100k lines per second [36]).

9.4.2 Design Considerations of AFM

The main design considerations of an AFM system include the probe and cantilever, the detection system, the scan stage as well as the imaging mode, all of which are discussed briefly below.

9.4.2.1 Imaging Mode

In order to measure the topography (and other properties) of the sample, the probe must be moved in a serial fashion from pixel to pixel; an electronic control loop is used to maintain a consistent probe-sample interaction force, and prevent damage to the tip and/or the sample [230]. The three main imaging modes available are named after the various electronic control loop schemes used; contact mode is the most commonly used [378] (and is indeed the scheme used in the present investigation), though there is also intermittent contact mode (or tapping mode) [379] [380] and non contact mode [381]. Contact mode is the imaging mode of the original AFM [382], and uses the simplest control system – the probe is held in continuous contact with the sample surface during scanning, and the force exerted on the sample by the probe tip is controlled by monitoring the deflection angle of the cantilever beam [230].

9.4.2.2 Probe Design

In terms of the probe design, the material will typically be silicon or silicon nitride, and the assembly consists of a micro-fabricated cantilever beam with a sharp detection tip (usually etched), at its free end [230]. Silicon nitride has a very low spring constant (between 0.006 and 1N/m) which helps to minimise the interaction force normal to the sample surface [230]. For contact mode, the cantilevers tend to be hundreds of microns in length with a fundamental resonant frequency of less than 10kHz [230]. It should be noted that probes with higher frequencies are generally more desirable, as the control system measures the amplitude od probe oscillation and is subsequently limited in its response speed by the frequency of the oscillation – the higher the frequency, the higher the number of pixels measured per second and the lower the overall imaging time [383] [384] [385] [386] [387].

9.4.2.3 Detection System

In terms of the detection system, the typical characteristics required are a bandwidth greater than 1MHz, and a sub-nanometre sensitivity to displacements and deflections of the cantilever beam. There are a range of techniques available to measure the motion of the cantilever; the most commonly used method is optical beam deflection [388] [389] [390] due to its ease of

implementation with relatively inexpensive components, but increased accuracy in cantilever deflection measurements can be achieved using the laser Doppler vibrometer (LDV) configuration [391] [392] [393], which is what has been used for the HS-AFM measurements here. This technique uses a laser beam and interferometer, where the interferometer splits the light into two parts; the reference beam points at the photo detector, while the measurement beam is incident on the cantilever [394]. This beam is reflected off the cantilever and onto a quadrupole photodiode; when the cantilever comes into contact with the sample, it is pushed up at the tip and causing the angle at which the light is reflected to change [392]. Depending on the velocity and displacement, this backscattered light is changed in frequency and phase, and the superposition of this light with the reference beam results in a 'modulated detector output' signal, which reveals the Doppler shift in frequency [394]. The load on the surface can then be calculated by measuring the displacement of the tip and using the cantilever's flexural spring constant [392]. The use of LDV to measure the z displacement of the cantilever tip is able to produce an instantly calibrated topographic map of the surface, and thus decreasing the overall time of measurement [391]. These measurements of probe deflection are input into a feedback loop [395] [396] [397] [398], as well as the specified setpoint value of frequency that should be maintained[17] [230]. A further advantage of contact mode is that it has the fastest feedback loop [399] of the various operating modes; the cantilever's response to the surface can be fed back to the feedback loop as fast as the detection system allows, rather than requiring a whole period of oscillation before the measured signal can be acted upon [230].

[17] Other measured parameters could include oscillation amplitude or deflection angle.

9.4.2.4 Scan Stage Design

The XYZ stages for translating the probe relative to the sample surface must be capable of small steps (in the sub-nanometre range) and fast linear motions; typically piezoelectric actuators are used with a mechanical assembly which enables stable, smooth motions with negligible out-of-plane vibrations and errors [230]. The faster the stage can move in the 'fast scan' direction, the more lines can be collected per second (resulting in a smaller pixel size and hence a better resolution), and the faster it can move in the 'slow scan' direction, the higher the frame rate; however, the speed at which the stage moves is limited by the stiffness of the stage, the speed at which the actuators can exert a sufficient force, and the resonant frequency of the stage [230].

It should also be noted that it is crucial to measure accurately the positional errors of AFM scan stages to analyse AFM images, especially when mosaicking individual images to create larger, high resolution composite images [400] [401].

9.5 Udimet 720Li γ’ volume fraction estimates

Table 33: ImageJ estimates for volume fraction of gamma' in Udimet 720Li samples, using SEM micrographs.

Sample	Micrograph	Volume fraction of γ’ phase
Part C	U720Li C_CBS_80x_02.tif	41.486
	U720Li C_CBS_100x_03.tif	40.98
	U720Li C_CBS_500x_04.tif	32.953
	U720Li C_CBS_1000x_05.tif	20.37
	U720Li C_CBS_2000x_06.tif	38.792
Part MR	U720Li MR_CBS_80x_01.tif	50.168
	U720Li MR_CBS_100x_02.tif	49.672
	U720Li MR_CBS_500x_03.tif	26.674
	U720Li MR_CBS_1000x_04.tif	25.637
	U720Li MR_CBS_2000x_05.tif	42.173
Part S	U720Li S_CBS_80x_01.tif	45.245
	U720Li S_CBS_100x_02.tif	44.495
	U720Li S_CBS_500x_03.tif	29.803
	U720Li S_CBS_1000x_04.tif	37.642
	U720Li S_CBS_2000x_05.tif	32.793

Table 34: ImageJ estimates for volume fraction of gamma' in Udimet 720Li samples, using optical micrographs.

Sample	Micrograph	Volume fraction of γ’ phase
Part C	C_Kallings_50x.jpg	32.78
	C_Kallings_100x.jpg	25.41
	C_Kallings_200x.jpg	24.049
	C_Kallings_500x.jpg	29.753
	C_Kallings_1000x.jpg	28.7
Part MR	MR_Kallings_50x.jpg	28.907
	MR_Kallings_100x.jpg	26.728
	MR_Kallings_200x.jpg	15.689
	MR_Kallings_500x.jpg	32.658
	MR_Kallings_Clump_1000x.jpg	29.872
	MR_Kallings_Normal_1000x.jpg	27.795
Part S	S_Kallings_50x.jpg	27.236
	S_Kallings_100x.jpg	24.985
	S_Kallings_200x.jpg	24.251
	S_Kallings_500x.jpg	28.533
	S_Kallings_Clump_1000x.jpg	29.105
	S_Kallings_Normal_1000x.jpg	32.773

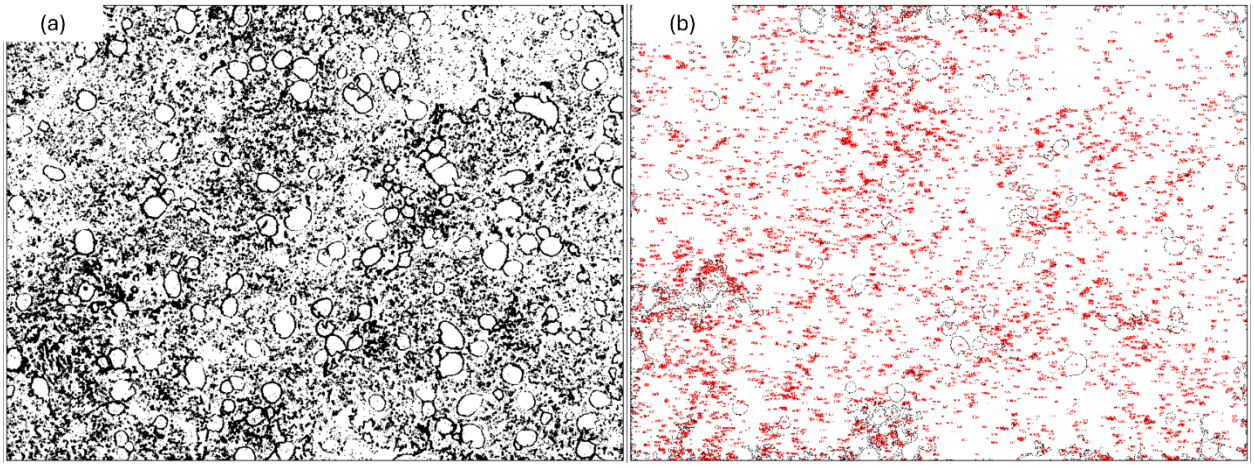


Figure 137: ImageJ analysis of a micrograph of Udimet 720Li sample 'Part C', showing (a) colour threshold image and (b) analysed particles.

9.6 RR1000 γ' volume fraction estimates

Table 35: ImageJ estimates of volume fraction of γ' phase in RR1000 samples.

Sample	Micrograph	Volume fraction of γ' phase
As-Forged	AF_50x.jpg	31.935
	AF_100x.jpg	34.699
	AF_500x.jpg	17.301
	AF_200x.jpg	29.075
	AF_1000x.jpg	18.178
	RR1000 AF CGrey Ti K.tiff	53.166
	RR1000 As-Forged_CBS_80x_01.tif	46.126
	RR1000 As-Forged_CBS_100x_02.tif	45.393
	RR1000 As-Forged_CBS_500x_03.tif	45.24
	RR1000 As-Forged_CBS_1000x_04.tif	45.495
	RR1000 As-Forged_CBS_2000x_05.tif	45.274
	RR1000 As-Forged_ClumpCity_CBS_250x_05.tif	43.103
	RR1000 As-Forged_ClumpCity_CBS_1000x_03.tif	42.841
	RR1000 As-Forged_ClumpCity_ETD_1000x_02.tif	40.231
	RR1000 As-Forged_Etched_ETD_80x_01.tif	23.571
	RR1000 As-Forged_Etched_ETD_100x_02.tif	38.918
	RR1000 As-Forged_Etched_ETD_500x_03.tif	46.386
	RR1000 As-Forged_Etched_ETD_1000x_04.tif	41.758
	RR1000 As-Forged_Etched_ETD_2000x_05.tif	39.646
	RR1000 As-Forged_Etched_ETD_10000x_06.tif	46.96
	RR1000 As-Forged_Etched_ETD_30000x_07.tif	29.024
Coarse	RR1000_Coarse_50x.tif	15.97
	RR1000_Coarse_100x.tif	37.511
	RR1000_Coarse_200x.tif	37.77

	RR1000_Coarse_200x_2.tif	52.366
	RR1000_Coarse_1000x.tif	34.613
	RR1000_CoarseM2_ETD_SE_5.00kV_0.20nA_500x_04.tif	40.502
	RR1000_CoarseM2_ETD_SE_5.00kV_0.20nA_2000x_06.tif	34.337
	RR1000_CoarseM2_ETD_SE_5.00kV_0.20nA_10000x_08.tif	44.766
	RR1000_CoarseM2_T1_A+B_5.00kV_0.20nA_500x_05.tif	24.091
	RR1000_CoarseM2_T1_A+B_5.00kV_0.20nA_2000x_07.tif	22.448
Fine	RR1000_Fine_50x.tif	31.461
	RR1000_Fine_100x.tif	27.088
	RR1000_Fine_500x.tif	33.053
	RR1000_Fine_1000x.tif	27.59
	RR1000_Fine_1000x_DF.tif	14.368
	RR1000_Fine_1000x_DF_2.tif	24.753
	RR1000_Fine_M1_ETD_SE_5.00kV_50pA_50000x_01.tif	33.096
	RR1000_FineM1_CBS_All_5.00kV_0.40nA_500x_06.tif	42.67
	RR1000_FineM1_CBS_All_5.00kV_0.40nA_1000x_07.tif	34.628
	RR1000_fineM1_ETD_SE_5.00kV_0.10nA_500x_04.tif	42.693
	RR1000_FineM1_ETD_SE_5.00kV_50pA_2000x_09.tif	31.445
	RR1000_FineM1_T1_A+B_5.00kV_0.10nA_500x_05.tif	29.362